ÉCOLE DOCTORALE D'ASTRONOMIE ET ASTROPHYSIQUE D'ILE-DE-FRANCE

UNIVERSITÉ Paris VII - Université Denis Diderot

Pour obtenir le grade de

DOCTEUR EN ASTRONOMIE ET ASTROPHYSIQUE

Présentée par

David CSEH

Laboratoire AIM - CEA/Service d'Astrophysique - Université Paris Diderot
Bat. 709, 91191 Gif-sur-Yvette, France

Ultraluminous X-ray Sources and Intermediate-mass Black Holes

---

Soutenue le 28 Sep 2012

Après avis de :	Christian MOTCH	Rapporteurs
	Thomas MACCARONE	

Devant le jury composé de :

Etienne PARIZOT	Université Paris VII	Président
Stephane CORBEL	CEA-Université Paris VII	Directeur de thèse
Christian MOTCH	Observatoire de Strasbourg	Rapporteur
Thomas MACCARONE	University of Southampton	Rapporteur
Didier BARRET	IRAP Toulouse	Examinateur
Guillaume DUBUS	IPAG Grenoble	Examinateur

2012

Abstract

More than ten years ago, the discovery of ultraluminous X-ray sources (ULXs) has opened up an entirely new field in astrophysics. Many ideas were developed to explain the nature of these sources, like their emission mechanism, mass, and origin, without any strong conclusions. Their discovery boosted the fields of X-ray binaries, accretion physics, stellar evolution, cosmology, black hole formation and growth, due to the concept of intermediate-mass black holes (IMBHs). Since their discovery is related to the domain of X-ray astrophysics, there have been very few studies made in other wavelengths. This thesis focuses on the multiwavelength nature of ultraluminous X-ray sources and intermediate-mass black holes from various aspects, which help to overcome some difficulties we face today.

First, I investigated the accretion signatures of a putative intermediate-mass black hole in a particular globular cluster. To this purpose, I characterized the nature of the innermost X-ray sources in the cluster. Then I calculated an upper limit on the mass of the black hole by studying possible accretion efficiencies and rates based on the dedicated X-ray and radio observations. The accreting properties of the source was described with standard spherical accretion and in the context of inefficient accretion.

Secondly, I attempted to dynamically measure the mass of the black hole in a particular ULX via optical spectroscopy. I discovered that a certain emission line has a broad component that markedly shifts in wavelength. I investigated the possibility whether this line originates in the accretion disk, and thus might trace the orbital motion of the binary system. I also characterized the parameters of the binary system, such as the mass function, possible orbital separation, the size of the line-emitting region, and an upper limit on the mass of the black hole.

Then I studied the environment of a number of ULXs that are associated with large-scale optical and radio nebulae. I use these nebulae as a calorimeters to infer the total intrinsic power of these ULXs, characterize the feedback on the environment, and compare to Galactic sources. I also investigated the power mechanism of inflating a bubble by jets. Then I discuss the current status of radio observations on ULXs, including ongoing radio surveys.

Finally, I studied HLX-1, which is likely the first bona fide IMBH. This involves radio observations and analysis of the radio data that led to a discovery of radio flares from this source during an X-ray state transition. From the strength of the flares, I provided additional constraints on the mass of the black hole and its accretion rate.

Resumé

La découverte des sources X ultralumineuses (de l'anglais Ultraluminous X-ray sources, ULXs) , il y a maintenant plus de dix ans, a contribué à l'éclosion d'un nouveau domaine de l'astrophysique. Plusieurs idées ont été développées afin d'expliquer la nature de ces sources, le mécanisme régissant leur émission, leur masse ou leur origine mais aucune n'a réellement abouti. La découverte de ces objets, en lien avec le concept de trou noir de masse intermédiaire, a accéléré l'étude des binaires X, de la physique de l'accrétion, de l'évolution stellaire, de la cosmologie, de la formation et de la croissance des trous noirs. Puisque leur découverte a été faite dans le cadre de l'astrophysique des hautes énergies, très peu de travaux ont été réalisés dans d'autres domaines de longueurs d'onde. Cette thèse s'articule autour d'une étude multi-longueurs d'onde des ULXs et des trous noirs de masse intermédiaire et tente de surmonter quelques unes des difficultés inhérentes à la compréhension de ces objets.

Dans une première partie, j'étudie les signatures des phénomènes d'accrétion d'un probable trou noir de masse intermédiaire dans un amas globulaire donné. Ainsi, j'ai, pour la première fois, caractérisé la nature de la source X centrale de cet amas. L'étude de différents taux et efficacités d'accretion possibles, basés sur des observations X et radio m'a ensuite permis de proposer une borne supérieure à la masse du trou noir. Les propriétés de l'accrétion de cette source ont été décrites grâce au modèle d'accrétion sphérique ainsi que dans le contexte de l'accrétion inefficace.

Dans un deuxième temps, j'ai tenté de mesurer dynamiquement la masse du trou noir dans une ULX donnée à l'aide de la spectroscopie dans le domaine visible. J'ai découvert qu'une raie d'émission possède une composante large et décalée en longueur d'onde de manière significative. J'ai étudié l'hypothèse que cette raie émane du disque d'accrétion et qu'elle puisse ainsi rendre compte de la dynamique orbitale du système binaire. J'ai également caractérisé les paramètres de ce système binaire tel que sa fonction de masse, sa séparation orbitale, la taille de la région émettrice et le borne upérieure à la masse du trou noir.

J'ai ensuite étudié l'environnement d'un certain nombre d'ULXs associés à des nébuleuses visibles à grande échelle en optique et en radio. J'utilise ces nébuleuses en tant que calorimètres afin d'en déduire l'énergie totale intrinsèque de ces ULXs, je caractérise la rétroaction avec l'environnement et je compare ces sources à des objets observés dans notre Galaxie. J'étudie également le mécanisme d'expansion des nébuleuses par jets. Par ailleurs, je fais également l'inventaire des observations radio relatives aux ULXs.

Finalement, j'ai étudié la source HLX-1 qui est probablement un bon candidat trou noir de masse intermédiaire en menant une campagne d'observations radio qui a abouti à la découverte de sursauts radio provenant de la source durant un état de transitoire d'émission X. L'intensité de ces sursauts m'a permis de contraindre davantage la masse du trou noir et son taux d'accrétion.

Kivonat

Az Ultrafényes Röntgenforrások (UR-ok; ULXs) több mint egy évtizeddel ezelőtti felfedezése egy teljesen új asztrofizikai területet nyitott meg. Számos elméleti modellt dolgoztak ki annak érdekeben, hogy leírják ezen források természetét, mint például a sugárzási mechanizmusukat, tömegüket, eredetüket, de egyik sem vezetett kézzelfogható eredményhez. Felfedezésük jelentősen kihatott a röntgen kettősök, az akkréciós fizika, a kozmológia es a fekete lyuk keletkezési és fejlődési elméleteire abból kifolyólag, hogy Közepes Tömegű Fekete Lyukakat (KTFLY-akat; IMBHs) felteteleznek e források mögött. Mivel felfedezésük a röntgencsillagászat területéhez kötődik, kevés eddigi tanulmányt végeztek más hullámhosszokon. A doktori dolgozat az Ultrafényes Röntgenforrások és Közepes Tömegű Fekete Lyukak egyszerre több hullámhosszon mutatott viselkedésére összpontosít, ami segít felülemelkedni néhány jelenlegi elméleti nehézségen.

Első lépésként egy potenciális közepes tömegű fekete lyuk akkréciós jeleit kutattam egy gömbhalmazban. Ennek érdekében elsőként határoztam meg a halmaz legbelső röntgenforrásainak természetét, majd felállítottam egy felső határt a fekete lyuk tömegére vonatkozólag a lehetséges akkreciós hatásfok és ráta tanulmányozásával, amihez rádió és röntgen adatot használtam. A forrás akkréciós tulajdonságait általános szférikus anyagbefogással illetve alacsony sugárzási hatásfokú akkrécioval írtam le.

Ezt követően, kíséreltet tettem egy UR-ban lévő fekete lyuk dinamikai tömegének meghatározására optikai spektroszkópiával. Felfedeztem, hogy egy bizonyos emissziós vonalnak egy jelentősen kiszélesedett komponense van, ami számottevő hullamhosszeltolódást mutat. Azt kutattam, hogy ez a vonal származhat-e az akkréciós korongtól, így esetlegesen reprezentálva a kettős rendszer keringési pályamozgását. Meghatároztam a kettős rendszer olyan fizikai paramétereit, mint például a tömegfüggvényét, pályaszeparációját, és a vonalat kisugárzó tartomány méretét.

Továbbá számos olyan UR közvetlen környezetét vizsgáltam, amelyek körül kiterjedt optikai köd, illetve rádió nebula van jelen. Ezeket a nebulákat kaloriméterként használva meghatároztam az UR-ok összenergiáját, környezeti hatásukat, majd ezeket összevetettem a Tejútrendszerben lévő hasonló forrásokkal. Továbbá azt kutattam, hogy milyen energiamechanizmusai és egyéb jellemzői lehetnek egy plazmanyaláb által történő nebulafejlesztésnek. Ezek után kitérek arra, hogy bemutassam az UR-ok jelenlegi összes rádióészleléseinek helyzetét.

Végezetül, a HLX-1 nevű forrást tanulmányoztam, ami nagy valószínűséggel az első igazi KTFLY. Ez olyan rádióészleléseket és adatanalízist foglal magában, ami rádió kitörések felfedezéséhez vezetett a forrás röntgenállapotainak átmenetei alatt. A kitörések nagyságából további megerősítéseket tettem a fekete lyuk tömegét és annak akkréciós rátáját illetően.

I dedicate this work to Bogi and to my parents.

Acknowledgements

First of all, I thank my love, Bogi, for her support and endurance in these three years.

I am greatly indebted to Stephane, who constantly supported during my PhD, introduced to the astrophysical community, and guided in science politics.

I am also grateful for him because, he made it possible to be part of the French spirit for these three years. He also made available a funding from the European Community's Seventh Framework Programme under grant agreement number ITN 215212 "Black Hole Universe" for my PhD.

I would like to thank the Black Hole Mafia: Elise, Yi-Jung, Salome, Ivi, Y-Y, Pieter, Refiz, Pablo, Tao, Teo, Holger for the great 3 years we spent together.

I am also indebted to my "weird uncle" Jorn, to my "weird aunt" Sera, Stephane, Jerome, Phil, Tom, Rudy, Tomaso, Emrah, Tiziana, Luciano for creating the Network that significantly improved my possibilities, abilities, skills, knowledge in many aspects.

I want to thank for my collaborators Phil, Fabien, Cornelia, Tom, Jerome, Natalie, Rob, Sean, Mathieu, Mickael, Emil, Hugh, Sandor, Zsolt, Valeriu, and many others, who helped in research.

I also enjoyed a great time, Paris, and many beers with the guys here in the lab, with Alexis, Doris, Diane, Pedro, Tatjana, Timi, Vera, Sacha, Michael, Kevin, Camille, Marin, Diana, Willy, and many others.

Contents

List of Figures

List of Tables

1 Introduction

Contents

1.1 Intermediate-mass Black Holes

Science is one of the methods we use to answer the "big questions" such as: From where do we come?, How was the world created?, What is our purpose? By applying the scientific method, our knowledge has gradually increased from the era when people believed that shiny bugs are stuck to the sky, to the embracing of concepts like the Big Bang, dark matter, dark energy and black holes, which we do not yet fully understand. Approaching the big questions from a scientific point of view means that we can use modern technology to collect data and gain information from it, and then we organize this in a coherent way, leading us to new findings towards the answers.

One possible approach is to investigate these questions within the wider concept the entire Universe: its birth, evolution, and building blocks. Probably one of the most astonishing fundamental interactions is gravity, which is extremely important as it regulates

locally and globally our environment from everyday life to outer space and to the edge of the Universe. One of the manifestations of gravity is the formation and evolution of black holes throughout the cosmic history. Black holes and dark matter halos are the fundamental building blocks of galactic evolution, accretion, and represent matter under extreme conditions (Volonteri, 2012). These objects provide the most extreme phenomenon of the Universe as they convert surrounding matter into energy.

Due to the process of accretion, different parts of black hole systems radiate across the entire electromagnetic spectrum. To study these objects holistically, multiwavelength techniques are required, and this means the usage of a variety of space- and ground-based instruments in nowadays astrophysics.

Black holes have so far been observed to exist in just two distinct mass classes. Supermassive black holes (SMBHs; $10^5 - 10^9$ $M_\odot$) exist in the center of galaxies and, when activated by accretion, can be powerful enough to be detected from the edge of the visible Universe. Stellar mass black holes (StMBH; 3–20 $M_\odot$) form in binary systems, and are thus a natural stage of massive star evolution, existing throughout the Milky Way. Why the largest mass detected is only around 20 $M_\odot$ is not fully understood but hints at an upper limit to the mass of the precursor star and the effects of stellar mass loss through winds. The origin and growth history of SMBHs is still unfolded.

Intermediate-mass black holes (IMBHs; 20 –10^5 $M_\odot$) may be the missing link between StMBHs and SMBHs. Proving the existence of IMBHs and revealing their nature would result in a radical change in our understanding of the origin and evolution of black holes. Proof of their existence would be a real challenge for theories of star formation, and have important implications for gravitational wave research. IMBHs also provide the best way out from the difficulties we face in black hole growth at early cosmological epochs.

Regardless of size and/or mass, black holes accrete material via accretion disks. Some combination of angular momentum, strong gravity effects and magnetic fields leads to the launching of relativistic jets (Fig. 1.1). Jets are extremely important to many fields, because they are thought to be responsible for the acceleration of the highest energy particles in the Universe. Jets from SMBHs regulate their environments out to distances that are comparable to the sizes of the host galaxies so that they can even change and alter galaxy evolution. Jets carry away energy from the system, both in the form of matter and electromagnetic fields. Furthermore, it is still unclear how they form and what is their composition. With so many unknown parameters, the physics of accretion is still not well understood and many hypotheses of models coexist. To understand the capability of black holes' jets to accelerate particles, as well as their feedback on their environment, there is an urgent need in the community to determine the parameters governing of black hole accretion and jet launching.

It has recently been proposed that the accretion physics around black holes can be scaled to all sizes, which is supported by studies suggesting that at least sometimes SMBHs act as scaled-up StMBHs (Merloni et al., 2003; Falcke et al., 2004; McHardy et al., 2006). It means that, when the timescale of a physical process in StMBHs is equivalent with the human timescale (e.g. weeks), the same process in supermassive ones happens on a cosmic timescale, like in millions of years, because their characteristic time-scale is proportional to their size which scales with black hole mass. However, there are many questions around the upscaling phenomena, such as its universality in the various accretion modes we witness in StMBHs. Thus if similar accretion processes exist in SMBHs, it could be more easily revealed with an even distribution of black hole population. Therefore, it is very interesting to investigate the nature of any IMBH, which may can fill the

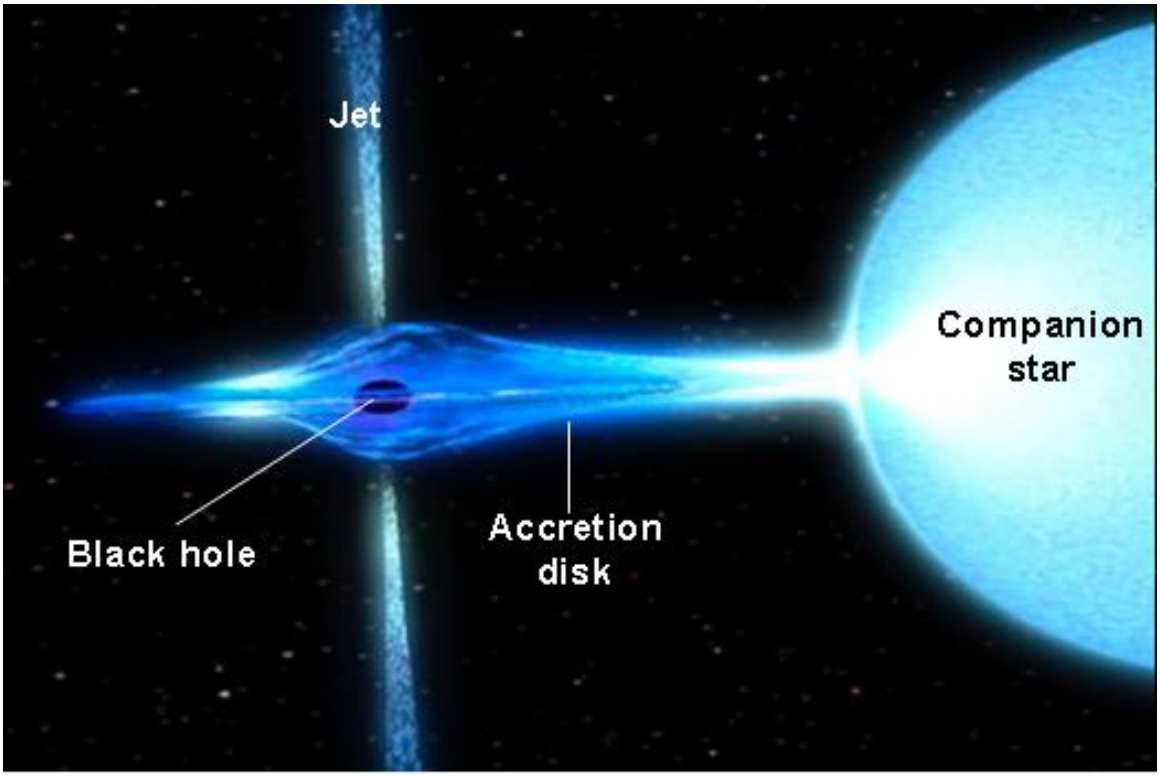

Figure 1.1: An artist's impression of a stellar-mass black hole system. Material accreted from the star forms an accretion disk around the black hole. A fraction of the accreted material is expelled from near the event horizon in the form of relativistic jets, which are comprised of particles and electromagnetic fields moving close to the speed of light. http://cse.ssl.berkeley.edu/hessi_epo/html/non-solar_pics/blackholebinary.jpg

gap between the two types.

1.1.1 Candidate Intermediate-mass Black Holes

In the early Universe, black holes are thought to have been formed along with the earliest collapse of matter into galaxies, as well as from the end product of the first massive stars. These early black holes likely seeded the SMBHs found today in the centers of almost all galaxies. These central black holes grew together with their galaxies, though it is still unclear how and when the first seed black holes at high redshift formed, and which accretion channel lead to $> 10^9$ $M_\odot$ SMBHs at z=6 (e.g. Ebisuzaki et al., 2001). It has also been proposed that IMBHs could form from the remnants of the very first generation, Population III stars (Madau & Rees, 2001) and have provided the seed for building up a SMBH via merging galaxies, and accretion (Ebisuzaki et al., 2001). Though, the viability of this view is not clear, and supporting evidence needs to be obtained from a study of candidate IMBHs formed recently in nearby galaxies from massive stars or via similar dynamical interactions. Considering a simple path of black hole growth via only accretion, Ebisuzaki et al. (2001) have shown that the growth for a black hole can be given

by:

$$t_{growth} = 0.45\,\mathrm{Gyr}\,\frac{\epsilon}{1-\epsilon}\,\lambda^{-1}\,\ln\left(\frac{M_{fin}}{M_{in}}\right) \tag{1.1}$$

where, M_{fin} is the final mass of the black hole, M_{in} is the initial mass of the black hole, ϵ is the radiative efficiency, and λ is the Eddington ratio (L_{bol}/L_{Edd}). This would lead to the conclusion that for an initial black hole formed at a high redshift (eg. $z = 20$), to reach 10^9 $M_\odot$ ~0.7 Gyr later, at z = 6, assuming standard $\epsilon = 0.1$ and continuous accretion at the Eddington-limit, it must have started with $M_{in} \simeq 100\,M_\odot$.

However, the origin of the first massive stars with 100 $M_\odot$ challenges astrophysics. Population III stars are though to be evolved in low metallicity environments of $Z \leq 10^{-5} Z_\odot$ (e.g. Abel et al., 1998). If the metallicity is low, then line cooling is negligible in the molecular clouds which results in higher temperature. Taking into account the scaling of the Jeans-mass with temperature, $M_J \propto T^{3/2}$, one might conclude that Population III stars could have much higher masses than a star can reach now. Furthermore, low (or zero) metallicity has another consequence: the opacity is lower in the stellar envelope so that it may be transparent to radiation pressure generated stellar winds, thus preventing mass loss and allowing the formation of a massive progenitor star that could directly collapse into a massive black hole (Fryer et al., 2001). However, the process of how a massive star ends up as a (massive) black hole is not well understood. What is more, after these early black holes are formed, they must grow quickly as shown above. Bondi-Hoyle accretion is often used to model early black hole growth, which describes spherical accretion of matter from the interstellar medium (ISM) onto a black hole:

$$\dot{M} = \frac{4\pi\rho G^2 M^2}{(c_s^2 + v_{rel}^2)^{3/2}} \tag{1.2}$$

where ρ and c_s are the density and sound speed of the flow in the vicinity of the black hole and v_{rel} is the velocity of the black hole relative to the local flow. One of the key problems with the growth of these early black holes is that accretion luminosity will preheat the matter, thus increasing the temperature, and so reducing the accretion rate. Also, the time needed for building up a SMBH is over the Hubble time and longer than the survival time of a molecular cloud (see review Miller & Colbert, 2004). It is even more challenging to explain how to secure a low temperature and high density environment for an off-nuclear object (like a ULX, see later).

It is often thought that a third path to form massive black holes is through dense stellar clusters. Depending on the initial conditions in a protogalaxy, e.g. in case of a local instability, stars may form a dense stellar cluster (see review Volonteri, 2012). Portegies Zwart & McMillan (2002) suggests that in these clusters, due to stellar dynamical interactions, a massive star of a 1000 $M_\odot$ may form via mergers. Also, if the metallicity is low, then this massive star may collapse directly into an IMBH by retaining most of the progenitors mass. However, as mentioned above, at the current cosmological epoch, the metal content of the Universe is much higher, which may cause strong mass loss via stellar winds, thus preventing the massive star to form a massive black hole.

Another aspect of IMBHs is that they might probe various type of accretion. For instance, black holes with a mass below 10^5 $M_\odot$ were predicted to accrete above their Eddington-limit (see below) at a redshift of z~6 (Wyithe & Loeb, 2011). Moreover, inspiralling IMBHs are predicted to produce significant gravitational wave radiation, making IMBHs important targets for the next generation of gravitational wave detectors (Ab-

bott et al., 2009); they also have other cosmological implications such as the search for dark matter annihilation signals (Fornasa & Bertone, 2008), and may have significantly contributed to the cosmic reionisation (Wang et al., 2010; Mirabel, 2011).

1.1.2 Accretion and the Eddington-limit

In the following I briefly describe the basics of accretion (Frank et al., 2002) onto a (Schwarzschild) black hole. Considering a black hole system, the gravitational energy and the angular momentum of the infalling matter are transformed into thermal energy and radiation. To bring an object of mass m from $R = \infty$ onto a circular orbit around a compact object of the mass M, the following equation applies:

$$\frac{mv^2}{R} = \frac{GMm}{R^2} \tag{1.3}$$

The energy is released by friction in the accretion disk and can be described as:

$$E_{acc} = E_\infty - E_R = 0 - \left(\frac{1}{2}mv^2 - \frac{GMm}{R}\right) = \frac{1}{2}\frac{GMm}{R} = \frac{1}{2}\left|E_{pot}\right| \tag{1.4}$$

Substituting the Schwarzschild radius, $R_S = \frac{2GM}{c^2}$, into the above equation, the luminosity is:

$$L_{acc} = \frac{dE_{acc}}{dt} = \alpha\frac{R_S}{R}\frac{dm}{dt}c^2; \;\; \alpha < \frac{1}{4} \tag{1.5}$$

For comparison, the efficiency of hydrogen burning is: $L_H \simeq 0.007\dot{m}c^2$, so accretion is the most effective way to transform mass into energy:

$$L_{acc} \simeq 4 \cdot 10^{45}\left(\frac{\dot{m}}{\mathrm{M}_\odot/\mathrm{yr}}\right)\mathrm{erg/s} \tag{1.6}$$

The maximum energy rate (Eddington luminosity; L_{Edd}) is reached when the radiation pressure generated by the accretion is higher than the gravitational acceleration per unit area. The energy flux through a surface with radius R is $\frac{L}{4\pi R^2}$, which results in a radiation pressure of $\frac{L}{4\pi R^2 c}$. Therefore, accretion stops when:

$$\frac{L}{4\pi R^2 c}\sigma_e \geq \frac{GM}{R^2}\left(m_p + m_e\right), \tag{1.7}$$

where $\sigma_e = \frac{8\pi}{3}\frac{e^4}{m_e^2 c^4}$ is the cross-section of Thomson-scattering. Thus the Eddington Luminosity is

$$L_{Edd} = \frac{4\pi cGMm_p}{\sigma_e} = 1.3 \cdot 10^{38}\left(\frac{M}{\mathrm{M}_\odot}\right)\mathrm{erg/s} \tag{1.8}$$

Typical temperatures of accreting material can be derived by assuming that the energy $L_{Edd}/2$ is released through thermal emission between R_S and $2R_S$:

$$\frac{L_{Edd}}{2} = \sigma_{SB}T^4\left(4\pi R_S^2 - \pi R_S^2\right) \simeq \sigma_{SB}T^4 3\pi R_S^2 \tag{1.9}$$

Then one obtains for a characteristic temperature:

$$T \simeq 3 \cdot 10^7\,\mathrm{K}\left(\frac{M}{\mathrm{M}_\odot}\right)^{-1/4} \simeq 1\,\mathrm{keV}\left(\frac{M}{\mathrm{M}_\odot}\right)^{-1/4} \tag{1.10}$$

1.2 Ultraluminous X-ray Sources

What is the nature of a nearby IMBH that we can study and deduce important information from, to understand the early universe? Among the best candidate IMBHs are ultraluminous X-ray sources (ULXs). In this Section, I will discuss the aspects and properties of ULXs and also show further reasons why (or why not) to consider them as IMBHs.

ULXs are thought to be good candidate IMBHs mainly because their X-ray luminosities exceed the Eddington limit of a 20-$M_{\odot}$ black hole. Therefore, by definition, ULXs have a bolometric luminosity $> 3 \times 10^{39}$ erg/s. However, this luminosity could still be reached by neutron stars or young supernova explosion events, so a bona fide ULX is defined to have X-ray luminosities at or above 1×10^{40} erg/s. The maximum luminosity of a ULX (found to date) reaches 10^{42} erg/s, which is already in the upper end of the X-ray luminosities of low luminosity AGN (LLAGN). On the other hand, what makes a ULX crucially distinguishable from LLAGN is that ULXs are non-nuclear sources, residing outside of the core of the host galaxy.

Turning to a historical perspective (see review Miller & Colbert, 2004), ULXs were first observed in the 1980s with the Einstein satellite (Fabbiano & Trinchieri, 1987). The Einstein satellite discovered that beyond AGN, many spiral galaxies had bright X-ray sources. Due to the insufficient resolution of the satellite ($\sim$1 arcmin), it was not possible to distinguish between nuclear, non-nuclear, and multiple objects as the origin of these X-ray sources. The idea that they could be supermassive black holes was challenged since there was no evidence in the optical band for an AGN. Their nature remained unknown due to the low quality X-ray spectral and imaging capabilities of the Einstein satellite.

The ROSAT X-ray satellite was launched in 1990, it had an angular resolution of 10-20 arcsec as well as a much improved sensitivity compared to the Einstein satellite. Many more ULXs were discovered (e.g. Colbert & Mushotzky, 1999; Roberts & Warwick, 2000; Lira et al., 2000; Colbert & Ptak, 2002) and it was found that some of these sources were not located at the nucleus of the host galaxy. The ROSAT spectrometer was the best that time, but only covered the 0.2-2.4 keV range, thus limiting the spectral study of ULXs. Despite these inabilities, ROSAT surveys started to boost ULX research. The birth of advanced X-ray telescopes like Chandra and XMM-Newton has led to a current survey sample of about 300-400 ULXs (e.g. Miller & Colbert, 2004; Sutton et al., 2012).

1.2.1 X-ray Spectra of Ultraluminous X-ray Sources

To unveil the details of ULX X-ray spectra, I briefly discuss some of the physical background of accretion from an accretion disk.

A fraction of the gravitational energy is transformed due to the viscosity in the accretion flow. In the standard disk model, the gravitational energy conversation to radiation is efficient, resulting in a "cool disk" ($T \sim 10^2 - 10^5$ K), which is assumed to be geometrically thin and optically thick. However, regardless of the disk model, the basic concept is that a disk has a significant amount of angular momentum per unit mass which needs to be eliminated to allow accretion by the central object (see review Armijo, 2012). Multiple viscous disk layers are often considered. Due to shearing of these layers, friction heats up the gas that cools by radiation. Friction also transports the angular momentum to the outer regions of the disk, layer by layer, which causes the expansion of the disk.

In the following, I will briefly mention the characteristics of the disk, paying special care to the assumptions and simplifications it involves, following Armijo (2012). Gener-

ally, this physical system is characterized by the Navier-Stokes equation, describing the motion of a viscous compressible fluid with a variable dynamic viscosity. Typically one employs the mass conservation law and then the momentum conservation law:

$$\rho\left(\frac{\partial}{\partial t}\mathbf{v}+(\mathbf{v}\nabla)\mathbf{v}\right)=\nabla T+\rho f_e=-\nabla p+\nabla\tau-\rho\nabla\Psi \tag{1.11}$$

Here, T is the stress tensor in the form of $T=-pI+\tau$, where I is the identity matrix, τ is the viscous stress tensor in the form of $\tau_{ij}=\mu\sigma_{ij}$, where μ is the dynamic viscosity and σ_{ij} is the shear tensor. Furthermore, the internal forces acting on the fluid is $-\nabla p+\nabla\tau$, while the external forces are from the gravitational potential $-\nabla\Psi$.

Considering cylindrical coordinates and simplifying symmetries by approximating $v_r(r,z)\simeq v_r(z)$, $v_\phi(r,z)\simeq v_\phi(r)$, $v_z\simeq 0$, leads to a vertical integration over the vertical coordinate with the scale of height of the disk as the integration limits: $\pm H(r)/2$. Also, this allows us to use quantities per unit surface instead of unit volume. Another simplifying assumption is that we neglect the gas gradient pressure along the radial direction, and assume $T_{rr}=T_{r\phi}=0$, which is a justified assumption due to the fact that $v_\phi >> v_r$. This way, the only important viscous force is between $r-dr, r$ creating a force per unit surface that exerts a torque that transports angular momentum. Typically, the radial acceleration due to the viscosity and the pressure gradient term is negligible compared with the gravitational forces in the radial direction.

The condition $v_z\simeq 0$ is equivalent to having a disk in hydrostatic equilibrium along the z-axis, thus the disk is confined to the equatorial plane. Considering the axial component of Eq. 1.11, and applying the condition leads to that the remaining terms are the pressure force in the vertical direction balancing the gravitational forces (from the compact object and from the disk):

$$\frac{1}{\rho}\frac{\partial p}{\partial z}=-\frac{\partial\Psi}{\partial z} \tag{1.12}$$

The pressure is typically composed as $p=p_{gas}+p_{tur}+p_{rad}$, where $p_{gas}=\rho c_s^2$, $p_{tur}=\rho<v_{tur^2}>$, $p_{rad}=aT^4/3$. In other words:

$$p=\rho c_s^2(1+\frac{<v_{tur}^2>}{c_s^2}+\frac{2aT^4}{3\Sigma c_s^2}H):=\rho c_s^2(1+\epsilon^2+\gamma^2 H) \tag{1.13}$$

Then one can calculate the effective scale height by writing $H=-\frac{dp}{d\rho}\frac{1}{g_z}$ where $g_z=GMz/r^3+2\pi G\Sigma z/H$ is the vertical acceleration. Thus:

$$H=\frac{c_s^2(1+\epsilon^2+\gamma^2 H)}{2\pi G\Sigma+\Omega_K^2 H} \tag{1.14}$$

where $\Omega_K=\sqrt{GM/r^3}$ is the Keplerian angular velocity.

Typically, this general model allows $H/r\leq 1$, while the Shakura-Sunyaev model allows geometrically thin disks, i.e. $H/r << 1$. However, in the inner region of the disk, where temperatures are high, H could be pumped up by the radiation pressure (i.e. $H\sim r$). This force could create a small hot corona in this region. Further simplifications can be made, such as assuming that radiation pressure is negligible, and the self-gravity dominates the disk (e.g. circumplanetary disks), and assuming that the turbulent velocity is in the order of the sound speed, which then leads to:

$$H\simeq\frac{c_s^2}{\pi G\Sigma} \tag{1.15}$$

When radiation pressure and the self-gravitation of the disk are negligible, we have:

$$H \simeq \frac{c_s\sqrt{1+\epsilon^2}}{\Omega_K} \tag{1.16}$$

The so-called standard disk model (Shakura & Sunyaev, 1973) describes this latter case, a geometrically thin non-self gravitating disk. This means that the scale height of the disk is much smaller than the radial distance ($H/r << 1$) and the mass of the disk is much smaller than the mass of the central object, so the gravitational influence of the disk is negligible. In the standard disk the turbulent fluid is described with a viscous stress tensor which is proportional to the total pressure:

$$\tau_{r\phi} = \alpha\rho c_s^2 = -\alpha p, \tag{1.17}$$

where α is a dimensionless constant between 0 and 1. The thin disk model describes the viscosity as due to turbulent motion, and the length-scale of the turbulent cells is in the order of the scale height ($l_{turb} \simeq H$), and the turbulent motion is assumed to be subsonic ($v_{turb} \simeq c_s$). The Navier-Stokes equation has to be supplemented with the specification of the kinematic viscosity. Therefore, considering Eq. 1.17, one can obtain the z-averaged (vertically integrated) kinematic viscosity as:

$$< \nu >= \alpha c_s H \tag{1.18}$$

The model further assumes that the turbulent viscosity scales with the velocity and the size of the turbulent cells $\nu \propto v_{tur} l_{tur}$.

In summary, the standard disk model assumes that the disk is in local thermodynamical equilibrium, does not advect heat inwards, and radiates the viscous heat efficiently as a blackbody; the change in gravitational energy is determined by the central object, and the disk is geometrically thin ($H/r << 1$), steady ($\partial/\partial t = 0$), and axissymmetric ($\partial/\partial\phi = 0$); the azimuthal motion dominates over the radial ($v_\phi >> v_r$), hydrostatic equilibrium is along the vertical axis, the viscous heat dissipation balances radiation output; and there are no magnetic fields in the disk.

Now let's consider the temperature profile of the disk. The viscous heat per unit volume can be expressed as:

$$q = \rho\nu\left(r\frac{d\Omega_K}{dr}\right)^2 \tag{1.19}$$

The radiative flux in the z-direction, in case of an optically thick disk is:

$$F = -D\frac{\partial u}{\partial z} = -\frac{4acT^3}{3\kappa\rho}\frac{dT}{dz} = \int_0^{H/2} q\,dz = q\,z \tag{1.20}$$

where $D = \lambda c/3$ is the diffusion coefficient, and $\lambda = 1/\kappa\rho$ is the photon mean free path, κ is the Rosseland-mean opacity, and $u = aT^4$ is the radiation energy density. The opacity of the disk is related to the optical depth as $\tau = \kappa\Sigma/2$. The right hand side of Eq. 1.20 shows that the radiated flux is compensated by the viscous dissipation heat ($Q_{diss} = Q_{rad}$).

The vertically integrated heat rate per unit area is:

$$Q_{diss} = \int_{-\,\mathrm{inf}}^{+\,\mathrm{inf}} q\,dz = \frac{3}{2}\nu\Sigma\Omega_K^2 = -\frac{3}{2}T_{r\phi}\Omega_K = -\frac{1}{2\pi}\sqrt{\frac{GM}{r^3}}\dot{M}\left(1-\sqrt{\frac{r_{lso}}{r}}\right). \tag{1.21}$$

On the other hand, $Q_{rad} = 2\sigma_{SB}T^4$, thus $T^4 = \frac{1}{2}Q_{diss}$ leading to:

$$T^4 = \frac{3GM\dot{M}}{8\pi\sigma_{SB}r^3}\left(1 - \sqrt{\frac{r_{lso}}{r}}\right). \tag{1.22}$$

It is clearly seen that when far away from the last stable orbit (r_{lso}), $r >> r_{lso}$, the temperature scales as:

$$T \propto r^{-3/4}. \tag{1.23}$$

This means that the inner disk is hotter then the outer disk, and this temperature profile is the main characteristic of the standard model.

1.2.1.1 Multicolor Disk (MCD)

This model (e.g. Makishima et al., 2000; Pizzolato et al., 2010) is a superposition of multiple blackbody up to a maximum color temperature (T_{in}). The model has two free parameters: the color temperature (T_{in}) at the innermost disk boundary, and the apparent inner disk radius (R_{in}) related to the actual inner disk radius as:

$$R_{disk} = \xi\kappa^2 R_{in} \tag{1.24}$$

and the local disk temperature is considered to scale as (see above, Eq. 1.23):

$$T(R) \propto R^{-3/4} \tag{1.25}$$

Here, $\kappa = 0.41$, a correction factor due to the fact that T_{in} occurs at a radius somewhat larger than R_{in}. ξ is the so-called spectral hardening factor, the ratio of color temperature to effective temperature and sensitive to the mass accretion rate, but insensitive to the black hole mass and disk viscosity.

This model gives the bolometric luminosity as:

$$L_{bol} = 4\pi\left(\frac{R_{in}}{\xi}\right)^2 \sigma_{SB}\left(\frac{T_{in}}{\kappa}\right) \tag{1.26}$$

where σ_{SB} is the Stefan-Boltzmann constant.

Considering that the last stable Keplerian orbit is at $3R_S$, so $R_{in} = 3\alpha R_S$, the bolometric luminosity emitted by the accretion disk:

$$L_{bol} = 7.2\times10^{38}\left(\frac{\xi}{0.41}\right)^{-2}\left(\frac{\kappa}{1.7}\right)^{-4}\alpha^2\left(\frac{M}{10\,\mathrm{M}_\odot}\right)^2\left(\frac{T_{in}}{\mathrm{keV}}\right)^4 \mathrm{erg/s}. \tag{1.27}$$

Using the Eddington-limit ($L_{bol} = \eta L_{Edd}$), one gets back Eq. 1.10 in a more sophisticated way:

$$T_{in} = 1.2\left(\frac{\xi}{0.41}\right)^{1/2}\left(\frac{\kappa}{1.7}\right)\alpha^{-1/2}\eta^{1/4}\left(\frac{M}{10\,\mathrm{M}_\odot}\right)^{-1/4}\mathrm{keV} \tag{1.28}$$

1.2.1.2 IMBHs inferred from X-ray spectral fitting

Historically, using the Einstein satellite, it was shown that some ULXs exhibit state transitions. The Japanese X-ray satellite, ASCA, had a spectral coverage of 0.4-10 keV, better than the ROSAT coverage, though with a lower angular resolution of ~ 1 arcmin. The ULXs spectra are typically fitted with a power-law, an MCD model for the disk, or both. When fitting an MCD model, the flux can be written as:

$$f(E) = \frac{\cos i}{R^2} \int_{r_{in}}^{r_{out}} 2\pi r B_E(T) dr \tag{1.29}$$

where i is the disk inclination,R is distance to the source, and $B(T)$ is the Planck function. This can be transformed to integration by temperature (dr –> dT), using Eq. 1.25. Thus, considering the thermal component of the spectrum, fitting an MCD model provides an inner disk temperature. As a next step, from Eq. 1.10 or Eq. 1.28, it is clearly seen, that StMBHs have hotter inner disk temperatures than SMBHs. Therefore, IMBHs should have an inner disk temperature in the order of 0.1 keV. Also, after expressing the Planck function at a given frequency (instead of energy or wavelength), one sees that the luminosity scales as $L_\nu \propto \nu^{1/3}$, which is valid in regions far away from the central object, where low temperature produces low-energy photons. Therefore, the MCD model describes the soft (or thermal) component of the X-ray spectrum.

Continuing our "time travel", for these initial studies with ASCA, the X-ray fits resulted in too high inner disk temperature for an IMBH, and it was also found that the power-law component had a photon index softer than for Galactic black hole binaries (Colbert & Mushotzky, 1999; Kubota et al., 2002). One particular explanation for this was to relax the assumptions of the thin disk model (Makishima et al., 2000). For instance, increasing κ (see Section MCD model) will lead to higher masses and also will increase the correction factor ξ. The main problem with ASCA was that its PSF was so large that the X-ray spectra were contaminated by some diffuse X-ray emission.

Turning to present day astronomy, many ULXs have high-quality Chandra or XMM-Newton spectra. It turned out that these spectra can often be fitted with a single component rather than two as in the ASCA era (Miller & Colbert, 2004). It was found that some of the ULXs can be fitted with a single power-law with a photon index of $\Gamma = 2$ similar to GBHBs, or with an MCD model with an disk temperature much less than obtained before (e.g. Roberts et al., 2001, 2002b; Strickland et al., 2001; Foschini et al., 2002; Kaaret et al., 2003). Another common feature of ULXs is that they do not show lines in their X-ray spectra, probably due to their high distance. However, in case of M82 X-1, which is a very strong and relatively nearby source, it shows a very broad Fe-K line (Strohmayer & Mushotzky, 2003). The presence of this line rules out beaming explanation of this ULX (see beaming later).

As mentioned above there is a relationship between the black hole mass and the inner disk temperature. One of the main arguments for ULXs being candidate IMBHs is their low inner disk temperature (Miller et al., 2004). This can be seen on Figure 1.2., which shows that ULXs form a distinct class by having cooler disk than GBHBs and a higher luminosity. This suggests that they may harbor IMBHs. Figure 1.2. also shows that when GBHBs are in a low state they can have a disk temperature close to the one of ULXs, but their luminosity is about two orders of magnitude less than the luminosity of ULXs (Miller et al., 2004).

On the other hand, there is still an ongoing debate on interpreting ULXs spectra. This

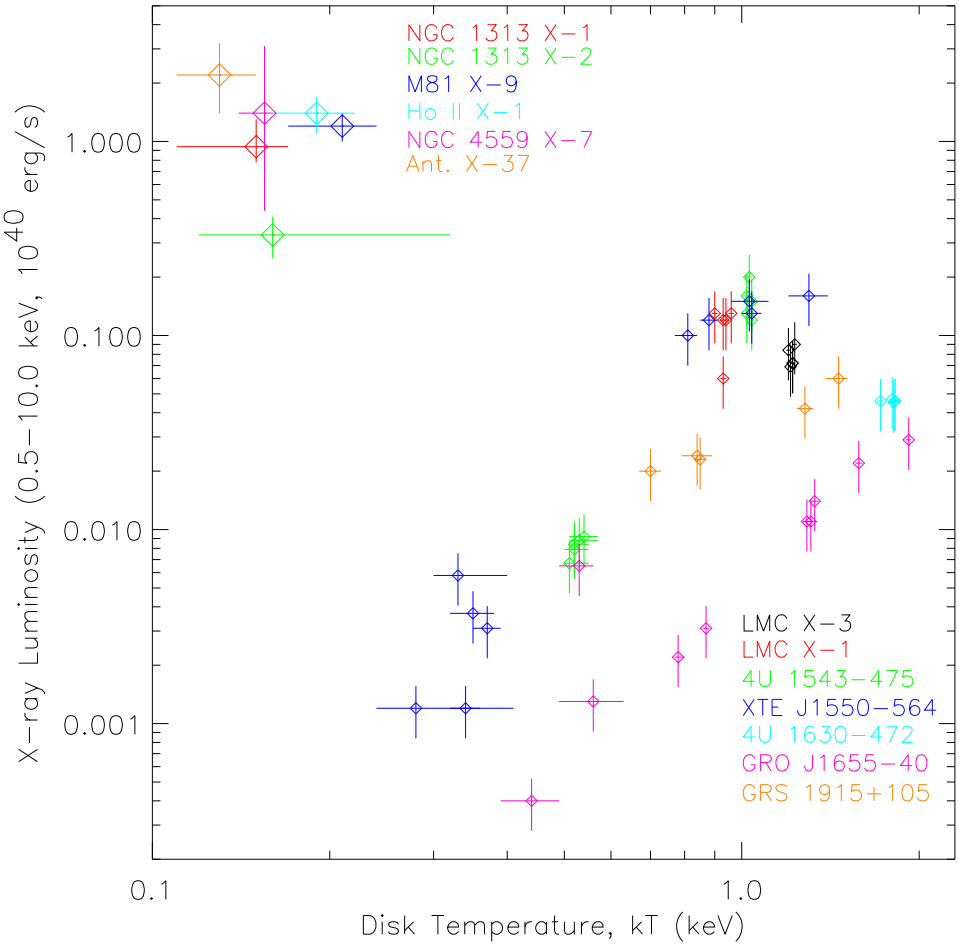

Figure 1.2: The image is taken from (Miller et al., 2004). The X-ray luminosity of a number of luminous ULXs and stellar-mass black holes in their brightest phases are plotted against disk temperatures. A number of low-luminosity black hole candidate are also added.

is primarily due to the co-existence of many accretion models, beyond the standard disk. In the following, I will describe the basic properties of the some of these accretion models concerned by ULXs.

1.2.1.3 Non-standard Disks and Accretion

These alternative models concern different accretion regimes: below, moderately and highly above the Eddington limit, and typically involve inefficient accretion flows.

ADAF: A family of accretion models, called advection dominated accretion flow (ADAF), exists in the sub-Eddington regime ($\dot{M}/\dot{M}_{Edd} < 0.1$). These models were mainly developed by Narayan & Yi (1994) and their main characteristic is that they involve advection into the transport equation. This means that instead having a balance between the heating by viscosity (q^+) and cooling by radiation (q^-), excess energy is stored in the gas and transported with the flow, representing "advection" of energy (q^{adv}). To compare with the standard disk: $q^- \simeq q^+ >> q^{adv}$, while in the ADAF model: $q^- << q^+ \simeq q^{adv}$

(Narayan, Lecture Notes [1]). An ADAF can be radiatively inefficient either because the heat rate of the gas is much less than the accretion time or the radiation is trapped in the flow. The latter one is described by so-called slim disk model (Abramowicz et al., 1988). An ADAF has high electron temperature of 10^{9-11} K, geometrically thick (H/r $\sim$ 0.6), and has low optical depth therefore it well describes the power-law component of the X-ray spectrum by Comtonization. Additionally, ADAF assumes a two-temperature accreting plasma, because, otherwise the electrons become highly relativistic, that would radiate so the flow would be radiatively efficient (Narayan, Lecture Notes).

Slim Disk: As mentioned above, if the radiation is trapped in the accretion flow, then the accretion can be described with the a slim disk. Due to the radiation trapping, a slim disk is still less luminous than the standard disk, even if the accretion rate is near or above the Eddington limit $0.1 < \dot{M}/\dot{M}_{Edd} < 10$) (Sądowski, 2009). The pressure gradient in the disk plane direction is dynamically important, and the radial temperature profile is nearly thermal:

$$T(R) \propto R^{-1/2} \tag{1.30}$$

Hyperaccretion: When the accretion rate is highly above the Eddington-limit (the mass inflow rate is up to 1000 $\dot{M}/\dot{M}_{Edd}$), the accretion is called hyperaccretion or simply super-Eddington accretion (Begelman, 2002; King, 2009). The prototype of this accretion is SS433. The corresponding "Polish doughnut" disk model describes an optically thick torus. It is also associated with highly rotational funnels that channel the incoming material along the poles, resulting in strong jets/outflows. So, the accretion is inefficient due to the fact that these large scale outflows expel the material before reaching the black hole.

In general, the bolometric luminosity can be written as:

$$L_{bol} \simeq \frac{L_{edd}}{b}\left(1 + \ln \frac{\dot{M}_{in}}{\dot{M}_{Edd}}\right) \tag{1.31}$$

where b is a beaming factor. (See later for a discussion on the importance of beaming). Interestingly, this accretion regime was first described by Shakura & Sunyaev (1973) along with the standard disk model. Another important feature is that King (2009) suggested that the beaming factor scales as $\dot{M}^{-2}$ leading to:

$$L \propto T_{in}^{-4} \tag{1.32}$$

A recent study made by Gladstone et al. (2009) on ULXs spectra argues that models of ULXs spectra are more physically motivated if fitted with a Comptonizing corona. However, it was found that the corona requires extremely high opacities (even higher than obtained for Compton-thick AGNs). Although, moderately high opacities might not be excluded for a hyperaccretion scenario (Poutanen et al., 2007). Furthermore, Gladstone et al. (2009) found that the spectra show a soft excess and a turnover at $\sim$4 keV which

[1] www.astro.iag.usp.br/$\sim$xiveaa/palestras/Narayan_Lecture2.ppt

might be indicative of new spectral features unique to ULXs. In this case, the soft excess is argued to originate not from a disk, hence casting doubt on the IMBH interpretation. On the other hand, fitting with an MCD + power-law model might result in a similarly good fit in a statistical sense. Without entering the debate of interpreting ULX spectra, it is clear that one need to develop an independent approach by using multiwavelength observations and studying the entire spectral energy distribution of ULXs (see e.g. Chapter 7) to avoid having to deal with these problems.

1.2.2 Properties of Ultraluminous X-ray Source Hosts and Environments

As noted by Miller & Colbert (2004), ULXs are hosted by all type of galaxies including, spirals, ellipticals, and dwarf irregulars. Considering the time scale of dynamical friction, a supermassive black hole would sink to the center of the host galaxy within the Hubble time. This means that the non-nuclear nature of the ULXs rules out that they are supermassive black holes. The dynamical friction time can be expressed as (Binney, 1987):

$$t_{fric} \simeq \frac{5 \times 10^9 \mathrm{yr}}{ln\Lambda} \left(\frac{r}{\mathrm{kpc}}\right)^2 \left(\frac{\sigma}{200\,\mathrm{km\,s^{-1}}}\right) \left(\frac{M}{10^7\,\mathrm{M_\odot}}\right)^{-1}, \tag{1.33}$$

where σ is the velocity dispersion, r is the distance from the dynamical center of the galaxy and $ln\Lambda$ is the natural log of the Debye number: $\Lambda = 4\pi n \lambda_D^3$, where n is the particle number and λ_D is the Debye-length. For instance, this leads to $t_{fric} \simeq 10^{10}\mathrm{yr}(10^5\mathrm{M_\odot/M})$ for M82 X-1 (Kaaret et al., 2001). Another implication of Eq. 1.33 is that more massive objects could be present at farther away from the center.

Furthermore, the most luminous ULXs were revealed in galaxies with high star formation rate, e.g. in Antennae, M82, Cartwheel, and Apr 299 (Fabbiano et al., 2001; Kaaret et al., 2001; Gao et al., 2003; Zezas et al., 2003). Later it was found that ULXs are also present in giant elliptical galaxies, e.g. in NGC 1399, NGC 4697 (Sarazin et al., 2003; Jeltema et al., 2003). Moreover, a fraction of these lower luminosity ULXs were associated with globular clusters (see Chapter 3 for further details on possible IMBHs in globular clusters). Therefore, it is interesting to ask whether there is a link between globular clusters and ULXs. It is particularly important to explore whether ULXs share some common properties with low-mass X-ray binaries (LMXBs) that are thought to be older systems and sometimes are associated with globular clusters (Sarazin et al., 2003). To understand possible links between ULXs and LMXBs one needs to delve into disk irradiation.

1.2.2.1 Disk Irradiation

Disk irradiation (see review Czerny et al., 2008) modifies the spectrum of the standard disk at X-ray and at optical/UV part of the spectrum. Here I will mostly concentrate on the optical part of the spectrum. In the X-ray part of the spectrum, the disk emission is modified, because it reflects the X-ray emission arriving from e.g. a hot corona surrounding the disk. This leads to the so-called reflection component. This component can arise either due to scattering or due to that the disk first absorbs and then re-emits the radiation. As a result one can see a Compton hump and X-ray emission lines, which are smeared and broadened due to o special and general relativistic effects.

Focusing on the optical part of the spectrum, beyond the X-ray irradiation, an irradiation due to the inner part of the disk is also present. Depending on the albedo of

the neutral gas or the ionized medium, the ratio between reflection and thermalization can be determined. This is particularly important, because the disk temperature can be increased by the thermalized flux, thus modifies the disk continuum. there are also differences between black holes with different masses. For instance, GBHBs have hotter disks than AGN and also have higher ratio of disk height to radius (H/r) at fixed Eddington rate, thus direct irradiation is more important for GBHBs (Czerny et al., 2008).

To take into account disk irradiation, usually one adds the incident radiation flux – which increases the disk temperature –, but still preserves the assumption of a local black body emission. Thus one usually considers a standard disk with a temperature profile ($T(r)$), height ($H(r)$) and a surface normal vector $\hat{s}(\mathbf{r})$. Following Frank et al. (2002), the X-ray flux crossing the disk surface at $\mathbf{r}$ is:

$$F = \frac{L_X}{4\pi d^2}(1-\beta)\cos\Theta \tag{1.34}$$

where $\mathbf{d} = d\hat{d} = \hat{d}\sqrt{r^2 + H^2(r)}$, the vector from the black hole to the surface element, β is the albedo, and $\cos\Theta = -\hat{s}\cdot\hat{d}$, the angle between the direction of the radiation and the disk surface normal vector. The effective temperature due to irradiation is defined as:

$$T^4_{Irr} = F/\sigma_{SB} = \frac{1}{3}T^4_0(r_{in}/d^2(1-\beta)\cos\Theta \tag{1.35}$$

and the total temperature for the disk surface element:

$$T^4_d = T^4(r) + T^4_{Irr} \tag{1.36}$$

One might also account for X-ray irradiation of the donor star, e.g. in black hole binary systems. This happens in a similar way:

$$T^4_{Irr,stellar} = \frac{1}{3}Q\delta T^4_0(r_{in}/d^2(1-\beta)\cos\Theta \tag{1.37}$$

but now using a stellar surface normal vector in defining Θ, Q is the transmission function, and δ is the fraction of intercepted X-ray flux converted to thermal energy. The transmission function describes how the X-ray is blocked by the accretion disk. The total temperature of the stellar surface is:

$$T^4_{stellar} = T^4_{grav} + T^4_{Irr,stellar} \tag{1.38}$$

where T_{grav} is the surface temperature obtained by using Kurucz stellar atmosphere models.

Then the total flux can be computed as summing up all the surface elements of the disk and the companion as:

$$F(\lambda) = \sum_i I_i(\lambda)\frac{A_i\cos\Theta_i}{D^2} \tag{1.39}$$

where $I_i(\lambda)$ is the intensity, $A_i\cos\Theta_i$ is the surface element area projected along the line of sight, and D is the distance to the observer. Typically the disk surface is treated as a blackbody ($I_i(\lambda) = B_\lambda(T_d)$).

A limited number of ULXs exist with suitable data to study disk irradiation in the optical part of the SED. These studies (see Chapter 4 for further details) led to a possibly common property that the optical counterpart of ULXs might be dominated by disk irradiation similar to LMXBs. On the other hand, the luminosity function of ULXs shows that bright ULXs could be also consistent with HMXBs (Figure 1.3.). Additionally, bright ULXs are generally found in star forming galaxies, i.e. these galaxies seems to be more efficient in producing ULXs, and a number of ULXs show correlation with the recent start formation rate (Feng & Soria, 2011).

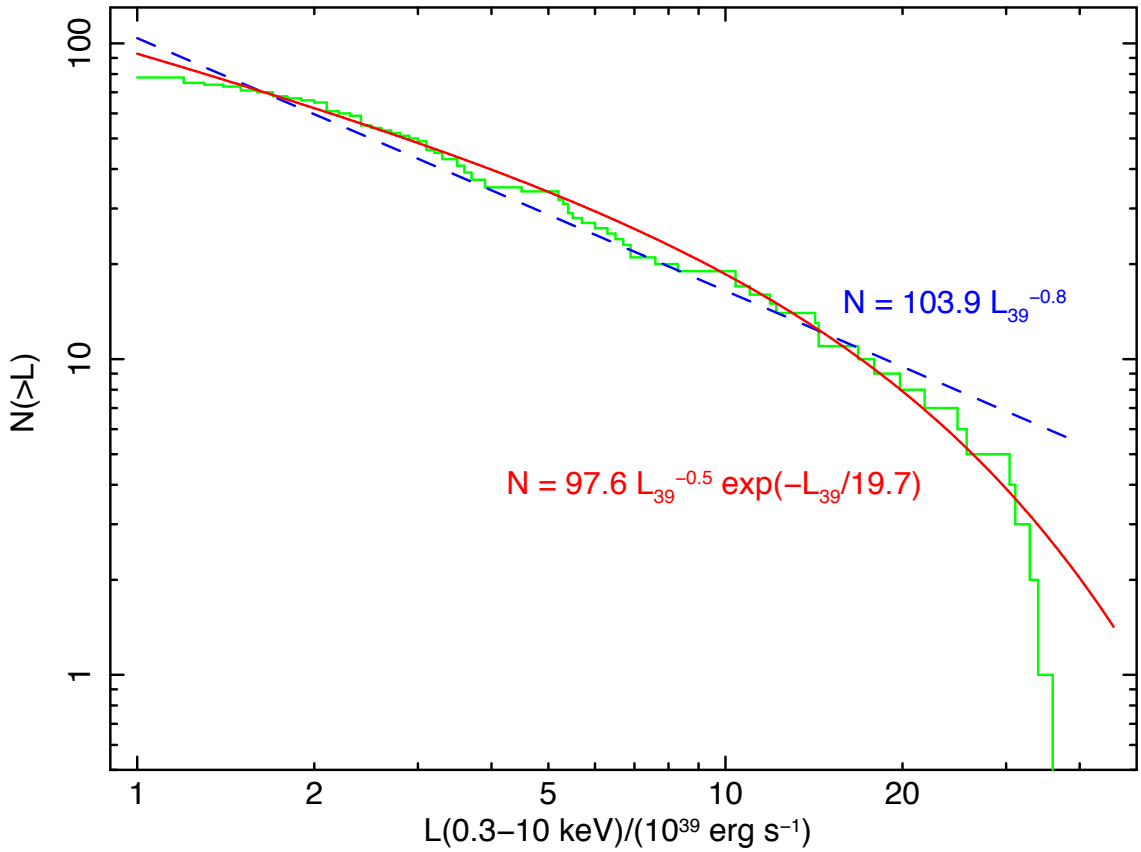

Figure 1.3: Cumulative ULX luminosity function from the Chandra survey of Swartz et al. (2011). At the low-energy end, it matches the slope and normalization of the HMXB distribution below 10^{39}erg/s

It is often speculated that ULXs show connection with star clusters, like young star-forming regions or globular clusters (Miller & Colbert, 2004). These clusters typically have masses $10^4 - 10^5$ $M_\odot$ e.g. in Antennae and M82, and 10^6 $M_\odot$ for massive globular clusters. The mass of these clusters might already limit the maximum mass of an IMBH to 10^5 $M_\odot$. However, there can be significant differences in the cosmic evolution of these clusters.

To study associations between ULXs and stellar clusters are particularly important to test the formation hypothesis of massive black holes in young stellar clusters. Swartz et al. (2009) found in a volume limited Chandra sample of 58 star-forming galaxies no statistically significant associations. Therefore, the formation of a massive black hole in

the core of young stellar clusters by stellar mergers and direct collapse (Portegies Zwart & McMillan, 2002; Portegies Zwart et al., 2004) might not be relevant for ULXs if one assumes that ULX systems contain a massive black hole. It was also found that most of the stellar clusters are not massive and compact enough for this runaway core collapse model (Feng & Soria, 2011). However, IMBHs formed this way could also be ejected by the current epoch (Portegies Zwart & McMillan, 2002; Portegies Zwart et al., 2004), and there are still a number of ULXs that could be associated to young stellar populations (e.g. Grisé et al., 2012).

It was also suggested by Zampieri & Roberts (2009) that ULXs may form in sub-solar metallicity environments, which would lead to the expectation that ULX contain black holes between 30-90 $M_\odot$, produced by stars with initial, main sequence mass above 40 $M_\odot$. This is a very practical explanation, because the formation of these very massive stellar remnant black holes would not require a special stellar evolution. Also, with such massive black holes, ULXs would not violate the Eddington limit. Zampieri & Roberts (2009) showed that a star with an initial mass of 100 $M_\odot$ would have a final mass of 3-6 $M_\odot$ for a metallicity of $Z \simeq Z_\odot$, and would have a final mass of $30 - 70$ $M_\odot$ for a metallicity of $Z \simeq 0.1 Z_\odot$ assuming that these massive stars collapse directly to form a black hole.

1.2.3 Temporal Variability of ULX Binaries

There are objects like very young supernova remnants, or collections of X-ray binaries, that can emit $\sim 10^{39}$ erg/s in X-rays. But the point is that, a supernova remnant would not be visible after a couple of years, and a cluster of normal X-ray binaries would not show random or irregular variability. ULXs typically display irregular variability at the level of $> 50\%$ on timescales of weeks to years (Miller & Colbert, 2004, and references therein). Additionally, short-time variability on timescales of minutes has also been noted for four ULXs (Feng & Soria, 2011, and references therein). The irregular variability indicates that ULXs are likely accreting (binary) systems. Longer term periodic variability due to an orbiting donor can be expressed as:

$$P = 2 \times 10^{-10} \left(\frac{\mathrm{a}}{\mathrm{km}}\right)^{3/2} \left(\frac{\mathrm{M}}{\mathrm{M}_\odot}\right)^{-1/2} \mathrm{day} = 3.65 \times 10^{2} \left(\frac{\mathrm{a}}{\mathrm{AU}}\right)^{3/2} \left(\frac{\mathrm{M}}{\mathrm{M}_\odot}\right)^{-1/2} \mathrm{day}. \quad (1.40)$$

Thus, for a black hole mass of 100 $M_\odot$, monthly monitoring can sample orbits of > 1 AU. There is no periodic variability found to date for ULXs (but see further details in Chapter 4).

Generally speaking, in a binary system the accretion is fed by the donor star. There are two main mechanisms to feed the black hole. On the first hand, systems can be fed by Roche-lobe overflow, which happens when the outer layers of the donor's envelope is pulled off by the gravitational force if the binary separation shrinks or the donor increase its radius. On the other hand, supergiant stars eject their mass in the form of stellar wind. A fraction of the material in the wind can serve as accreting material when captured by black hole. These systems are called wind-fed. Given the possible link between ULXs and LMXBs, it might be that ULX systems are also typically Roche-lobe fed.

The gravitational field created by the donor and the black hole can be described with equipotential surfaces. The connected equipotentials are called Roche lobes. The point where the two potential surface are connected is called the 1st Lagrange point and this is

the point where mass transfer occurs. The shape of these equipotential surfaces is governed by the mass ratio (q) and the binary separation (a). If the actual size of the star is less than (or just equal to) its Roche lobe, then mass transfer can only happen via wind feeding, because at the surface of the Roche lobe the velocity and the pressure is zero. Once the star fills its Roche lobe, mass transfer occurs through the L1 point. Following Frank et al. (2002), the Roche lobe geometry can be described with an approximate analytic formula:

$$\frac{R_2}{a} = \frac{0.49q^{2/3}}{0.6q^{2/3} + \ln(1+q^{1/3})} \tag{1.41}$$

Note that, a further simplification can be made for $0.1 < q < 0.8$, the above equation can be approximated as:

$$\frac{R_2}{a} = \frac{2}{3^{3/4}}\left(\frac{q}{1+q}\right)^{1/3} = 0.462\left(\frac{M_2}{M_1+M_2}\right)^{1/3} \tag{1.42}$$

As a consequence, the mean stellar density of the Roche lobe-filling donor is governed by the binary period (after using Kepler 3rd law):

$$\rho_{mean} = 3M_2/4\pi R_2^3 \simeq 3^5\pi/8GP^2 = 110P_{hour}^{-2}\mathrm{g/cm^3} \tag{1.43}$$

As the mass transfer process will change the mass ratio, the period and separation of the binary will also be changed due to momentum conservation. The orbital angular momentum is:

$$J = (M_1a_1^2 + M_2a_2^2)2\pi/P = M_1M_2\left(\frac{Ga}{M_1+M_2}\right)^{1/2}. \tag{1.44}$$

Assuming that the mass lost by the donor is accreted by the black hole ($\dot{M}_1 + \dot{M}_2 = 0$, $\dot{M}_2 < 0$). Then:

$$\frac{\dot{a}}{a} = \frac{2\dot{J}}{J} + \frac{2(-\dot{M}_2)}{M_2}\left(1 - \frac{M_2}{M_1}\right) \tag{1.45}$$

If conservative mass transfer ($\dot{J} = 0$) takes place from the less massive to the more massive object then the binary system expands ($\dot{a} > 0$), conversely the binary separation shrinks. This also affects the Roche lobe size. Differentiating Eq. 1.42 leads to:

$$\frac{\dot{R}_2}{R_2} = \frac{\dot{a}}{a} + \frac{\dot{M}_2}{3M_2} \tag{1.46}$$

and combining this with Eg. 1.45 leads to:

$$\frac{\dot{R}_2}{R_2} = \frac{2\dot{J}}{J} + \frac{2(-\dot{M}_2)}{M_2}\left(\frac{5}{6} - \frac{M_2}{M_1}\right) \tag{1.47}$$

On the other hand, it cannot be excluded that ULXs are wind fed systems. Wind fed systems typically involve an early type (O or B) star. The stellar-wind of an early type star is intense ($10^{-6} - 10^{-5}$ $\mathrm{M_\odot/yr}$), with supersonic velocities:

$$v_w(r) \sim v_{escape}(R_*) = \left(\frac{GM_*}{R_*}\right)^{1/2} \tag{1.48}$$

The capture of the wind will occur in a cylindrical region with an axis along the relative wind direction – relative to the orbital velocity of the compact object– at a radius of:

$$r_{acc} \sim GM_{BH}/v_{rel}^2. \tag{1.49}$$

Assuming a simplification that the relative wind speed is $v_{rel} = v_w$, then the fraction of the wind captured by the black hole can be obtained by comparing the mass-flux into the accretion cylinder of radius r_{acc}, with the total mass loss rate ($-\dot{M}_w$) of the star:

$$\frac{\dot{M}}{-\dot{M}_w} \simeq \frac{\pi r_{acc}^2 v_w(a)}{4\pi a^2 v_w(a)} = \frac{G^2 M_{BH}^2}{a^2 v_w^4(a)}, \tag{1.50}$$

where a is the orbital separation. From Eq. 1.49 we find that:

$$\frac{\dot{M}}{-\dot{M}_w} \simeq \frac{1}{4}\left(\frac{M_{BH}}{M_*}\right)^2 \left(\frac{R_*}{a}\right)^2. \tag{1.51}$$

For typical XRB parameters, this equation implies accretion rates of $10^{-4} - 10^{-3}$ times the wind mass loss rate, $-\dot{M}_w$. Thus wind fed accretion is very inefficient compared to Roche lobe overflow. Only because the mass-loss rates themselves are large, wind-fed sources are observable. However, for ULXs the "typical" binary parameters are unconstrained.

The observable quantities in a binary system are the period, radial velocity amplitude and the mass function. The companion star has a circular motion about the center of mass, so the radial velocity amplitude K_2 is given by:

$$K_2 = \frac{2\pi}{P} a_2 \sin i \tag{1.52}$$

where a_2 is the distance from the center of the companion to the center of mass, and i is the inclination. Then using Kepler 3rd law and $a_2 = M_1 a/(M_1 + M_2)$ one can obtain the mass function:

$$f_2 = \frac{M_1^3 \sin^3 i}{(M_1 + M_2)^2} = \frac{K_2^3 P}{2\pi G} \tag{1.53}$$

For a particular study of the binary parameters in a ULXs system proceed to Chapter 4.

1.3 Jets and Synchrotron Emission

Accreting objects are not just characterized by an accretion disk but also necessarily by their jets. In this Section I briefly discuss the emission properties of an astrophysical jet. Jets usually emit most prominently in the radio band and their emission mechanism is due to non-thermal continuum radiation. In strong magnetic fields, the Lorentz force accelerates the plasma particles to ultra-relativistic speed, which results in polarized synchrotron radiation. A single particle, due the Lorentz force, moves on a helical path along the magnetic field line with a gyration frequency of (e.g. Lang, 1999):

$$\nu_g = \frac{qB}{2\pi\gamma_e m_e c} \sin\Psi, \tag{1.54}$$

where q is the charge, B is the magnetic field, γ_e is the Lorentz factor (see later) of a single particle, and Ψ is the pitch angle, the angle between the magnetic field strength

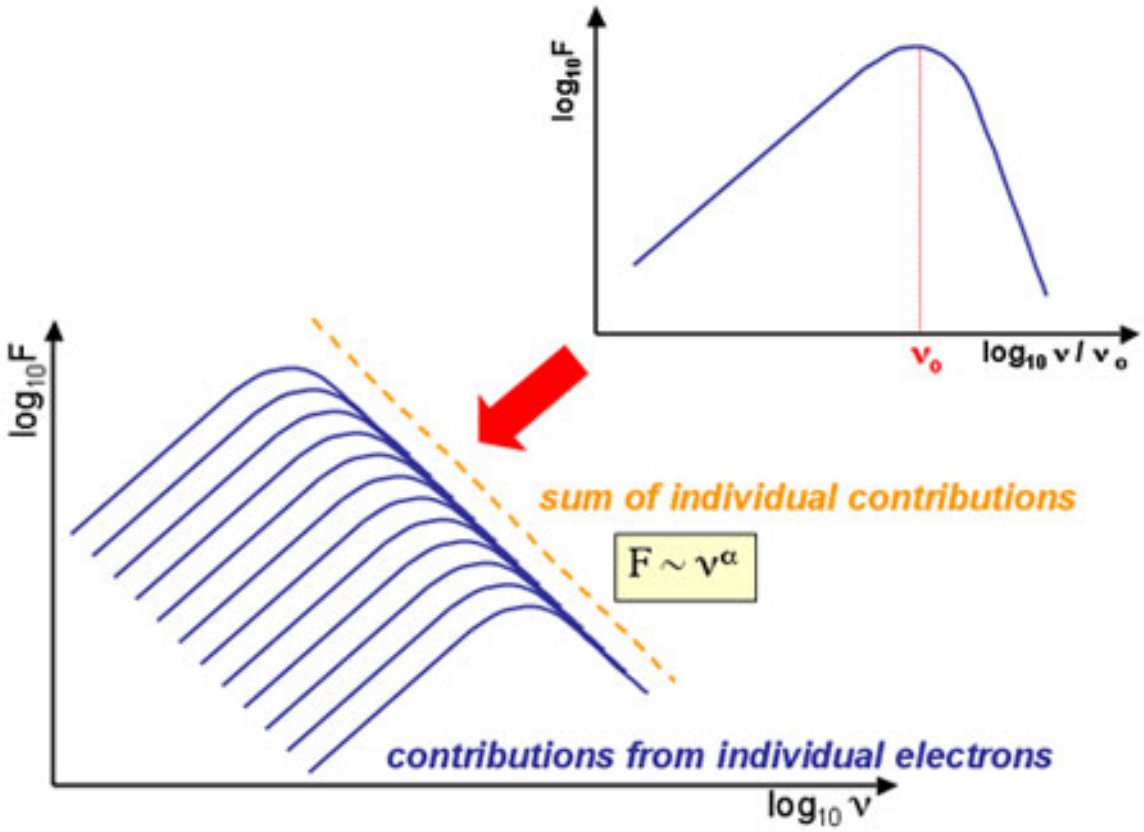

Figure 1.4: The figure shows the synchrotron spectrum of an individual electron and the spectrum of an ensemble of electrons as building up from the individual spectra. http://astronomy.swin.edu.au/cosmos/s/synchrotron+emission

(B) vector and the velocity vector. The radiation profile of a single particle is asymmetric; the synchrotron emission has a maximum near a critical frequency :

$$\nu_c = \frac{3}{4\pi}\frac{qB}{m_e c}\gamma_e^2 \sin\Psi. \tag{1.55}$$

With multiple particles, many harmonics of the gyrofrequency will appear, and these are so close to each other that the resulting spectrum will necessarily be continuous. The (radio) plasma is a freely expanding supersonic jet which is responsible for the synchrotron radiation.

Self-absorption of the emission happens below a frequency where the kinetic temperature equals the brightness temperature. The radiation spectrum is the superposition of self-absorbed synchrotron spectra. In jets, a "core" is often defined as the surface corresponding to the optical depth of $\tau = 1$ at a given frequency, therefore the position of the core is frequency dependent.

In the case of synchrotron radiation the velocity of the plasma blob is $\beta = v/c$, and the bulk Lorentz factor is:

$$\gamma = (1 - \beta^2)^{-1/2}. \tag{1.56}$$

The radiated power of the ultra-relativistic electrons is coming from a tiny solid angle that is proportional to $1/\gamma$. Assuming that the distribution of the electrons are homogeneous

and isotropic, then their energy distribution can be written in a power-law form:

$$N(E) = K_0 E^{-p}, \tag{1.57}$$

as well as the distribution of their Lorentz factors:

$$N(\gamma_e) = N_0 \gamma_e^{-p}. \tag{1.58}$$

The flux density will depend on the p parameter of the energy distribution, and the SED of the radiation can be approximated as $S_\nu \sim \nu^\alpha$ (see below), where S_ν is the flux density, ν is the frequency, and α is the spectral index, which can be obtained as $\alpha = (1-p)/2$. The approximation of $\alpha = (1-p)/2$ is valid in the optically thin case, in case of spatially extended emission. In extended parts of the jet the radiating material cannot re-absorb its own radiation, so the radiation is transparent. In the optically thick case, i.e. synchrotron self-absorption, the electrons are able to emit and absorb photons, which give energy to the charged particles. In the optically thick part of the spectrum, $\alpha = 5/2$. This value has never been observed. The optically thick spectrum is typical for the compact, flat-spectrum part of the jet. Additionally, the turnover frequency (where the kinetic and brightness temperatures are equal) depends on the magnetic field and the optical depth of the source. Note that, this is exactly why the single turnover frequencies are different; if they were not different then the superposition of the spectra would never become flat.

The total energy loss rate by synchrotron radiation can be written as (when averaged over an isotropic distribution of pitch angles) (Longair, 1994) :

$$-\dot{E}_{sy} = \frac{4}{3}\sigma_T c U_{mag} \gamma^2 \beta^2 \ \text{Watt}. \tag{1.59}$$

Then the radiation spectrum of a power-law distribution in case of a random magnetic field:

$$S(\nu) = a(p)\frac{\sqrt{3}q^3 B K_0}{4\pi\epsilon_0 c m_e}\left(\frac{3qB}{2\pi\nu m_e^3 c^4}\right)^{(p-1)/2} = const * \nu^\alpha \tag{1.60}$$

where $a(p)$ is a constant dependent on p (see this function in Chapter 5).

It is worth noting here that the loss rate of an ultra-relativistic electron (v –> c) by inverse Compton scattering in a radiation field of energy density U_{rad} is:

$$-\dot{E}_{IC} = \frac{4}{3}\sigma_T c U_{rad} \gamma^2, \tag{1.61}$$

which has the same form as Eq. 1.59., only the source of the electric field is different (U_{rad} or U_{mag}).

Inverse Compton emission is an important process particularly at high energies, as in this process photons gain energy from moving electrons. Therefore this process needs a "seed" radiation field. This seed field can have several origins, e.g. the cosmic microwave background, or it can originate in the Galaxy, such as from optical photons due to all the stars. Considering compact objects, e.g. GBHBs, the low energy thermal photons from the disk are scattered to higher energies on an electron distribution called the "corona". However, what might be more important, is that the seed photon field can originate from the synchrotron photons as well. So, the synchrotron photons can be inverse Compton scattered on their own electrons, which is called synchrotron self-Compton (SSC). Therefore, the origin of a fitted power-law component can be purely from the jet, even without

employing a corona (e.g. Markoff et al., 2001). Although, in this case, one needs to have radio emission – particularly a jet – to ensure that the synchrotron process is present. Then, depending on the Lorentz factors of the electrons, the radio (and infrared) photons can be upscattered to X-ray and γ-ray energies. In conclusion, the jet contribution to the entire SED of e.g. compact objects, AGNs, due to these two processes is likely important.

1.3.1 Minimum Energy Condition

For extended sources with a volume V, the optically thin synchrotron luminosity can be related to the energy spectrum of the ultra-relativistic electrons and the magnetic field, $L_\nu \sim \nu^{-\alpha}$ (Longair, 1994), so that:

$$L_\nu = A(\alpha) V K_0 B^{1+\alpha} \nu^{-\alpha} \tag{1.62}$$

where $A(\alpha)$ is a constant. Writing the energy density in relativistic electrons ϵ_e, the total energy present in the source responsible for the radio emission is:

$$E_{tot} = V\epsilon_e + V\frac{B^2}{2\mu_0} \tag{1.63}$$

So, if V is known, the radio luminosity is produced either by a large flux of relativistic electrons in a weak magnetic field or vice versa. Between these two extremes of dominant magnetic field and dominant particle energy, there is a minimum total energy requirement. One can also take account of the protons, assuming that they have energy β times that of the electrons, then the total particle energy is $\epsilon_{tot} = (1+\beta)\epsilon_e = \eta\epsilon_e$, so:

$$E_{tot} = \eta V \int_{E_{min}}^{E_{max}} K_0 E N(E) dE + V\frac{B^2}{2\mu_0} \tag{1.64}$$

We know that the maximum intensity of synchrotron radiation occurs at $\nu = 0.29\nu_c = CE^2B$, where $C = 1.22\times10^{10}/(m_e^2c^4)$. So the relevant range of electron energies is $E_{max} = \sqrt{\frac{\nu_{max}}{CB}}$, and $E_{min} = \sqrt{\frac{\nu_{min}}{CB}}$, where ν_{min} and ν_{max} are the frequency range where the radio spectrum is known. After integrating, one can obtain E_{total}. Minimising this function, a minimum total energy can be found with respect to B. This particular magnetic field is called the equipartition magnetic field and corresponds to approximate equality of the energies in relativistic particles and magnetic field. This is referred as equipartition or minimum energy condition. However, if one knows the radio luminosity only at one frequency, then $\nu = \nu_{min}$ can be set and can be obtained a lower limit to the energy requirements, which should be considered as an order of magnitude estimate (Longair, 1994). Unfortunately there is no physical justification for the source components being close to equipartition. Also, the amount of energy stored in protons is unknown. It also has to be assumed that the particles and magnetic field fill the source volume uniformly.

1.3.2 Beaming

A further alternative explanation of the ULX phenomena exists, namely that the X-ray flux could be enhanced due to beaming. There are two types of models that involve beaming. The first one, as mentioned before, is mechanical beaming, and the second one is relativistic beaming. The model of mechanical beaming is related to super-Eddington

disks, that generate winds which are channelled along the poles, and may form jets or outflows (Begelman, 1979). The other model invokes the standard relativistic beaming (Körding et al., 2002), when the radiation is Doppler boosted due to small viewing angles of relativistic jets. This model also assumes that the jet dominates in the X-rays. Given the lack of jet emission among the majority of the ULXs in the radio band, the latter case seems to be unlikely. The first model cannot be ruled out if mild beaming (a factor of maximum 10) and super-Eddington accretion is assumed.

Another way to gain more information on whether ULXs are beamed is to study their environment. There are a number of ULXs associated with optical and radio bubbles. Most of these optical bubbles show strong He II λ4686 Å emission. This high excitation line is due to the strong X-ray/UV source. Given the morphology of these bubbles, one can assume an isotropic optical luminosity. Employing irradiation models, from the integrated flux of the He II line, one can obtain the required X-ray ionizing rate needed to excite this line. Pakull & Mirioni (2002) found that X-ray luminosities inferred this way are consistent with the X-ray luminosity of the ULXs, and concluded that the X-ray radiation is isotropic or at most mildly beamed. Later on, other studies confirmed these findings (see Chapter 4 and Chapter 5).

Observations by Roberts et al. (2002a) show that fraction of ULXs are located in cavities that are not associated with emission-line optical nebulae. It could be that the gas is cleared away by shocks as indicated by the presence of both photoionization and shock-ionization (Pakull & Mirioni, 2003). This is especially interesting because the origin of the optical bubble around IC 342 X-1 (Roberts et al., 2003), and MF16 in NGC 6946 (Roberts & Colbert, 2003) was interpreted as due to supernova remnants. It is still an open question whether jet ionization is a possible alternative to supernova shock ionization. See Chapter 5 and 6 for further details. It is therefore interesting to investigate the total energy content of the shock-ionized bubbles, and compare to the energy content of SNe to determine whether there is a substantial need for additional energy supply - other than the putative initial explosion of a standard SN- in the form of jets.

In general, due to a supernova explosion, a large amount of kinetic energy is injected to the environment. The gas in the environment can then be heated by other SN explosions, stellar winds, collisions, resulting in a large-scale bubble, whose expansion will depend on the ambient density as well as the total injected energy rate. In the model of Weaver et al. (1977), three regions can be distinguished in the bubble as moving out from the center: the region of the stellar wind or the source of kinetic power, the region of the shocked stellar wind and the shocked interstellar gas. Other regions could be defined as well, due to forward and reversed shocks; however, these regions are probably not relevant in a later evolutionary stage. Basically three stages of evolution are considered in an ideal model. In the first stage, the bubble is expanding so fast that radiative losses in the gas are negligible, and the dynamics can be described with an adiabatic flow. In the second stage, the bubble expands, cools by radiation and the swept-up interstellar gas collapses into a thin shell in the region of the shocked interstellar gas. In this evolutionary stage, the region of the shocked wind still conserves energy, while in the final stage, radiative losses affect the dynamics of the region of the shocked wind as well (Weaver et al., 1977).

This idealized model concerns an isotropic input energy with a constant rate of inflation. The bubble is also assumed to expand in a spherically symmetric way into an ambient medium with uniform density. This results in a "self-similar" expansion. Given that ULXs bubbles have large size but are still expanding, the suitable evolutionary stage

is the second one, described above. In this phase the radius of the region where the source of input energy dominates is much less than the radius to the thin shell. Due to the high temperature between the two regions, the time for a sound wave to cross this region is small compared with the age. So, in this entire region it can be assumed that the pressure (p) is uniform and the thermal energy dominates over the kinetic energy. The mass of the shell can be defined as $m = \frac{4\pi}{3} R^3 \rho$. Using energy and momentum conservation laws, the momentum equation of the shell is (Weaver et al., 1977):

$$\frac{d}{dt}(m\dot{R}) = 4\pi R^2 p \tag{1.65}$$

The mechanical and thermal energy (E_{th}) balance is:

$$\frac{dE_{th}}{dt} = L - 4\pi R^2 p\dot{R} \tag{1.66}$$

where L is the input energy rate. Combining the above equations and using that $E_{th} = \frac{3}{2}pV$, the radius of the bubble can be found as:

$$R = \left(\frac{125}{154\pi}\right)^{1/5} L^{1/5}\rho^{-1/5}t^{3/5} \tag{1.67}$$

Also, using shock models for a one-dimensional radiative flow structure where the rate of ionization, recombination, excitation and radiative transfer and cooling are solved numerically (e.g. MAPPINGS) provide the velocity by comparing measured line flux ratios (e.g. He II over Hβ etc.) in the optical spectrum (Dopita & Sutherland, 1996). The total radiative flux and flux in the Balmer lines also scale with the shock velocity and density, thus from Balmer line fluxes, the total radiative power can be obtained. With these parameters all the physical characteristics (e.g. radius, expansion velocity, age, mean density, input energy) of the bubble can be constrained (see Chapter 5).

1.4 Similarities between GBHBs, SMBHs and ULXs

In this section, I will highlight the possible common links between the behavior of GBHBs and SMBHs. This is an important step in order to understand the nature of ULXs, i.e. whether (or not) they can be treated as IMBHs.

1.4.1 Hardness Intensity Diagram and Jets

First of all, during an outburst of a GBHB it often shows a typical pattern. This pattern, often referred as a "turtle head", is drawn on the hardness intensity diagram (HID). The HID basically shows the X-ray evolution of an outburst (Figure 1.5.).

The HID can be divided into X-ray states on the basis of the X-ray hardness ratio between the power-law (hard component) and the disk (soft component). Similarly, it has two well-defined regions: the hard state and the soft state; it is similar to a disk fraction luminosity diagram. Between these two states the physical background is rather unclear (see review McClintock & Remillard, 2006) . Another important property of an X-ray outburst is that a source during the hard state is associated with compact jets (see review Fender et al., 2009), i.e. a synchrotron spectrum in the radio domain with a flat (or slightly inverted) spectral index. During the evolution of the outburst, between state transitions

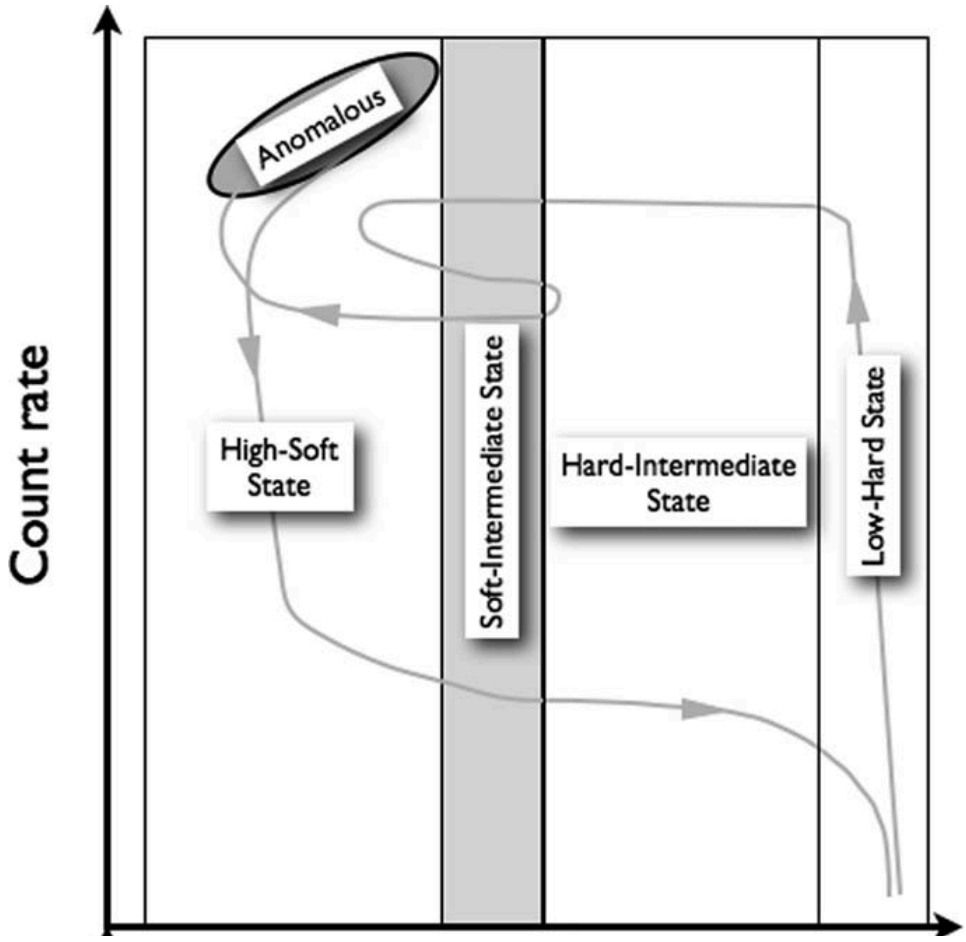

Figure 1.5: The so-called "turtle head" pattern is a schematic representation the evolutionary track of an outburst of a GBHB. The image is from Belloni (2010).

from hard to soft states, the jet is quenched and reappears when the source transits back to the hard state. Although, before the quenching of the jet, in the (hard) intermediate state, the sources are associated with variable radio flares, jet ejections/blobs, rather than steady compact jets. This manifests in an optically thin (steep-spectrum) synchrotron radio emission.

Another important property of GBHBs regarding the HID is that an empirical correlation between the X-ray and radio luminosity has been found (e.g. Corbel et al., 2003), when the sources are in the X-ray hard state. This cast doubts about a full understanding of the outburst behavior of an accreting system and demanded to consider jets as essential elements of accretion.

1.4.2 Fundamental Plane of Black Holes: Mass Scaling

It is clear that an accreting (binary) system cannot be considered as just a disk (or disk and corona), but that jets also need to be taken into account. The realization of this fact prompted the consideration of accreting systems in a new manner. In 2003 and 2004, two groups independently found that the above correlation is not just valid for GBHBs, but also for SMBHs (Merloni et al., 2003; Falcke et al., 2004), although, it is not straightforward. First of all, the evolutionary and outburst time-scale of SMBHs are much longer

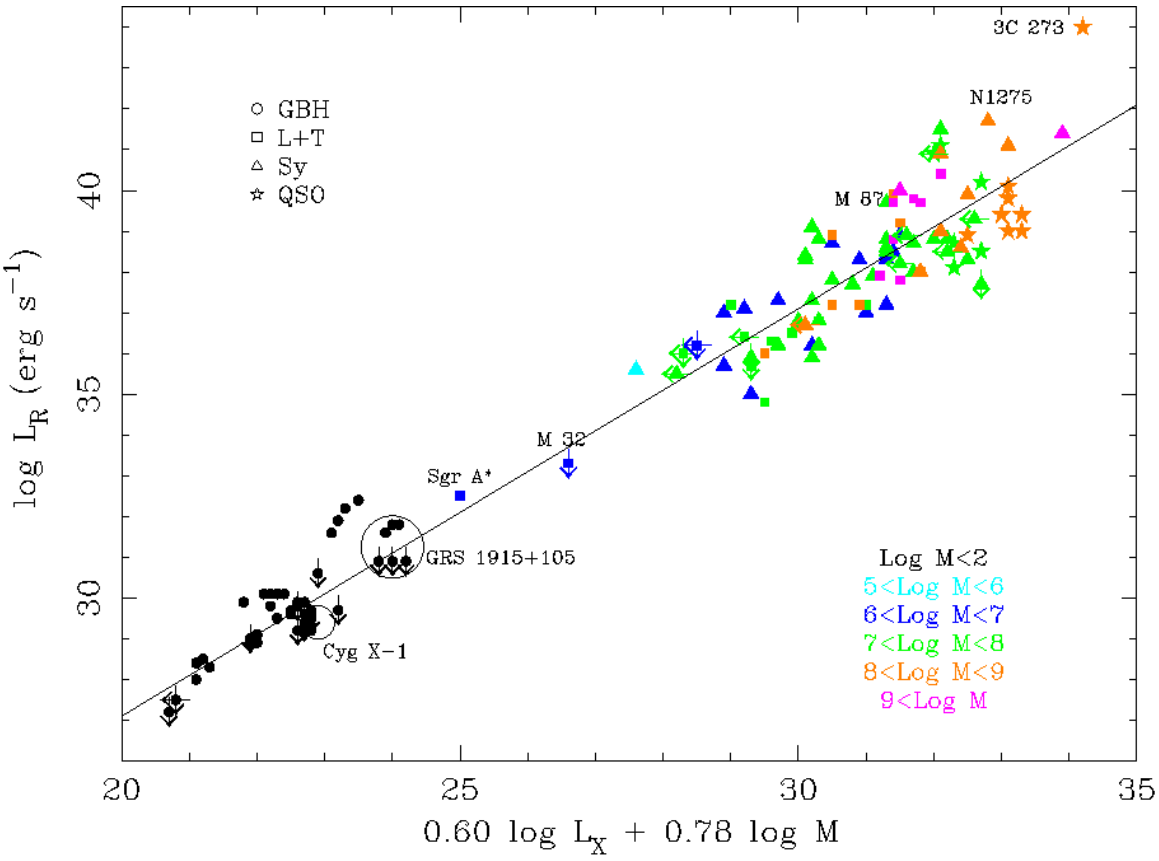

Figure 1.6: The fundamental plane of black holes (Merloni et al., 2003). The figure shows the radio luminosity as a function of X-ray luminosity "corrected" with the mass of the black hole.

than for GBHBs, so it is difficult to have an HID for a single SMBH. One needs to construct a sample that consists of radio loud objects as there is no correlation in GBHBs in the soft state where jets are quenched (see later). Using a suitable sample, it was found that a correlation holds when the correlation of the GBHBs is scaled by the mass of the black holes, to SMBHs. This implied that the physical characteristics of an accretion system scales by the mass of the black hole (whether linearly or not), which might not be that surprising given that even Einstein predicted it. Moreover, later on it was found that the correlation is much tighter when considering a sample of radio loud SMBHs that can be treated as a scaled-up population of hard state objects (Körding et al., 2006a). For instance, objects like low-luminosity AGN (LLAGN) and FR I galaxies, but not FR II and Seyferts. In other words, it was realized that the physics is scaled not just by the mass of the black hole but also by the accretion rate. In summary, the fundamental plane of accreting objects is a correlation among the X-ray luminosity, radio luminosity and mass of the black hole.

One of the most compelling models that links the physics between the disk and jet components, describes a symbiotic behavior of the two components (Falcke & Biermann, 1995). This model basically connects the standard disk with a canonical conical jet model (Blandford & Königl, 1979) in a way that the total jet power is a constant fraction of the accretion power available in the disk. Similarly, there is another successful model, based on the fact that the properties of an accreting system can be expressed in units of the grav-

itational radius. It assumes that the jet structure and dynamics are invariant under the changes of $R_g \propto M$ and $\dot{m}$, i.e it employs a scale-invariant jet model (Heinz & Sunyaev, 2003). However, there is a major difference between the two models. The first one favors a jet-dominated accretion flow (Falcke et al., 2004), the other prefers an ADAF (Merloni et al., 2003). Due to the scatter on the fundamental plane and due to the similarity between the predicted scaling laws of these two models, it is not possible to distinguish between the type of accretion flow from the fundamental plane alone. As a conclusion, on the basis of the current theoretical interpretation, the fundamental plane works best when considering sources in the hard state, i.e. when the accretion is radiatively inefficient, either jet or advection dominated.

Currently, the major research focus is to find good candidate IMBHs that could fill the gap between the two populations of the black holes on the fundamental plane. Therefore, ULXs are important not just because they are potential IMBHs, but they can serve as tests for the above accretion models as well. This involves the search for potential IMBHs, e.g. studying globular clusters by using the fundamental plane as a tool (see Chapter 3.). Furthermore, the ultimate proof that a number of ULXs are indeed IMBHs, has to come from a dynamical mass measurement (see Chapter 4.).

There are many open questions even regarding the standard picture of GBHBs. For instance, in the soft state, where the sources are thought to be disk dominated, in certain cases, one sees broad X-ray lines in the spectrum with P Cygni profiles, indicative of disk winds (Neilsen & Lee, 2009). These winds may be important for understanding why jets are quenched, which is unknown. This might also help to understand the X-ray spectra of ULXs, given that the jet quenching process is related to the high or high/soft X-ray states. This is interesting because there are no ULXs found to be associated with a compact jet to date. Certain ULXs are only found to be associated with large scale optical and radio bubbles, but some of them are possibly inflated by a jet (see Chapter 5). Also, there is one, or rather the first exceptional case, where radio flares are detected from a ULX during an X-ray state transition (see Chapter 7).

2 Instruments

Contents

In this Chapter I will introduce the main astronomical facilities, e.g. VLA, ATCA, VLT and Chandra, that I have used for obtaining data or calibrated and analyzed it's data for my research. I have used data from the EVN, Hubble and Swift/XRT as well. Also, an astronomical instrument is best characterized by its resolution and sensitivity, therefore I will pay a special attention to this.

2.1 Radio Observatories

2.1.1 The Very Large Array (VLA)

The Very Large Array (VLA) [1] is operated by the National Radio Astronomical Observatory (NRAO) in Socorro, New Mexico, US. The VLA has 27 antennas with a size of 25 meter that are linked with optical fibers. The Y-shaped array is situated on the Plains of San Agustin. The array – in its most extended configuration – has resolution equivalent with a single dish of a size of 36 km and has a sensitivity of a dish with a diameter of 130 meter. Additionally, this is the same telescope that Jodie Foster used in the movie called Contact.

In recent years, the VLA has undergone a crucial technical development. Its receivers were replaced. To reflect these upgrades it was renamed to the Extended VLA (EVLA)

[1] http://www.vla.nrao.edu/

Figure 2.1: The Very Large Array showing the Y-shape. http://images.nrao.edu/Telescopes/VLA

Table 2.1: Overall EVLA performance (goal)

Parameter	VLA	EVLA	Factor
Continuum Sensitivity (1-σ, 9 hr)	10 μJy	1 μJy	10
Maximum BW in each polarization	0.1 GHz	8 GHz	80
Number of frequency channels at max. BW	16	16384	1024
Maximum number of freq. channels	512	4194304	8192
Coarsest frequency resolution	50 MHz	2 MHz	25
Finest frequency resolution	381 Hz	0.12 Hz	3180
Number of full-polarization sub-correlators	2	64	32
Log (Frequency Coverage over 1-50 GHz)	22%	100%	5

and it is currently named the Karl. G. Jansky VLA (JVLA). The new receivers have 2–8 GHz bandwidth (BW) instead of 50 MHz, thus the sensitivity of the array is dramatically increased, as are many other abilities of the array (see Table 2.1). Also, the VLA is providing almost the best angular resolution among the connected element arrays. Its resolution covers a range of 46 arcsec to 43 milli-arcsec, depending on observing frequency and array configuration (see Table 2.2).

The EVLA has other advantages over the VLA; for instance, it can perform imaging of extended low-brightness sources with tens of arcsecond resolution and microKelvin brightness sensitivity. Regarding its imaging capability, the achievable spatial dynamic range is greater than 10^6, its frequency dynamic range is greater than 10^5, and its image field of view is greater than 10^9 with full spatial frequency sampling. Additionally, it is operated with dynamic scheduling, based on weather, array configuration, and science requirements [2].

[2]http://www.aoc.nrao.edu/evla/

Table 2.2: Configuration properties of the EVLA

Configuration	A	B	C	D
Bmax (km1)	36.4	11.1	3.4	1.03
Bmin (km1)	0.68	0.21	0.0355	0.035
	Synthesized Beamwidth (arcsec)			
74 MHz (4 band)	24	80	260	850
1.5 GHz (L)	1.3	4.3	14	46
3.0 GHz (S)	0.65	2.1	7.0	23
6.0 GHz (C)	0.33	1.0	3.5	12
8.5 GHz (X)	0.23	0.73	2.5	8.1
15 GHz (Ku)	0.13	0.42	1.4	4.6
22 GHz (K)	0.089	0.28	0.95	3.1
33 GHz (Ka)	0.059	0.19	0.63	2.1
45 GHz (Q)	0.043	0.14	0.47	1.5

2.1.2 The Australia Telescope Compact Array (ATCA)

Figure 2.2: The Australia Telescope Compact Array[2]

The Australia Telescope Compact Array[3] is located near Narrabri, NSW, Australia. It is similar to EVLA, a connected element array, with six 22-m radio antennas. ATCA is a valuable array with which to observe sources on the Southern Hemisphere. It is operated by the Commonwealth Scientific and Industrial Research Organisation (CSIRO).

A new broadband backend system, the Compact Array Broadband Backend (CABB), was installed on ATCA. This provides an increased bandwidth of 2 GHz (from 128 MHz), which is a factor of 16 improvement. Also, this resulted in an improved in continuum

[3]http://www.narrabri.atnf.csiro.au/

Table 2.3: Properties of the ATCA

Band name	16cm	6cm	3cm	15mm	7mm	3mm
Band code	L / S	C	X	K	Q	W
Frequency range (GHz)	1.1-3.1	4.4-6.7	8.0-10	16-25	30-50	83 -105
Fractional frequency range	95%	39%	22%	44%	50%	24%
Primary beam	42′ - 15′	9′	5′	2′	70″	30″
Strongest confusing source (mJy)	140 - 24	2.3	0.4	–	–	–
Array assumed below	6km	6km	6km	6km	6km	H214
Synthesized beam	9″ - 3″	2″	1″	0.5″	0.2″	2″
Centre frequency assumed below (GHz)	2.1	5.5	9.0	17.0	40.0	95.0
Flux sensitivity (mJy/beam) (10 min)	0.03	0.05	0.06	0.05	0.10	0.73
Flux sensitivity (uJy/beam) (12 hr)	4	5	7	6	11	86

sensitivity by a factor of about four due to the higher data sampling. Regarding the CABB-upgraded ATCA spectral line performance, there is also an improvement not just at higher observing frequencies, but it also involves the possibility to study spectral lines simultaneously using this wider bandwidth. A bandwidth of 2 GHz with 2048 $\times$ 1-MHz channels or optionally a fine resolution of 0.5 kHz in up to 16 zoom bands in each IF is available.

2.2 Optical Observatory

2.2.1 The Very Large Telescope (VLT)

Figure 2.3: The Very Large Telescope[3]

The Very Large Telescope array (VLT)[4] is located at an altitude of 2635 m, in Cerro

[4]http://www.eso.org/public/teles-instr/vlt.html

Paranal, Chile. The VLT is operated by the European Southern Observatory. It has four Unit Telescopes (UT) with primary mirrors of 8.2-m and four movable Auxiliary Telescopes with 1.8-m mirrors. The Unit Telescopes are named Antu, Kueyen, Melipal and Yepun. The optical designs are Ritchey-Chretien reflectors with active optics. The telescopes can be operated in an interferometer mode, with a maximum baseline of 130 meter. On the other hand the Unit Telescopes can be operated individually and they can successfully image a source with a magnitude down to 30 within an hour of exposure time. It is interesting to note that with such an instrument one can see sources billion times fainter than one could see with a human eye.

It has several instruments available, including spectrographs. I used the visual and near-UV focal reducer and low dispersion spectrograph (FORS-2), mounted on UT1 (Antu). Its field of view is 6.8 $\times$ 6.8 arcminute, in standard resolution mode, and 4.25 $\times$ 4.25 arcminute in high resolution mode. Its wavelength range is between 330 and 1100 nm, the mosaic detector has 2 $\times$ 2k $\times$ 4k pixel CCDs providing a pixel scale of 0.25 arcsecond/pixel or 0.125 arcsecond/pixel, depending on the resolution mode. It has a spectral resolution of 100 – 400, i.e. $\sim$ 2 Å at best.

2.3 X-ray Observatory

2.3.1 Chandra

Figure 2.4: The Chandra X-ray Observatory[4]

Chandra[5] was launched on July 23, 1999, and the Chandra X-ray Observatory is operated by NASA. The Chandra telescope consists of four pairs of mirrors and their support structure. Chandra mirrors are required an unprecedented polishing process to a smoothness of a few atoms and an alignment of a about a micrometer.

There are two imaging instruments with four CCDs at the focal plane, ACIS (Advanced CCD Imaging Spectrometer) and HRC (High Resolution Camera). These cameras record the image focused by the mirrors, in a way that they register the number of X-ray photons at a given position, energy and time. On the other hand the LETG (Low Energy Transmission Grating Spectrometer) and HETG (High Energy Transmission Grating Spectrometer) spectrometers consist of six CCDs and are used to study the X-ray spectrum in a way that these instruments diffract the X-rays, which depends on the energy of incoming photons.

[5]http://chandra.harvard.edu/

The CCDs are front-side illuminated and are sensitive to 0.2-10 keV X-ray energy band. During the process of absorbing an X-ray photon in the silicon plate, a number of electrons are produced. This number has statistical fluctuation that limits the energy resolution of the ACIS CCDs. In general, the energy resolution is a function of the energy band and the readout noise of the CCDs, but the latter one is at the theoretical limit due to CCD fabrication techniques. The rms of the energy resolution is between 20 and 140 eV corresponding to an energy range of 0.1 – 10 keV. The on-axis effective area is 110 cm^2 at 0.5 keV for the S3 chip, the maximum readout rate per channel is 100 kpix/s. It has a point source sensitivity of 4×10^{-15} erg cm^{-2} s^{-1} in 10^4 second, and it has a pixel size of 0.49 arcsec.

3

An IMBH in the Globular Cluster NGC 6388?

Contents

This chapter is based on the content of my first paper (Cseh et al., 2010).

Radio observations of NGC 6388: an upper limit on the mass of its central black hole

D. Cseh, P. Kaaret, S. Corbel, E. Körding, M. Coriat, A. Tzioumis and B. Lanzoni
2010, MNRAS, 406, 1049

In this chapter I describe deep radio observations with the Australia Telescope Compact Array (*ATCA*) of the globular cluster NGC 6388. My aim was to set constraints on the mass of the putative IMBH located at the cluster center of gravity. To this purpose I studied the accretion signatures. In first hand I analysed archival Chandra data in order to reveal the nature of the innermost X-ray sources to constrain whether their position match the cluster center of gravity and whether they exhibit an X-ray spectrum consistent with a black hole. Then I showed that there is no radio source detected with a r.m.s. noise level of 27 μJy at the cluster centre of gravity or at the locations of any of the *Chandra* X-ray sources in the cluster. Due to the fact that the central X-ray sources have low X-ray luminosities in Eddington units, I apply the formula from the fundamental plane of accreting black holes, which is a relationship between X-ray luminosity, radio luminosity and black hole mass. I place an upper limit of $\sim$1500 $M_\odot$ on the mass of the putative intermediate-mass black hole located at the centre of NGC 6388. On the other hand, the X-ray luminosities are also consistent with the Bondi-Hoyle accretion process, therefore I also discussed the observed accretion signatures in that framework. I discussed the uncertainties of this upper limit and compared to the previously suggested black hole mass of 5700 $M_\odot$ based on surface density profile analysis at the end of this Chapter as well as the caveats of this method.

3.1 Introduction and NGC 6388

Following the early discoveries of X-ray sources in globular clusters in the mid-1970s (Clark, 1975), it was proposed that the X-ray emission of these clusters was due to accretion of intracluster material released by stellar mass loss onto central black holes (Bahcall & Ostriker, 1975; Silk & Arons, 1975). This initiated a debate about whether globular clusters contain black holes of intermediate masses (i.e. greater than the $\sim$ 30 $M_\odot$ limit for black holes formed through normal single star evolution, but less than the 10^5 $M_\odot$ seen in the smallest galactic nuclei). Considering the evolution of globular clusters, it is expected that when they orbit through the Galactic plane they lose their light mass content due to dynamical interactions. Given the ages of these clusters these interactions can happen also multiple times resulting in a cluster that has a typically very low gas content or density. Therefore detecting accretion signatures from black holes might be challenging.

On the other hand, the evolution of globular clusters leaves open questions about the black hole content and formation in these clusters. In general, the colour-magnitude diagram of Galactic globular clusters show a distinct main-sequence, main-sequence turn-off, horizontal and giant branches of a single co-eval stellar population (Benacquista & Downing, 2011). This means, stars only differ by their masses that is determined by the initial mass function (IMF). In this model the stars or not massive enough to form black holes, just to form neutron stars. On the contrary, observations showed systematic light element variation from star to star, which led to models where a globular cluster experiences several bursts of star formation leading to multiple stellar populations with sightly different chemical compositions. The effect of relativistic binaries on these models is still to be explored (see review Benacquista & Downing, 2011).

Black holes are strongly affected by mass segregation because they are much more massive than the average mass of stars, and during their dynamical evolution they may be exchanged to binaries in the dense cores of globular clusters (Benacquista & Downing, 2011). Using simulations, Portegies Zwart & McMillan (2000) found that only 8% of black holes were retained by their parent clusters while 61% were ejected as singles and 31% were ejected as binaries. Furthermore, Gültekin et al. (2004) found that it was not possible to create a merged black hole with a mass $>$240 $M_\odot$, because it was either ejected or there were insufficient amount of gas to grow a massive black hole. On the other hand, some study suggests that dynamical processes in the inner regions of globular clusters may lead to the formation of black holes of $\sim 10^3$ $M_\odot$ (Miller & Hamilton, 2002). These difficulties of stellar dynamics have prompted a search for accretion constraints on the presence of intermediate-mass black holes.

Despite the theoretical difficulties, there are possibly several observational indications for black holes in globular clusters. To date five good candidate stellar-mass black holes (StMBHs) are known, based on their X-ray luminosity and X-ray variation (Maccarone et al., 2011). However, the most interesting question arises about IMBHs, as indirect evidence of the existence of IMBHs comes from the study of the central velocity dispersion of stars in specific globular clusters. For example, by using velocity dispersion measurements, it was proposed that IMBHs may exist in M 15, NGC 6752, ω Cen, 47 Tuc and G1 with masses of about 10^3-10^4 $M_\odot$. Figure 3.1 shows the best candidate IMBH hosts that are globular clusters. It also shows the expected mass of the IMBH at the cluster center of gravity in NGC 6388 in red.

Considering the methods of detecting accretion signatures, it was pointed out by Mac-

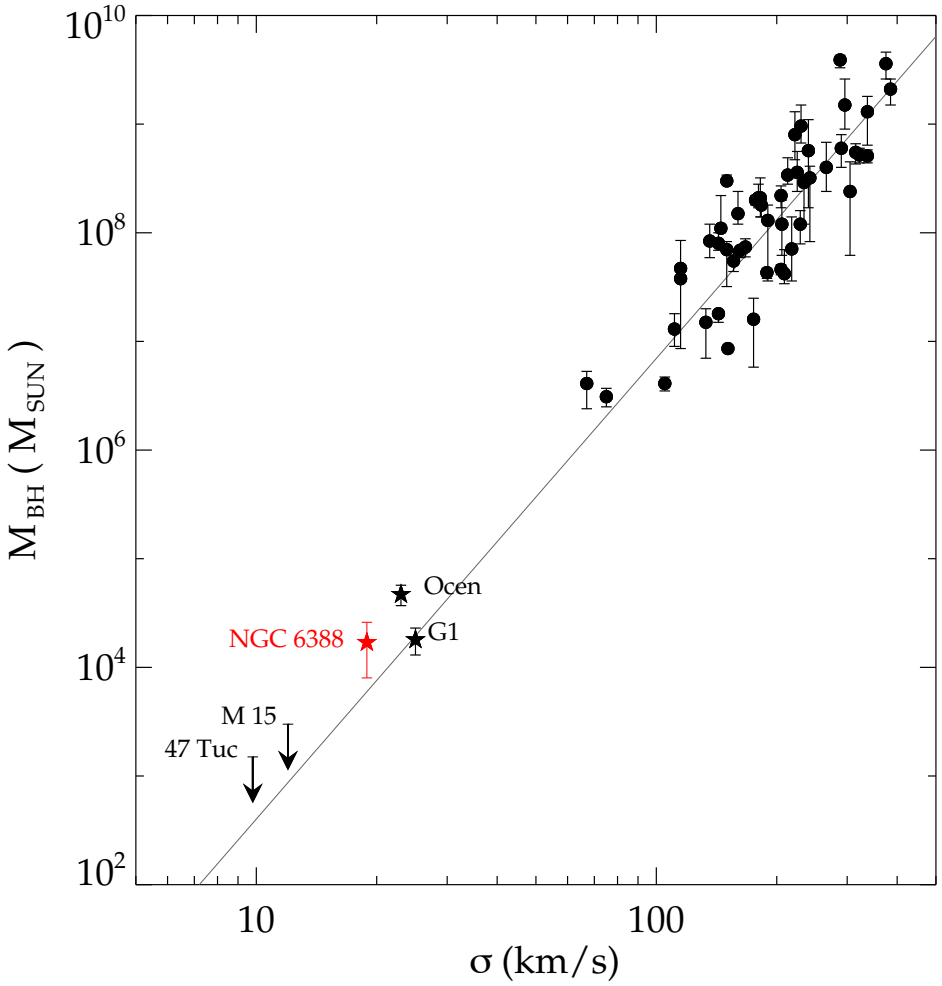

Figure 3.1: This image was taken from Lützgendorf et al. (2011). The M-σ relation for galaxies at the high mass range (filled circles) and the first globular clusters with potential black hole detection (filled stars). The slope of the line $\log(M/M_{\odot}) = \alpha + \beta \log(\sigma/200\text{km s}^{-1})$ with $(\alpha, \beta) = (8.12 \pm 0.08, 4.24 \pm 0.41)$

carone (2004); Maccarone et al. (2005) that deep radio searches may be a very effective way to detect intermediate-mass black holes in globular clusters and related objects. This is because for a given X-ray luminosity, supermassive mass black holes produce far more radio luminosity than stellar-mass black holes. In addition, the relation between black hole mass and X-ray and radio luminosity empirically appears to follow a "fundamental plane" (see Chapter 1), in which the ratio of radio to X-ray luminosity increases as ∼0.8 power of the black hole mass (Falcke & Biermann, 1996, 1999; Merloni et al., 2003; Falcke et al., 2004). Also, as the luminosity of accretion onto a black hole decreases, the ratio of radio to X-ray power increases (Corbel et al., 2003; Gallo et al., 2003).

Searches for radio emission from globular clusters have mostly yielded only upper limits (Maccarone et al., 2005; de Rijcke et al., 2006; Bash et al., 2008; Cseh et al., 2010; Lu & Kong, 2011; Wrobel et al., 2011) (Table 3.1). Although, the cluster G1 in M31 seems to have evidence for harbouring an intermediate-mass black hole (Ulvestad et al., 2007), including radio detection. I note that Miller-Jones et al. (2012) recently reported no radio emission from G1 using sensitive EVLA (The Extended Very Large Array) measurements.

Table 3.1: Recent radio continuum observations and upper limits on globular cluster black holes

Cluster name	Distance (kpc)	$F_{r,5GHz}$ (μJy)	$M_{BH,rad}$ ($M_\odot$)	$M_{BH,dyn}$ ($M_\odot$)
NGC 6388	11.6	<81	<735-1500	5700
(new values)	-	<42	<600	17000
ω Cen	5.3	<20	<1100-5200	12000
47 Tuc	4.5	<40	<520-4900	1500
NGC 2808	9.5	<162	< 1800-8500	2700
M15	10.3	< 25	<700-4900	1000
M62	6.9	< 36	< 600-2900	3000
M80	10.0	<36	<1100-5300	1600
NGC 6397	2.7	< 216	< 900-4300	50
G1	780	<28	<4500	18000
M54	26.3	<51	<14500	9400

The majority of the values are taken from Lu & Kong (2011) (and references therein). For M54, the $M_{BH,rad}$ was calculated based on values reported by Wrobel et al. (2011). The radio flux $F_{r,5GHz}$ is the 3-σ upper limit except for G1. $M_{BH,rad}$ shows the upper limits on BH mass, estimated from accretion signatures and $M_{BH,dyn}$ shows the dynamical mass estimates.

This casts further doubts about the possibility to detect accretion signatures. It cannot yet be excluded that the radio emission from G1 is variable, or it could also be possible that the previously detected radio emission originated from an extended object similar to radio nebulae around ULXs.

Given the low gas density in a globular cluster, we also have to consider the Bondi accretion process, which is the spherical infall of the intracluster material onto a black hole. Accretion theory suggests that the Bondi-Hoyle rate (Bondi & Hoyle, 1944) overestimates the actual accretion rate by 2-3 orders of magnitude (Perna et al., 2003). Perna et al. (2003) argues that this overestimation manifests in the fact there are no isolated neutron stars detected at ROSAT sensitivity, despite their large number in the Galaxy and their predicted visibility in X-rays as a result of accretion from the interstellar medium. Thus, the X-ray luminosities from accretion of the interstellar medium by intermediate-mass black holes in globular clusters are likely to be well below detection limits of current X-ray observatories. Therefore it is interesting to calculate the Bondi-rate and examine whether an X-ray source could potentially be an IMBH on the basis of the "allowed" range of Bondi-rates and efficiencies. On the other hand, considering the prediction of Miller & Hamilton (2002), that the black holes should have about 0.1 per cent of the total cluster mass, the radio luminosities of the brightest cluster central black holes may be detectable with existing instrumentation (Maccarone, 2004).

I add here that beyond globular clusters, there are other possibilities for intermediate-mass black holes. They may be produced in the core collapses of $\sim 100 - 1000$-$M_\odot$ Population III stars, e.g. Fryer et al. (2001) (Chapter 1). Other good candidates for hosting intermediate-mass black holes are thought to be young dense star clusters (Portegies Zwart & McMillan, 2002; Portegies Zwart et al., 2004; Gürkan et al., 2004) and ultraluminous X-ray sources (Chapter 1), whose X-ray luminosities well exceed the Eddington luminosity of a ten solar-mass compact object (Kaaret et al., 2001; Zampieri & Roberts, 2009).

Table 3.2: Properties of NGC 6388

Parameter	Value
RA (J2000)	17h 36m 17s
DEC (J2000)	-44° 44′ 08″
Galactic Longitude l	345.56
Galactic Latitude b	-6.74
Distance from the Sun R_{SUN}	11.6 kpc
Core Radius r_c	7.2″
Central Concentration c	1.8
Heliocentric Radial Velocity V_r	81.2 ± 1.2 km/s
Central Velocity Dispersion σ	18.9 km/s
Age	11.5 ± 1.5 Gyr
Metallicity [Fe/H]	-0.6 dex
Integrated Spectral Type	G2
Reddening E(B-V)	0.38
Absolute Visual Magnitude M_V	-9.42 mag

NGC 6388 is a typical globular cluster residing in our Galaxy. However, multiple stellar populations are present. As noted above, globular clusters with multiple stellar populations might be better candidates for containing black holes. Other evidence supporting the idea that globular clusters, like NGC 6388, contains an IMBH comes from the down-scaling of the M-σ relation (see Fig. 3.1).

Furthermore, evidence favouring an intermediate-mass black hole in NGC 6388 is that the observed surface density profile has a power-law shape with a slope $\alpha = -0.2$ in the inner ten arcseconds of the cluster (Fig. 3.2). The surface brightness and the projected density profiles of the majority of globular clusters can be fitted by models characterized by King models (King, 1966) that usually consist of an extended isothermal core and a tidally truncated envelope. However, there is a fraction ($\sim$15%-20%) of Galactic globular clusters that do not exhibit an extended core; instead, they exhibit a power-law behavior S(r) $\propto$ r^{α}, with α ranging from -0.8 to -1.0 (Lanzoni et al., 2007). These are called post core collapse clusters, because this power-law behavior is thought to originate from the evolution of stellar systems that have experienced the collapse of the core (Lanzoni et al., 2007). On the other hand, the slope of NGC 6388 is shallower than expected for a post core collapse cluster. Considering numerical and theoretical predictions, the slope is consistent with the presence of an intermediate-mass black hole (Baumgardt et al., 2005; Miocchi, 2007). However, it is worth adding that a recent simulation (Vesperini & Trenti, 2010) shows that shallow cusps in the surface brightness profile appear naturally during the dynamic evolution of star clusters without an IMBH. Therefore their presence in an observed profile cannot be used as a strong argument in favor of the presence of a central IMBH, but it certainly does not rule it out. In any case, the surface density profile provided an estimated mass of 5700 ± 500 $M_{\odot}$ (Lanzoni et al., 2007) for the central black hole in NGC 6388 and it motivated us to propose radio observations of the source.

Here, I report on radio observations with the Australia Telescope Compact Array (*ATCA*) of NGC 6388 that led to an upper limit on the mass of the putative intermediate-mass black hole located at the centre of NGC 6388. I discuss the analysis of an archival *Chandra* observation and our new *ATCA* radio observations of NGC 6388. Then, I discuss the results of the X-ray and radio observations. Finally, I discuss the methodology for set-

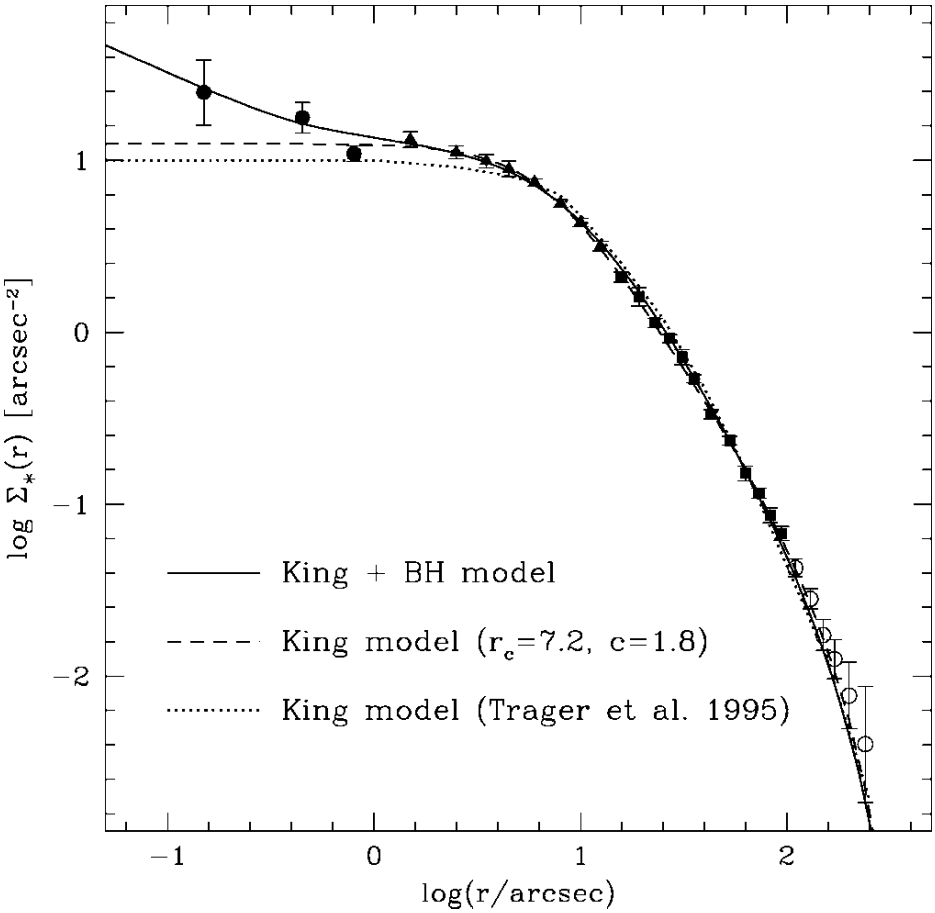

Figure 3.2: This image was taken from Lanzoni et al. (2007). The surface brightness profile of NGC 6388 shows a clear cusp for the inner 10 arcseconds. The observed surface density profile obtained by star counts from the combined photometric data set: ACS/HRC (filled circles), WFPC2 (filled triangles), ACS/WFC (filled squares), and WFI (open circles). The single-mass King model that best fits the profile, excluding the innermost ($r \leq 1''$) points, is shown as a dashed line. It is characterized by a sizable core radius ($r_c = 7.2''$) and an intermediate concentration (c = 1.8). The solid line shows the profile of the model including a 5.7×10^3 M_{BH} in the cluster center.

ting an upper limit on the mass of a central black hole in NGC 6388 and the uncertainties.

3.2 Chandra Observation

NGC 6388 was observed with the Chandra X-Ray Observatory (Weisskopf et al., 2002) using the Advanced CCD Imaging Spectrometer spectroscopy array (ACIS-S) in imaging mode. The *Chandra* observation (ObsID 5055; PI Haldan Cohn) began on 21 April 2005 02:28:32 UT and had a useful exposure of 45.2 ks. Although an analysis of the *Chandra* data was recently published by Nucita et al. (2008), we improved the localisation of the X-ray sources in the centre of the cluster by removing the pixel randomisation[1].

The *Chandra* data were subjected to standard data processing (CIAO version 4.1.2 using CALDB version 4.1.4) and then reprocessed to remove pixel randomisation because

[1]http://cxc.harvard.edu/ciao3.4/threads/acispixrand/

Table 3.3: X-ray sources in the core of NGC 6388

	S/N	RA	DEC	Counts
1	17.7	17 36 17.683	-44 44 16.78	439
2	13.9	17 36 16.941	-44 44 9.90	289
3	10.3	17 36 17.332	-44 44 8.36	237
4	8.6	17 36 18.184	-44 43 59.53	114
5	8.1	17 36 17.518	-44 43 57.17	102
6	8.1	17 36 16.625	-44 44 23.43	130
7	7.1	17 36 17.312	-44 44 7.10	157
8	6.9	17 36 17.010	-44 44 3.06	84
9	6.8	17 36 17.243	-44 44 10.38	87
10	6.1	17 36 17.119	-44 44 12.83	77
11	5.3	17 36 17.161	-44 44 1.92	61
12	4.5	17 36 17.188	-44 44 7.61	69
13	4.4	17 36 17.346	-44 43 53.73	36
14	4.2	17 36 18.053	-44 44 4.30	32
15	4.1	17 36 17.401	-44 44 3.19	30
16	3.7	17 36 16.872	-44 44 12.85	35
17	3.6	17 36 17.325	-44 43 57.21	23
18	3.4	17 36 17.051	-44 44 12.44	41

we are interested in sources in the crowded region near the cluster centre. We also applied an aspect correction as described on *Chandra* aspect webpages[2]. The total event rate on the S3 chip was less than 1.7 c/s throughout the observation indicating there were no strong background flares.

3.2.1 Chandra Imaging

We first constructed an image of the full area viewed by the ACIS-S3 chip using all valid events in the 0.3–8 keV band. The *Chandra* aspect uncertainty is $0.6''$ at 90 per cent confidence[3]. To attempt to improve on this we searched for X-ray sources with counterparts (Kaaret, 2002) in the 2MASS catalogue of infrared sources with a J magnitude brighter than 14 (Skrutskie et al., 2006). We excluded sources within $40''$ of the cluster centre due to the source crowding in that region. We choose X-ray sources which are likely foreground stars by selecting those with soft spectra (Kong, 2007), specifically those with more counts in the 0.5–1.5 keV band than in the 1.5–6 keV band (Grindlay et al., 2001). There are 10 such sources with a detection significance above 3σ. Of these 10, one at $\alpha_{\rm J2000} = 17^h36^m4.^s55, \delta_{\rm J2000} = -44^\circ45'24.''2$ is located within $0.23''$ of a 2MASS source and a second at $\alpha_{\rm J2000} = 17^h36^m25.^s99, \delta_{\rm J2000} = -44^\circ47'53.''3$ is within $0.37''$ of a 2MASS source. There are 636 such 2MASS sources in the search area of 2.25×10^5 $''^2$. With 10 X-ray sources, the probability of one chance overlap within $0.4''$ is 0.0014 and the probability of two chance overlaps is 2×10^{-4}. Thus, the *Chandra* astrometry appears to be accurate to within $0.4''$.

We then constructed images of a $38'' \times 38''$ region centered on the cluster core with pixels which are $0.25'' \times 0.25''$ in the 0.3–8 keV and 2–10 keV bands. We searched for

[2]http://cxc.harvard.edu/ciao/threads/arcsec_correction/index.html#calc_corr
[3]http://cxc.harvard.edu/cal/ASPECT/celmon

sources in the 0.3–8 keV image using the *celldetect* tool in *CIAO*. A list of detected sources with significance of 3σ or higher is given in Table 3.3.

Table 3.3 includes for each source: the source number; S/N – the significance of the source detection as calculated by *celldetect*; RA and DEC – the position of the source in J2000 coordinates - note that, while the relative positions should be accurate to $0.2''$, there is an $0.4''$ overall astrometric uncertainty; Counts - total counts in the 0.3–8 keV band.

Fig. 3.3 shows an X-ray image of the core of NGC 6388 in the 2–10 keV band with the position of the cluster center of gravity, $\alpha_{\rm J2000} = 17^h36^m17.^s23, \delta_{\rm J2000} = -44^\circ44'7.''1$ (Lanzoni et al., 2007), superimposed. The radius of the circle is $0.5''$ which is equal to the sum in quadrature of the *Chandra* aspect uncertainty of $0.4''$ (see above) and the uncertainty of $0.3''$ in the position of the centre of gravity. Two of the *Chandra* sources lie near the centre of gravity error circle. The error circle for source #12 overlaps the edge. Source #7 lies $0.9''$ from the centre of gravity. If we use the coordinates calculated from the 2–10 keV image (and not 0.3–8 keV as above), then source #12 moves inside the centre of gravity error circle, while source #7 moves further away.

3.2.2 X-ray Spectra of Source 12 and 7

We extracted X-ray spectra for these two sources using circular extraction regions with radii of 1.5 pixels centred on the coordinates given in Table 3.3. The extraction radius is smaller than usual for *Chandra* sources, but this is necessary given the source crowding. The 80 per cent encircled power radius is $\sim$0.7 arcsec[4] thus, the measured source fluxes were increased by a factor of 1.2 to account for the flux outside the extraction region. We fitted the X-ray spectra using the *Sherpa* spectral fitting package and response matrices calculated using the `mkacisrmf` tool in *CIAO*. We used the χ^2-Gehrels statistic to evaluate the goodness of fit due to the low numbers of counts in some spectral bins.

A good fit, $\chi^2/{\rm DoF} = 2.9/8$, was obtained for source #12 with an absorbed power-law spectrum with a photon index, Γ=1.90 ± 0.45 and an equivalent hydrogen absorption column density of $N_H = (3.8 \pm 1.8) \times 10^{21}\,{\rm cm}^{-2}$. The absorbed flux in the 0.3–8 keV band was $2.4 \times 10^{-14}\,{\rm erg\,cm^{-2}\,s^{-1}}$ and the unabsorbed flux was $4.0 \times 10^{-14}\,{\rm erg\,cm^{-2}\,s^{-1}}$ in the 0.3–8 keV band and $2.15 \times 10^{-14}\,{\rm erg\,cm^{-2}\,s^{-1}}$ in the 2–10 keV band.

An absorbed power-law provided a good fit for the spectrum of source #7, $\chi^2/{\rm DoF} = 7.8/16$. The best fit parameters were a photon index, Γ=1.66 ± 0.27 and an equivalent hydrogen absorption column density of $N_H = (3.5 \pm 1.3) \times 10^{21}\,{\rm cm}^{-2}$. The lower bound on $N_H = 2.2 \times 10^{21}\,{\rm cm}^{-2}$ was fixed to the Galactic HI column density along the line of sight. The absorbed flux in the 0.3–8 keV band was $4.8 \times 10^{-14}\,{\rm erg\,cm^{-2}\,s^{-1}}$ and the unabsorbed flux was $6.9 \times 10^{-14}\,{\rm erg\,cm^{-2}\,s^{-1}}$ in the 0.3–8 keV band and $4.6 \times 10^{-14}\,{\rm erg\,cm^{-2}\,s^{-1}}$ in the 2–10 keV band.

3.3 ATCA Observations

We observed NGC 6388 with the Australia Telescope Compact Array in configuration 6D (baselines up to 6 km) between 24 and 28 December 2008. The data were obtained simultaneously at 8384 & 9024 MHz and at 18496 & 18624 MHz with 16 h and 17 h on-source integration time, respectively. We observed in phase-reference mode; the phase calibrator was 1740-517 and the primary calibrator was PKS 1934-638. The data reduction was performed using the MIRIAD software package (Sault et al., 1995) in a standard way.

[4] http://cxc.harvard.edu/proposer/POG/pdf/MPOG.pdf; page 93; figure 6.7

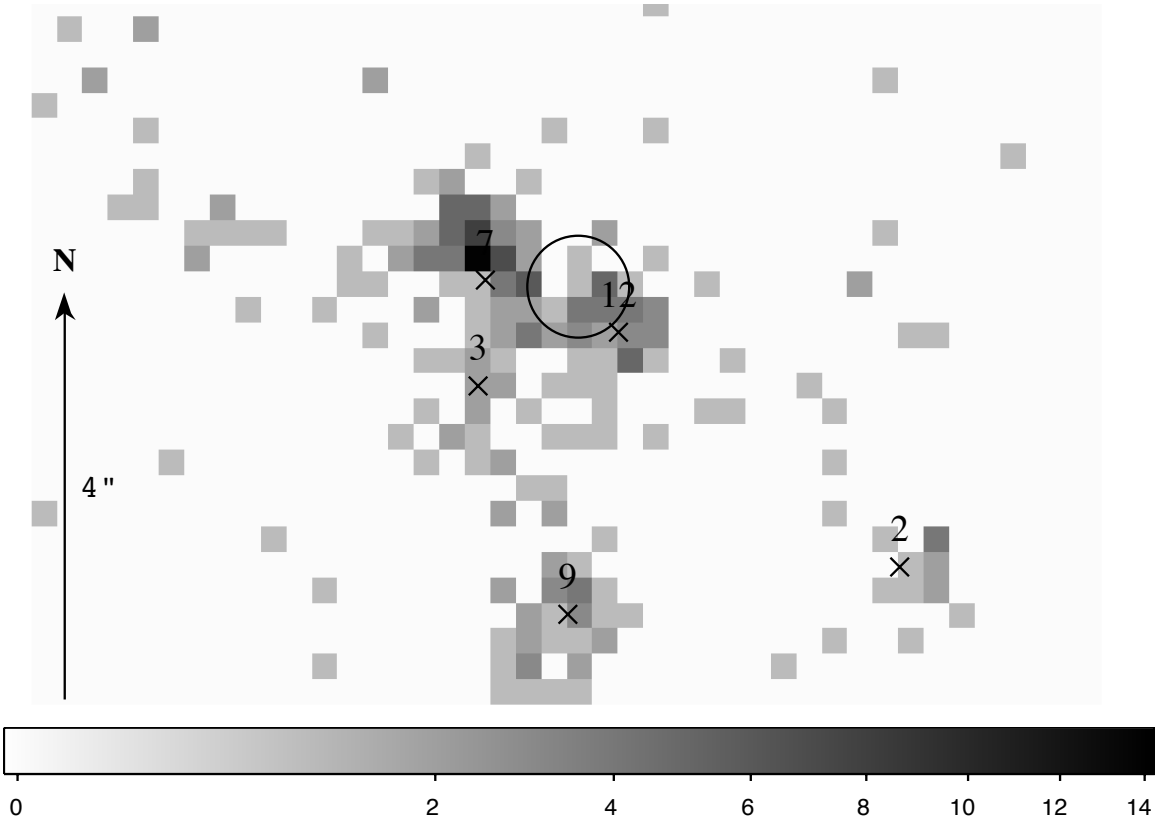

Figure 3.3: X-ray image of the core of NGC 6388 in the 2-10 keV band with pixel size of $0.25''$. The gray scale indicates X-ray intensity and ranges from 0 to 14 counts per pixel. The crosses mark the positions of X-ray sources listed in Table 3.3. The circle indicates the error circle for the cluster centre of gravity including the uncertainty relative to the *Chandra* reference frame.

3.3.1 Radio Non-detection

After reduction of the *ATCA* radio data, we found there are no radio sources detected in association with the cluster centre of gravity nor at the locations of any of the *Chandra* X-ray sources within the cluster (Fig. 3.4). We assumed a flat spectrum (as likely for a low-luminosity accreting black hole) in order to combine the data sets to achieve the best noise level. In naturally weighted maps, by combining 8.4 & 9 GHz data the rms noise level was 27 μJy and combining 18.5 GHz & 18.6 GHz data the rms was 54 μJy. Combining all of the datasets did not lead to better rms as the higher frequency data is more noisy. Therefore, our best achieved rms noise level at radio frequencies is 27 μJy.

3.4 Discussion and Interpretation

Considering the best achieved r.m.s. value obtained from our *ATCA* radio observations and adopting a 3σ upper limit, the upper limit on the radio flux of any (undetected) source is estimated to $F_R < 81$ μJy/beam. The distance of NGC 6388 was adopted from Dalessandro et al. (2008) with the value of 13.2 $\pm$ 1.2 kpc. Therefore, we obtained an upper limit for the radio luminosity of the putative intermediate mass black hole in NGC 6388 of $L_R < 8.4 \cdot 10^{28}$ erg s^{-1} at 5 GHz ($L_R = \nu F_\nu$, where we assumed a flat radio spectrum, as is likely for a low-luminosity accreting black hole).

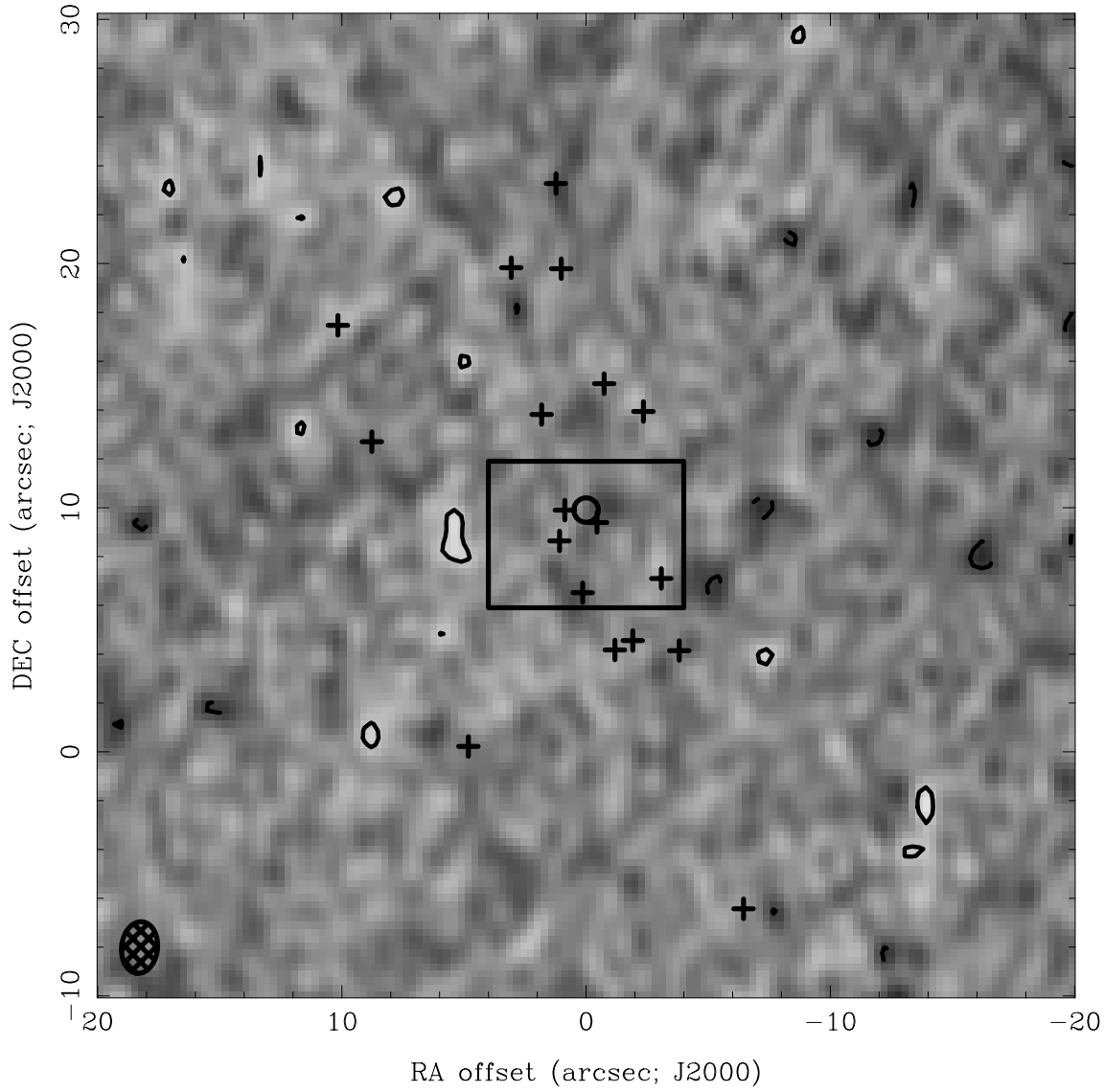

Figure 3.4: The naturally weighted *ATCA* image of NGC 6388 combined at 8.4 GHz & 9 GHz. The positive contour levels increase by a factor of 2. The first contours are drawn at -81 & 81 μJy/beam. (There are no higher contours than the first ones). The beam size is 2.1 $\times$ 1.5 arcsec at a position angle of 6°. The central circle indicates the cluster center of gravity at $\alpha_{\rm J2000} = 17^h36^m17.^s23, \delta_{\rm J2000} = -44°44'7.''1$ with a radius 0.5″ of the uncertainty. The crosses mark the positions of the *Chandra* sources. The rectangle indicates the *Chandra* image showed previously.

Previously, Nucita et al. (2008) found that three of the *Chandra* sources (# 12, 7 and 3) coincide with the cluster centre of gravity. They did not attempt to resolve these three sources spatially and therefore obtained one averaged spectra for the three sources. After reanalysing the data and removing the pixel randomisation, we find that only one source (#12) is consistent with the location of the centre of gravity (see Section 3.1). In addition, we successfully measured the spectrum of each source individually. The unabsorbed X-ray flux of source #12 is $F_X = 4.0 \cdot 10^{-14}$ erg cm^{-2} s^{-1}, and the corresponding X-ray luminosity is $L_X = 8.3 \cdot 10^{32}$ erg s^{-1} in the 0.3–8 keV band. We will use this value in all subsequent analysis.

3.4.1 Nature of the Innermost X-ray Sources

A study of the colour-colour diagram of the X-ray sources throughout the cluster revealed that most of them seem to be low mass X-ray binary, one source is probably a high-mass X-ray binary and four others are soft sources (Nucita et al., 2008). Nucita et al. (2008) treated the three central *Chandra* sources as one and noted that the difference between the X-ray flux of these sources measured by *XMM-Newton* in 2003 versus by *Chandra* in 2005 is a factor of only 1.11 . This may indicate that variability of the X-ray sources is small, but there are only two observations.

From our X-ray data analysis, we managed to localise three separate sources in the centre of the cluster. We studied their X-ray colours and used the source classification method of Jenkins et al. (2005). This revealed that source #3 is very soft, probably a cataclysmic variable. Source #7 seems to be an X-ray binary and source #12 is either an absorbed source or an X-ray binary.

The X-ray luminosity of source #12 is consistent with the accretion luminosity of even a 10 solar-mass black hole in quiescence. On the basis of the X-ray spectra, there is no real clue to distinguish between an intermediate-mass black hole and low mass X-ray binary. Source #12 has a power-law spectrum with $\Gamma \approx 1.9$ which is consistent with the spectra of quiescent stellar-mass BH which have $\Gamma \approx 2.0$ (Hameury et al., 2003; Corbel et al., 2006, 2008), but is also consistent with the spectrum expected from a quiescent intermediate-mass black hole. Thus, the localisation, the source categorisation of Jenkins et al. (2005), and the X-ray spectrum all favour source #12 as the best candidate to be considered for further analysis as a potential intermediate mass black hole.

3.4.2 Upper Limit on the Mass of the Central Black Hole

The fundamental plane of accreting black holes is a relationship between X-ray luminosity, radio luminosity and black hole mass (Merloni et al., 2003; Falcke et al., 2004). The relations between mass accretion rate and radio luminosity has been studied for black hole X-ray binaries and low luminosity active galactic nuclei. It is found that the X-ray luminosity is uniquely determined by the black hole mass and radio luminosity via a linear equation in logarithm space. This relationship is referred as "the black hole fundamental plane". It is valid for hard state objects i.e. for objects accreting at low Eddington value. This relation requires radiatively inefficient accretion, like advection dominated or jet dominated accretion flows.

If one investigates in more detail whether the X-ray source satisfies the criteria for radiative inefficiency, as required for application of the fundamental plane (Körding et al., 2006a), we can conclude, that even if $M = 10\,\mathrm{M}_{\odot}$, the ratio of X-ray luminosity to Eddington luminosity, $L_X/L_{Edd} \simeq 10^{-6}$. So, the source needs to be accreting at a low Eddington-fraction. Taking this into account and assuming that the central source is a black hole, we can set constraints on the mass of the black hole using the relationship found by Merloni et al. (2003):

$$\log M = 1.28 \log L_R - 0.76 \log L_X - 9.39 \tag{3.1}$$

or the similar relation found by Körding et al. (2006a):

$$\log M = 1.55 \log L_R - 0.98 \log L_X - 9.95. \tag{3.2}$$

We note that the relation (Eq. 3.2) found by Körding et al. (2006a), which considered flat spectrum, low-luminosity radio sources, such as those we expect in the centre of

dwarf galaxies or globular clusters, more likely reflects the present case. However Eq. 3.1 provides results that are consistent within the uncertainties. As Eq. 3.2 gives a higher mass and has less scatter than Eq. 3.1 (even than the equation found by Gültekin et al. (2009)), we use the value given by Eq. 3.2 in all subsequent analysis.

Inserting the measured X-ray luminosity (L_X) of source #12 and the measured upper limit on its radio luminosity (L_R) into Eq. 2 leads to an upper limit for the mass M of the central black hole of $< 735\ M_\odot$. However, we must consider the intrinsic scatter in the measured fundamental plane relation of 0.12 dex ($\sim$ 32 per cent) within one σ (and the uncertainty of the distance). Therefore the result is $M < 735 \pm 244\ M_\odot$. We adopt the 3-σ upper limit, $\approx 1500 M_\odot$, as a conservative limit on the black hole mass.

If source #7 actually lies at the cluster centre of gravity instead source #12, then we note that source #7 has a harder spectrum than #12, being still consistent with a low luminosity accreting black hole and that the difference between their X-ray flux is a factor of 2. Thus, this would not change the results described above. If none of the X-ray sources are associated with the cluster centre of gravity, then we can not use the fundamental plane to obtain a limit on the black hole mass.

3.4.3 Bondi-Hoyle Accretion

In this section, we investigate more in detail the consistency of the X-ray emission of source #12 with Bondi-Hoyle accretion and compare NGC 6388 with the cluster G1. For a black hole of mass M moving with velocity v through gas with hydrogen number density n and sound speed c_s, the expected accretion rate via the Bondi-Hoyle process (Bondi & Hoyle, 1944) is

$$\dot{M} \simeq 4\pi (GM)^2 m_p n (v^2 + c_s^2)^{-3/2} \tag{3.3}$$

where $\mathrm{m_p}$ is the proton mass (Pooley & Rappaport, 2006). The expected X-ray luminosity is then

$$L_X \simeq \epsilon \cdot \eta \cdot \dot{M} c^2 \tag{3.4}$$

and parametrized for NGC 6388 is

$$L_X \simeq \epsilon \cdot \eta \cdot 8.8 \cdot 10^{36} \left(\frac{M_{\mathrm{BH}}}{10^3 \mathrm{M}_\odot}\right)^2 \left(\frac{V}{15 \mathrm{km/s}}\right)^{-3} \left(\frac{n}{0.1}\right) \frac{\mathrm{erg}}{\mathrm{s}} \tag{3.5}$$

where V denotes $(v^2 + c_s^2)^{1/2}$, ϵ is the efficiency for converting accreted mass to radiant energy in the accretion flow of the black hole, and η indicates the fraction of the Bondi-Hoyle accretion rate that is accreted by the black hole.

The intracluster gas density can vary in the $\sim 0.1{-}1$ cm^{-3} range (Pooley & Rappaport, 2006). For NGC 6388 the gas density is not measured. Ionised gas with an electron density of $n \simeq 0.1$ cm^{-3} has been detected in the globular cluster 47 Tuc (Freire et al., 2001). Recent studies on their stellar populations find similar ages for NGC 6388 as 47 Tuc (Moretti et al., 2009), therefore we set n = 0.1 cm^{-3} for NGC 6388. (However a higher gas content may be expected for NGC 6388). We also set v=0 km/s and c_s = 15 km/s.

Now, the key factors determining the luminosity are the radiative efficiency of accretion (ϵ) and the fraction of Bondi-Hoyle accretion rate that reaches the black hole (η). Considering our previously obtained 3-σ upper limit on mass of $\sim$1500 M$_\odot$ and taking $\eta = 1$, we find that the lowest allowed radiative efficiency is $\epsilon \simeq 10^{-4}$, similar values have been found for other systems in the radiatively inefficient regime (Fender et al.,

2003; Körding et al., 2006b). The highest value of radiative efficiency can be taken as 0.1, i.e. for a radiatively efficient Schwarzschild black hole. So, ϵ can vary in the $[10^{-4}, 0.1]$ range.

Perna et al. (2003) showed that the lack of detection of isolated neutron stars accreting from interstellar medium implies a fraction of Bondi-accretion of the order of $10^{-3} - 10^{-2}$, see also (Pellegrini, 2005). However, there is evidence that the central black hole of globular clusters can accrete at a higher fraction of the Bondi-rate than suggested by Perna et al. (2003).

G1 is an enigmatic star cluster in M 31 thought by some to be a globular cluster, but by others to be the core of a stripped dwarf galaxy (Meylan et al., 2001) and contains multiple stellar populations. Dynamical evidence in G1 suggested the presence of a 20 000 solar mass black hole (Gebhardt, Rich & Ho 2002, 2005). X-ray observations revealed an X-ray source with a 0.2–10 keV luminosity of $2 \cdot 10^{36}$ erg s^{-1} (Trudolyubov & Priedhorsky, 2004) and (Pooley & Rappaport, 2006). A radio source was also detected at the location of the core of the cluster of G1. The measured radio flux (28 μJy) was in good agreement with the predictions (30 and 77 μJy) (Maccarone & Koerding, 2006; Ulvestad et al., 2007). Although, Kong et al. (2010) find that the X-ray emission is still consistent with a single X-ray binary or a collection of X-ray binaries.

Ulvestad et al. (2007) find the most plausible scenario is that G1 accretes at closer to 0.1 of the Bondi-rate with a radiative efficiency under 0.01. It is therefore possible that the fraction (η) of the Bondi-Hoyle accretion is as high as 0.1.

Taking the value - as there is no evidence for pulsar detection in NGC 6388 - obtained by Perna et al. (2003) (see also (Pellegrini, 2005)) as a low end and the value of G1 as a high end, the fraction of the Bondi-rate (η) can vary on the $[10^{-3}, 0.1]$ range.

Now, we discuss two scenarios: first, we set the fraction of the Bondi-rate to $\eta = 0.1$ and we assume inefficient accretion ($\epsilon = 10^{-4}$) and secondly, we set $\eta = 10^{-3}$ and we assume efficient accretion ($\epsilon = 0.1$). Using Eq. 3.5, other cases will lead lower values of black hole mass than derived from the fundamental plane. In order to reproduce the measured X-ray luminosity (by using Eq. 3.5), the first scenario will give an estimate of $\sim$3070 M$_\odot$ for the mass of the putative central black hole mass. Such a black hole mass is inconsistent with the derived mass on the fundamental plane. Additionally, this value is even higher than the value of 2600 M$_\odot$, which one can obtain considering the raw estimate that, the black hole mass is 1/1000 of the total stellar mass ($2.6 \cdot 10^6$ M$_\odot$; (Lanzoni et al., 2007)) of the globular cluster (Miller & Hamilton, 2002); therefore this scenario is less favourable. The second scenario will result in a black hole mass of $\sim$970 M$_\odot$. This is formally consistent with the one-sigma value derived from the fundamental plane. Although, given the high uncertainties of ϵ and η and the intrinsic scatter of the fundamental plane, our conservative upper limit on the mass of the putative intermediate-mass black hole is 1500 M$_\odot$, the 3-σ upper limit derived from the fundamental plane.

3.5 Summary and Conclusions

Lanzoni et al. (2007) reported the possible presence of a black hole with a mass of 5700 $\pm$ 500 M$_\odot$ at the centre of the globular cluster NGC 6388. *Chandra* and *XMM-Newton* observational data analysis were carried out by Nucita et al. (2008). Removing the pixel randomisation allowed us to identify a unique source coincident with the cluster centre of gravity with properties consistent with those expected for a black hole accreting at a low rate. With the X-ray detection and optical surface density fit, the only missing piece

of the puzzle was a radio detection. On the basis of the X-ray luminosity, Nucita et al. (2008) predicted an upper limit of < 3 mJy radio flux on NGC 6388. Deep radio observations with the Australia Telescope Compact Array allowed us to reach a sensitivity of 27μJy/beam, but did not reveal any radio sources within the cluster. We interpreted the radio non-detection by using the fundamental plane relating the radio and X-ray properties of black holes accreting at low rates, assuming that the X-ray flux is related to a black hole accretion luminosity. We obtained an upper limit on the black hole mass of $M < 735$ M$_\odot \pm 244$ M$_\odot$ (1σ). Taking into account the uncertainties on the radiative efficiency of accretion and on the fraction of Bondi-Hoyle accretion rate reaching the black hole, we concluded that the centre of NGC 6388 can not host a black hole with a mass in excess of 1500 M$_\odot$ at a 3σ confidence level.

More recent and deeper radio observations with the ATCA have been performed by Bozzo et al. (2011) due to the CABB upgrade (Wilson et al., 2011).They found a more stringent upper limit on the mass of the central BH of 600 M$_\odot$, which is a factor of 2.5 lower than my previously reported value. On the other hand, Lützgendorf et al. (2011) reports a black hole mass of $(17 \pm 9) \times 10^3$ M$_\odot$, much higher than reported by Lanzoni et al. (2007). They estimate the mass using new spectroscopic data, containing integral field unit measurements, providing kinematic signatures in the center of the cluster and also photometric data that give information of the stellar density. Their value estimated from surface density profile fitting and also from the M-σ relationship seems to be consistent.

Any radio emission certainly could trace only the accretion signature of any kind of black hole. However, because in globular clusters the gas content is pretty low, the presence of low-accretion or quiescent black holes is not surprising. One can solve the discrepancy between the mass estimates between the two methods by simply checking the required accretion rate from a $(17 \pm 9) \times 10^3$ M$_\odot$ black hole. This high mass indicates that both, the radiative efficiency and the Bondi-rate are small. Furthermore this mass would imply very small values of radiative efficiency of 10^{-4} and of the Bondi-rate of 10^{-3}. Additionally, this mass would imply an accretion rate of 10^{-10} in Eddington units, if accretion does not happen via the Bondi-Hoyle process, and in this accretion regime the fundamental plane has never been tested. Wrobel et al. (2011) also estimates accretion rates of 10^{-10} for the globular cluster M54. These accretion rates certainly indicate black holes in quiescence. However, Sgr A, A0620, V404 Cyg show radio emission at accretion rates of 10^{-9} (Corbel et al., 2008), which could indicate that accretion does not happen via an accretion disk in globular clusters. On the other hand, radio observations cannot exclusively rule out the presence of an IMBH which is accreting at very low Eddington rates, or being in quiescence in the sense of Bondi-accretion.

4

Dynamical Mass of NGC5408 X-1

Contents

This chapter is based on the content of my paper (Cseh et al., 2011).

Broad Components in Optical Emission Lines from the Ultraluminous X-ray Source NGC5408 X-1

D. Cseh, F. Grise, S. Corbel, P. Kaaret

2011, ApJ, 728, L5

In this Chapter, I present a high-resolution optical spectra of the ultraluminous X-ray source NGC 5408 X-1. It shows a broad component with a width of $\sim$750 km/s in the HeII and Hβ lines in addition to the narrow component observed in these lines and [O III]. A new analysis of moderate-resolution spectra shows a similar broad component in the HeII line. The broad component likely originates in the ULX system itself, probably in the accretion disk. The central wavelength of the broad HeII line is shifted by 252 ± 47 km/s between the two observations. If this shift represents motion of the compact object, then its mass is less than $\sim$1800 $M_{\odot}$. Furthermore, I briefly discussed the future steps of reducing uncertainties in the parameter space of the binary system. This system might serve as a unique possibility to dynamically constrain the mass of a ULXs.

4.1 Introduction

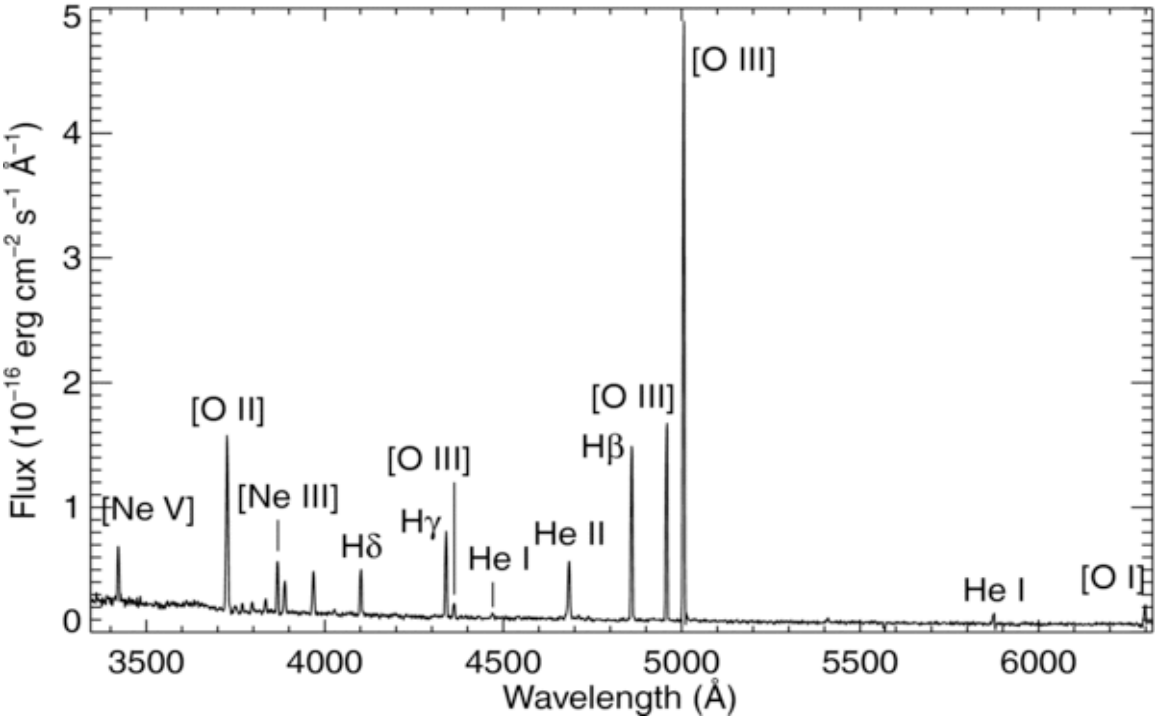

Figure 4.1: The image is taken from Kaaret & Corbel (2009) and shows the spectrum of the optical counterpart of NGC 5408 X-1. The dereddened flux is plotted vs. redshift-corrected wavelength.

NGC 5408 X-1 is one of the best intermediate mass black hole candidates because it powers a radio nebula requiring an extremely energetic outflow (Kaaret et al., 2003; Soria et al., 2006a; Lang et al., 2007). In addition, the photoionized nebula requires an X-ray luminosity above $3 \times 10^{39}\,\mathrm{erg\,s^{-1}}$ (Kaaret & Corbel, 2009). Also, quasi-periodic X-ray oscillations at low frequencies could suggest a high compact object mass (Strohmayer et al., 2007).

The optical counterpart to NGC 5408 X-1 was identified by Lang et al. (2007) and optical spectra were obtained by Kaaret & Corbel (2009). Optical emission (Fig. 4.1) can arise either from a companion star, from an accretion disk or from a nebula surrounding the compact object. A blue or hot continuum and broad emission lines would be indicative of optical emission from the accretion disk. Also, the observed continuum emission may arise from a nebula or reprocessing of X-rays in an accretion disk. The study by Kaaret & Corbel (2009), showed that there is no sign of any absorption lines. Instead, we found high excitation lines, many of which are forbidden, indicating that the optical light arises from a surrounding nebula that is X-ray and UV photoionized by a central source that is truly ultraluminous; does not require significant beaming. The continuum emission is consistent with an accretion disc.

Kaaret & Corbel (2009) found that the HeII line from NGC 5408 X-1 was broader than the forbidden lines. Permitted lines produced in the high-density environment of an accretion disk can be broad, reflecting the distribution of velocities within the optical emitting regions of the disk. Furthermore, since the accretion disk moves with the com-

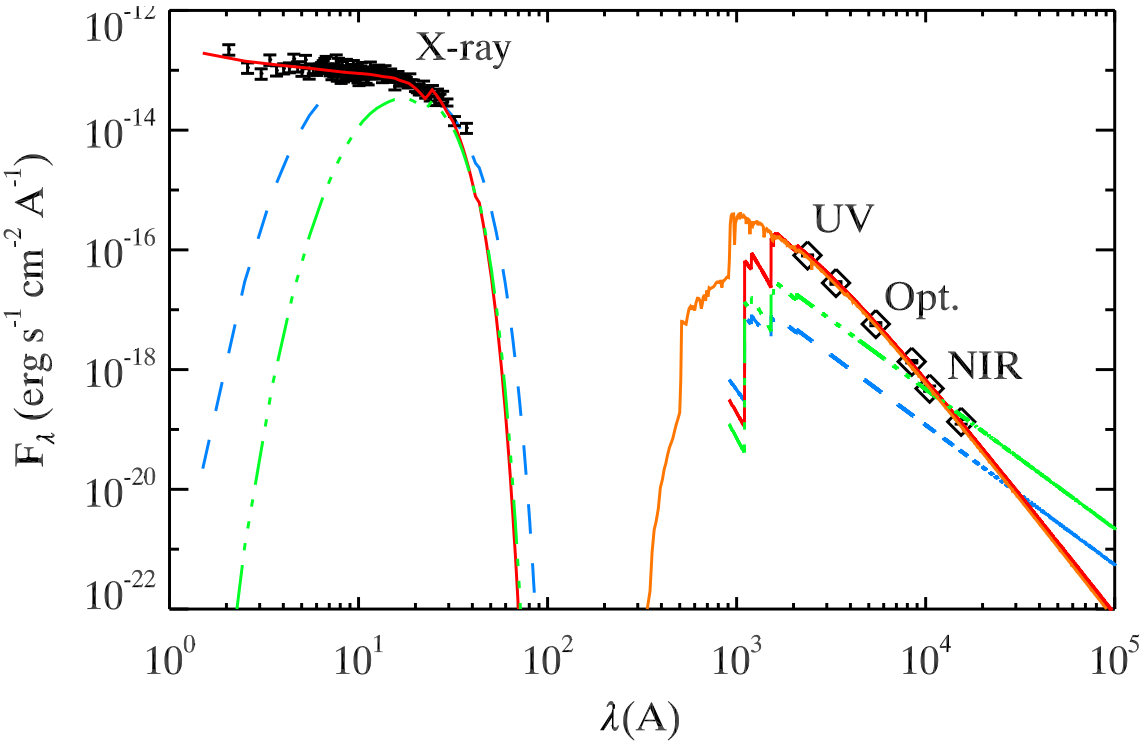

Figure 4.2: This image is taken from (Grisé et al., 2012) and shows the SED of NGC5408 X-1. The green, solid line corresponds to a B0I supergiant, while the red, solid line corresponds to disk irradiation model.

pact object, the line velocity shifts may provide means to constrain the compact object mass. This technique was demonstrated by Hutchings et al. (1987) and Soria et al. (1998). for the persistent black hole candidate LMC X-1.

4.1.1 Difficulties in Dynamical Mass Constraints

The most prominent difficulty arises from the fact that nearby ULXs are at a distance of 3-5 Mpc. This results in dim (V∼22-24 mag) optical counterparts. Also, Tao et al. (2011) studied the variation and color of ULX counterparts using archival Hubble Space Telescope data. They found that the flux of the counterparts are consistent with disk irradiation and there are only two cases (from 13) where the counterpart could be consistent with a donor star.

Similarly, a detailed observational campaign covering X-rays, UV, optical and infrared revealed that the SED of NGC 5408 X-1 (Fig. 4.2) can be consistent with a B0I supergiant as well as with disk irradiation. Therefore, it is likely that the majority of ULXs act like low-mass X-ray binaries (LMXBs) in terms of their optical spectra is dominated by disk irradiation. Also, we note, there are two other ULXs whose optical spectrum possess absorption lines from a donor: P13 (Motch et al., 2011) and M101 ULX-1. However, in these cases the ULXs just hit the definition value of 3×10^{39} erg/s X-ray luminosity, therefore they might not be representatives of bona fide ULXs.

On the other hand, given the lack of absorption lines, one has to find alternative ways, such as the He II line. Despite the fact that it was shown that the He II line can trace the orbital motion of certain binary systems, counterexamples as shown in Fig. 4.3 do exist.

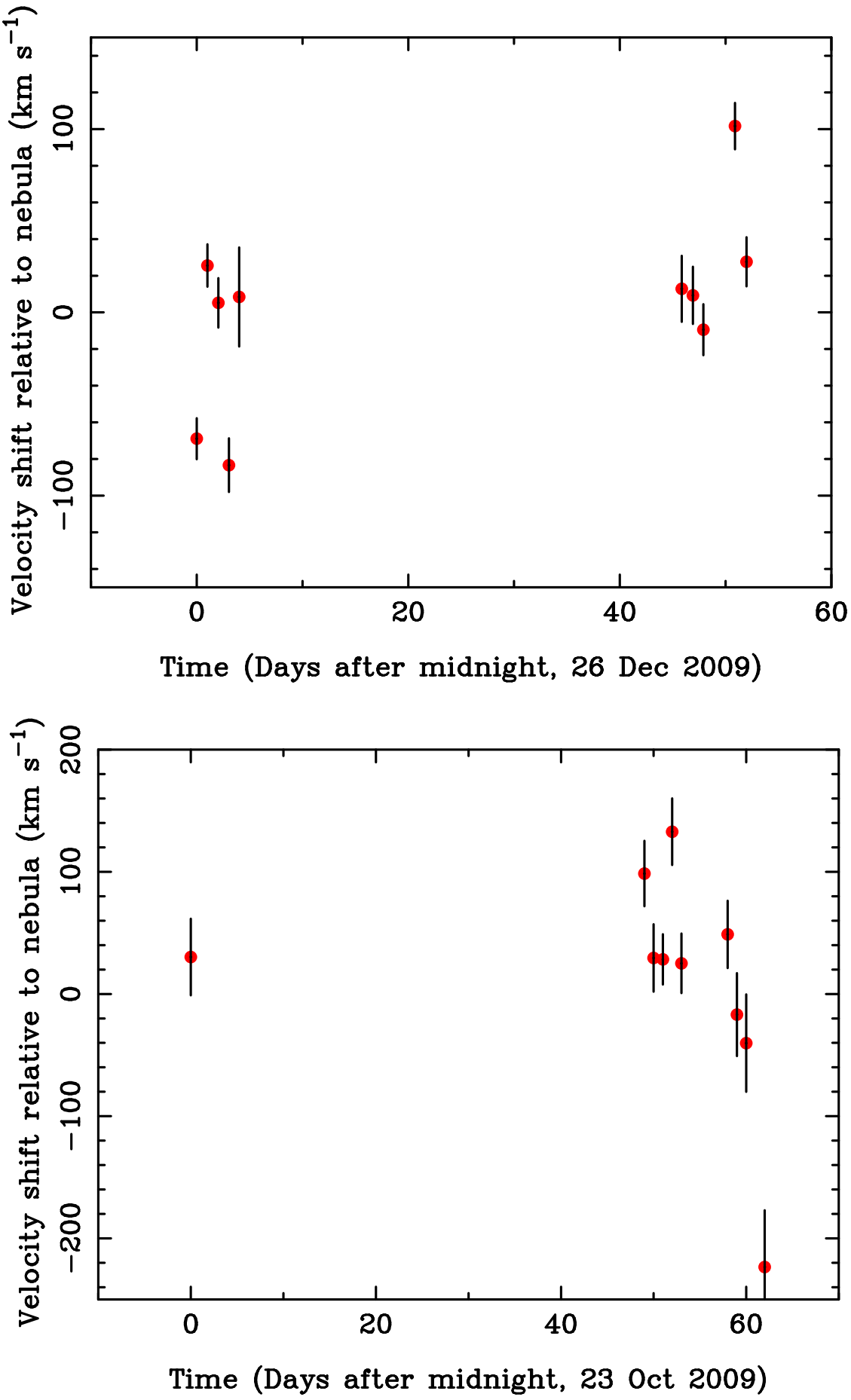

Figure 4.3: This image is taken from (Roberts et al., 2011), showing the "radial velocity curve" of ULXs Holmberg IX X-1 (top) and NGC 1313 X-2 (bottom).

In these cases, the He II line does not trace the orbital motion, because the wavelength shift of the lines are aperiodic. This could be due to several reasons, such as the random motions in the disk, the He II line may originate other sites than the disk, or the nebular and disk component of the He II line is blurred due to insufficient spectral resolution, or due to differing viewing geometries of the system.

To study the HeII line profile of NGC 5408 X-1 in more detail, we obtained new observations using the FORS-2 spectrograph on the European Southern Observatory Very Large Telescope (VLT) with a high resolution grism and reanalyzed our previous FORS-1 observations (Kaaret & Corbel, 2009).

4.2 Observations and Analysis

FORS-2 observations of NGC 5408 X-1 were obtained on 12 April 2010 using the GRIS_1200B and GRIS_1200R grisms with a slit width of $1.0''$ covering the spectral range 3660−5110 Å and 5750−7310 Å with dispersion 0.36 Å pixel^{-1} and 0.38 Å pixel^{-1} and spectral resolution $\lambda/\Delta\lambda = 1420$ and $\lambda/\Delta\lambda = 2140$ at the central wavelength, respectively. The observation block (OB) consisted of three 849 s exposures with a 12 pixel offset along the spatial axis between successive exposures. CCD pixels were binned for readout by 2 in both the spatial and spectral dimensions. We also reanalyzed all six OBs of the previous FORS-1 observations (Kaaret & Corbel, 2009), hereafter the low resolution data (LRD), taken using the GRIS_600B grism which has a spectral resolution of $\lambda/\Delta\lambda = 780$ at the central wavelength and with three shifted exposures per OB. The average seeing for our new observations was 0.72 and 0.62 arcsecond for the blue and red spectra, respectively. The average seeing of the six OBs of the LRD were 0.87, 0.82, 0.96, 1.28, 0.64, 0.57 arcsecond, respectively.

Data reduction was carried out using the Image Reduction and Analysis Facility (IRAF)[1] (Tody, 1993). First, we created bias and flat-field images, then applied these to correct the spectrum images. The three exposures in each OB were aligned then averaged to eliminate bad pixels and cosmic rays using the `imcombine` task with the `ccdclip` rejection algorithm.

As the continuum emission of the ULX counterpart is faint, we could not trace its spectrum. Following Kaaret & Corbel (2009), we used the bright nearby star at 2MASS (Skrutskie et al., 2006) position $\alpha_{\rm J2000} = 14^h03^m18.^s97, \delta_{\rm J2000} = -41°22'56.''6$ as a reference trace. The trace position on the spatial axis varied less than half a pixel along the whole length of the dispersion axis. The trace for the ULX counterpart was centered on the HeII $\lambda4686$ emission line profile. The smallest possible trace width, 2 pixels corresponding to $0.5''$, was used to best isolate the ULX emission from the nebular emission. Background subtraction was done with a nearby trace. The HgCdHeNeA lamp and standard star LTT7379 were used for wavelength and flux calibration. An atmospheric extinction correction was applied using the IRAF built-in Cerro Tololo Inter-American Observatory (CTIO) extinction tables. To estimate the reddening, we used the Balmer decrement of Hδ/Hβ, we find $E(B-V) = 0.08 \pm 0.03$ in agreement with Kaaret & Corbel (2009). We corrected for reddening using the extinction curve from Cardelli et al. (1989) with $R_V = 3.1$.

To study the kinematics, we need to characterize the instrumental resolution in order

[1]IRAF is distributed by the National Optical Astronomy Observatory, which is operated by the Association of Universities for Research in Astronomy, Inc., under cooperative agreement with the National Science Foundation.

to obtain intrinsic line widths. After applying the dispersion correction to the lamp spectrum, we measured the full width at half maximum (FWHM) of several lines, excluding saturated ones, by fitting Gaussians with the IRAF `splot` subroutine. The instrumental FWHM was 2.24 Å and 5.08 Å for the high and low resolution data, respectively. The error on the instrumental FHWM was estimated by finding the standard deviation of the FWHM for several different lines.

For the HeII, Hβ and [OIII] emission lines, see Fig. 4.4, 4.5, 4.6 and Table 5.3, we first fitted the continuum with a second order polynomial to a region around each line excluding the line itself by visual examination. We estimated the measurement errors by calculating the root mean square deviation of the data in the same region. Then, we performed a non-linear least squares fit using the `LMFIT` subroutine of the Interactive Data Language version 7.0 and based on "MRQMIN" (Press et al., 1992). We fitted the line profiles iteratively, first using one Gaussian which converged on the narrow component, then using a sum of two Gaussians with initial parameters adjusted to achieve convergence. All six parameters in the two Gaussian fit were free to vary. The errors on the parameters were calculated by the fitting routine in a way that the uncertainty for the ith parameter derives from the square-root of the corresponding diagonal element of the covariance matrix. The intrinsic line width was calculated assuming the measured line width is the quadrature sum of the intrinsic and instrumental widths and the error on the intrinsic line width included a term for the uncertainty in the instrumental FHWM.

For the Hα line, we fitted the sum of four Gaussians, because the [NII] lines lie on the red and blue parts of the line wing. Initial fits to the Hα and red [NII] lines provided initial values for a fit with four Gaussians. Because the blue [NII] line has very low signal to noise ratio, the widths of the two [NII] lines were set equal, the wavelength offset was fixed at -35.44 Å, and the amplitude of the blue line was set to 1/3 of the red line (Osterbrock & Ferland, 2006).

4.3 Results

The improved resolution of the new data clearly resolves a broad component in the HeII line profile, see Fig. 4.4, 4.5, 4.6. and Table 5.3. The centroid is shifted from the nebular component by $+0.87\pm0.26$ Å in the red direction. We also searched for broad components in other lines. Hβ has a broad component with a FWHM similar to the HeII line but shifted by -0.52 ± 0.32 Å towards the blue, rather than the red. In contrast, a single Gaussian provides a good fit to the forbidden [OIII] line and there is no evidence for a broad component, as expected if the line is emitted only from the nebula.

Then we fitted the HeII line profiles of the six OBs of the LRD, see Fig. 4.7, 4.8, 4.9 and Table 5.3. The flux variation of the overall line profiles correlates with the seeing, e.g. OB5 has the best seeing and the highest flux. We detected a broad component in the HeII line in OB3, OB5, and OB6. We did not significantly detect a broad component in OB1, OB2 and OB4. This may be due to seeing or variations in the flux of the broad component.

We note that Kaaret & Corbel (2009) reported lower fluxes for HeII, [NeV], and the continuum emission for OB4 (with by far the worst seeing) as compared to the other OBs, while the other line fluxes remained relatively constant. Our new analysis suggests that this is due to changes in the seeing. If the emitting region is smaller than the $0.51''$

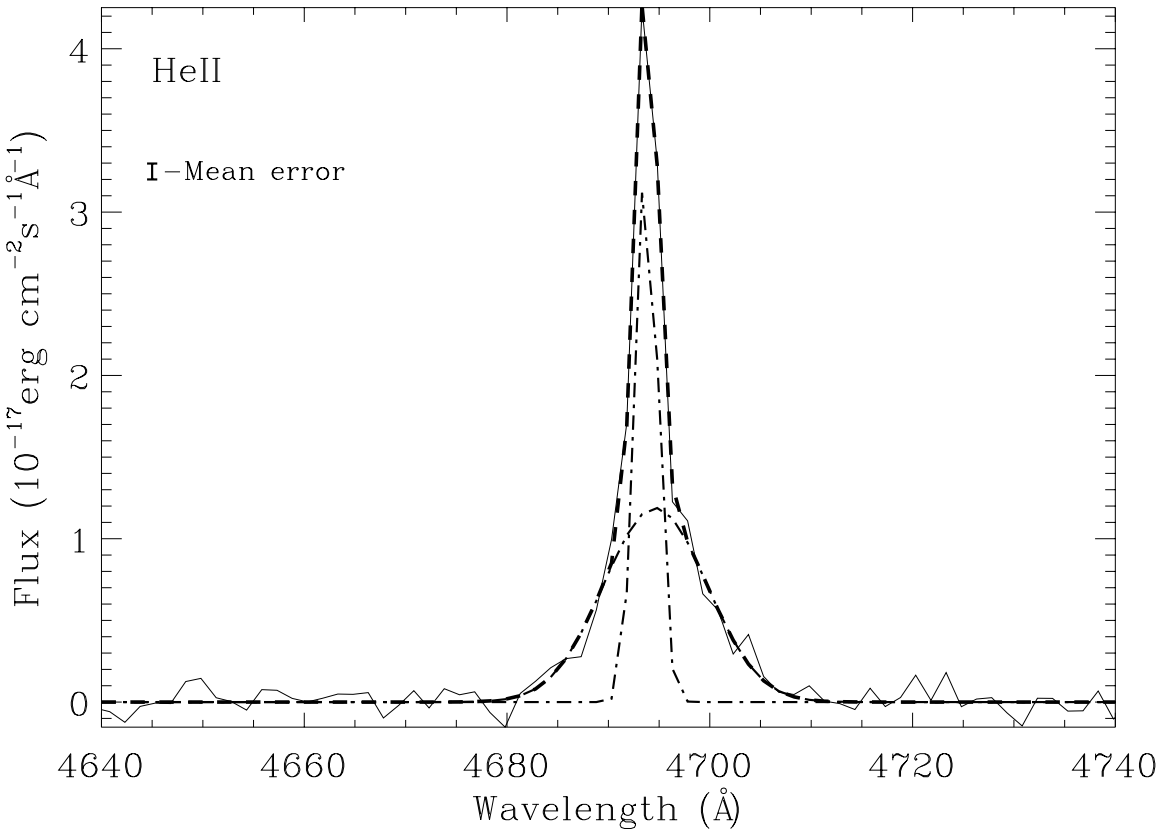

Figure 4.4: HeII line from the new, high resolution data. Result of line fit with two Gaussian components are shown as the separate components plotted with dashed-dot lines and the overall fit plotted with dashed lines.

Table 4.1: Line fit results.

Line	Wavelength (Å)	FWHM (Å)	Flux	Velocity (km s^{-1})	χ^2_ν
HeII	4693.75 ± 0.04	2.54 ± 0.14	3.39 ± 0.13	76.3 ± 3.4	0.94
	4694.62 ± 0.26	11.98 ± 0.74	1.19 ± 0.10	752.0 ± 46.4	
Hβ	4869.73 ± 0.01	2.28 ± 0.05	8.37 ± 0.11	25.2 ± 3.3	1.08
	4869.21 ± 0.32	12.49 ± 0.94	0.71 ± 0.07	756.9 ± 57.5	
[O III] λ4959	4967.52 ± 0.01	2.48 ± 0.03	8.42 ± 0.08	64.6 ± 1.7	1.08
HeII OB3	4693.90 ± 0.15	5.15 ± 0.52	1.34 ± 0.19	52.0 ± 33.3	1.04
	4692.08 ± 0.77	11.09 ± 1.44	0.56 ± 0.20	630.5 ± 91.8	
HeII OB5	4693.80 ± 0.12	5.81 ± 0.41	1.74 ± 0.17	179.8 ± 25.7	1.03
	4690.03 ± 1.43	11.75 ± 1.33	0.49 ± 0.13	678.0 ± 84.7	
HeII OB6	4693.97 ± 0.12	5.56 ± 0.46	1.70 ± 0.23	143.7 ± 29.5	0.95
	4689.94 ± 1.70	10.82 ± 1.55	0.53 ± 0.15	610.7 ± 98.9	
HeII AVG	4693.89 ± 0.08	5.50 ± 0.26	1.58 ± 0.10	135.0 ± 16.6	1.15
	4690.82 ± 0.68	11.47 ± 0.73	0.53 ± 0.09	657.5 ± 46.3	

The table gives the: line identification, central wavelength, measured FWHM, flux in units of 10^{-17} erg cm^{-2} s^{-1}, intrinsic FWHM in velocity units, and χ^2_ν of the line profile fit. The first row for each spectral line shows the parameters of the narrow component and the second row shows the parameters of the broad component (except for [O III]).

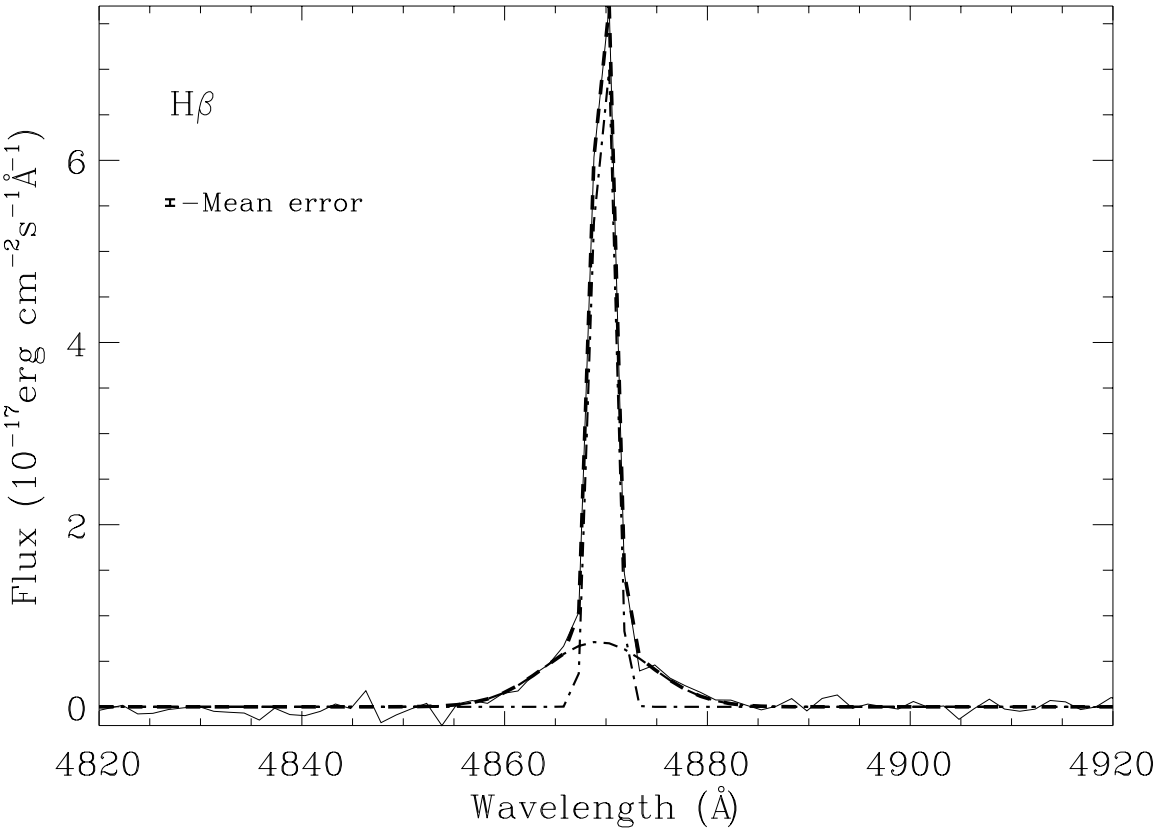

Figure 4.5: Hβ line from the new, high resolution data. Result of line fit with two Gaussian components are shown as the separate components plotted with dashed-dot lines and the overall fit plotted with dashed lines.

slit used for the LRD, then poor seeing will decrease the flux through the spectrometer. If these emission components are enhanced close to the ULX system while the other line emission is uniform, then the poor seeing in OB4 would produce the observed changes in flux. Thus, there is no evidence for temporal variability of the continuum or line emission. However, the subtraction performed by Kaaret & Corbel (2009) to isolate continuum emission arising from near the ULX is still justified; the separation of components is spatial instead of temporal.

The HeII line parameters are consistent between OB3, OB5, and OB6. The wavelength shifts of the HeII broad component of OB3, OB5 and OB6 relative to the narrow component are -1.82 ± 0.78 Å, -3.77 ± 1.44 Å and -4.03 ± 1.70 Å into the blue direction instead of the red as in the HRD, and are consistent within one σ. We averaged the spectra for these three observations and fit the resulting line profile. The fit results are listed as HeII AVG in Table 5.3. The shift of average line profile is -3.07 ± 0.68 Å.

The HeII broad component width is consistent between the new and old data. The narrow component is wider in the old data because we do not resolve the nebular lines. The line fluxes are higher in the new data, most likely due to the wider slit. The centroids of the narrow component are consistent, while the wavelength shift of the HeII broad component between the old and new data is $\Delta\lambda = 3.94 \pm 0.73$ Å.

Fitting the Hβ line of the LRD, we did not get a good fit, due to the lack of spectral resolution and the low broad to narrow flux ratio. We could not fit the bluer Balmer lines

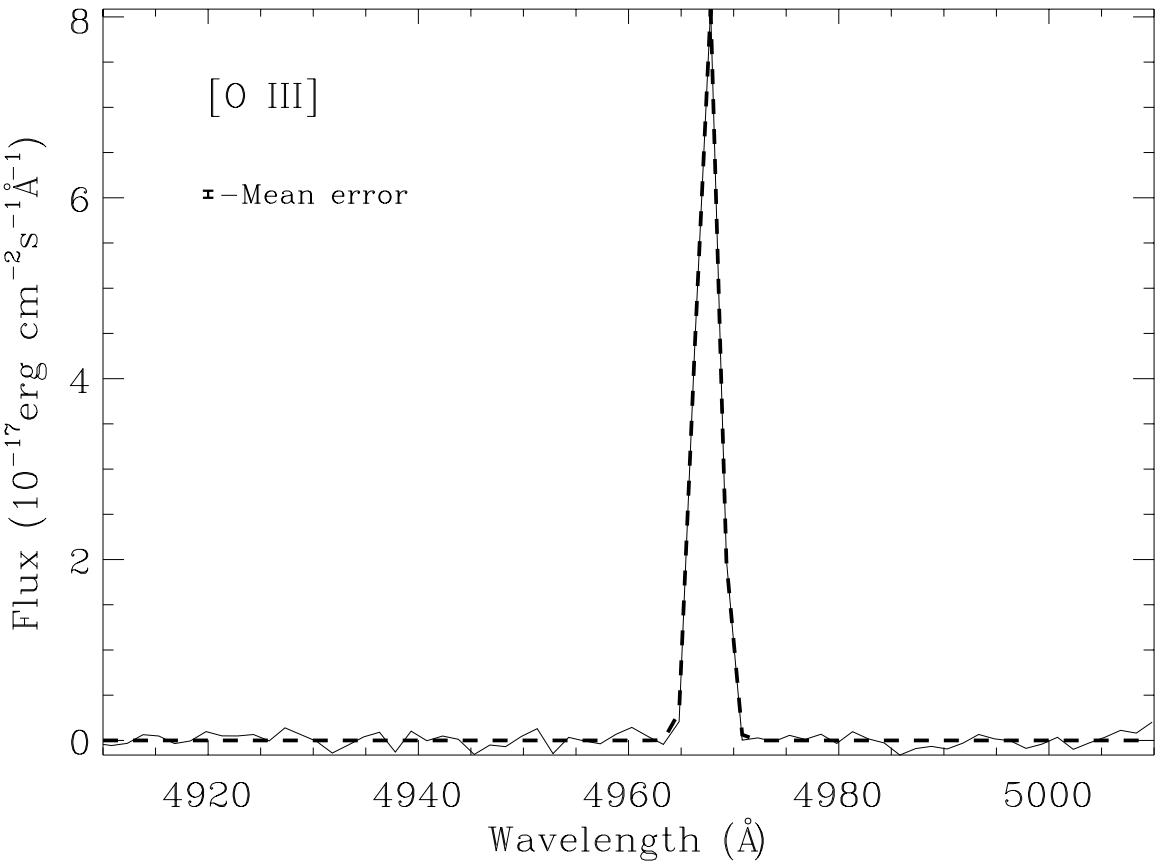

Figure 4.6: [O III] line from the new, high resolution data. Result of line fit with a single Gaussian component is shown.

because of their low S/N ratios. We did fit the Hα line in the new data. Although we do not obtain a good fit ($\chi^2_\nu = 4.9$) because of the complicated line profile (i.e. the two [NII] lines lie on the red and blue wing of the Hα line), we find that there is a broad component with a width of 19 Å, while the width of the nebular component is 2.7 Å. The [NII] lines are narrow, with a typical width of 3 Å, quantitatively supporting that the forbidden, nebular lines do not have broad components.

4.4 Discussion

Our new, high-resolution spectra show narrow nebular lines and broad components in the HeII, Hβ, and Hα lines. Our previous, moderate-resolution spectra show a broad component in the HeII line. There is no broad component in the [O III] nebular lines in either the new or old spectra. There is still no sign of any absorption lines in the new spectra.

4.4.1 The Line Emitting Region

The broad components of both HeII and Hβ have widths ∼750 km/s, consistent with production in the accretion disk, and are roughly Gaussian, instead of having P-Cygni profiles that would indicate origin in a wind. Following Porter (2010), we estimate the

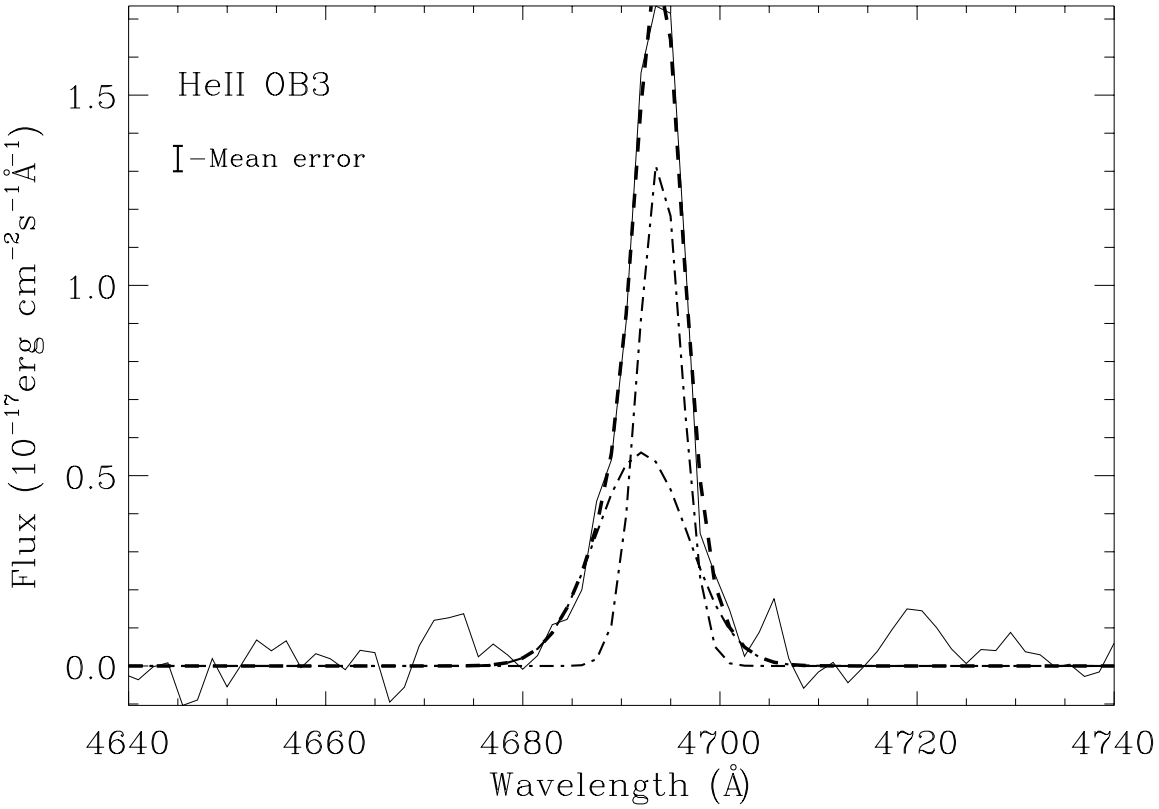

Figure 4.7: HeII line from the low resolution data: OB3. Result of line fit with two Gaussian components are shown as the separate components plotted with dashed-dot lines and the overall fit plotted with dashed lines.

size of the line-emitting region, R_{le}, by assuming the line-emitting gas is in Keplerian orbits around a compact object, thus

$$R_{le} \leq GM/v^2 \tag{4.1}$$

We find $R_{le} < 2.35 \left(\frac{M_{\rm BH}}{1500\,{\rm M}_\odot}\right)$ AU, which for a mass of 10 $M_\odot$ would give an upper limit of 3.4 $R_\odot$. This is consistent with origin of the broad HeII line in the accretion disk.

The broad line components are shifted relative to the narrow components. In the new data, the shifts are small compared to the line width, $+56 \pm 17$ km/s for HeII and -33 ± 20 km/s for Hβ. These shifts are consistent only at the 3σ level, which might indicate a difference in the spatial origin of the lines. However, this is still consistent with production of both lines within the disk since random motions within the disk and variation between the emission regions could produce shifts that are small compared to the line widths, as observed.

The central wavelength of the HeII broad component shifts markedly between the odld and new data, $\Delta\lambda = 3.94 \pm 0.73$ Å or $\Delta v = 252 \pm 47$ km/s. This shift is a substantial fraction of the line width. The shift could be due to random motion within the disk, differing viewing geometries (Roberts et al., 2011), or orbital motion of disk (and the compact object). Alternatively, the shift could be due to a disk wind or a photoionized stellar wind. If the shifts in the broad component of the HeII line are due to orbital motion, then this would provide a means to determine the orbital period and would also

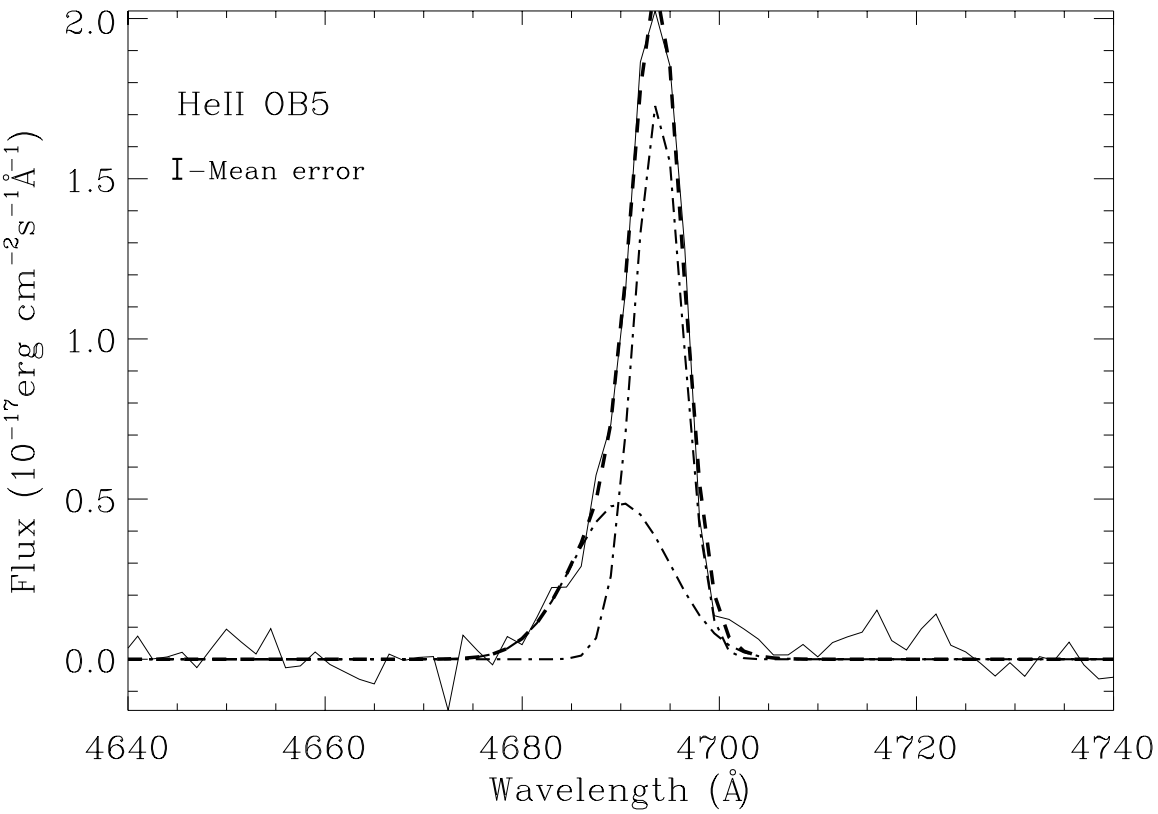

Figure 4.8: HeII line from the low resolution data: OB5. Result of line fit with two Gaussian components are shown as the separate components plotted with dashed-dot lines and the overall fit plotted with dashed lines.

provide a measurement of the mass function for the secondary star. Thus, a program of monitoring NGC 5408 X-1 with high-resolution optical spectroscopic observations would be important in extending our understanding of the physical nature of this system.

4.4.2 The Binary System

In this section, we make some speculations based on interpretation of the shift in the broad component of the HeII line as due to orbital motion. One can express the mass function and the compact object mass, M_x, in terms of the orbital period, P, the velocity excursion, K_x, and the companion mass, M_c, as

$$f_x = \frac{PK_x^3}{2\pi G} = \frac{M_c \sin^3 i}{(1+\frac{M_x}{M_c})^2} \leq M_c \tag{4.2}$$

$$M_x = (M_c \sin i)^{\frac{3}{2}} \left(\frac{PK_x^3}{2\pi G}\right)^{-\frac{1}{2}} - M_c \tag{4.3}$$

where i is the inclination angle and G is the gravitational constant. From the shift of the HeII line quoted above, we constrain the semi-amplitude of the radial velocity $K_x \geq \Delta v/2 = 126 \pm 24$ km/s. Thus, if the maximum mass of the companion and the orbital period are known, then Eq. 2 leads to an upper bound on the mass of the compact object.

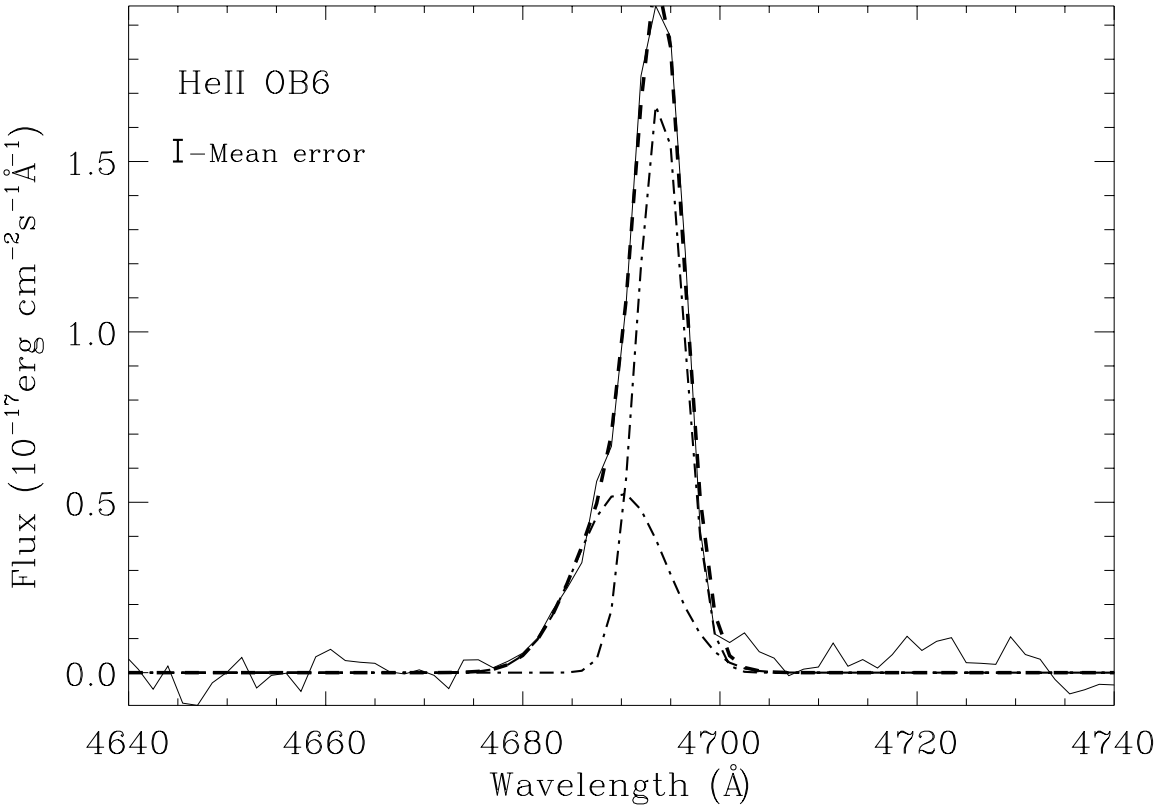

Figure 4.9: HeII line from the low resolution data: OB6. Result of line fit with two Gaussian components are shown as the separate components plotted with dashed-dot lines and the overall fit plotted with dashed lines.

The binary system has a visual magnitude $v_0 = 22.2$ that gives an upper limit on the absolute magnitude of the companion of $V_0 = -6.2$ at a distance of 4.8 Mpc (Karachentsev et al., 2002). Unfortunately, this places little restriction on the companion mass as even O3V stars, with masses of 120 $M_\odot$, are allowed. However, very high mass stars have very short lifetimes, no more than a few million years. There is no evidence of a dense stellar association near NGC 5408 X-1 and origin in the closest super-star cluster would require a transit time to the present location on the order of 30 Myr (Kaaret et al., 2004a). Thus, the companion mass is likely significantly lower, near 20 $M_\odot$ or less similar to found from studies of the stellar environments of other ULXs (Grisé et al., 2008, 2011). Figure 4.10. shows the upper bound on the compact object mass for donors of 120 $M_\odot$ and 20 $M_\odot$ as a function of orbital period. High black hole masses are excluded, except for very short periods. We note that the HeII line shift was the same in OB3 versus OB5 and OB6, taken one day apart, suggesting that the period is longer than few days. Thus, the black hole mass is likely below ∼1800 $M_\odot$. The more probable companion mass of 20 $M_\odot$ or less would imply smaller black hole masses, less than 112 $M_\odot$.

As a further constraint, we note that the orbital separation should be larger than the size of the emitting region, calculated above. Assuming a circular orbit, the orbital separation of the compact object is

$$a = \left(\frac{G(M_c + M_x)P^2}{4\pi^2} \right)^{\frac{1}{3}} \tag{4.4}$$

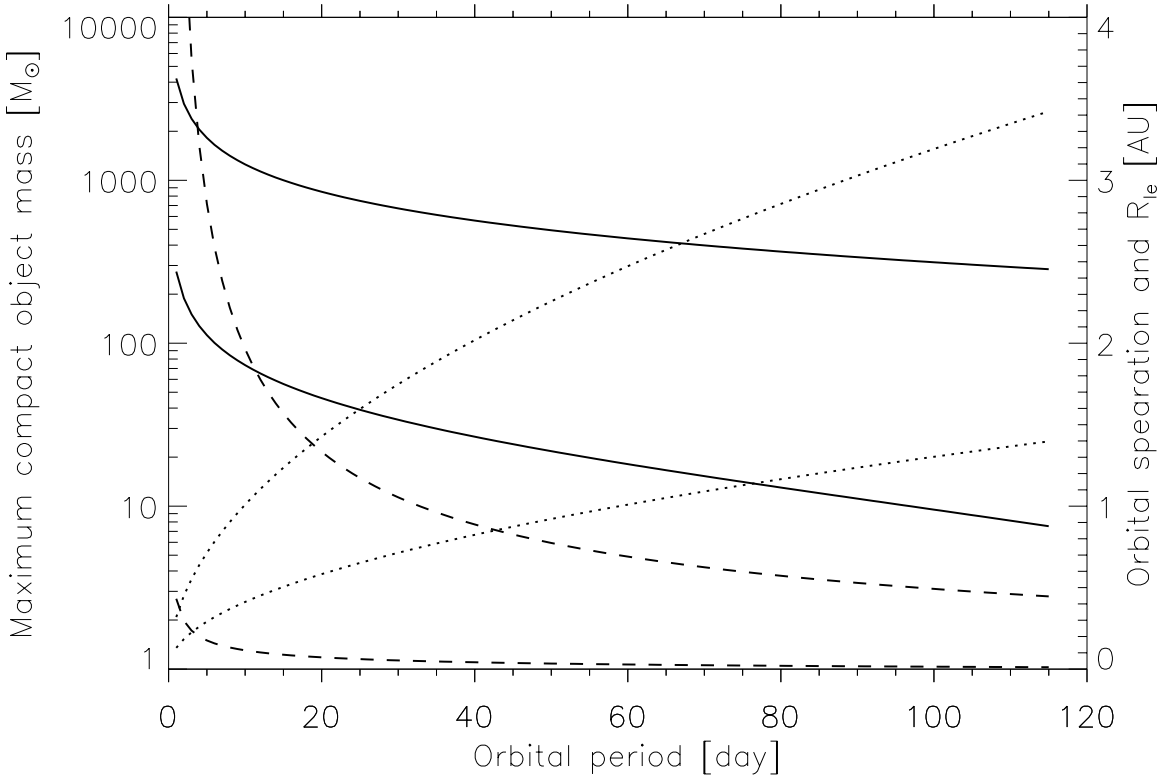

Figure 4.10: Properties of the binary system as a function of orbital period. The two solid lines show the mass of the compact object; the upper line is for an 120 $M_\odot$ donor and the lower line is for a 20 $M_\odot$ donor (left vertical scale). The orbital separation is shown as dotted lines with values read on the right vertical scale; the upper line for an 120 $M_\odot$ and the lower is for 20 $M_\odot$ donor (right vertical scale). The two dashed lines show the upper limit on the size of the line-emitting region; the upper line is for an 120 $M_\odot$ donor and the lower line is for a 20 $M_\odot$ donor (right vertical scale). The intercept of the dotted and dashed lines provides a limit on the period and consequently on the mass of the black hole.

Figure 3. shows the the orbital separation as a function of period. Also shown is the size of the line-emitting region, R_{le}, versus period. Both are calculated using the maximum black hole mass for each period assuming an 120 $M_\odot$ or 20 $M_\odot$ donor. The orbital separation is greater than the upper limit of the size of the line-emitting region when the compact object mass is below 875 $M_\odot$ for an 120 $M_\odot$ companion and below 128 $M_\odot$ for a 20 $M_\odot$ companion. These masses are reduced if the inclination is lowered. These results suggest that the most probable black hole mass is at most a factor of several above the usual stellar-mass black hole range.

Strohmayer (2009) proposed an orbital period of $P = 115.5 \pm 4.0$ days for NGC 5408 X-1, based on variations in the X-ray emission. With $P = 115.5$ days, the mass function is $f_x = 24.0 \pm 13.4$ $M_\odot$, implying a lower bound on the companion mass $M_c \geq 10.6$ $M_\odot$. It is interesting to determine if this period is consistent with other constraints on the system. An orbital period of $P = 115.5 \pm 4.0$ days would require a mean stellar density of $\rho = 1.5 \times 10^{-5}$ g cm^{-3} and, thus, a supergiant companion if mass transfer proceeds via Roche-lobe overflow (Kaaret et al., 2006; Strohmayer, 2009). In particular, late F and early G supergiants have densities close to that required, although we caution that the high mass transfer rate needed to power the ULX may distort the spectral type of the star.

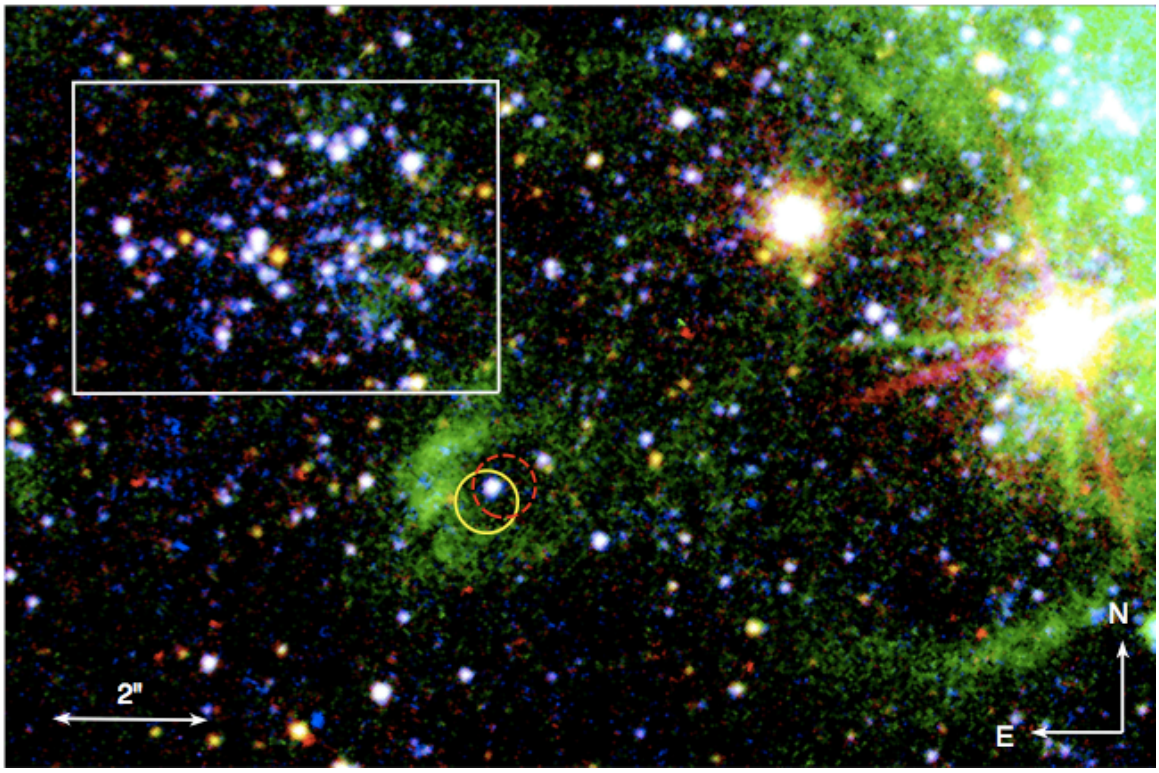

Figure 4.11: The image is adapted from Grisé et al. (2012) and shows a massive star forming region near NGC 5408 X-1.

Such stars have masses of 10–12$M_\odot$, consistent with the minimum mass derived from the mass function, and absolute magnitudes close to or below the upper limit quoted above. The stellar radii are large, up to 0.7 AU, but smaller than the orbital separation for this period and mass. However, a companion mass so close to the lower bound on the mass function would require a very low mass compact object. For a companion mass of 10–12 $M_\odot$, the compact object would have to be below 1 $M_\odot$, which seems unlikely. For a 5 $M_\odot$ black hole, one would need a donor of about 17 $M_\odot$ if the system is edge on. A higher black hole mass or a less extreme inclination would require an even higher mass companion. These high companion masses contradict the required stellar density; there is no star with both $M_c \geq 17\ M_\odot$ and $\rho \sim 1.5 \times 10^{-5}$ g cm^{-3}. Thus, either the orbital period is not near 115 days or mass transfer does not proceed via Roche-lobe overflow. We note that Foster et al. (2010) have suggested that 115 day periodicity may, instead, indicate a super-orbital period.

4.5 Conclusions: Towards a More Constrained Parameter Space

In summary, I set constraints on the binary system, in particular on the mass function and orbital separation. However, the orbital period was not well constrained leading to high uncertainties in the parameter space. In the near future, I will rely on more measurement points in the velocity curve with a forthcoming ESO VLT program, and which will improve the constraints. Also, recently Grisé et al. (2012) studied a massive star forming region (SFR) nearby NGC5408 X-1 (Fig. 4.11). Using the color information of the stars, we found that the SFR contains young massive stars. Therefore, it is likely that the ULX

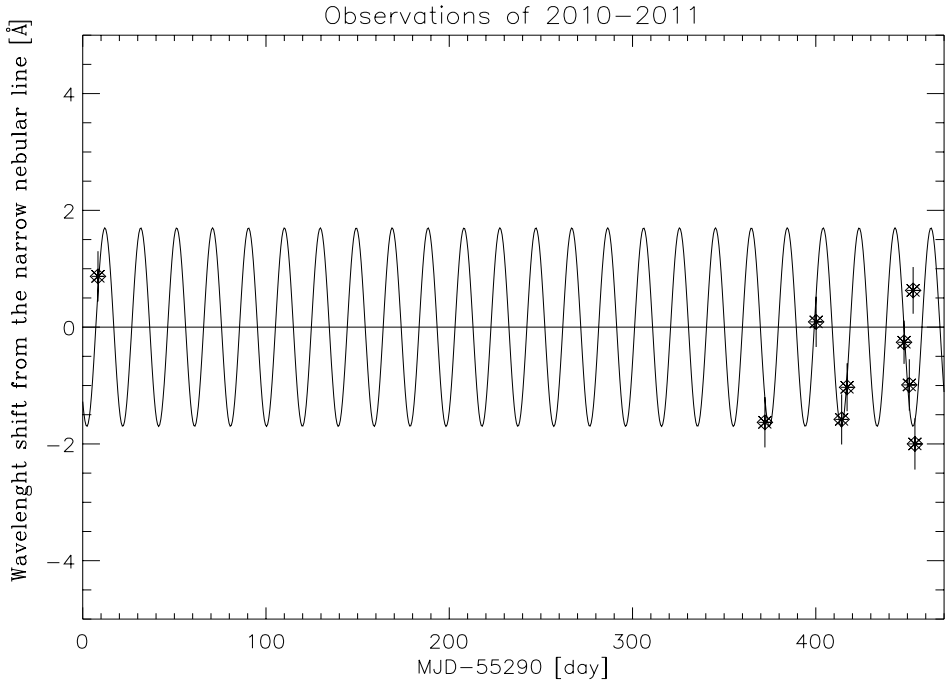

Figure 4.12: Radial velocity curve of NGC 5408 X-1, covering 2010-2011.

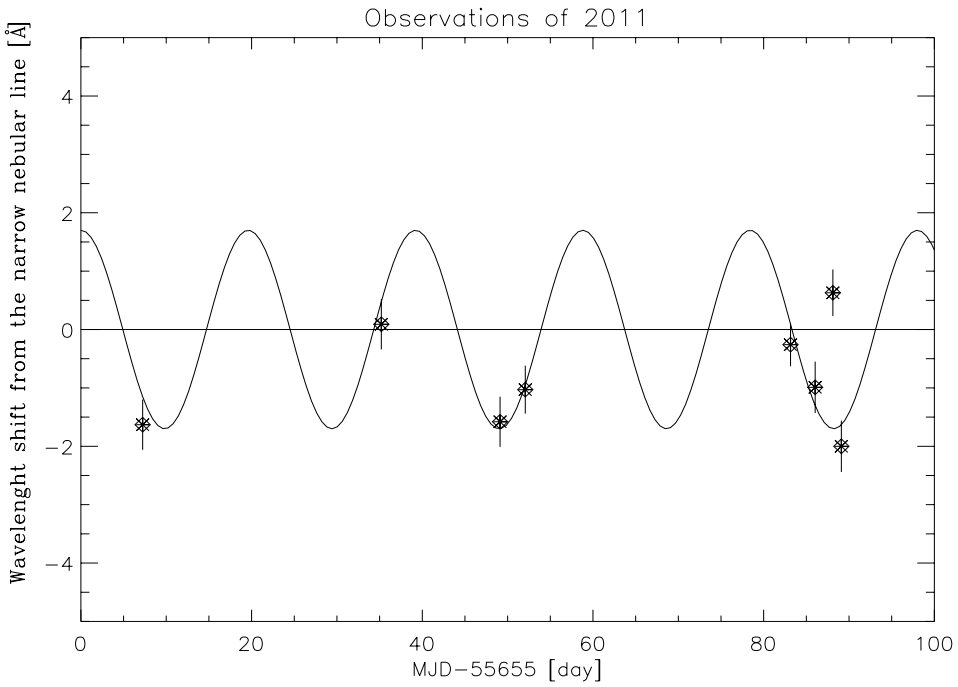

Figure 4.13: Radial velocity curve of NGC 5408 X-1, showing only the 2011 observations.

donor star also has similar age and mass, and so these observations can better constrain the mass of the donor star.

Another important point is that my new measurements from 2011 (Fig. 4.12 and Fig. 4.13) suggest that the shift of the broad component indeed might reflect the orbital

motion of the disk. This is also a significant step forward as previously I had only two measurements. The statistics are sparse due to the lack of observations, so the radial velocity curve cannot be fitted at the moment. In Fig. 4.13. an overplotted curve is shown, which seems to follow the measured points. On the other hand, the new data suggests that the putative orbital period is less than ∼40 days, thus excluding the periodicity of 115 days found by Strohmayer (2009) as orbital period. Furthermore, the shifts in the wavelength are typically the same as found between the first two observations; however, random motions still cannot be excluded until one constrains an orbital period.

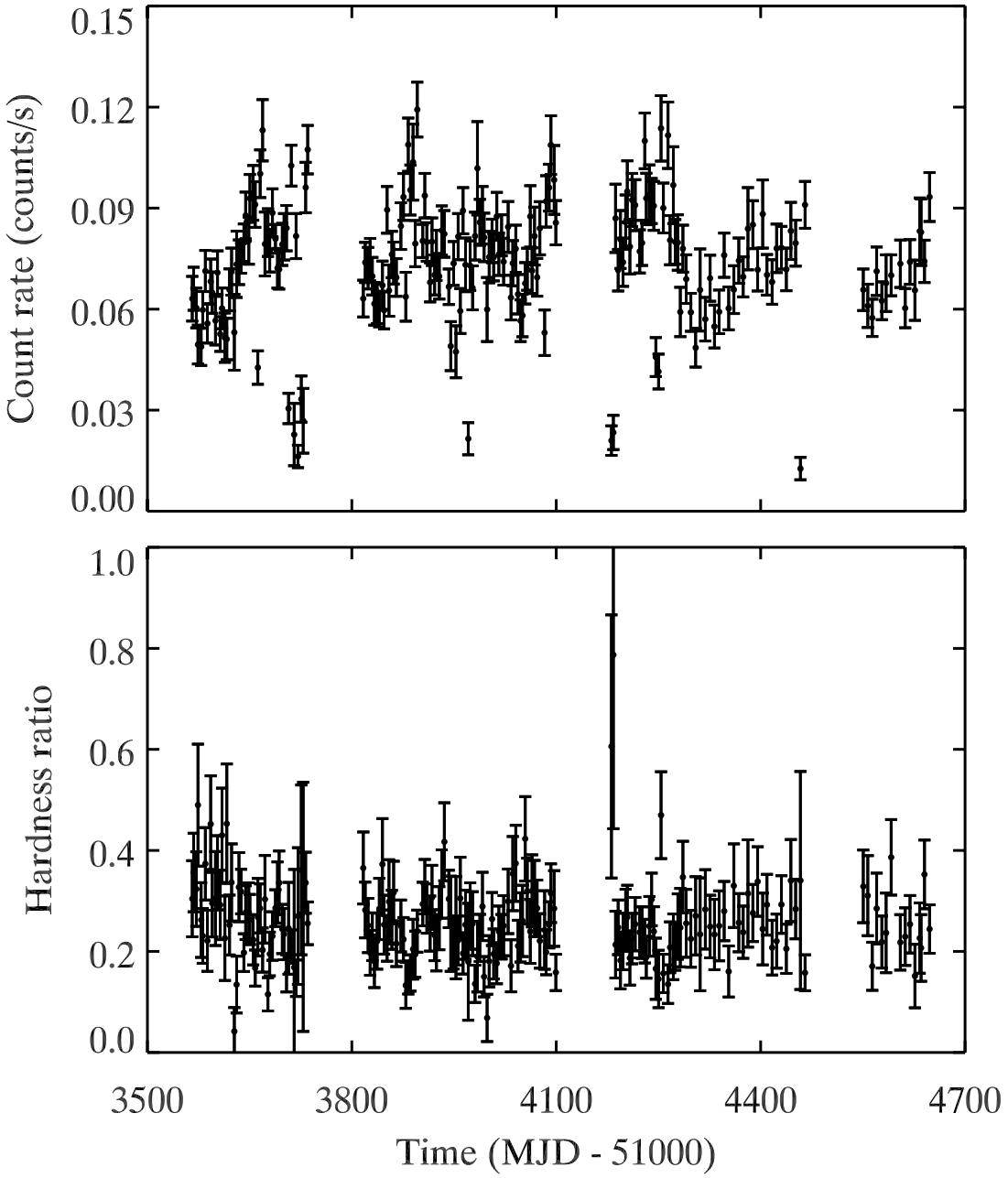

Figure 4.14: Swift X-ray light curve of NGC5408 X-1.

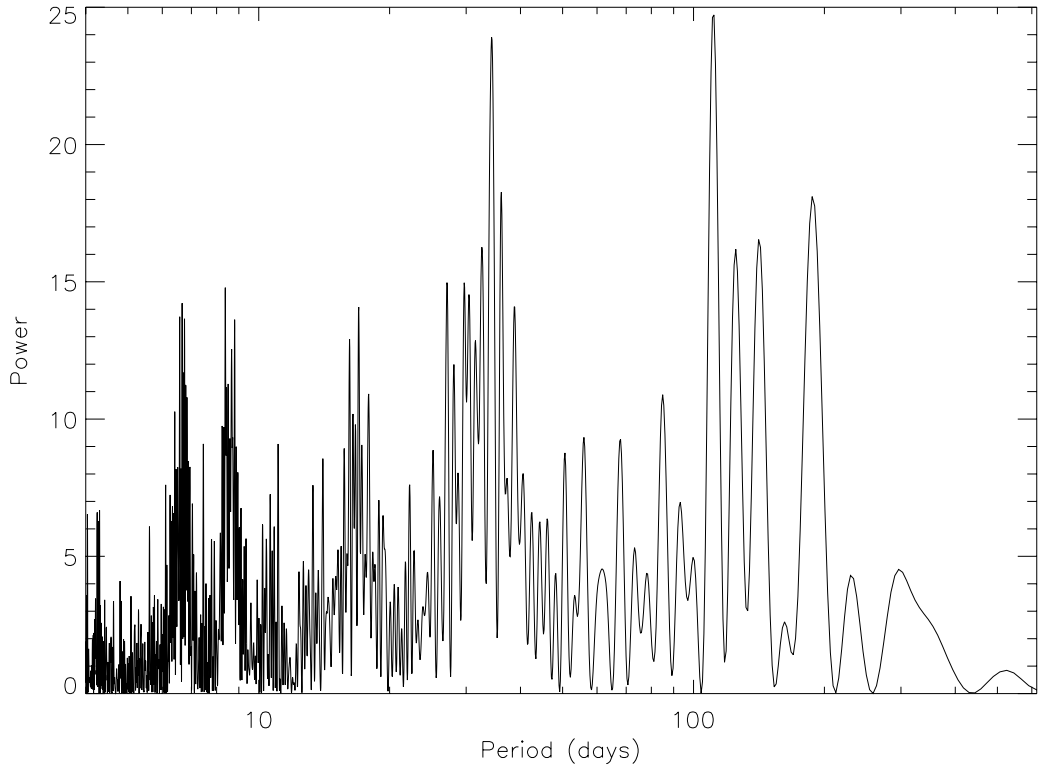

Figure 4.15: Power Density Spectra of NGC5408 X-1

Moreover, our recent SWIFT/XRT monitoring campaign (Fig. 4.14) also confirms that there is no significant periodicity in the X-rays on a much longer temporal baseline. This is shown in Fig. 4.15 provided by F. Grise. It is important to note that the X-ray light curve shows a dipping feature. Although this dipping seems to be aperiodic, it might set some constraints on the inclination of the system i.e. the disk might be more edge-on than face-on. On the other hand, I also found during the 2011 VLT observations that the broad component of the He II line occasionally disappears. This might affect the proper sampling of the velocity curve in the coming period. We suspect that if the optical emission originates due to disk irradiation, then the disappearance of the broad component happens when the X-ray count rate drops. This will be tested in the near future.

As a conclusion, using the 2011 data, I was able to set a more stringent limit on the mass of the black hole using a periodicity of <40 days, and also better constrain the parameters of the binary system (Cseh et al., 2011). The obtained mass function is $f_m = 4.35 \pm 1.5 \mathrm{M}_\odot$ assuming an orbital period of $P = 20$ days, which is plotted in Fig. 4.13. With the conservative assumption on the donor mass of $M = 20\ \mathrm{M}_\odot$ (Grisé et al., 2012), the mass function would imply an upper bound on the mass of the black hole of $M_{\mathrm{BH}} \leq 70 - 90\ \mathrm{M}_\odot$.

Assuming that even if the line shifts represent random motions in the disk, one still may constrain limits on the mass of the BH assuming that the random motions likely follow a quasi-Keplerian orbit and that the size of line-emitting region should be smaller than the orbital separation of the binary system (Cseh et al., 2011). Thus, NGC 5408 X-1 seems to have a black hole with a mass no greater than one can deduce from the

Eddington limit. However, this needs to be tested more in detail, but the case of a 10^4-$M_\odot$ black hole would be likely unphysical for this system.

5
Black Hole Powered Nebulae

Contents

This chapter is based on the content of my paper (Cseh et al., 2012).

Black Hole Powered Nebulae and a Case Study of the Ultraluminous X-ray Source IC342 X-1

D. Cseh, S. Corbel, P. Kaaret, C. Lang, F. Grise, Z. Paragi, A. Tzioumis, V. Tudose and H. Feng
2012, ApJ, 749, 17

In this Chapter, I present new radio, optical, and X-ray observations of three Ultraluminous X-ray sources (ULXs) that are associated with large-scale nebulae. I report the discovery of a radio nebula associated with the ULX IC342 X-1 using the Very Large Array (VLA). Complementary VLA observations of the nebula around Holmberg II X-1, and high-frequency Australia Telescope Compact Array (ATCA) and Very Large Telescope (VLT) spectroscopic observations of NGC5408 X-1 were also presented. I studied the morphology, ionization processes, and the energetics of the optical/radio nebulae of IC342 X-1, Holmberg II X-1 and NGC5408 X-1. The energetics of the optical nebula of IC342 X-1 was discussed in the framework of standard bubble theory. The total energy content of the optical nebula is 6×10^{52} erg. The minimum energy needed to supply the associated radio nebula is 9.2×10^{50} erg. In addition, I detected an unresolved radio source at the location of IC342 X-1 at VLA scales. However, our Very Long Baseline Interferometry (VLBI) observations using the European VLBI Network likely ruled out the presence of any compact radio source at milli-arcsecond (mas) scales. Using a simultaneous Swift X-ray Telescope measurement, I estimated an upper limit on the mass of the black hole in IC342 X-1 using the "fundamental plane" of accreting black holes and obtain $M_{\rm BH} \leq (1.0 \pm 0.3) \times 10^3$ $\rm M_{\odot}$. Arguing that the nebula of IC342 X-1 is possibly inflated by a jet, I estimated accretion rates and efficiencies for the jet of IC342 X-1 and compared with sources like S26, SS433, IC10 X-1.

Note that, the next chapter is closely related to the current one: I show results of an archival analysis aiming to detect radio counterparts of other ULXs (with or without known optical bubbles). I also proposed ATCA observations on a volume limited sample to detect radio bubbles around ULXs and to detect possible compact jets or flares. Additionally, a peculiar a new (peculiar) radio source was found and investigated in detail.

5.1 Introduction

Several ULXs show emission-line optical nebulae, which can be used as calorimeters to infer the total intrinsic power of the ULX (Pakull & Mirioni, 2002, 2003; Russell et al., 2011b). In general, the nebulae around ULXs are either photoionized due to the high X-ray and UV luminosity of the compact object (Pakull & Mirioni, 2002, 2003; Kaaret et al., 2004b; Kaaret & Corbel, 2009; Moon et al., 2011), or shock-ionized driven by jets, outflows, and/or disk winds (Pakull & Mirioni, 2002; Roberts et al., 2003; Abolmasov et al., 2007). In several cases, two-component optical line profiles are present, indicating a mixture of the two mechanisms or alternatively that the narrow line could be due to the shock precursor.

Another common feature is the presence of the high-ionization He II emission line. It can have various origins: the nebula, the donor, the accretion disk, or a disk wind. The ionizing photon rate needed to produce the narrow high-excitation He II line of the nebulae in photoionized sources indicates that their X-ray emission is at most mildly beamed (Pakull & Mirioni, 2002, 2003; Kaaret et al., 2004b; Kaaret & Corbel, 2009; Moon et al., 2011).

Only a handful of radio detections of ULXs have been made so far, including NGC5408 X-1 (Kaaret et al., 2003; Soria et al., 2006a; Lang et al., 2007), Ho II X-1 (Miller et al., 2005), and MF16 (van Dyk et al., 1994; Lacey et al., 1997), if it is not considered a supernova remnant (Matonick & Fesen, 1997). Most of these sources show large nebulae ($>\sim$50 pc) that are likely powered by continuous energy input from the ULX. Shock-dominated ones are probably powered in the same manner as the W50 nebula is powered by the Galactic binary SS433 (Dubner et al., 1998). However, the ULX radio nebulae require greater total energy content than W50. A similarly powerful nebula, S26, was found by Pakull et al. (2010) in optical and Soria et al. (2010b) in radio. For other possible radio associations with ULXs, we refer the reader to Sánchez-Sutil et al. (2006); Soria et al. (2006b); Mezcua & Lobanov (2011), however, in these cases, the optical and radio counterparts do not seem to match astrometrically.

The X-ray spectra of ULXs share some similar properties with the canonical black hole states of Galactic black hole binaries (GBHBs). A number of ULXs show state transitions (Kubota et al., 2001; Feng & Kaaret, 2006, 2009; Godet et al., 2009; Grisé et al., 2010; Servillat et al., 2011). In GBHBs during the X-ray hard state, the sources are associated with self-absorbed compact jets (Corbel et al., 2004; Fender et al., 2004). Given the similarities between ULXs and GBHBs, it is interesting to investigate the presence of such compact jets for ULXs with hard X-ray spectra.

Here, I present new radio and optical observations of two ULXs that are associated with large-scale nebulae: Holmberg II X-1 (Ho II X-1) and NGC5408. In addition, I present discovery of a radio nebula associated with IC342 X-1. Then the energetics of the optical and radio nebulae and the jet properties of IC342 X-1 are investigated in detail.

5.2 Observations, Analysis, and Results

5.2.1 VLA Observations of IC342 X-1 and Ho II X-1

Observations of IC342 X-1 and Ho II X-1 were carried out using the C- and B-array configurations of the Very Large Array (VLA) of the National Radio Astronomy Observatory

Table 5.1: Summary of observations

Source	Inst.(Config.)	Central Frequency	On-source Time	Observation Date	Flux
IC342 X-1	VLA (B)	4.8 GHz	3.2 h	6 Dec 07	2.0±0.1 mJy
IC342 X-1	VLA (C)	4.8 GHz	3.2 h	25 Apr 08	*
Ho II X-1	VLA (B)	4.8 GHz	3.2 h	8 Dec 07	613±61μJy
Ho II X-1	VLA (C)	8.5 GHz	3.2 h	21 Apr 08	395±40μJy
N5408 X-1	ATCA (6D)	5.5 GHz	12 h	23 Aug 09	226±33μJy
N5408 X-1	ATCA (6D)	9 GHz	12 h	23 Aug 09	137±36μJy
N5408 X-1	ATCA (6D)	17.9 GHz	12 h	23 Aug 09	76±20μJy
N5408 X-1	VLT (-)	575-731 nm	0.7 h	12 Apr 10	-
IC342 X-1	EVN (-)	1.6 GHz	12 h	15 Jun 11	$\leq$ 21μJy**
IC342 X-1	Swift/XRT (PC)	0.3 - 10 keV	9.4 ks	15 Jun 11	2.67***

*B and C configuration data were combined.**Three-sigma upper limit.***Unabsorbed flux in units of 10^{-12} erg cm^{-2} s^{-1}.

(NRAO). The observations were made at 4.8 and 8.5 GHz (VLA program code: AL711) and the details are summarized in Table 1. Data calibration, combination in the (u,v) plane and imaging were carried out using the NRAO Astronomical Image Processing System (AIPS: e.g., Greisen (2003)). We adjusted the Robust weighting parameter between 0 and -2 to bring out the fine-scale radio emission and parameters are identified in image captions.

5.2.1.1 Radio detection of IC342 X-1

Figure 5.1 shows the 5 GHz VLA B- and C-array combined image of IC342 X-1 with Robust=0 weighting overlaid on the Hα HST image of Feng & Kaaret (2008). Extended radio emission is present surrounding the position of IC342 X-1. Diffuse emission is detected at up to the 10-σ level with peak intensity of $\sim$120 μJy beam^{-1} and the estimated total flux density in the nebula is $\sim$ 2 mJy. The corresponding luminosity at a distance of 3.9 Mpc (Tikhonov & Galazutdinova, 2010) is $L_{neb} = 1.8 \times 10^{35}$ erg s^{-1}; with $L = \nu L_{\nu}$. We find that the size of the nebula is 16″ × 8″, which corresponds to 300 pc × 150 pc. We estimate the volume of the nebula by taking a sphere with a diameter of 12″. Comparing the 5 GHz radio map to the Hα image, the optical and the radio nebulae are both elongated in the NE–SW direction, possibly exhibiting a shock-front. The size of the radio nebula is consistent with the size of the optical nebula (Pakull & Mirioni, 2002; Grisé et al., 2006; Feng & Kaaret, 2008).

Figure 5.2 illustrates a more uniformly weighted image of the 5 GHz radio emission surrounding IC342 X-1. We weighted the radio image with a robust parameter of -2 in order to resolve out the diffuse nebular emission and show the fine scale structure. The strongest radio emission appears towards the NE of the ULX and is coincident with the strongest Hα emission. The radio emission extends farther to the NE in regions of little or no Hα emission.

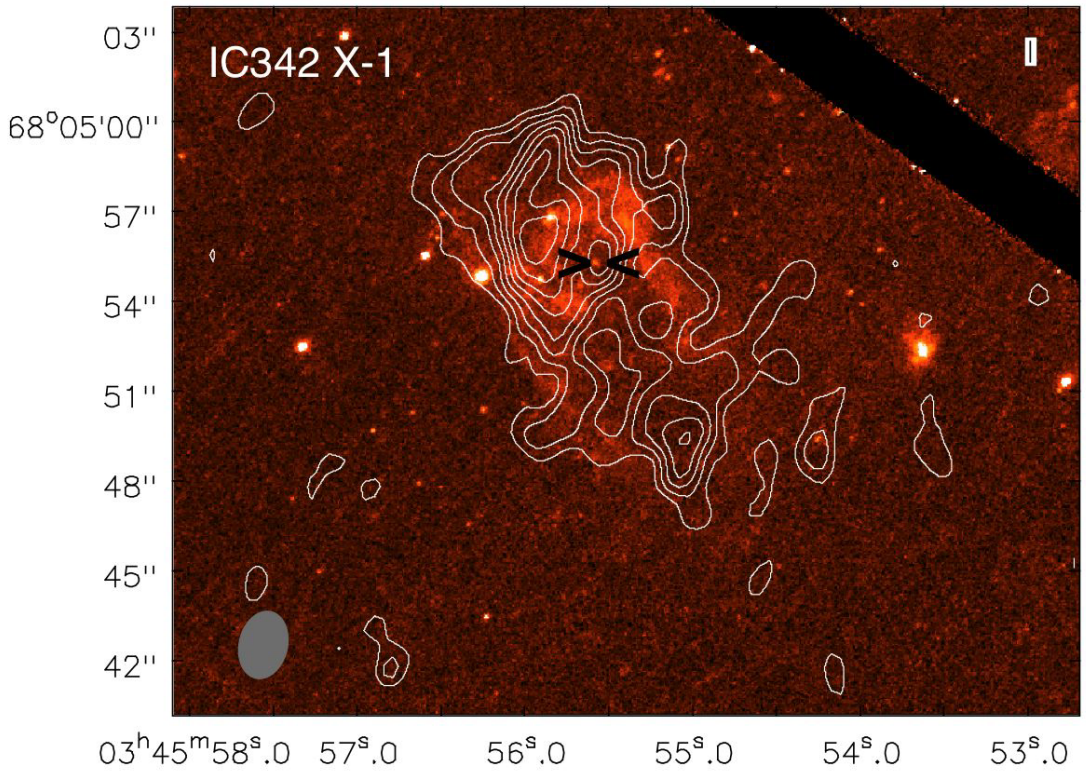

Figure 5.1: VLA 5 GHz image of IC342 X-1 overlaid on the Hα HST image. Contours represent radio emission and are drawn at 3, 4, 5, 6, 7, 8, 9, and 10 times the rms noise level of 11 μJy beam^{-1}. The peak brightness is 122.4 μJy beam^{-1}. The resolution of the image is 2.3″ $\times$ 1.6″ at PA=-13° and the image was made with Robust=0 weighting. The sign '$><$' marks the X-ray position of the ULX.

Table 5.2: Hubble images and source parameters

Name	Narrow Band Filter	Centered on	Ref.	Dist.	Optical diam.	Radio diam.
IC342 X-1	F658N	Hα	1	3.9 Mpc	190 pc	225 pc
Ho II X-1	FR462N	He II	2	3.39 Mpc	45 pc	60 pc
Ho II X-1	FR505N	Hβ	2	-	101 pc	-
N5408 X-1	F502N	[O III]λ5007	3	4.8 Mpc	60pc	40 pc

References: 1 - Feng & Kaaret (2008), 2 - Kaaret et al. (2004b), 3 - Grisé et al. (2012)

Figure 5.2 also reveals an unresolved radio source at the location of IC342 X-1. This unresolved source is detected with a flux density of $\sim 96.3\,\mu$Jy at the 6.5-σ level. The corresponding luminosity is 8.8×10^{33} erg s^{-1}. The HST position of the ULX is RA=03h45m55.61s, Decl.= +68°04′55.3″ (J2000.0) with the 90% positional errors of 0.2 arcsec (Feng & Kaaret, 2008). We obtained the position of the radio peak of RA=03h45m55.54s, Decl.= +68°04′55.18″ using the MAXFIT task of AIPS. The distance between the two positions is ∼0.4 arcsec. Using the AIPS task JMFIT, we estimate a radio positional uncertainty of ∼0.1 arcsec at one sigma. Therefore the optical and radio positions are consistent using 90% positional errors.

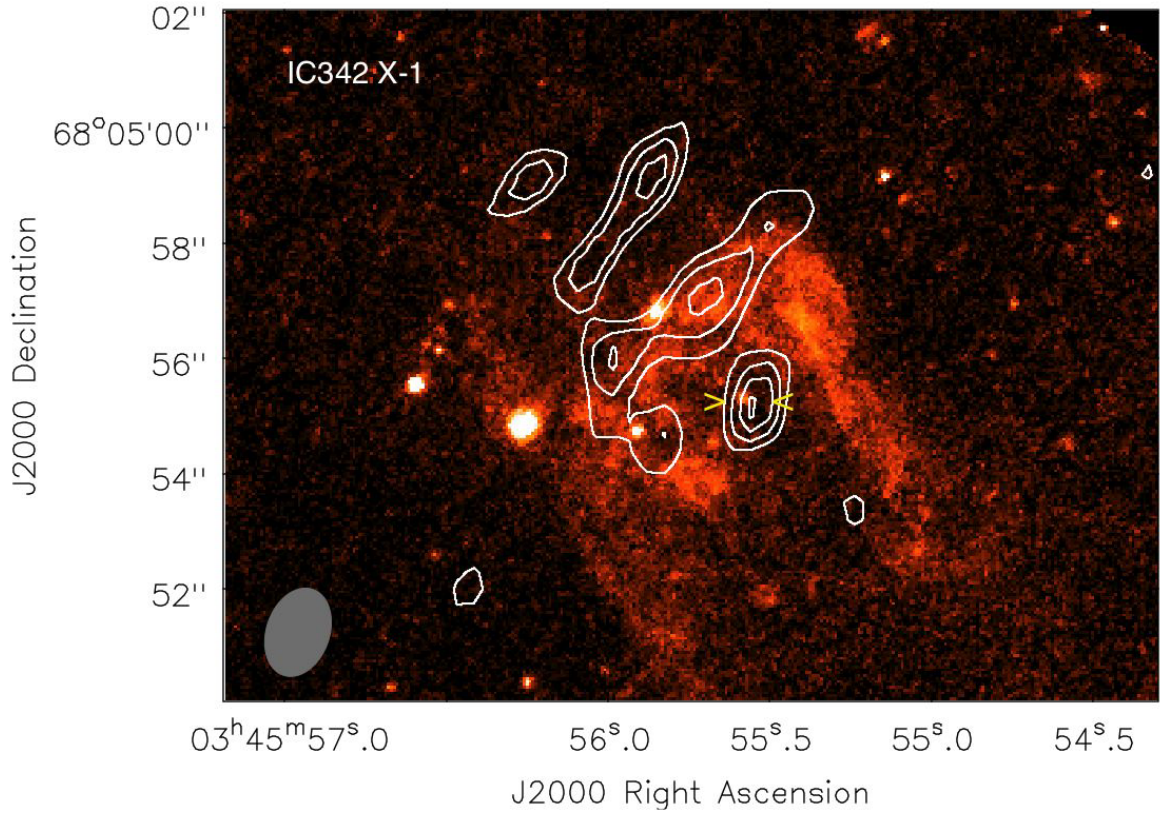

Figure 5.2: VLA 5 GHz image of IC342 X-1 overlaid on the Hα HST image shown in Figure 5.1. This image was made with Robust=-2 weighting and therefore the largest extended features are missing. The resolution is 1.6" $\times$ 1.1" at PA=$-19°$. Contours represent radio emission and are drawn at 3, 4, 5, and 6 times the rms noise level of 15 μJy beam^{-1}. The peak brightness is 96.3 μJy beam^{-1}. The sign '$><$' marks the X-ray position of the ULX.

5.2.1.2 Multi-frequency radio observations of Ho II X-1

The radio nebula of Ho II X-1 was first detected at 1.4 and 5 GHz by Miller et al. (2005). Here, we have conducted observations of Ho II X-1 at 5 and 8 GHz in order to constrain the shape and spectrum of the radio nebula. Figure 5.3. shows the VLA images of Ho II X-1 overlaid on HST He II and Hβ images from Kaaret et al. (2004b). On the left, the unweighted (Robust=0) 5 GHz B-array image is shown. The right panel shows a Robust=-1 image made at 8 GHz using the C-array configuration. The asymmetric morphology of the nebula might indicate some outflows or ambient density gradient to the West.

Previously, the radio spectrum was not well constrained; Miller et al. (2005) had high uncertainties on the flux at 5 GHz of Ho II X-1. However, we now have flux density measurements at three frequencies (1.4, 8 and 5 GHz, using the image from Miller et al. (2005) at 1.4 GHz) and Figure 5.5. illustrates the fitted three-point spectral index of $\alpha = -0.53 \pm 0.07$, ($S \sim \nu^{\alpha}$). The radio spectrum is consistent with optically thin, synchrotron emission, further constraining the nebular nature of the radio counterpart of this ULX nebula. The integrated flux density of the nebula is 1.05$\pm$0.10 mJy, 613$\pm$61 μJy and 395$\pm$40 μJy at 1.4, 5 and 8 GHz.

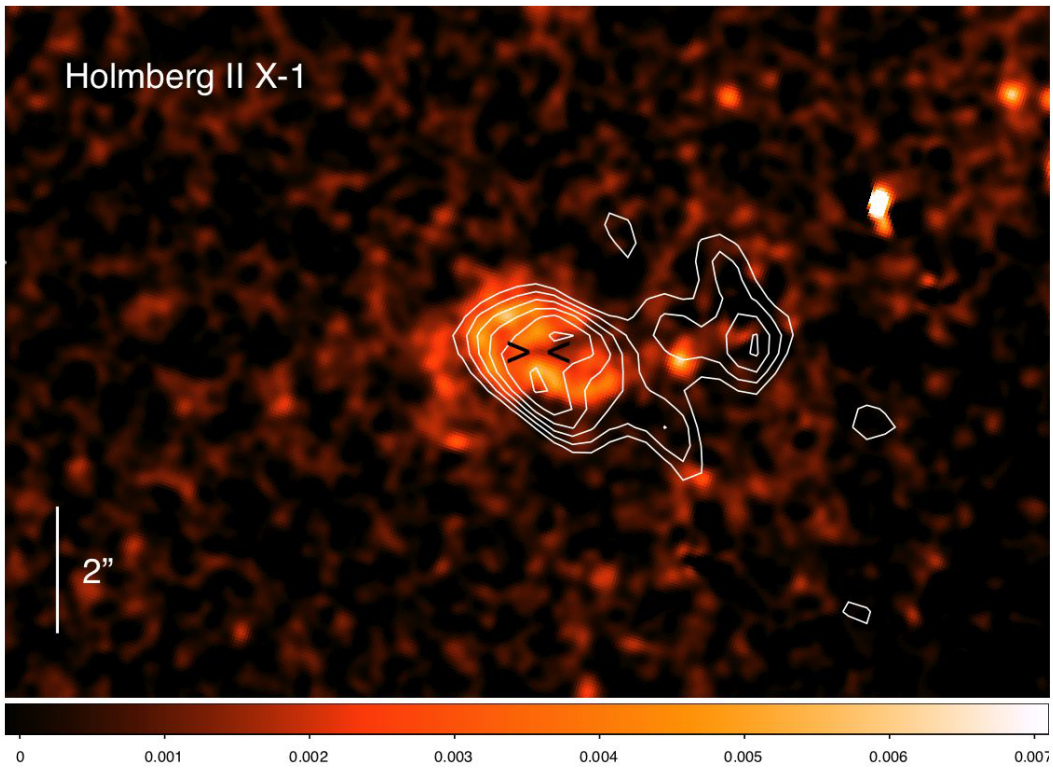

Figure 5.3: The 5 GHz VLA B-array image of **Ho II X-1** overlaid on the He II HST image. Contours represent radio emission at levels of 3, 4, 5, 6 and 7 times the rms noise level of 14 μJy beam^{-1}. The peak brightness is 114 μJy beam^{-1}. The image was made using Robust=0 weighting and the resolution is $1.5” \times 1.0”$ at PA=34°. The North direction is up.

5.2.2 Swift/XRT and EVN Observations of IC342 X-1

5.2.2.1 VLBI observation

We conducted simultaneous X-ray and radio measurements of the VLA core (see Sec. 2.2.1.) to test its compactness in order to estimate the mass of the BH (see Sec. 3.4) with the minimum uncertainty. To check whether the VLA core is consistent with a compact jet at 10 mas scale, we carried out European VLBI Network (EVN) observations (EVN program code: EC032) at 1.6 GHz. The 12-hour observations were accommodated on June 15, 2011 from 03:30 to 15:30 (UT), simultaneously with the Swift/XRT observations. The participating VLBI stations were Effelsberg (Germany), Jodrell Bank Lovell Telescope, Cambridge (United Kingdom), Medicina, Noto (Italy), Toruń (Poland), Onsala (Sweden), Urumqi (P.R. China), Svetloe, Zelenchukskaya, Badary (Russia) and the phased array of the Westerbork Synthesis Radio Telescope (WSRT; The Netherlands). The aggregate bitrate per station was 1024 Mbps. There were eight 8 MHz intermediate frequency channels (IFs) in both left and right circular polarisations.

The source was observed in phase-reference mode. This allowed us to increase the coherent integration time spent on the target source and thus to improve the sensitivity of the observations. Phase-referencing involves regularly interleaving observations between the target source and a nearby, bright, and compact reference source. The delay, delay rate, and phase solutions derived for the phase-reference calibrator (J0344+6827)

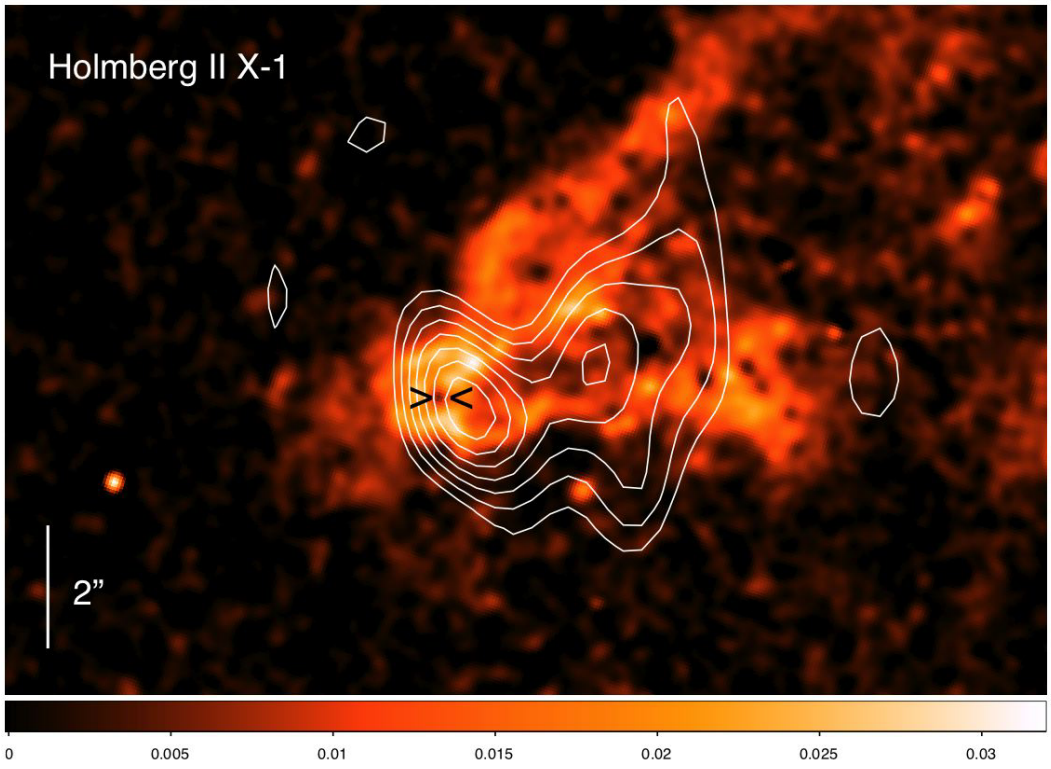

Figure 5.4: The 8.5 GHz VLA C-array image of **Ho II X-1** overlaid on the Hβ HST image. Contours represent radio emission at levels of 3, 4, 5, 6 and 7 times the rms noise level of 15 μJy beam^{-1}. The peak brightness is 145 μJy beam^{-1}. The image was made using Robust=-1 weighting and the resolution is $2.36” \times 1.75”$ at PA=3°. The sign '$><$' marks the X-ray position of the ULX. The North direction is up.

was interpolated and applied to the target within the target-reference cycle time of 5 min. The target source was observed for 3.5-min intervals in each cycle.

AIPS was used for the VLBI data calibration following standard procedures (Diamond, 1995). The visibility amplitudes were calibrated using system temperatures and antenna gains measured at the antennas. Fringe-fitting was performed for the calibrator sources using 3-min solution intervals. The calibrated visibility data were exported to the Caltech Difmap program (Shepherd et al., 1994) used to make a naturally weighted VLBI image. The achieved 1-σ rms noise level was 7 μJy beam^{-1} and we did not detect any source above the 3-σ noise level in a field of view of 700 $\times$ 700 mas. Therefore, the VLA core is likely to be a clump of emission from the nebula. Our EVN observation places a 3-σ upper limit on the flux density of $F_\nu \leq 21$ μJy and on the luminosity of the putative compact jet of $\leq 1.9 \times 10^{33}$ erg s^{-1}.

5.2.2.2 Swift observation

The Swift X-ray Telescope (XRT) obtained 9394 seconds of good exposure in its photon-counting (PC) mode on June 15, 2011, from 02:57:31 to 17:47:47 (UT). We retrieved level two event files and used the default data screening methods as described in the XRT

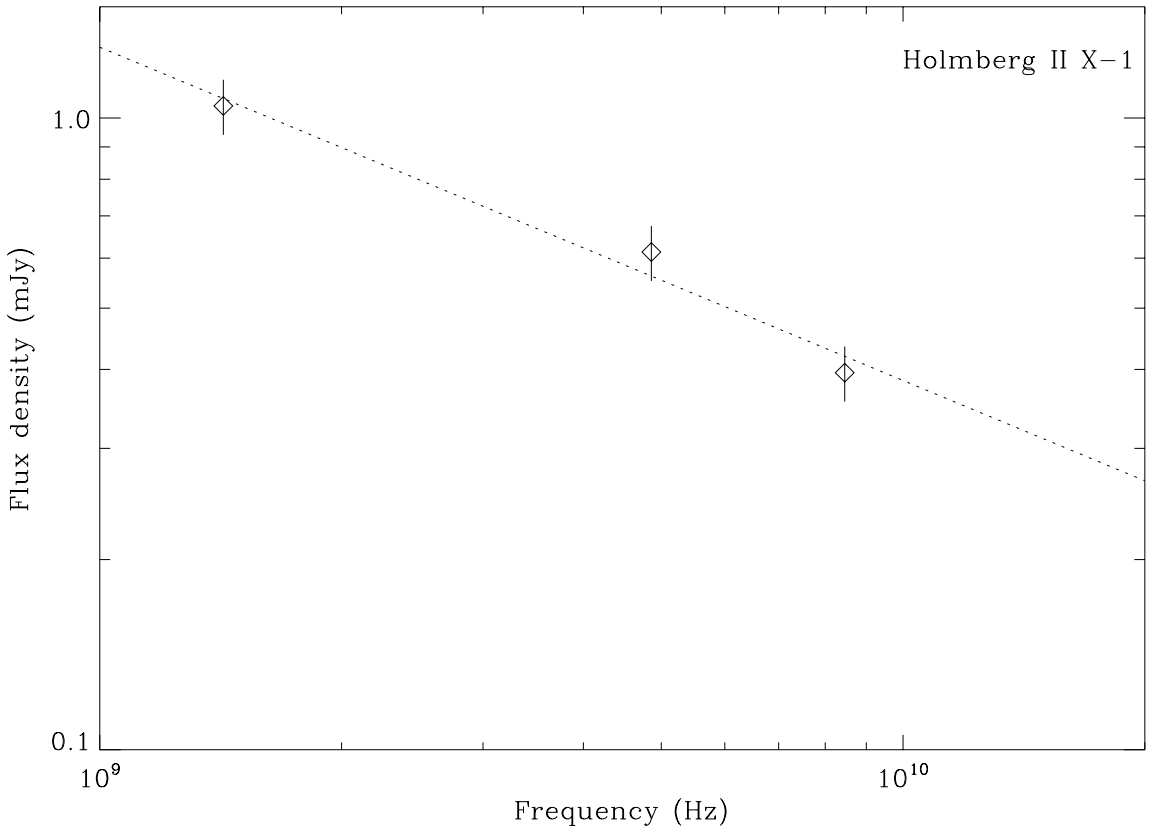

Figure 5.5: The radio spectrum of the nebula of **Ho II X-1**. The best fit spectral index is $\alpha = -0.53 \pm 0.07$ for a flux density, $S \propto \nu^{\alpha}$.

user's guide[1]. We extracted an X-ray spectrum for the source using a circular extraction region with a radius of 20 pixels (corresponding to 90% of the PSF at 1.5 keV); the background was estimated from a nearby circular region with a radius of 40 pixels and subtracted. We fitted the X-ray spectrum using the XSPEC (Arnaud, 1996) spectral fitting tool and the swxpc0to12s6_20070901v011.rmf [2] response matrix.

Fitting the spectrum in the 0.3-10 keV band, with an absorbed power-law, leads to a good fit with $\chi^2/\mathrm{DoF} = 14.7/25$ with a photon index of $\Gamma = 1.57^{+0.29}_{-0.26}$ and an equivalent hydrogen absorption column density of $N_{\mathrm{H}} = 4.5^{+2.0}_{-1.5} \times 10^{21}$ cm^{-2}. The absorbed flux in the 0.3-10 keV band was $1.97{\times}10^{-12}$ erg cm^{-2} s^{-1}. The source clearly has a hard X-ray spectrum with a flux slightly lower than any of the previous XMM observations. The column density is consistent within the errors with the XMM values from Feng & Kaaret (2009). The unabsorbed flux is 2.67×10^{-12} erg cm^{-2} s^{-1}, corresponding to an unabsorbed luminosity of 4.86×10^{39} erg s^{-1} in the 0.3-10 keV band at a distance of 3.9 Mpc.

[1] http://heasarc.nasa.gov/docs/swift/analysis/
[2] http://heasarc.nasa.gov/docs/swift/proposals/swift_responses.html

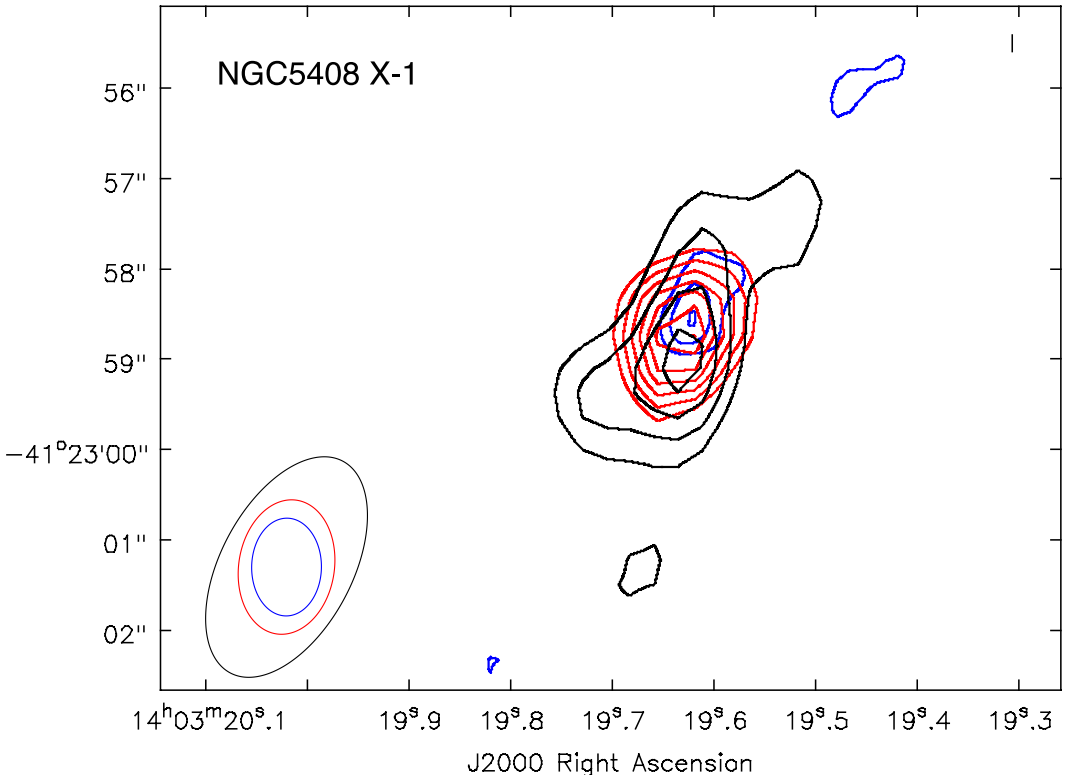

Figure 5.6: The 5.5 (red), 9 (black) and 18 (blue) GHz ATCA 6D-array image of **NGC5408 X-1**. Contours represent radio emission at levels of 3, 4, 5, 6 and 7 times the rms noise level of 23, 17 and 13 μJy beam^{-1}, respectively. The peak brightnesses are 208, 110, 66 μJy beam^{-1}. The image was made using uniform weighting at 5.5 GHz and natural weighting at 9 and 18 GHz and the resolutions are $1.5" \times 1.0"$ at PA=$-9°$, $2.6" \times 1.5"$ at PA=$-28°$, $1.0" \times 0.8"$ at PA=$-1°$ at 5.5, 9 and 18 GHz, respectively.

5.2.3 ATCA Observations of NGC5408 X-1

The radio nebula of NGC5408 X-1 was the first detected radio counterpart of a ULX (Kaaret et al., 2003). Later, it was confirmed that it is an extended source (Lang et al., 2007). We obtained deep high-frequency ATCA CABB (Compact Array Broadband Backend) (Wilson et al., 2011) observations to better constrain the morphology and the high-frequency part of the radio spectra of the nebula at 5.5, 9, and 18 GHz.

We observed NGC5408 X-1 with the CABB-upgraded ATCA in configuration 6D (baselines up to 6 km) on 2009 Aug 23 (program code: C1159). The data were obtained simultaneously at 5.5 & 9 GHz and at 17 & 19 GHz with 12 h on-source integration time for both sets (Table 1.). We observed in phase-reference mode; the phase calibrator was 1424-418 and the primary calibrator was PKS 1934-638. The data reduction was performed using the MIRIAD software package (Sault et al., 1995). We combined the 17 GHz and 19 GHz images in order to enhance sensitivity.

Fig. 5.6 shows the ATCA images of the nebula surrounding NGC5408 X-1 at 5.5, 9 and 18 GHz. The 5.5-GHz image was uniformly weighted, and the 9 and 18-GHz maps were naturally weighted in order to achieve the best sensitivity. Plotting the geometric mean beam size vs. the flux density, Lang et al. (2007) found that the turnover indicates that the radio emission is resolved with an angular size of 1.5–2.0 arcsec. Our new radio images

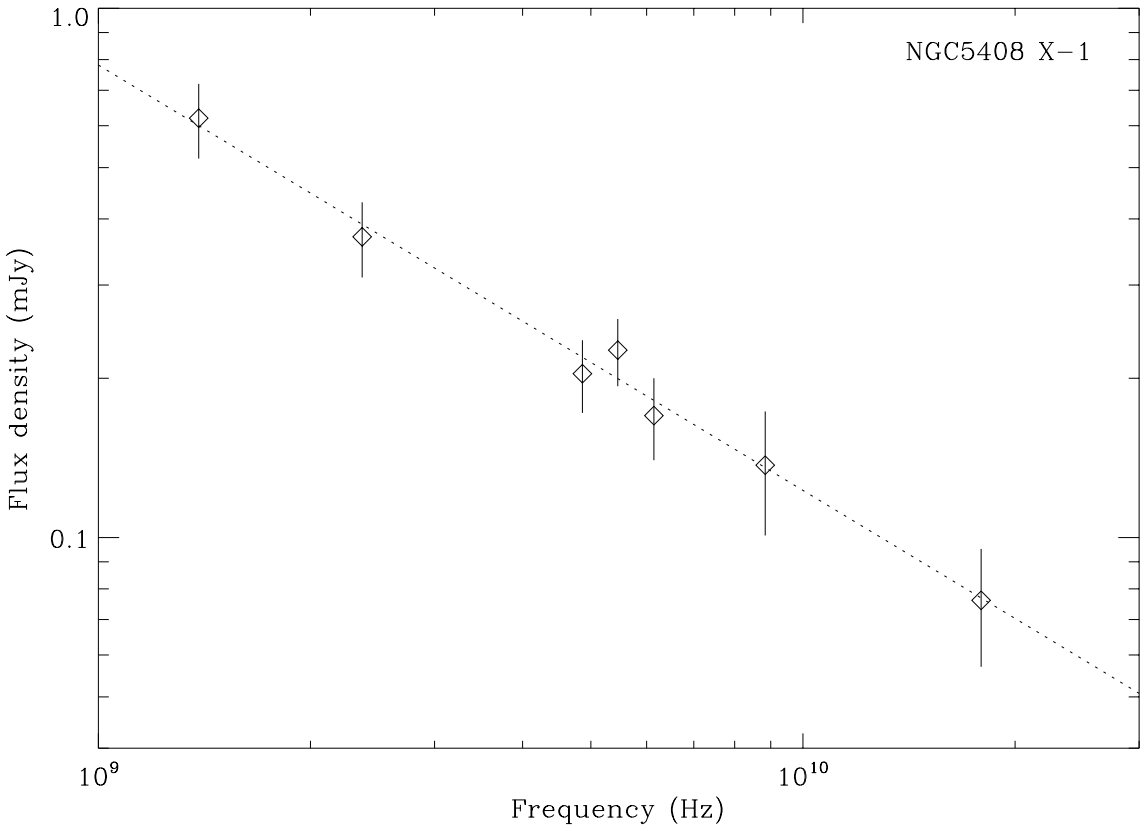

Figure 5.7: The radio spectrum of the nebula of **NGC5408 X-1**. The best fit spectral index is $\alpha = -0.8 \pm 0.1$ for a flux density, $S \propto \nu^{\alpha}$.

show that the size of the nebula is consistent with the previously estimated angular size. At 9 and 18 GHz the source extent is only slightly larger than the corresponding beam sizes, but the elongated contours suggest that the nebula is resolved. This is typical for a weak, optically thin, steep-spectrum source, i.e. going towards higher frequencies, one gains resolution while the relative sensitivity decreases.

We used all available measurements to fit the radio spectrum. Fig. 5.7 shows previous measurements (Lang et al., 2007) and our new ones; combined they cover the 1.4 – 18 GHz frequency range. Our new flux densities are 226±33, 137±36, and 76±20 μJy at 5.5, 9, and 18 GHz, respectively. The fitted radio spectral index of NGC5408 X-1 is $\alpha = -0.8 \pm 0.1$. This is the best constrained spectrum of a ULX nebula to date and is consistent with previous results suggesting optically thin synchrotron emission (Soria et al., 2006a; Lang et al., 2007).

Fig. 5.8 shows the ATCA image at 18 GHz, overlaid on the HST image of the optical nebula of NGC5408 X-1 of Grisé et al. (2012). The HST filter was centered on the forbidden [O III] nebular emission line (Table 2). The optical image shows a one-sided shell-like structure displaced from the ULX which might be due to geometrical effects like limb brightening towards the NE. We find that the radio emission at 18 GHz originates "inside" the optical nebula, however it is possibly an effect of the steep radio spectrum.

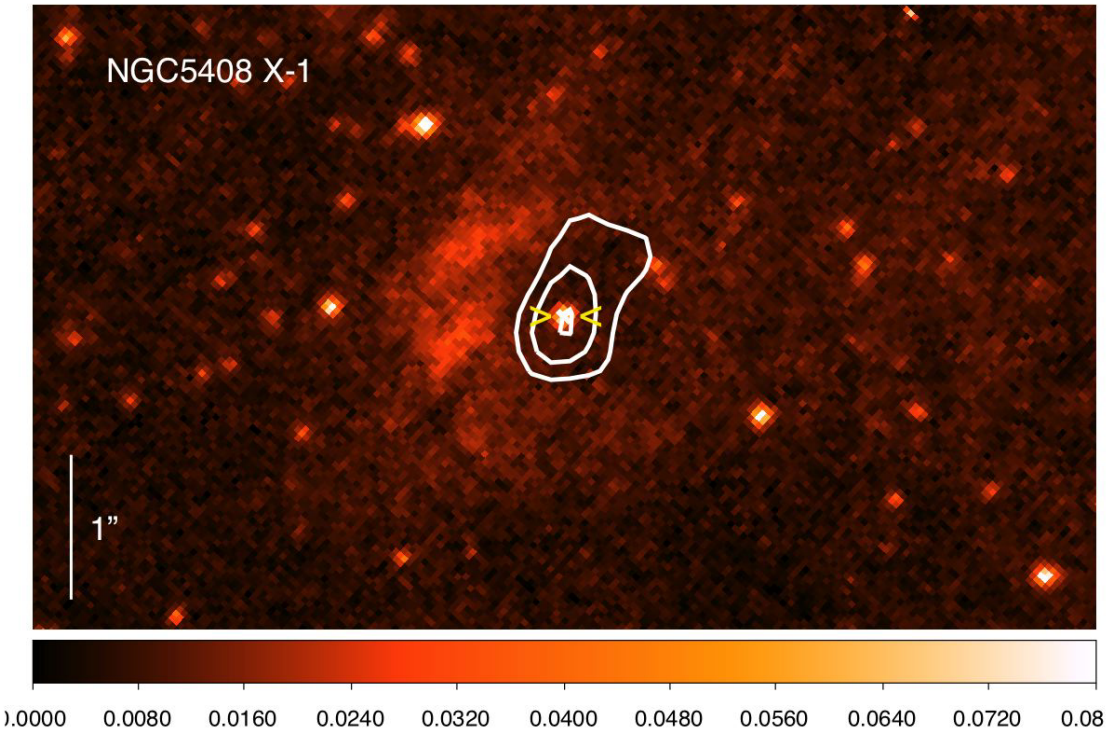

Figure 5.8: The 18 GHz ATCA 6D-array, naturally-weighted image of **NGC5408 X-1** overlaid on the [O III] HST image. The sign '$>$ $<$' marks the X-ray position of the ULX. The North direction is up.

5.2.4 ESO VLT Observations of NGC5408 X-1

As one can gain information about the ionization process from the line flux ratios of Hα versus the forbidden sulphur lines, we conducted VLT observations. VLT FORS-2 observations of NGC5408 X-1 were obtained on 12 April 2010 using the GRIS_1200R grism with a slit width of $1.0''$ covering the spectral range 5750$-$7310 Å with dispersion 0.38 Å pixel^{-1} and spectral resolution $\lambda/\Delta\lambda = 2140$ at the central wavelengths, respectively. The observation block (OB) consisted of three 849 s exposures with a 12 pixel offset along the spatial axis between successive exposures. CCD pixels were binned for readout by 2 in both the spatial and spectral dimensions. The average seeing for our new observations was 0.62 arcsecond.

Data reduction was carried out using the Image Reduction and Analysis Facility (IRAF)[3] (Tody, 1993). First, we created bias and flat-field images, then applied these to correct the spectrum images. The three exposures in each OB were aligned then averaged to eliminate bad pixels and cosmic rays using the `imcombine` task with the `ccdclip` rejection algorithm.

As the continuum emission of the ULX counterpart is faint, we could not trace its spectrum. Following Kaaret & Corbel (2009), we used the bright nearby star at 2MASS

[3]IRAF is distributed by the National Optical Astronomy Observatory, which is operated by the Association of Universities for Research in Astronomy, Inc., under cooperative agreement with the National Science Foundation.

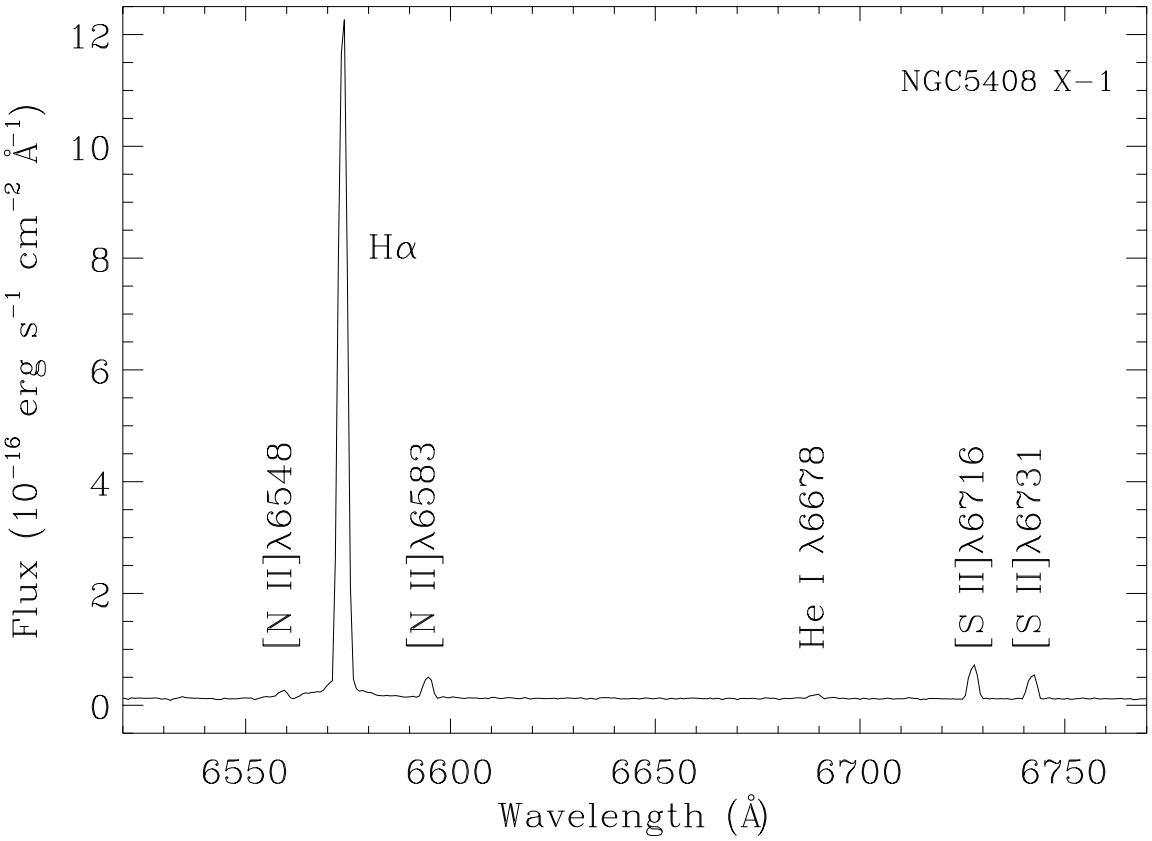

Figure 5.9: VLT optical spectrum of the nebula around **NGC5408 X-1**. The dereddened flux is plotted vs. wavelength and no redshift correction was applied.

(Skrutskie et al., 2006) position $\alpha_{\rm J2000} = 14^h03^m18.^s97, \delta_{\rm J2000} = -41°22'56.''6$ as a reference trace. The trace position on the spatial axis varied less than half a pixel along the whole length of the dispersion axis. A trace width of 8 pixels corresponding to 2″ was used in order to accept a large fraction of the nebular emission. Background subtraction was done with a trace close by. The HgCdHeNeA lamp and standard star LTT7379 were used for wavelength and flux calibration. An atmospheric extinction correction was applied using the IRAF built-in Cerro Tololo Inter-American Observatory (CTIO) extinction tables. To estimate the reddening, we used the Balmer decrement of Hδ/Hβ, we find $E(B-V) = 0.08 \pm 0.03$ in agreement with Kaaret & Corbel (2009). We corrected for reddening using the extinction curve from Cardelli et al. (1989) with $R_V = 3.1$.

Fig. 5.9 shows the optical spectrum of NGC5408 X-1. This portion of the optical spectrum shows the forbidden sulphur and nitrogen lines and the $H\alpha$ line. The lines are at wavelengths of 6558.9 ([N II]), 6573.7 (Hα), 6594.4 ([N II]), 6727.6 ([S II]), and 6742.0 ([S II]) in units of Å. The corresponding fluxes are 0.46 ± 0.02, 33.1 ± 0.1, 1.07 ± 0.02, 1.57 ± 0.01, 1.15 ± 0.01 in the units of 10^{-16}erg s^{-1} cm^{-2}. The Gaussian FWHMs of the lines represent the instrumental resolution of ∼2.4 Å.

5.3 Discussion

5.3.1 The Optical Nebula Around IC342 X-1

In this section we use models developed for expanding bubbles to calculate parameters of the nebula based on the observed optical properties. We follow the formalism developed by Weaver et al. (1977) and Ostriker & McKee (1988) describing the hydrodynamic structure of a bubble. These formulae are valid for shock-dominated sources, i.e. jet or wind inflated bubbles, but not for photoionized bubbles. As IC342 X-1 is considered to be a shock-dominated source (Pakull & Mirioni, 2002; Roberts et al., 2003; Abolmasov et al., 2007), we can apply the well-known self-similar expansion law as a function of time, t:

$$R = \left(\frac{125}{154\pi}\right)^{1/5} \left(\frac{L_{tot}}{\rho_0}\right)^{1/5} t^{3/5} \tag{5.1}$$

where L_{tot} is the mechanical luminosity (corresponding to a jet or a wind or an initial explosion energy), R is the radius of the bubble expanding with velocity $v_{exp} = \dot{R}$ into the ISM. The mass density ρ_0 is assumed to be constant and $\rho_0 = \mu m_p n$, where $\mu = 1.38$ is the mean atomic weight, m_p is the proton mass and n is the hydrogen number density. The characteristic age of the bubble is $\tau = 3R/5v_{exp}$. The kinetic energy carried by the swept-up mass in the expanding shell is $E_k = \frac{15}{77} L_{tot} t$, while the energy emitted (the cooling) by the fully radiative shock expanding into the ISM is $E_{rad} = \frac{27}{77} L_{tot} t$. The thermal energy of the gas between the reverse shock and the swept-up shell is $E_{th} = \frac{5}{11} L_{tot} t$. Thus, the total energy is $E_{tot} = E_k + E_{rad} + E_{th} = L_{tot} t$.

Feng & Kaaret (2008) found that the bright main body of the nebula has an angular diameter of about $6''$ in the $H\alpha$ image. (Pakull & Mirioni, 2002; Grisé et al., 2006; Feng & Kaaret, 2008) report an additional elongated structure to the South-West. Considering the entire structure of the bubble, we estimate the volume of the optical nebula by taking a sphere with a diameter of $\sim 10''$, which corresponds to ∼190 pc at a distance of 3.9 Mpc Tikhonov & Galazutdinova (2010).

The high flux ratio between the forbidden [S II] lines at 6,716 Å and 6,732 Å and the Balmer Hα line indicates the presence of shock-ionized gas. Abolmasov et al. (2007) infer a shock velocity of $v_{exp} \simeq 20 - 100$ km s^{-1}; however, line ratios of a standard library of radiative shock models, e.g. He II vs. Hβ is 0.036±0.015, suggest a shock velocity of $\simeq 100$ km s^{-1} (Allen et al., 2008). Using this velocity, we find the characteristic age of the bubble is $\tau = 5.6 \times 10^5$ yr. Feng & Kaaret (2008) found that the color-magnitude diagram suggests that the minimum stellar age in the environment of the ULX is 10 Myr. The characteristic age of the nebula is much shorter and might suggest that the nebula formation is not related to the formation of the central BH or BH progenitor, instead it might represent the actively accreting phase of the binary.

Recalling the scaling of the total radiative flux and the flux in the Balmer lines (Dopita & Sutherland, 1996; Abolmasov et al., 2007) [4]:

$$L_{H\beta} = 6.53 \times 10^{-3} \left(\frac{v_{exp}}{100\,\mathrm{km\,s^{-1}}}\right)^{-0.59} L_{rad} \tag{5.2}$$

So, the total shock power represented as radiative losses is $L_{rad} = 1.2 \times 10^{39}$ erg s^{-1}, using the $H\beta$ flux of Abolmasov et al. (2007) of 4.3×10^{-15}erg s^{-1} cm^{-2}. As a consequence,

[4] We note, that there is a typo in Eq. 3.3 of Dopita & Sutherland (1996) (and consequently in Eq. 1 of Abolmasov et al. (2007)), pointed out to us by M. W. Pakull. The numerical factor should read 1.14×10^{-3} rather than 2.28×10^{-3} as the maximum radiative flux is $\frac{1}{2}\rho v^3$ and not ρv^3.

the total mechanical luminosity is $L_{tot} = \frac{77}{27} L_{rad} = 3.4 \times 10^{39}$ erg s^{-1}, and the total kinetic power carried by the swept-up mass is $L_k = 6.6 \times 10^{38}$ erg s^{-1}. Similarly, the internal (thermal) luminosity is $L_{th} = 1.5 \times 10^{39}$ erg s^{-1}. The energy, we see at t=τ is $E_{tot} = L_{tot}\tau = 6.0 \times 10^{52}$ erg. From Eq. 1 one can derive that $n = 1.0$ cm^{-3} by substituting R, τ, L_{tot}. The optical swept-up mass is then $M = \mu n m_p V = 2.4 \times 10^{38}$ g or $M = 1.2 \times 10^5$ M$_\odot$.

IC342 X-1 is sometimes considered as a SN remnant (Roberts et al., 2003, eg.). Here we intend to show that the total energy content does not depend significantly on the interpretation of the origin of the bubble. A SNR in the pressure-driven snowplow stage – ie. radiative dominant phase following the adiabatic phase – has an initial explosion energy, E_i(Cioffi et al., 1988):

$$E_i = 6.8 \times 10^{43} \left(\frac{R}{\mathrm{pc}}\right)^{3.16} \left(\frac{v_{exp}}{\mathrm{km\,s^{-1}}}\right)^{1.35} \left(\frac{n}{\mathrm{cm^{-3}}}\right)^{1.16} \mathrm{erg} \tag{5.3}$$

We have treated the metallicity correction factor, $\zeta_m^{0.161}$, as 1 for clarity (Cioffi et al., 1988; Thornton et al., 1998). Substituting $R,\ v$ – and taking $n = 1.0$ cm^{-3} (see above), we obtain $E_i = 6.0 \times 10^{52}$ erg. We note that a similar formula of Chevalier (1974) provides $E_i = 5.0 \times 10^{52}$ erg. This initial energy is remarkably high, although somewhat expected as a single/simple SNR will not remain visible once it has expanded beyond $R \simeq 100$ pc with a canonical $E_i \simeq 10^{51}$ erg (Matonick & Fesen, 1997; Roberts et al., 2003). The estimated energy is in good agreement with the total energy content of the bubble, E_{tot}, within model uncertainties. We note that an SNR nature for the nebula around IC 342 X-1 is strongly challenged by its high shock velocity coupled with large size (Pakull & Grisé, 2008).

5.3.2 The Radio Nebula Around IC342 X-1

When radiation is via synchrotron emission, one can assume equipartition between energy of relativistic particles and the magnetic field. We calculate the minimum total energy of the radio nebula that corresponds to equipartition (Longair, 1994):

$$E_{min} = 3 \times 10^{13} \eta^{4/7} \left(\frac{V}{\mathrm{m^3}}\right)^{3/7} \left(\frac{\nu}{\mathrm{Hz}}\right)^{2/7} \left(\frac{L_\nu}{\mathrm{W\,Hz^{-1}}}\right)^{4/7} \mathrm{erg} \tag{5.4}$$

where $\eta - 1$ is the ratio of energy in protons to relativistic electrons, V is the volume, ν is the observing frequency and L_ν is the synchrotron luminosity. As is customary, we do not account for relativistic protons, therefore $\eta - 1 = 0$ (eg. Fender et al., 1999). Substituting the corresponding values of $V \simeq 1.79 \times 10^{56}$ m^3, $\nu = 5 \times 10^9$ Hz, $L_\nu = 3.64 \times 10^{18}$ W Hz^{-1} and a filling factor of unity, we find the energy required to power the nebula is $E_{min} = 9.2 \times 10^{50}$ erg. This suggests that the radio-emitting material carries a fraction $\sim 10^{-2}$ of the initial energy. For comparison, the energy carried by mildly relativistic material in normal Type Ic supernovae has been suggested to be at most 10^{-4} (Paragi et al., 2010), while for the jet inflated bubble around the extragalactic microquasar S26, this fraction is a few times 10^{-3} (Soria et al., 2010b). These fractions suggest that most of the energy is stored in protons, nuclei, and non-relativistic bulk motion.

We calculate the magnetic field strength corresponding to the minimum energy condition (Longair, 1994)

$$B_{min} = 1.8 \times 10^{10} \left(\frac{\eta L_\nu}{V}\right)^{2/7} \nu^{1/7}\ \ \mu\mathrm{G} \tag{5.5}$$

where the units and inputs are the same as above. We obtain $B_{min} = 7.4\,\mu$G.

Using the magnetic field strength we can estimate the total number of relativistic electrons (Longair, 1994)

$$N = \frac{L_\nu}{B_{min}} \left(A(p)(p-1) \left(m_e c^2\right)^{p-1} \left(\frac{2\pi m_e}{|e|}\right)^{\frac{p-1}{2}} \right)^{-1} \tag{5.6}$$

where

$$A(p) = 2.344 \times 10^{-25} (1.253 \times 10^{37})^{\frac{p-1}{2}} a(p) \tag{5.7}$$

and

$$a(p) = \frac{\sqrt{\pi}}{2} \frac{\Gamma(\frac{p}{4} + \frac{19}{12})\Gamma(\frac{p}{4} - \frac{1}{12})\Gamma(\frac{p}{4} + \frac{5}{4})}{(p+1)\Gamma(\frac{p}{4} + \frac{7}{4})} \tag{5.8}$$

Here m_e is the mass of the electron, e is the charge of the electron, c is the speed of light and $p = 2\alpha + 1$, where α is the spectral index; and $S \sim \nu^{-\alpha}$ is assumed in the above equation; the units are in SI. We assume, a spectral index of $\alpha = -0.8$, equivalent with the value of NGC 5408 X-1, which has the best constrained radio spectra to date. The function $A(p)$ equals about 38113 for $p = 2.6$, where p corresponds to the assumed spectral index of -0.8. We obtain the total number of relativistic electrons $N = 1.6 \times 10^{52}$. The total mass of the relativistic matter accounting one proton for each electron, $M_{sy} = N m_p = 2.7 \times 10^{28}$ g, or $M_{sy} = 1.3 \times 10^{-5} \mathrm{M}_\odot$.

When energy loss is due to synchrotron radiation, the lifetime of an electron is (Longair, 1994; Tudose et al., 2006)

$$\tau_{sy} = 2.693 \times 10^{13} \left(\frac{\nu}{\mathrm{Hz}}\right)^{-1/2} \left(\frac{B_{min}}{\mu\mathrm{G}}\right)^{-3/2} \ \mathrm{yr} \tag{5.9}$$

Substituting $\nu = 5 \times 10^9$ Hz and $B_{min} = 7.4\,\mu$G, we find $\tau_{sy} = 18.8$ Myr. So, consistently, the cooling time-scale is $\sim$34 times longer than the age of the bubble and $\sim$2 times higher than the minimum age of the ULX stellar environment.

We note that the value of η, the energy ratio of relativistic protons to electrons, can be estimated from the high-energy part of SNR spectra (Abdo et al., 2010; Acciari et al., 2011). Assuming IC342 X-1 has a ratio similar to that found for a scenario in which the high-energy gamma-rays from the Tycho SNR are produced by leptons (Acciari et al., 2011), then $\eta - 1 = 10^2$ and the minimum energy obtained from Eq. 5.4 is increased by a factor of $\eta^{4/7} = 100^{4/7} = 13.9$. This would mean that $E_{min}/E_{tot} = 0.2$. Instead, if the gamma-ray emission from Tycho is from hadrons, then $\eta - 1 = 2.5 \times 10^3$ and E_{min}/E_{tot} would be $\simeq 1.3$. Thus, if the high-energy gamma-ray emission of shock inflated bubbles originates from the same electron distribution that produces the radio, then via the η parameter, the value of E_{min} could increase, but interestingly, does not violate the total energy obtained from the optical.

5.3.3 The Radio and Optical Nebulae of Ho II X-1 and NGC 5408 X-1

5.3.3.1 Ho II X-1

Our new, higher resolution VLA radio observations clearly reveal that the morphology of the radio nebula follows the structure of the optical one (Fig. 5.3). The radio nebula is resolved with a size of 5.5″ × 2.7″, corresponding to $\sim$ 81 pc × 40 pc. One could

argue that this morphology reflects either a jet activity or an outflow. However, Pakull & Mirioni (2002); Kaaret et al. (2004b) showed, that the nebula of Ho II X-1 is consistent with photoionization by the central compact source. On the other hand, a complex velocity structure in the inner regions of the optical nebula indicates the impact of the central object also in the form of winds or jets (Lehmann et al., 2005). As the [S II] vs. Hα ratio is $\ll 1$ (Abolmasov et al., 2007), i.e. collisional excitation of the nebula is negligible, the morphology probably reflects an outflow rather than a well-collimated jet. This outflow is either relatively weaker than a jet – thus preventing shock-ionization – or the outflow is more isotropic than collimated. We note that weakly collimated outflows, in addition to jets, have been directly observed in SS433 with VLBI (Paragi et al., 1999). In addition, the asymmetry of the outflow is probably due to the fact that the nebula is density bounded to the East and South of the central object Pakull & Mirioni (2002); Kaaret et al. (2004b).

Furthermore, the minimum energy required to power the radio nebula of Ho II X-1 is 2.6×10^{49} erg with a magnetic filed strength of 13μG and the synchrotron lifetime is $\tau_{sy} = 25$ Myr (Miller et al., 2005). This energy requirement is a factor of 35 less than needed for IC342 X-1, a shock-dominated source, which might also support a weak or uncollimated outflow.

Interestingly, Grisé et al. (2010) studied an X-ray state transition of Ho II X-1 and found that it is difficult to interpret the thermal component of the X-ray spectra as disk emission or thermal Comptonization. On the other hand, this thermal component might be linked to the complex velocity structure of the nebula, ie. it might be due to a disk wind that results in a complex velocity structure of the nearby environment. We note that disk wind signatures have been found for GRS1915+105 (Neilsen & Lee, 2009) and SS433 (Fabrika, 2004), i.e. for sources likely accreting above their Eddington-limit. Searching for relativistic disk lines and/or Fe K absorption line variation in the X-ray spectrum of ULXs might help disentangle whether some of these ULXs are similar to high-accretion rate Galactic binaries.

5.3.3.2 NGC5408 X-1

Fig. 5.8. shows a shell-like optical morphology of NGC5408 X-1 and a filled structure of the radio nebula with a maximum intensity near the ULX. The optical nebula is resolved, with a diameter of $\sim$ 2.5", corresponding to $\sim$ 60 pc (Grisé et al., 2012), which is much smaller than the optical nebula of IC342 X-1. Probably, the nebula is powered only by photoionization without any jet or outflow activity. Our optical spectra also suggest this, as the [S II] vs. Hα line ratio is $\ll 1$ (Fig. 5.9.). Furthermore, the energy needed to power the radio nebula of NGC5408 X-1 is 3.6×10^{49} erg with an equipartition field of 16μG and a synchrotron cooling time of $\tau_{sy} = 20$ Myr (Lang et al., 2007), which is, similar to Ho II X-1, a factor of 25 less than the energy needed to power the radio nebula of IC342 X-1.

5.3.3.3 Comparison to Ho IX X-1 and MF16

It is interesting to note that similarly to Ho II X-1, Ho IX X-1 also shows dynamical motion close to the center of the nebula (Moon et al., 2011). However, to argue that its origin is due to outflows/disk winds is more challenging, because the [S II] vs. Hα ratio in Ho IX X-1 indicates shock ionization. It is also unknown if a velocity dispersion – on the order of $\sim$1000 km/s – is present, which could be indicative of a disk wind.

MF16 is shock-heated but also contains high excitation lines with two component emission lines (Abolmasov et al., 2008). The radio counterpart shows a marginally re-

solved radio source at ~ 1.1 arcsec resolution corresponding to ~ 25 pc (van Dyk et al., 1994) with a spectral index of $\alpha = -0.7$. Because of the elongated nebula, Abolmasov et al. (2008) argues that we see a similar system to SS433, but with a jet pointing close to our line of sight. In addition, Kaaret et al. (2010) found the presence of a UV nebula beyond the optical one. This is the only UV nebula found to be associated to a ULX, so it is difficult to address its origin. Given the size of the radio and optical bubbles, it can be still argued that the source is a result of an energetic supernova explosion.

5.3.4 Upper Limit on the Mass of the Black Hole in IC342 X-1

Self-absorbed compact jets are ubiquitous in the X-ray hard states of GBHBs (Corbel et al., 2004; Fender et al., 2004). IC342 X-1 was found to have a hard X-ray spectrum in all available XMM-Newton and Chandra observations covering the period from 2001 to 2006 (Feng & Kaaret, 2008, 2009) as well as in our recent Swift/XRT measurement (see Sec. 2.4.1.). Thus, the presence of compact jets is expected if the hard X-ray spectrum is equivalent to the canonical hard state of GBHBs.

In addition, the morphology of the radio nebula is somewhat similar to the system SS433/W50 and may suggest a jet orientation along an axis slightly East of North (Feng & Kaaret, 2008). As we pointed out earlier, an unresolved radio source is detected at the location of the ULX. This morphology might argue against the notion that the compact emission is the hot spot at the end of the jet pointing close to our line of sight. To test the compactness of this emission, we conducted VLBI measurements using the EVN (Sec 2.2) and we did not detect any source above the 3-σ noise level, so it is likely to be consistent with a clump of emission from the nebula and might be an effect of a steep radio spectrum. We can set an upper limit on the flux of the putative compact jet of 1.9×10^{33} erg s^{-1}, using our 3-σ noise level of 21 μJy.

When black holes are in the hard state, i.e. their accretion is radiatively inefficient and perhaps advection dominated or jet dominated, a relationship holds between X-ray luminosity, radio luminosity and black hole mass (Merloni et al., 2003; Falcke et al., 2004). This relationship, the fundamental plane of black holes, has been studied on a wide mass range from black hole X-ray binaries to low luminosity active galactic nuclei. Using the correlation with the minimum scatter (Körding et al., 2006a):

$$\log\left(\frac{M}{\mathrm{M}_\odot}\right) = 1.02^{-1}\left(1.59\log\left(\frac{L_R}{\mathrm{erg\ s^{-1}}}\right) - \log\left(\frac{L_X}{\mathrm{erg\ s^{-1}}}\right) - 10.15\right). \quad (5.10)$$

and our radio and X-ray measurements, one can estimate the upper limit of the mass of the black hole in IC342 X-1. However, we must consider the intrinsic rms scatter in the measured fundamental plane relation of 0.12 dex within one σ. Substituting the upper limit of radio luminosity of the putative compact jet ($L = 1.9 \times 10^{33}$ erg s^{-1}) and the simultaneously measured X-ray luminosity $L_X = 4.86 \times 10^{39}$ erg s^{-1}, we estimate the mass of the black hole to be $M_{\mathrm{BH}} \leq (1.0 \pm 0.3) \times 10^3$ M$_\odot$. This limit is valid only if IC 342 X-1 enters the canonical hard state. We note that further observations could help place tighter constraints on the BH mass or help test if ULXs exhibiting hard X-ray spectra are, indeed, in the radiatively inefficient, hard X-ray state (see section 3.5.1).

5.3.5 Comparison of IC342 X-1 with S26, IC10 X-1 and SS433

In this section we compare IC342 X-1 to sources whose jet power and accretion rate has been estimated from extended emission in optical and/or radio. Table 5.3 shows the main characteristics of the specific sources: the average X-ray luminosity (L_X), the jet power

Table 5.3: Comparison with X-ray sources embedded in nebula

Name	L_X (erg/s)	Q_j (erg/s)	$M_{\rm BH}$ ($M_\odot$)	E_{tot} (erg)	τ (yr)	E_{min} (erg)
IC342 X-1	1.6×10^{40}	3.4×10^{39}	$\leq 1000^*$	6.0×10^{52}	5.6×10^5	9.2×10^{50}
S26	6.2×10^{36}	5×10^{40}	n/a	3.16×10^{53}	2×10^5	10^{50}
IC10 X-1	1.5×10^{38}	1.27×10^{39}	23-34	2×10^{52}	5×10^5	n/a
SS433	$\sim 10^{36}$	2×10^{38}	16	2×10^{51}	2×10^5	10^{49**}

The Table shows the average X-ray luminosity (L_X), the time-averaged jet power estimated from the environment (Q_j), the mass of the black hole ($M_{\rm BH}$), the total energy content(E_{tot}), the lifetime of the bubble (τ), and the minimum energy estimated from the radio counterpart of the nebulae (E_{min}). SS433 (Kirshner & Chevalier, 1980; Begelman et al., 1980; Dubner et al., 1998; Blundell et al., 2008; Perez M. & Blundell, 2009; Fabrika, 2004). S26 (Pakull et al., 2010; Soria et al., 2010b).IC10 X-1 (Lozinskaya & Moiseev, 2007; Bauer & Brandt, 2004). *Estimated using the fundamental plane.**This value was calculated using Eq. 4 using the parameters found by Dubner et al. (1998): a radius of ∼30 pc, a distance of 3 kpc, a radio flux density of 71 Jy at 1.4 GHz, and taking a spectral index of -0.48 between 85 MHz and 5 GHz. We note that this value is two orders of magnitude larger than that quoted by Dubner et al. (1998), however consistent with the value of Begelman et al. (1980).

estimated from the environment (Q_j), the mass of the black hole ($M_{\rm BH}$), the total energy content (E_{tot}), the lifetime of the bubble (τ), and the minimum energy estimated from the radio counterpart of the nebula (E_{min}).

The nebula around IC10 X-1 is sometimes considered to be the result of a hypernova event (Lozinskaya & Moiseev, 2007). However, its size is much larger than allowed by the surface brightness versus size (Σ-D) relation for explosive events, i.e. supernovae (Yang & Skillman, 1993), suggesting that it is powered, instead, by the central BH (Bauer & Brandt, 2004). S26 is another outlier source in the Σ-D relation and it has been revealed that the bubble is powered by a jet (Pakull et al., 2010; Soria et al., 2010b). Therefore, we will consider IC10 X-1 as a black hole powered nebula. We note that "black hole powered nebula" means there is a significant and continuing outflow from the central black hole powering the nebula and does not argue against the formation of the black hole in a SN explosion.

Considering S26, the X-ray photon index is $\Gamma = 1.4$ (Soria et al., 2010b), consistent with a source being in the hard state. However, no radio core was detected with a 3-σ upper limit of 0.03 mJy, which is one third of the peak intensity of IC342 X-1; and the total jet power of S26 is an order higher than for IC342 X-1 (Table 3). Using the fundamental plane (Eq. 7.9), we obtain an upper limit on the mass of $M \simeq (1.0 \pm 0.4) \times 10^7$ $M_\odot$. Given that $Q_j \propto \dot{M}$ in the hard state (Körding et al., 2006b, 2008b) and assuming similar accretion efficiencies for IC342 X-1 and S26; then one can speculate on the basis of the ratios of the jet powers that the average mass accretion rate of S26 is ∼15 times higher than that of IC342 X-1.

IC10 X-1 has an X-ray photon index of $\Gamma = 1.83$, potentially being in the hard state (Bauer & Brandt, 2004). Using the fundamental plane and adopting the average X-ray luminosity of 1.5×10^{38} erg s^{-1} and a mass of ~ 30 $M_\odot$ (Table 5.3), the expected core radio flux is then ~ 10 μJy at a distance of 0.7 Mpc. Thus, the source could be detectable with e-MERLIN or the EVLA.

5.3.5.1 Jet characteristics, accretion rates and efficiencies

In this and the following sections we investigate the possibility that the nebula around IC342 X-1 is powered by a jet and the consequences regarding the jet properties.

The elongated morphology of the nebula and its shock-ionized nature could be indicative of jet inflation. If the nebula is inflated by a jet, then the total power available in the bubble has to be equal with the time-averaged total jet power, ie. Q_j=L_{tot}, derived from the optical bubble (Pakull et al., 2010; Soria et al., 2010b) We note that calculating the jet power using the minimum energy (E_{min}) derived from the radio bubble would lead to an underestimation. One might account for the kinetic energy associated with the bulk motion of the jet as $E_j = (\gamma - 1)E_{min}$ in the case that the jet consists of an e^-e^+ plasma and a magnetic field. When accounting for one 'cold' proton for each relativistic electron: $E_j = (\gamma - 1)(E_{min} + Nm_pc^2)$ (Fender et al., 1999), where γ is the Lorentz factor and c is the speed of light. One would underestimate the total jet power required for E_j, because the second term's contribution with $2.6 \times 10^{-2}E_{min}$ is negligible, so the kinetic energy of the bulk motion would be only $E_j \simeq E_{min}$, using a Lorentz factor of $\gamma = 2 - 5$. This underestimation could be either due to a mild deviation from equipartition, resulting in $E_{radio,tot}/E_{min} = 10 - 100$ (eg. Paragi et al., 2010) or due to the fact that the kinetic power associated to the bulk motion is transferred to thermal ions also (Soria et al., 2010b).

In general, the total jet power is a constant fraction (f) of the available accretion power [however see Coriat et al. (2011) for possible variation of f]. Thus, we can write

$$Q_j = fQ_{acc} = f\dot{M}_{acc}c^2, \;\; f < 1 \tag{5.11}$$

where f is typically in the range of 10^{-3} to 10^{-1} (Falcke & Biermann, 1995, 1999).

Taking a constant rate of energy input that is characterized by the power of the jet, the rest-mass transport along the jet, $\dot{M}_j$, is (Kaiser & Alexander, 1997):

$$\dot{M}_j = \frac{Q_j}{(\gamma - 1)c^2} \tag{5.12}$$

Taking a minimum Lorentz factor of $\gamma = 2$ (Mirabel & Rodríguez, 1999; Fender, 2003), we find $\dot{M}_j \simeq 6.0 \times 10^{-8}$ $M_\odot$ yr^{-1} (3.8×10^{18} g s^{-1}).

Körding et al. (2008b) found that the total jet power could be estimated from the flux of the compact jet as:

$$Q_j \simeq 7.2 \times 10^{36} \left(\frac{L_{jet,radio}}{10^{30}\,\mathrm{erg\,s^{-1}}} \right)^{12/17} \mathrm{erg\,s^{-1}} \tag{5.13}$$

This relationship was found for FR I and FR II radio galaxies and scaled to Cyg X-1. [See Gallo et al. (2005) and Russell et al. (2007) for the jet power estimation of Cyg X-1]. Substituting the total jet power obtained from the optical nebula ($Q_j = 3.4 \times 10^{39}$ erg s^{-1}), we find that the expected average luminosity of the putative radio core would be 6.1×10^{33} erg s^{-1}. Not detecting a compact jet with an upper limit of 1.9×10^{33} erg s^{-1} could mean that either its flux is variable, and currently below our detection limit but with an average above, or the hard X-ray spectrum does not represent the canonical hard state of GBHBs.

In addition, it is possible to estimate the accretion rate, for hard state objects, based on the luminosity of the compact radio jet (Körding et al. (2006b, 2008b); and references therein):

$$\dot{M} \simeq 4 \times 10^{17} \left(\frac{L_{jet,radio}}{10^{30}\,\mathrm{erg\,s^{-1}}} \right)^{12/17} \mathrm{g\,s^{-1}} \tag{5.14}$$

For IC342 X-1, we obtain an upper limit, due to the fact that we do not detect a compact jet, of $\dot{M} \leq 8.2 \times 10^{19}$ g s^{-1} (1.3×10^{-6} $M_\odot$ yr^{-1}). This rate is close to the Eddington

rate for a $100M_{\odot}$ compact object. Comparing the accretion rate to the jet mass loss rate of $\dot{M}_j \simeq 3.8 \times 10^{18}$ g s^{-1} leads to the conclusion that the jet efficiency is $f \geq 0.046$. This would be a typical value for a jet efficiency and could be consistent with the assumption of Körding et al. (2008b) of f=10^{-1} for obtaining the relationship of Eq. 5.14.

Let us compare IC342 X-1 to the peculiar sources SS433 and GRS1915+105. The jet mass flow rate in SS433 is $\dot{M}_j = 5 \times 10^{-7}$ M$_{\odot}$ yr^{-1} and the available accretion rate is $\dot{M} = 10^{-4}$ M$_{\odot}$ yr^{-1} (Perez M. & Blundell, 2009; Fabrika, 2004), so the jet efficiency is $f = 5 \times 10^{-3}$, which is also within the typical range for black hole jets. Comparing the accretion rate of IC342 X-1 to SS433, we find $\dot{M}_{\rm IC342X-1}/\dot{M}_{\rm SS433} \geq 10^{-2}$. In contrast, the accretion rate of IC342 X-1 might be an order of magnitude higher than the rate of GRS 1915+105 of $\sim 10^{19}$ g s^{-1} (eg. Rushton et al., 2010). It is interesting to note that if one takes the lifetime of the surrounding bubble, and assumes a constant accretion rate (Begelman, 2002), the compact object in SS433 could accrete $\sim$20 M$_{\odot}$. During the lifetime of the nebula, the compact object in IC342 X-1 could accrete only $\leq$1 M$_{\odot}$. This comparison of accretion rates suggests that there is no need to invoke super-Eddington accretion for IC342 X-1 if the mass of black hole is above $\simeq$100 M$_{\odot}$.

5.4 Conclusions

I studied the radio and optical nebulae of three ULXs. One of these ULXs, IC342 X-1, is a newly discovered radio association.

- I confirmed that the radio spectra of the nebulae surrounding Ho II X-1 and NGC5408 X-1 are consistent with optically thin synchrotron emission.
- I estimated the energy needed to supply both the optical and radio nebulae around IC342 X-1. The energy needed, 6×10^{52} erg, is ~ 2 orders of magnitude higher than the explosion energy of a SN. By comparing the age of the bubble to the stellar environment, I found that the nebula is much younger, indicating that the nebula formation is not necessarily related to the formation of the black hole progenitor.
- I estimated that the minimum energy needed to power the radio nebula of IC342 X-1 is 9.2×10^{50} erg, at least an order of magnitude higher than those of Ho II X-1 and NGC5408 X-1. The fraction of energy carried by relativistic material is relatively high.
- In addition to discovery of a radio nebula around IC342 X-1, I found a radio component unresolved on VLA scales, that was not detected with VLBI. This puts an upper limit on the flux density of a compact jet. The ULX was found with a hard X-ray spectrum in observations spanning ~ 10 years. Use of the 'fundamental plane' of accreting black holes, which is valid for hard state objects, would place an upper limit on the mass of the black hole in IC342 X-1 of $(1.0 \pm 0.3) \times 10^3$ M$_{\odot}$.
- According to the above properties of IC342 X-1, I argued that the nebula is possibly inflated by a jet. I found that the calculated time averaged jet power, jet efficiency, and available accretion power could be consistent with that the nebula is inflated by a jet.

In summary, the energetics of the surrounding nebula along with the possible jet properties and accretion rate support the idea that the nebula surrounding IC342 X-1 could be an inflated bubble driven by the jets from the central black hole.

Another important point of my study was the attempt to link the ionization processes of these nebulae to the X-ray spectral behaviour of the ULXs. I showed examples for photoionization, shock-ionization and for the mixture of these two processes. For all kinds of ionization processes, there is an example where a radio counterpart is present. However, the morphologies of both optical and radio nebulae might reflect some connection with the central engine. One clear example could be Holmberg II X-1. For instance, Gladstone et al. (2009) suggests that the source is in the "ultraluminous" state, ie. soft excess in a high/soft X-ray state, which is reminiscent of high or super-Eddington accretion or Compton thick accretion. As mentioned in Chapter 1, usually super-Eddington disks generate winds that are channelled along the poles, and may form jets/outflows (Begelman, 1979). It has also been recently found for Galactic BH binaries (GBHBs), that equatorial winds are associated with their thermal dominant X-ray state (Neilsen & Lee, 2009; Ponti et al., 2012). So it might be a viable explanation that the thermal component of the X-ray spectrum of Holmberg II X-1 is also linked to the inner velocity structure of the nebula, i.e. the thermal component might be due to winds. To test this hypothesis, I have submitted a high-resolution EVLA proposal to directly image the putative outflow.

6

Ongoing Work on ULX Radio Surveys – an Extragalactic Microquasar Found?

Contents

In this Chapter, I present results of new and archival radio data analysis aiming to detect new radio counterparts of known ULXs. To this purpose, I proposed an ATCA survey on a volume limited sample to detect radio bubbles around ULXs and to detect possible compact jets. This resulted in the strongest flux upper limits on the presence of radio bubbles. Additionally, partial analysis of the ATCA survey data revealed a new peculiar source in NGC 247. I present archival XMM-Newton, Chandra, and Hubble observations of this new source to discuss its nature.

6.1 Radio Surveys

To date, there have been no systematic radio surveys looking for ULXs. However, there were a couple of cross-correlation made between some ROSAT and XMM-Newton ULXs and the FIRST VLA catalog, and between some Chandra ULXs and the FIRST catalog (Sánchez-Sutil et al., 2006; Pérez-Ramírez et al., 2011). Given that the FIRST catalog has a sensitivity at a level of 1 mJy and a resolution of 5 arcsec, and given the relatively large PSF of ROSAT and XMM-Newton, these correlations did not reveal any firm counterparts (Sánchez-Sutil et al., 2006; Soria et al., 2006b; Mezcua & Lobanov, 2011). In fact, within the handful of matches found, all have a position discrepancy from 1.5 arcsec to 5 arcsec. This is relatively large compared to the size of an extended radio bubble of about 2 arcmin (see previous Chapter). It is also worth noting that all the firm radio counterparts found to date have a total flux density at or below 1-mJy. This prompted the need for systematic radio surveys on ULXs.

Sensitive radio surveys are now possible with the e-MERLIN, EVLA and ATCA broadband receiver upgrades, providing a factor of 10 or better sensitivity. Additionally, e-MERLIN has a much better angular resolution than ATCA or EVLA in the centimeter bands. One of the e-MERLIN Legacy projects, called LEMMINGs, includes a survey of nearby galaxies (including ULXs), but given the delay in e-MERLIN commissioning, it has not yet provided results. This motivated us to propose a volume limited sample survey on nearby ULXs as complementary to the LEMMINGs survey. This proposal was submitted to EVLA and ATCA to cover Northern and Southern hemispheres, and I am the PI of the ATCA proposal. The proposed survey involves using the EVLA and ATCA in their highest resolution configuration to improve the possible astrometry matches compared to FIRST, and it only involves ULXs with a XMM-Newton (and Chandra) position.

The project aims to detect ULX radio bubbles, and possible compact jets and/or flares from ULXs. Our sample is drawn from Winter et al. (2006), who examined archival XMM-Newton data to construct a sample of ULXs within 4 Mpc. They required XMM-Newton integration times greater than 10 ksec in order to fit the X-ray spectra of the candidates accurately, and reached a sample of 32 galaxies (including some with no ULX). The X-ray spectra were used to evaluate whether the candidates were formally ULXs in either a "high state" (luminous, thermal-dominated spectrum, accretion presumably near the Eddington limit) or in a "low state" (less luminous, power-law spectrum, sub-Eddington sources), which might be analogous to the high/soft and the low/hard state of individual Galactic BH binaries. To further justify this inclusion, different epochs of XMM-Newton data for the source in Holmberg II show it to be a high-state ULX at one time and a low-state ULX at another. Of the 32 galaxies in the Winter et al. (2006) sample, 4 contain ULXs or candidate ULXs and lie at negative declinations, meaning that they are good targets for the ATCA. These 4 galaxies provide a sample of 10 ULXs for ATCA observation, including 8 high-state ULXs, and 2 low-state ULXs.

Additionally, during my PhD, I was continuously reducing archival radio data to hunt for radio counterparts of known ULX optical bubbles. This was done in a way that I reduced and analyzed several data sets, which involves the position of the ULX within half of the primary beam. These individual archival data sets were stacked together to reach the best sensitivity.

6.2 Results and Discussion

This archival search and the partial analysis of the ATCA survey led to strongest upper limits on radio flux, that I summarize in Table 6.1.

Table 6.1: Summary of radio counterparts of ULXs

Source	Distance	Optical Neb.	Ionization Process	Radio Neb.	S_{5GHz} or 3-σ limit	Ref.
	Mpc				μJy	
IC342 X-1	3.9	Y	S	Y	2 mJy	1, Chap. 5
Holmberg II X-1	3.4	Y	P	Y	610	1,2, Chap. 5
NGC5408 X-1	4.8	Y	P	Y	220	1,3, Chap. 5
MF16	5.1	Y	S	Y	740	4
Holmberg IX X-1	3.6	Y	S	N	<20	Archive
M81 X-6	3.63	Y	P	-	-	-
M101 ULX-1	7.2	Y	S	N	<30	Archive
NGC1313 X-1	3.7	Y	P	N	<100	Archive
NGC1313 X-2	3.7	Y	S	N	<100	Archive
NGC5204 X-1	4.3	Y	S	N	<50	Archive
NGC4559 X-7	9.7	Y	P?	-	-	-
NGC4559 X-10	9.7	Y	S	-	-	-
ESO243-49 HLX-1	95	N	-	Flare	50	5, Chap. 7
M82 X-1	3.5	N	-	N	<48	Archive
NGC247 XMM1	3.4	N	-	N	<30	Survey
NGC247 XMM2	3.4	N	-	N	<30	Survey
NGC247 XMM3	3.4	N	-	N	<30	Survey
Circinus XMM1	4	N	-	N	<330	Archive
Circinus XMM2	4	N	-	N	<1.2 mJy	Archive

The first three sources are already presented in the previous Chapter. The last part of the table shows ULXs with no optical bubbles. The rest of the sources presented in this table have emission-line optical nebula (Pakull & Mirioni, 2002, 2003; Abolmasov et al., 2007; Russell et al., 2011b; Tao et al., 2011, and references therein). Additionally, I also show HLX-1 (see next Chapter) in this table. MF16 is a nebula around NGC6946 ULX-1, M81 X-6 is also known as NGC3031 X-11 (and M81 X-9?). References: 1 (Cseh et al., 2012), 2 (Miller et al., 2005), 3 (Kaaret et al., 2003), 4 (van Dyk et al., 1994), 5 (Webb et al., 2012).

This survey was partially motivated to understand why some optical nebulae do not have any strong radio counterpart. As seen from Table 6.1., it cannot be said that a significant number do not have such a counterpart. The most natural explanation could be the limitation of the detection threshold. On the other hand, this might not be a viable answer in view of the strong upper limits that resulted from my archival analysis (and the survey). Comparing the fluxes of detected radio bubbles of > 200 μJy to the average upper limit obtained of about 50 μJy, might suggest that these radio counterparts do not exist. However, given the low number of the sources in the sample, this statement is statistically irrelevant at this stage. But for the time being, one might assume that the above statement is correct. Then the question becomes what could be the reasons for the non-existence of radio bubbles, and bubbles in general.

Probably the most relevant parameter to form a bubble is the initial density of the interstellar medium (ISM). If this density is relatively low at the beginning of the active lifetime of the ULX, then it is possible that it will not develop a bubble. Or perhaps it will develop a bubble with a short life time. Alternatively, some of the ULXs could be too young to witness a developed bubble, sustained either by photo- or shock-ionization. It could be also possible that certain ULXs are different from each other, meaning that certain class of ULXs never enter a jet dominated phase. This could be tested by the fractional number of shock-ionized bubbles of a larger sample. However, this latter explanation might be too speculative, given that we do not have good knowledge from bubbles of either GBHBs (or ULXs). Similarly, from about of 25 known GBHB, there are

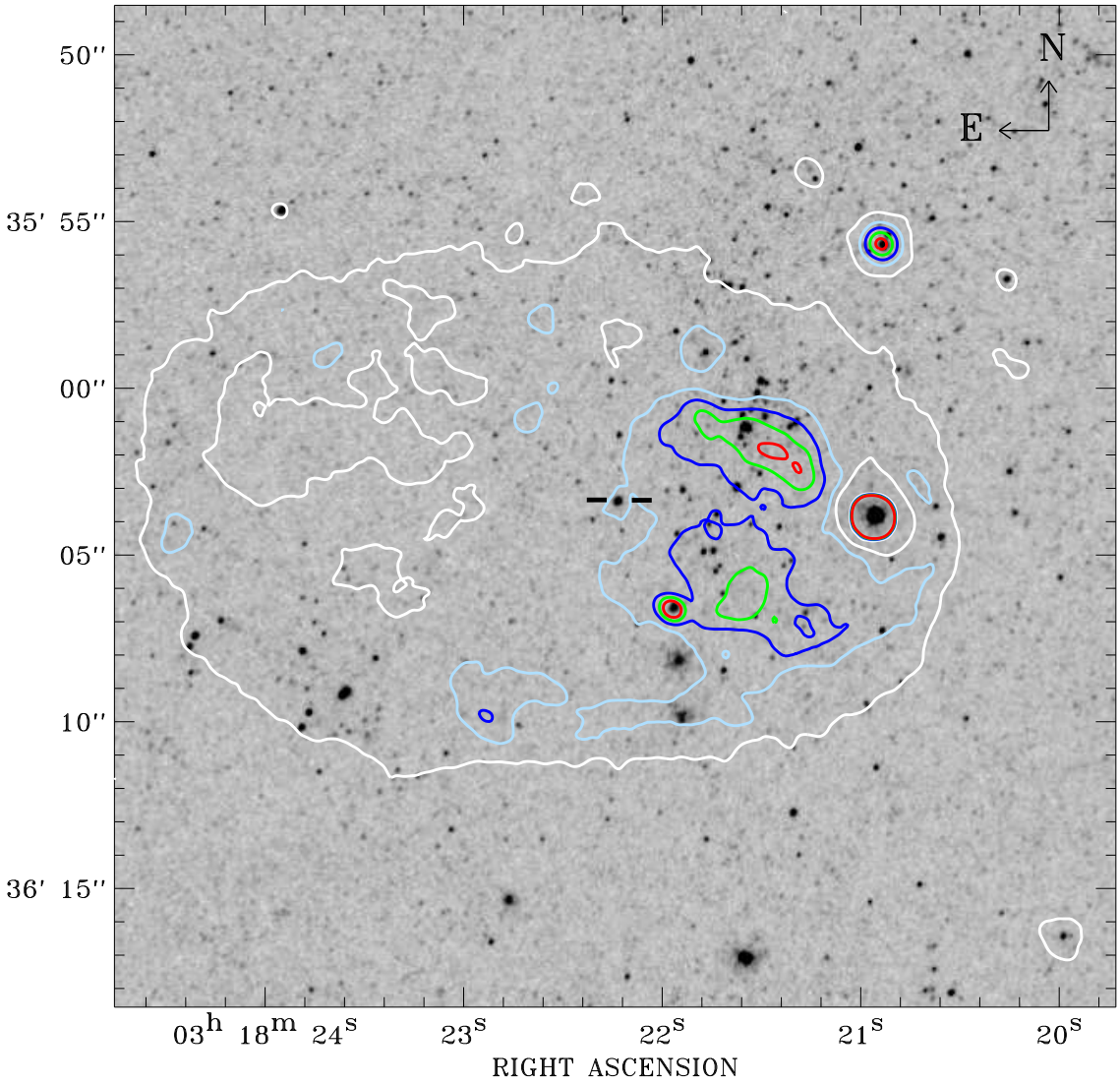

Figure 6.1: The figure is taken from (Grisé et al., 2008) and shows the HST image of the optical nebula around NGC1313 X-2, using the F345W filter. 1″ corresponds to 19.4 pc. The ULX counterpart is the bright point-like source at the center of the image. Contours of the Hα emission (at 10, 30, 50, 70 and 90% flux level above the background) are overplotted. The blue contours represent two young stellar associations.

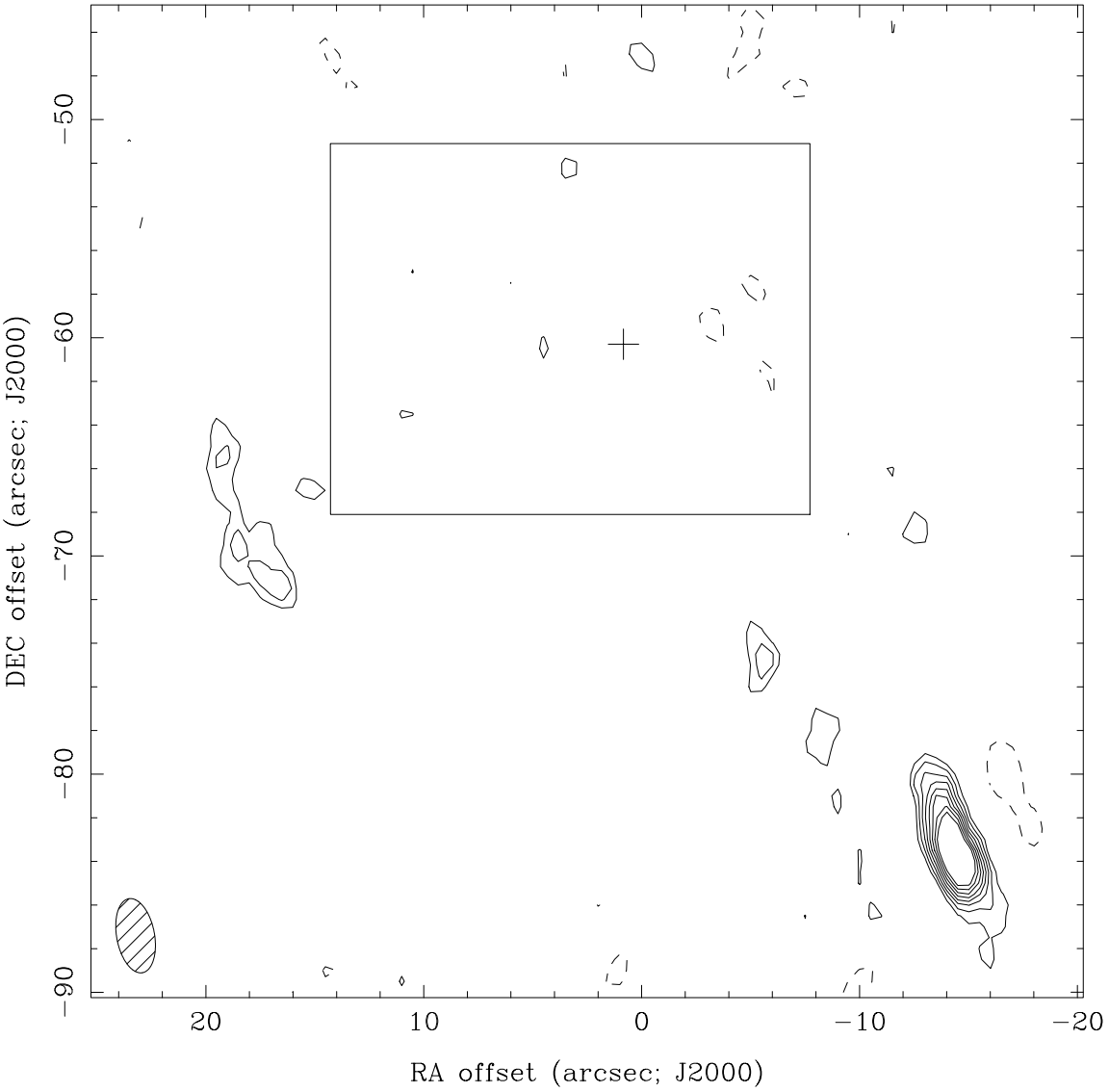

Figure 6.2: The 5&9 GHz naturally weighted ATCA image showing the vicinity of the optical nebula around NGC1313 X-2. The location of the optical nebula (see Fig. 6.1) is indicated by the ractangle, the cross marks the position of the ULX. Contours represent radio emission at levels of 3, 4, 5, 6, 7, 8, 9 and 10 times the rms noise level of 30 μJy beam^{-1} (see Table 6.1).

only a few examples where the source is surrounded by a bubble. These are LMC X-1 (Pakull & Angebault, 1986), SS433, and Cyg X-1. These sources reside in relatively dense regions of the Galaxy, so the importance of the initial density of the ISM might be supported. However, we might face even bigger difficulties when we take into account the fact that SS433 is thought to be a super-Eddington accretor (Fabrika, 2004) and Cyg X-1 is not. Furthermore, there is no synchrotron radio bubble around Cyg X-1, just a shock front which is aligned with the major axis of the compact jet (Gallo et al., 2005).

Taking the example of the optical bubble around NGC1313 X-2 (see Figure 6.1.), that has a size of > 400 pc (Pakull & Mirioni, 2002), it might suggest that the bubble is too large, and hence too old. If ULXs are at an old age, then one might not see any radio counterpart – as shown in Fig. 6.2 – because they could already be cooled.

I showed that radio bubbles are present regardless of the dominant ionization process of the optical bubble. Here, I would conclude that we do not have enough sources from the standard GBHB class that show associated optical or radio bubbles (Cseh et al., 2012). One might take into account sources from outside the Galaxy to compare with ULXs, but then we would have to face the same sensitivity limitations. There are at least two examples, S26 and the bubble around IC 10 X-1, as presented in the previous chapter. These cases are unclear. For instance, the mass of the black hole in S26 is unknown. It is also unknown whether it is an extragalactic microquasar, a more massive black hole (e.g. 100 $M_\odot$) with obscured X-ray luminosity, or perhaps represents a new class of ultra-powerful sources (UPSs), as presented by C. Motch at the Athena Paris Day in February 2012. Similarly, IC 10 X-1 is sometimes thought to be a hypernova remnant and it might have a more massive black hole of 23-34 $M_\odot$, which might complicate the picture. These sources might be different due to their environment, or might indeed fall in the class of UPSs due to a more massive black hole, and/or might represent a stellar evolution that is not well known to date; similar to the stellar evolution of the progenitor of a ULX or an IMBH.

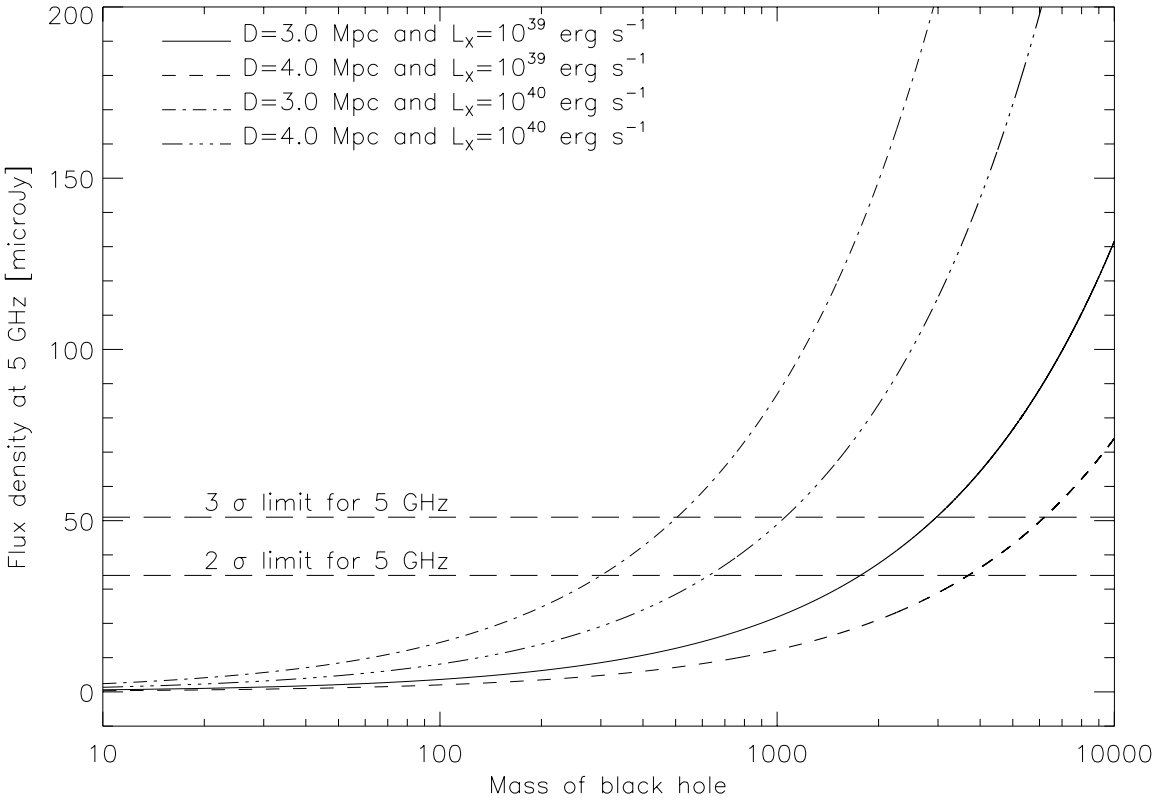

Figure 6.3: Predicted radio flux densities for nearby ULXs using the fundamental plane.

Turning to jets and flares, there is no ULX associated with a compact jet or flare, with the exception of HLX-1 (see next Chapter). Figure 6.3. shows the expected radio flux densities at 5 GHz for nearby ULXs as a function of black hole mass using the fundamental plane. Applying the radio upper limits above, one might conclude that ULXs with black hole masses of 10^4 $M_\odot$ can be ruled out. However, caution needs to be taken here, as the X-ray and radio luminosities are not measured simultaneously, which might intro-

duce an even larger error than the intrinsic scatter of of 0.12 dex within the fundamental plane. Therefore, the deduced mass limits might be accurate to an order of magnitude. Moreover, it is still not clear whether ULXs follow the same phenomenology as GBHBs, and if they have X-ray hard state (see HLX-1 in next Chapter). Unfortunately, this limit still involves the definition of an IMBH at the upper end of the mass range of 10^5 $M_\odot$, although, in several cases the radio upper limit of 20-30 μJy already implies an upper limit on the black hole mass of 10^3 $M_\odot$. The limit of 10^3 $M_\odot$ might imply lower ULX masses than previously thought. However, any statements must be reserved until after the full analysis of the EVLA and ATCA survey is complete, because at the moment we lack good statistics with the few number of sources we have.

6.3 Data Analysis of a Radio Source Found in the ATCA Survey

Deep surveys are valuable not just because of their systematic nature, but also, sometimes they might reveal previously unknown sources. In the following, I will describe my work on a new radio source found in the survey sample, in NGC 247, which is a spiral galaxy at a distance of 3.4 Mpc. Note that, the Hubble data reduction part, the X-ray spectral fitting part, and the source interpretation benefited from discussions with F. Grise and S. Farrell.

6.3.1 ATCA Observation

We obtained deep dual-frequency ATCA CABB (Compact Array Broadband Backend) (Wilson et al., 2011) observations of NGC 247, as part of the radio survey. The CABB-upgraded ATCA allowed us to reach unprecedented noise levels in the field. ATCA was in 6A configuration (it's highest resolution mode). The observation was made on 2011 Dec 15 (program code: C2588, PI: Cseh). The data were obtained simultaneously at 5.5 & 9 GHz with 12 h integration time. We observed in phase-reference mode; the phase calibrator was 0116-219 and the primary calibrator was PKS 1934-638. The data reduction was performed using the MIRIAD software package (Sault et al., 1995). After the individual analysis of the separate bands, I also combined the 5 GHz and 9 GHz images in order to enhance sensitivity.

I fitted the source with a point source model at 5&9 GHz, 5 GHz and 9 GHz. The measured flux densities are 106 ± 13 μJy, 112 ± 20 μJy, 60 ± 19 μJy, respectively. The corresponding two-point spectral index is $-1.24^{+0.94}_{-1.09}$, $S \sim \nu^{\alpha}$. I also obtained the position of the source at a location of RA=00h47m03.31s, Decl.= -20°45'46.21" (J2000.0), with a positional error of 0.12" in RA and 0.48" in Decl. The 5-GHz flux would correspond to a radio luminosity of 7.3×10^{33} erg s^{-1} at a distance of 3.4 Mpc.

6.3.2 Archival Search in Existing Catalogs

I first searched in general catalogs like NED and Simbad, that resulted in no matches. Then I searched in X-ray catalogs, and the source was found in the Second ROSAT PSPC, if the PSF of 10" is taken into account. The source was also found in the XMM-Newton archive, if a search radius of 1.5" is taken into account. The source was not found at any other wavelength covering radio to UV, in other existing catalogs. In summary, this source is first detected in radio and has a possible X-ray counterpart.

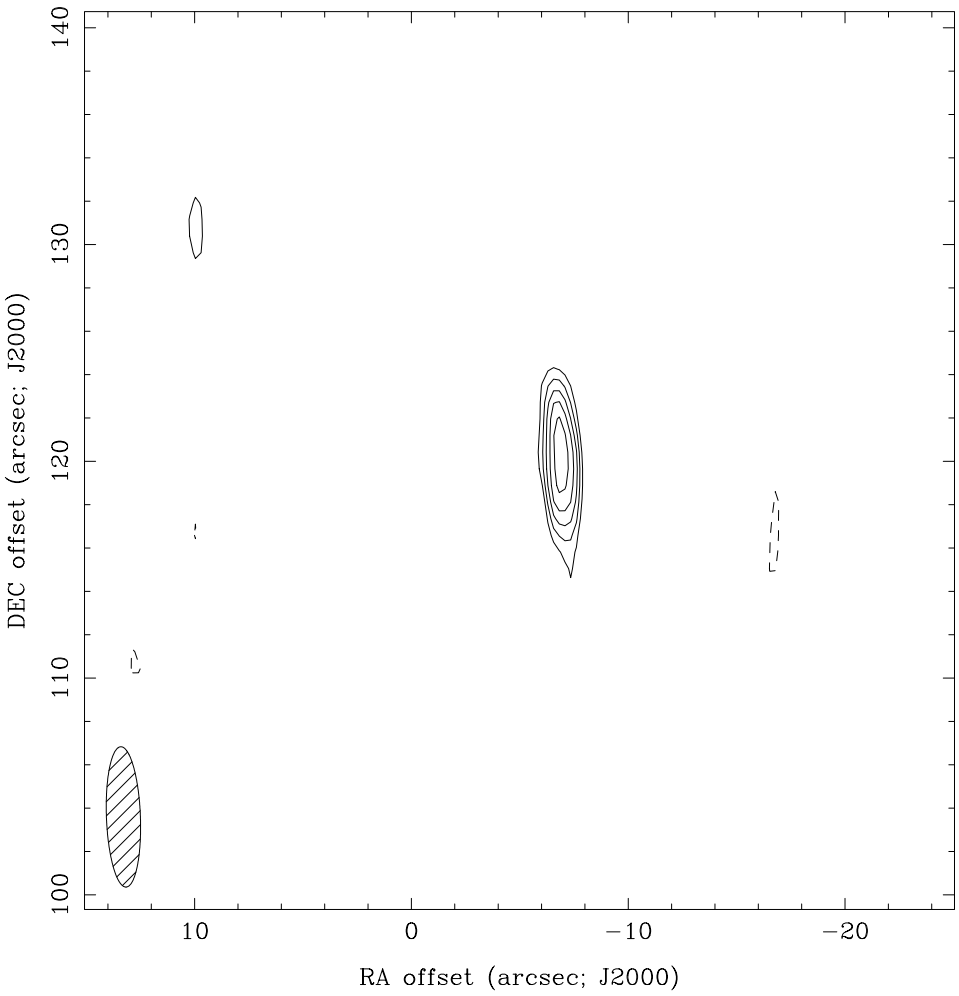

Figure 6.4: The 5&9 GHz ATCA 6A-array image of the source. Contours represent radio emission at levels of 3, 4, 5, 6, 7 and 8 times the rms noise level of 12 μJy beam^{-1}. The peak brightness is 91 μJy beam^{-1}. The image was made using natural weighting and the resolution is $6.5" \times 1.6"$ at PA=2°.

I found and analyzed two archival XMM-Newton data sets and a recent, archival Chandra observation. Given that faint sources are probably not in catalogs, I also analyzed the deepest Hubble observation available in the archive.

6.3.3 XMM-Newton

The first observation was performed on 2009 Dec 27 (PI: H. Feng), lasting for about 35 ks, with the prime full window for the three cameras. The analysis of this data was partially done before by Jin et al. (2011). However, in order to gain X-ray spectral information on the source, I reanalyzed the full data set and extracted the spectrum of the source following standard procedures [1]. In this observation, the thin filter was chosen for the PN and medium filter for the MOS. Event lists were created from the observation data files using SAS with recent calibrations. To minimize background contamination, I selected good time intervals (GTIs) where the 10-15 keV count rate of the whole CCD was lower

[1] http://xmm.esac.esa.int/sas/current/documentation/threads/

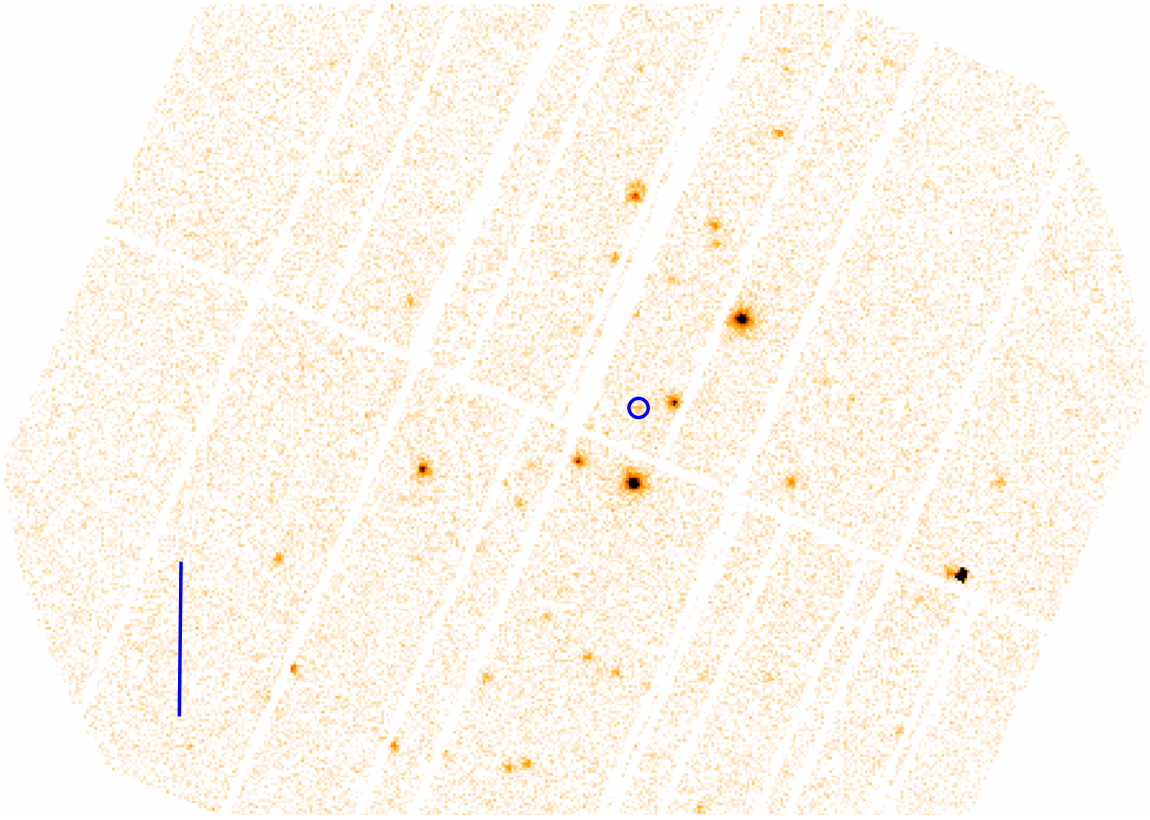

Figure 6.5: XMM-Newton EPIC PN image of the source in the 0.2-12 keV band with pixel size of 4 arcsec. The line in the bottom left corner has a size of 4 arcmin. The north direction is up.

than 0.5 for the MOS and 1.5 for the PN. This resulted in 23 ks of clean exposure for the PN and 31 ks for the MOS.

Images in five energy bands, 0.2-0.5 keV, 0.5-1 keV, 1-2 keV, 2-4.5 keV, and 4.5-12 keV were created for each CCD with a pixel size of 4.0" from events with FLAG = 0 and PATTERN $\leq$ 4 for the PN or PATTERN $\leq$ 12 for the MOS. The **edetect chain** tool was used to detect point sources simultaneously on the images. I detected the source on PN and MOS2, but not on MOS1. Jin et al. (2011) report the detection of the source under source number 33. They performed an astrometric correction and provide the source position as RA=00h47m03.23s, Decl.= -20°45'45.9" (J2000.0) with an error of 1.2 arcsec. I find a match in position within the error of 1.5 arcsec provided by **edetect chain** tool. The position reported by Jin et al. (2011) is consistent with the radio position within the $1-\sigma$ error.

The extraction radius is smaller than usual for PN sources, but this is necessary given the crowded field. The 80 per cent encircled power radius is $\sim$ 25 arcsec [2] so, the measured source fluxes were increased by a factor of 1.2 to account for the flux outside the extraction region. The source was detected with 127 total counts in 22.85 ks, corresponding to an average count rate of 0.00555. The obtained flux, using **edetect chain**, in the 0.2-12 keV band is $(1.46 \pm 0.48) \times 10^{-14}$ erg cm^{-2} s^{-1}, including the flux correction indicated above. This value is consistent with the values reported by Jin et al. (2011).

The second data set was observed on 2001 July 08 (PI: M. Watson) with 17 ks. The

[2] http://xmm.esa.int/external/xmm_user_support/documentation/uhb_2.5/node17.html

thin filter was chosen for the PN and also for the MOS. Due to strong background flares during the observation, the resulted GTIs were 1.6 ks for the PN and 5.6 ks for the MOS. I selected GTIs with a count rate lower than 1.5 for the PN and lower than 0.35 for the MOS. Source detection was performed as described above. Due to the small GTIs, I did not detect the source, either on PN or on MOS cameras.

6.3.4 X-ray Spectral Fitting

Due to the thin filter on the PN, the number of photons detected with the PN is about 2 times that with MOS2. I used both the PN and MOS data for spectral analysis. The energy spectrum was extracted in the 0.3-10 keV band from events in a 25″-radius circular region due to a crowded field with FLAG and PATTERN the same as those used in creating the image. The background was subtracted from events in a nearby circular region with a radius of 45″ on the same CCD at a similar distance from the CCD center.

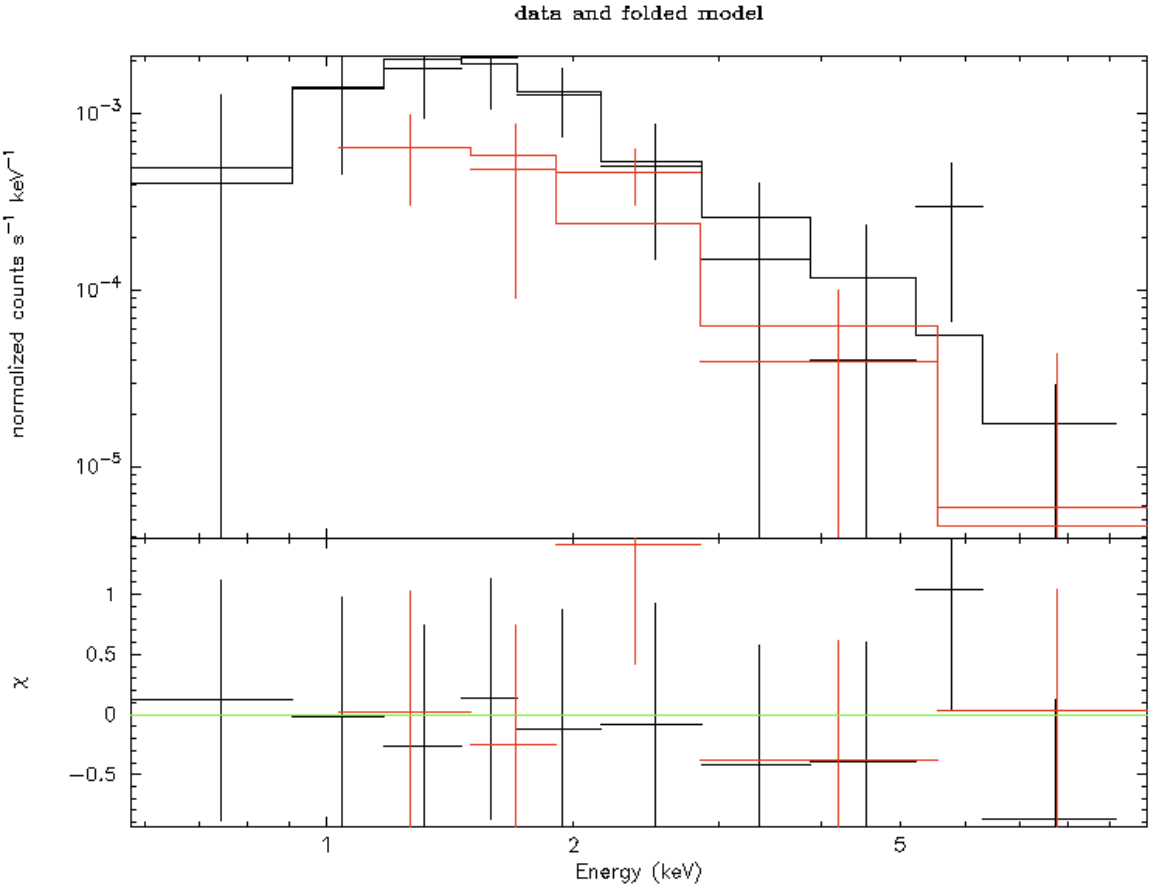

Figure 6.6: The PN and MOS spectra fitted with an absorbed powerlaw

I fitted the PN and MOS spectra simultaneously, using the XSPEC (Arnaud, 1996) spectral fitting tool (Fig. 6.6.). I grouped the spectra with a minimum of 20 counts as needed for χ^2 statistics and I used the Wilms abundances (Wilms et al., 2000).

Fitting the spectrum in the 0.3-12 keV band, with an absorbed (PHABS) power-law, leads to a good fit with $\chi^2/\mathrm{DoF} = 4.5/12$ with a photon index of $\Gamma = 2.94^{+3.50}_{-0.44}$ and an equivalent hydrogen absorption column density of $N_{\mathrm{H}} = 1.4^{+2.9}_{-1.1} \times 10^{22}$ cm^{-2}. The

absorbed flux in the 0.3-12 keV band was 1.4×10^{-14} erg cm^{-2} s^{-1}. The unabsorbed flux is 7.9 $\times10^{-14}$ erg cm^{-2} s^{-1}, corresponding to an unabsorbed luminosity of 1.0×10^{38} erg s^{-1} in the 0.3-12 keV band at a distance of 3.4 Mpc.

I use WebPIMMS to obtain upper limits on the PN flux for the second data set. WebPIMMS requires that the input count rate is from an extraction radius of 15" (roughly 72% of the total counts) [3]. The total counts found at the position of the source is 13. This transfers to total counts of 27.91, which corresponds to a 0.9987 confidence, i.e. to a 3-σ upper limit (Gehrels, 1986). The corresponding upper limit on the average count rate is 0.017 counts per second. Using the Galactic hydrogen column density calculator[4], towards the source, I obtain $N_H = 1.55 \times 10^{20}$ cm^{-2}. This is negligible compared to the intrinsic column density obtained from the X-ray fit. Assuming an intrinsic column density and a power-law photon index obtained from the spectral fit, the 3-σ upper limit on the flux at the source location in the 0.3-12 keV band is 6.8×10^{-14} erg cm^{-2} s^{-1} and the unabsorbed flux limit is 4.4×10^{-13} erg cm^{-2} s^{-1}. Using the same inputs, a face value on the net counts would correspond to a flux of 3.3×10^{-14} erg cm^{-2} s^{-1} and to an unabsorbed flux of 2.1×10^{-13} erg cm^{-2} s^{-1}. This limit is at least a factor of three above the flux deduced from the X-ray fit.

6.3.5 Chandra

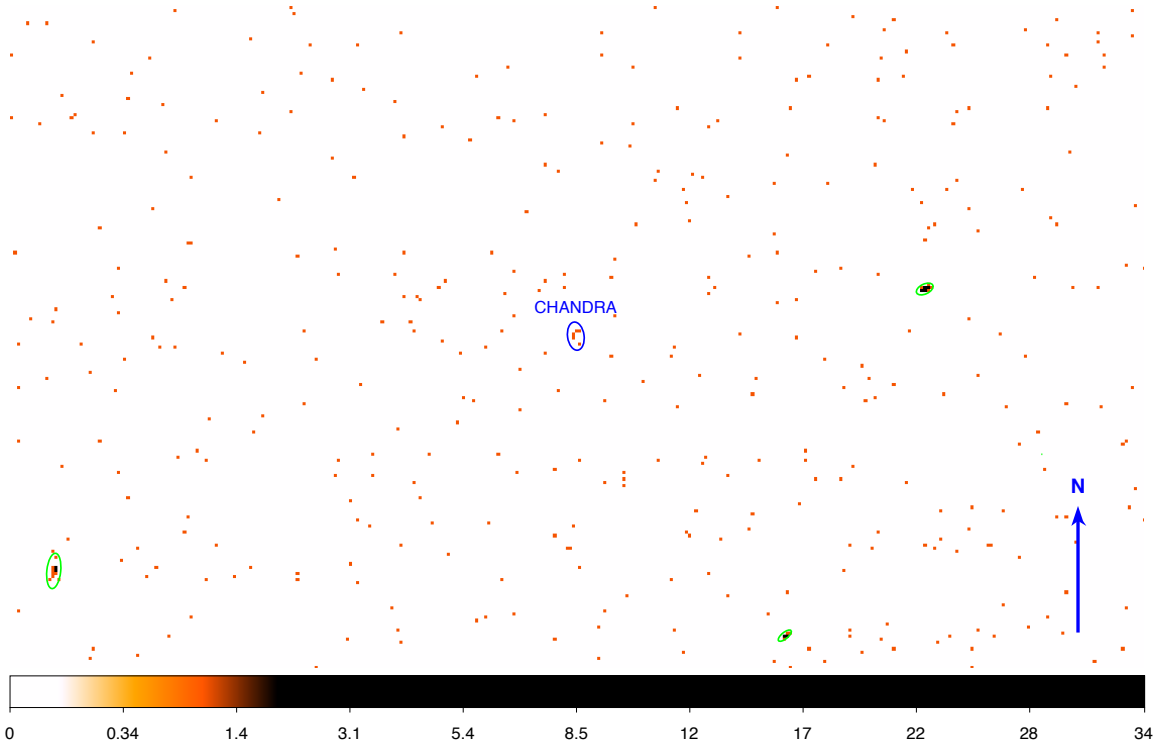

Figure 6.7: Chandra X-ray image of the source in the 0.3-10 keV band with pixel size of 0.5 arcsec. The color-scale indicates X-ray intensity and ranges from 0 to 34 counts per pixel. The arrow points to North and has a size of 20 arcsecond

[3] http://xmm.esac.esa.int/external/xmm_products/slew_survey/upper_limit/UpperLimitServer_userguide.shtml
[4] http://cxc.harvard.edu/toolkit/colden.jsp

NGC 247 was observed with the Chandra X-Ray Observatory using the Advanced CCD Imaging Spectrometer spectroscopy array (ACIS-S) in imaging mode. The Chandra observation (ObsID 12437; PI H. Feng) began on 2011 Feb 01 14:31:09 UT and had a useful exposure of 5 ks.

The Chandra data were subjected to standard data processing (CIAO version 4.3 using CALDB version 4.4.6). I checked for background flares on the S3 chip in the 0.3-10 keV band using a nearby region with a radius of 50 arcsec and found that there were no strong background flares.

I then constructed images of the S3 chip with a pixel size of 0.5 arcsec in the 0.3-10 keV bands. I searched for sources in the 0.3-7 keV band following standard procedures[5], using the **wavedetect** tool in CIAO with an exposure map created by the **fluximage script**. The source was detected at RA=00h47m03.28s, Decl.= -20°45'45.89'' (J2000.0) with a positional error of 0.33 arcsec with a total of 5 counts at a S/N level of 2.5. This position is consistent with the radio and XMM-Newton position within the errors.

The Chandra source had an average count rate of 0.001 in the 0.3-7 keV band. Using WebPIMMS, with the same photon index and column density as above, the predicted flux in the 0.3-12 keV is 9.4×10^{-15} erg cm^{-2} s^{-1} and the unabsorbed flux is 6.0×10^{-14} erg cm^{-2} s^{-1}. This would correspond to an unabsorbed luminosity of 8.3×10^{37} erg s^{-1} in the 0.3-12 keV band at a distance of 3.4 Mpc. This value is consistent with the flux obtained from the X-ray fit of the XMM data.

6.3.6 ROSAT

I found a nearby ROSAT source, cataloged as 2RXPJ004703.4-204544, with a count rate of $(1.5 \pm 0.6) \times 10^{-3}$ cts/s obtained with the PSPC instrument. Given that the ROSAT is sensitive in the 0.3-2.4 keV band, I fitted the XMM spectra in this band. Using WebPIMMS, with the obtained photon index of 2.6 and hydrogen column density of 1.2×10^{22} cm^{-2}, the predicted flux is $(1.0 \pm 4.1) \times 10^{-13}$ erg cm^{-2} s^{-1}, and the unabsorbed flux $(3.8 \pm 1.5) \times 10^{-13}$ erg cm^{-2} s^{-1}, in the 0.3-12 keV band. This would correspond to an unabsorbed luminosity of 5.3×10^{38} erg s^{-1} in the 0.3-12 keV band at a distance of 3.4 Mpc. However, as the ROSAT band significantly differs from the band of XMM-Newton, it is not clear whether the extrapolation is correct.

6.3.7 Hubble

Given the small error on the Chandra X-ray position and a good match with the ATCA position, I attempted to find an optical counterpart of the source using archival Hubble data.

First, I retrieved Level 5 file (ObsID 10915) made with the Advanced Camera for Surveys (ACS) using the F814W filter, from the Hubble Legacy Archive (HLA)[6]. During the pipeline calibration, after drizzling, the geometric distortion is removed but the sky remains flat so both surface and point-source relative photometry are correct in the resulting files. The photometric zero point in the header allows conversion from electrons/seconds to absolute flux units [7]. The flux scale corresponds to 7.07236×10^{-20} erg cm^2 Ang^{-1} electron^{-1}, the pivot wavelength is 8059.75 Å, and the total exposure was 1534 sec.

[5] http://cxc.harvard.edu/ciao4.4/threads/wavdetect/

[6] http://hla.stsci.edu/

[7] http://www.stsci.edu/hst/HST_overview/instruments

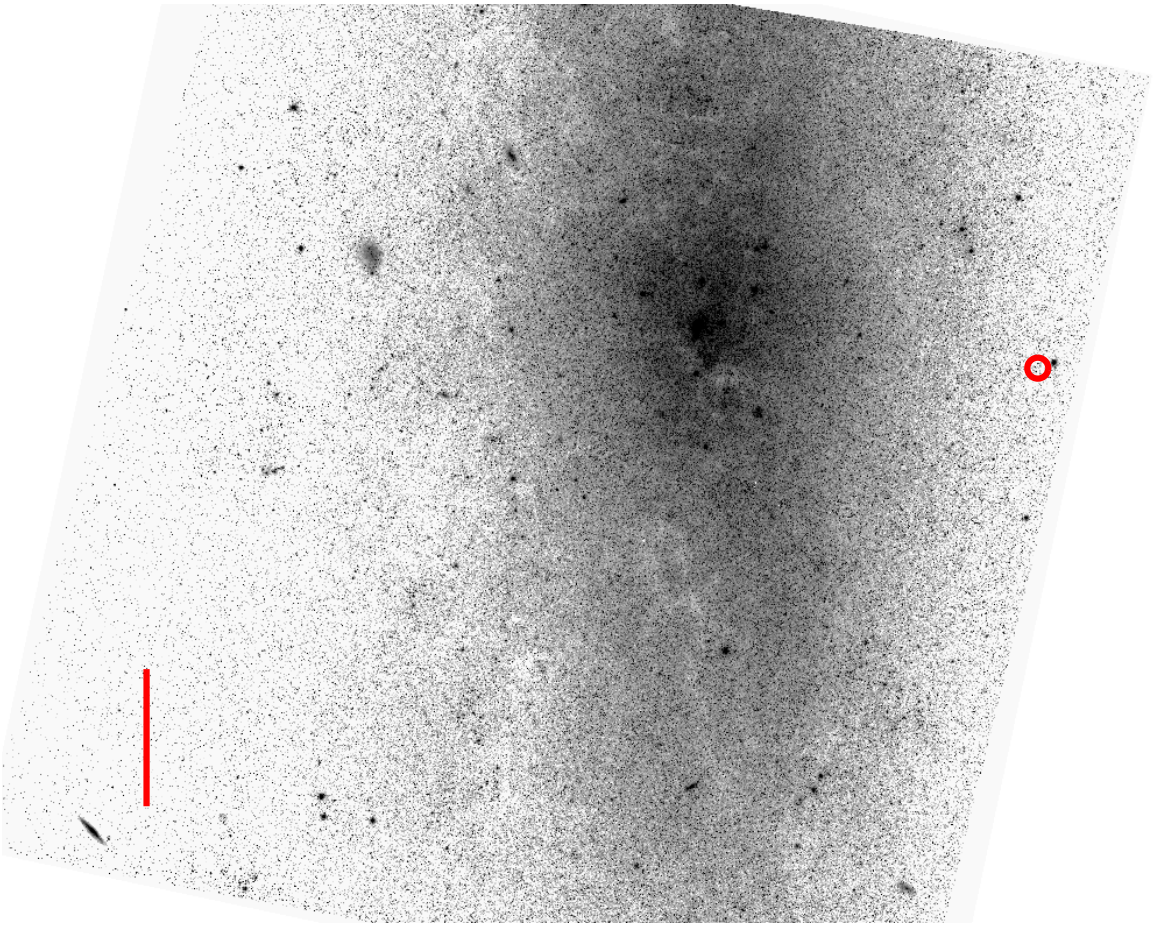

Figure 6.8: Hubble image of NGC247. The line in the bottom left corner has a size of 29.5 arcsec. The red circle to the right indicates the location of the source of interest. The north direction is up.

Fig. 6.8 indicates the location of the source with respect to the core of NGC 247. Figure 6.9 shows the nearby region of the source of interest with the ATCA and Chandra positions. The intercept region of the two error circles might indicate an optical point-like counterpart at the location of the source of interest.

I performed photometry on the above source. The zero point for F814W is ABmag= 25.51994 and STmag=26.78213, for observations after 2006 July 4 [8]. Note that, the 10-σ point-source detection limit is ABmag=25.8 for the F814W filter. Using the IRAF DAOPHOT package, I determine the FWHM of the PSF as 2 pixels, which is a typical value for HST; this represents an enclosed energy of 0.603 (Sirianni et al., 2005). The aperture correction (AC) from 0.5" to infinity is 0.087 ± 0.001 and at a pivot wavelength of 8069 Å, AC_λ=0.54 (Sirianni et al., 2005). Using DAOPHOT with a radius of 0.1", I find an instrumental magnitude (Imag) of the source of 16.41 ± 0.06. Then I use the following equation to calculate the OB magnitude:

$$OBmag = -2.5 \log(10^{-(Imag/2.5/Exposure)}) - AC - AC_\lambda. \quad (6.1)$$

I find OBmag=-1.25. One need to add the corresponding zero point to obtain the magnitudes: $M_{814W} = OBmag + ZPT$. So the Vega magnitude is $M_{814W} = 24.27 \pm 0.06$ and

[8] http://www.stsci.edu/hst/acs/analysis/zeropoints

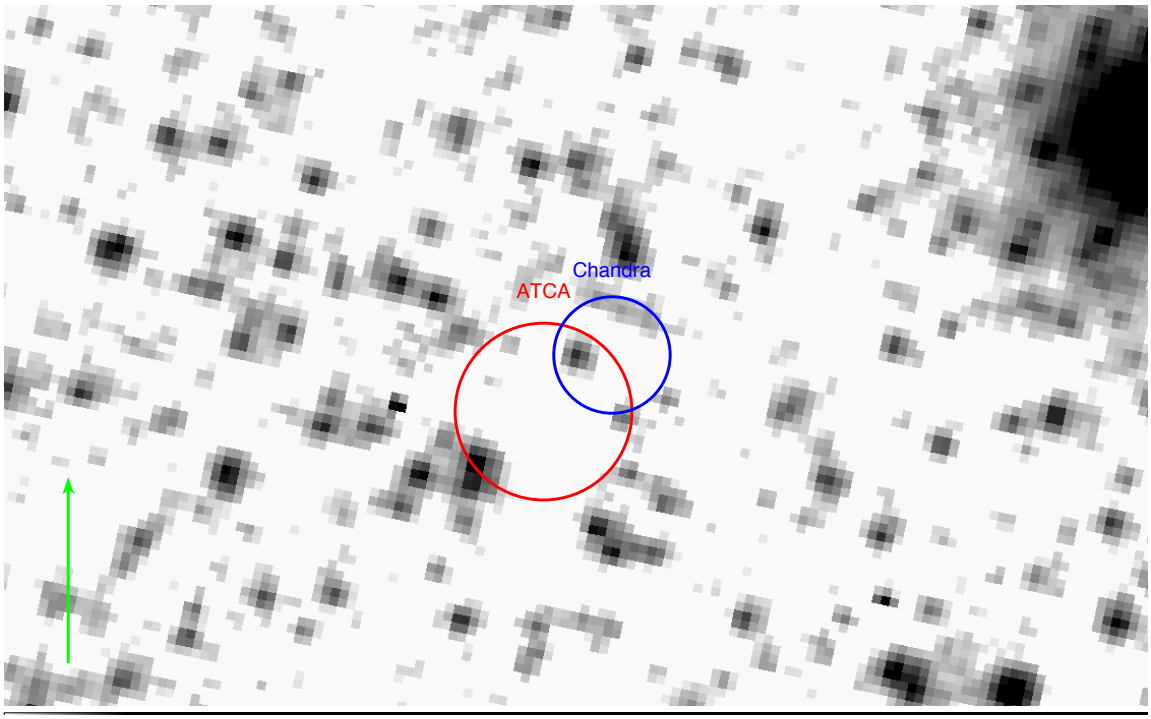

Figure 6.9: Hubble image of the source of interest. The line has a size of 1 arcsec and points towards the North direction. The ATCA and the Chandra positions with error circles are also plotted.

the ST magnitude is $M_{814W,ST} = 25.53 \pm 0.06$. Then the flux is calculated as:

$$F = 10^{(STmag+ZPT)/(-2.5)} \tag{6.2}$$

so, $F_{F814W} = 2.33 \times 10^{-19}$ erg s^{-1} cm^{-2} Å^{-1}.

In order to gain information on the optical color of the source, I retrieved Level 5 file (ObsID 10915) made with the ACS using the F606W filter, from the HLA. The zeropoint for F606W is STmag=26.67444 for observations after 2006 July 4 [9]. I find that the FWHM of the PSF is 2 pixels, representing an enclosed energy of 0.656. The AC correction is $AC = 0.088$ and $AC_\lambda = 0.46$ at pivot wavelength of 5918 Å. I find an instrumental magnitude of 17.36 ± 0.15, which transfers to $OBmag = -0.24$. Therefore, the Vega magnitude is $M_{606W} = 26.18 \pm 0.015$, and the ST magnitude is $M_{606W,ST} = 26.43 \pm 0.015$. Then, the flux of the source is $F_{606W} = 9.7 \times 10^{-20}$ erg s^{-1} cm^{-2} Å^{-1}.

The source was detected in both F814W and F606W filters, but not in F475W. The source appears to be of red color (F606W - F814W) $\simeq 1.9$.

6.4 Source Interpretation

Regarding the location of the source, the ATCA and Chandra positions are consistent within the error circles. The ATCA and Chandra counterparts of the source are also consistent with the XMM-Newton position within the errors, and could be consistent with the ROSAT source within the ROSAT PSF. Using the 2MASS point source catalog

[9] http://www.stsci.edu/hst/acs/analysis/zeropoints

and the USNO-B1.0 catalog, the astrometry of the Chandra data appears to be correct at about 0.7 arcsec. Furthermore, the astrometry of the Hubble data appears to be correct at about 0.5 arcsec, using the same catalogs. The chance probability to have a radio and an X-ray source coincident is much lower than to have a radio source coincident with an optical source. Therefore, in the following I assume that the radio and X-ray sources are the counterparts of the same object. For the optical source, I will discuss separate cases when a counterpart is assumed.

The radio spectral index has high errors, but seems to be consistent with a steep-spectra, with optically thin emission. This spectral index could be consistent with a flare from a stellar-mass black hole or with the core of an LLAGN.

Considering the X-ray measurements, the Chandra and XMM-Newton fluxes are consistent with a constant within the errors. These measurements cover more than a year, and given that there is no flux decrease in the X-rays, a putative SNR might immediately be ruled out. Comparing the XMM-Newton flux to the ROSAT flux, it might indicate a variability by a factor of 3-6. However, it is not clear whether the extrapolation to the 0.2-12 keV band is correct. The X-ray photon index can also be consistent with a stellar-mass black hole or with an AGN.

The positional uncertainty of the Hubble image and the relatively crowded field requires to investigate three possibilities: 1) the radio source has a point-like optical counterpart, 2) the radio source does not have an optical counterpart, and alternatively 3) the radio source has a spatially resolved optical counterpart, as many of those are located near the radio error circle.

1) The putative point-like optical counterpart is very faint, it is almost at the HST detection limit. The color index of 1.9 indicates a red source. This color could be consistent with a globular cluster (priv. com. S. Farrell) or a background AGN. 2) If there is no optical counterpart, then an AGN and a globular cluster might be ruled out leaving the only possibility of a microquasar. 3) Alternatively, a globular cluster might be resolved if located within 4 Mpc. There are many resolved optical sources near the radio error circle, which could indicate the presence of a globular cluster. However, the optical colors of those sources were not calculated.

As a next step, I investigate whether the source could be located in the Galaxy. The Galactic coordinate of NGC247 is 114, -83.5. Given the high longitude, it is unlikely that we witness a compact Galactic object in the line of sight. Placing the source at 10 kpc, its X-ray luminosity would be $\sim 10^{33}$ erg/s. In principle, this X-ray luminosity might be consistent with an extreme cataclysmic variable (CV); however, most of the CVs have an X-ray luminosity below 10^{29} erg/s and show a soft X-ray emission (Pretorius & Knigge, 2012). Alternatively, the X-ray luminosity could be consistent with a magnetar in quiescence (Levin et al., 2010). However, a radio loud magnetar has two orders of magnitude higher radio flux and a highly inverted radio spectral index (Levin et al., 2010). Therefore, a Galactic origin of the source of interest might be ruled out assuming it is not a quiescent GBHB.

Placing the source at 3.4 Mpc, the X-ray luminosity would be of 10^{38} erg/s. This luminosity is typical for stellar-mass black holes. Galactic black hole binaries show radio flares at 1-10 Jy level. Scaling this radio flux by the distance of 3.4 Mpc would predict a flaring flux of 0.01-0.1 mJy. This is in good agreement with the measured radio flux of 112 μJy at 5 GHz. Therefore, a flaring microquasar, or a microblazar with beamed radio emission is strongly supported by the X-ray and radio data. If there is no optical counterpart or if the counterpart is consistent with an old cluster (either resolved or not)

would also support the presence of a microquasar. Alternatively, the color index of 1.9 might be similar to a microquasar in a high/soft state (Russell et al., 2011a).

If the source is placed at 100 Mpc, its X-ray luminosity would be about 10^{41} erg/s. LLAGNs are defined with an X-ray luminosity below 10^{42} erg/s (de Gasperin et al., 2011), so the source could be consistent with an LLAGN. On the other hand, the putative optical counterpart is very faint, appears to be of red color, and the source is not cataloged in infrared or UV. Comparing the color index of 1.9 with typical colors of LLAGNs in the same HST bands (González Delgado et al., 2008), I find that it is extremely red for a LLAGN.

One could tentatively use the fundamental plane, with the caution that the X-ray and radio measurements were not taken simultaneously. Also, the radio spectral index does not indicate a compact jet. Assuming that the flaring emission is a factor of 100 stronger than the continuum emission, the obtained mass would be 267 ± 85 $M_\odot$ at 3.4 Mpc. This would rule out a background LLAGN. Placing the source at 100 Mpc and using a face on value on the radio flux, the radio luminosity would be 6.7×10^{36} erg/s. Then, the fundamental plane would predict a mass of $(1.8 \pm 0.6) \times 10^7$ $M_\odot$. This mass is consistent with a LLAGN. At this stage, a firm conclusion cannot be drawn by using the fundamental plane.

In summary, the data supports a flaring microquasar or a microblazar with beamed radio emission. The source could possibly be located in an old stellar cluster in NGC247. Future deep, simultaneous X-ray and radio measurements could confirm the nature of the source by using the fundamental plane and by studying possible variability in the radio and the X-ray band.

7

Jet Ejection Events from the Best Candidate IMBH ESO243-49 HLX-1

Contents

A jet ejection event during state transition of the intermediate mass black hole HLX-1

N. Webb, D. Cseh, E. Lenc,
O. Godet, D. Barret, S. Corbel, S. Farrell, R. Fender, N. Gehrels, I. Heywood
2012, Science, 337, 554

In this Chapter, I focused on my contribution to the above paper. This involves observation, reduction and analysis of the radio data, preparation of the supporting online material regarding the radio observations, and the preparation 50% of the figures and 100% of the tables that are involved in the main body of the paper. Moreover, I heavily contributed to the preparation of the manuscript text and the interpretation of the results. On the other hand, my contribution does not involve the analysis of the X-ray data.

Relativistic jets have been observed from stellar mass black holes ($\sim$3-30 $M_\odot$) as well as supermassive black holes ($\sim 10^6$- 10^9 $M_\odot$) found in the centers of most galaxies. Jets should also be produced by intermediate mass black holes ($\sim$30-10^5 $M_\odot$), although evidence for this third class of black hole has until recently been weak. I report the detection of transient radio emission at the location of the intermediate mass black hole candidate ESO 243-49 HLX-1, which is consistent with a discrete jet ejection event. These observations also allowed to refine the mass estimate of the black hole to be between $\sim 9 \times 10^3$ $M_\odot$ and $\sim 9 \times 10^4$ $M_\odot$. Furthermore, I concluded with possible future steps towards unification of black holes with an evenly populated mass distribution.

7.1 Introduction

7.1.1 Candidate Intermediate-mass Black Holes

Although one of the explanations of the ULXs phenomena is that their mass is consistent with IMBHs, there are many other explanations, such as beaming or super-Eddington accretion. On the other hand, there is an emerging subclass of ULXs, called hyperluminous X-ray sources (HLXs), with their major characteristic: an X-ray luminosity above $L_X > 10^{41}$ erg/s. This extremely large luminosity cannot be explained either with beaming or with super-Eddington accretion. In principle, even the combination of these processes could lead to an X-ray luminosity of only $L_X \simeq 10^{41}$ erg/s. Thus, HLXs are the best IMBH candidates to date. About ~ 18 such sources are known (Gao et al., 2003; Walton et al., 2011; Sutton et al., 2012); however, most of their distances are unconstrained, i.e. some of them could be background, low-luminosity AGN (LLAGN).

Another important point is that all length scales of an accreting black hole system can be expressed in units of the gravitational radii. This means that the kinetic power output of any black hole is scale invariant (Heinz & Sunyaev, 2003). In this model, jets are expected from every black hole system regardless of the mass of the black hole. The presence of jets, however, depends on accretion rate. If one compares black holes at similar accretion rates, then jet emission, which is most frequently detected through radio emission, is not only to be expected from stellar mass black holes and supermassive black holes, but from IMBHs as well. This includes ULXs, however, to date, no variable radio emission associated with jets has been detected from ULXs, despite numerous observing campaigns (Körding et al., 2005; Freeland et al., 2006). On the contrary, non-varying nebula-like extended radio emission, which is likely to be powered by the central black hole, has been detected around some ULXs (Kaaret et al., 2003; Miller et al., 2005; Cseh et al., 2012).

7.1.2 HLX-1

ESO 243-49 HLX-1 (HLX-1) was discovered serendipitously using XMM-Newton on 23 November 2004 in the outskirts of the edge-on spiral galaxy ESO 243-49, 8″ from the nucleus (Farrell et al., 2009). The distance to HLX-1 measured from its Hα emission line confirms that ESO 243-49 is the host galaxy (Wiersema et al., 2010). HLX-1 therefore has a maximum unabsorbed X-ray luminosity, assuming isotropic emission, of 1.1×10^{42} ergs s^{-1} (Farrell et al., 2009). The non-nuclear location of this point source and the fact that it exceeds the Eddington luminosity for a stellar mass black hole by three orders of magnitude, qualify it as a ULX. From the X-ray luminosity and the conservative assumption that this value exceeds the Eddington limit by at most a factor of 10 (Begelman, 2002), a lower limit of 500 $M_\odot$ was derived for the mass of the black hole (Farrell et al., 2009). The maximum mass, however, is not constrained. Because the X-ray to optical flux ratio (Farrell et al., 2009; Soria et al., 2010a) is far greater than expected from an AGN without an estimate of this maximum mass, it could still be argued that HLX-1 is a non-nuclear supermassive black hole (e.g. Guedes et al., 2009). The optical SED of HLX-1 is likely consistent with a young stellar cluster; however, it is strongly affected by disk irradiation (Farrell et al., 2012).

HLX-1 is not only a ULX, but currently the best intermediate mass black hole candidate. The Swift/XRT lightcurve (Fig. 7.1) shows that HLX-1 is regularly undergoing X-ray outburst. These outbursts show a FRED pattern, ie. a fast rise followed by an ex-

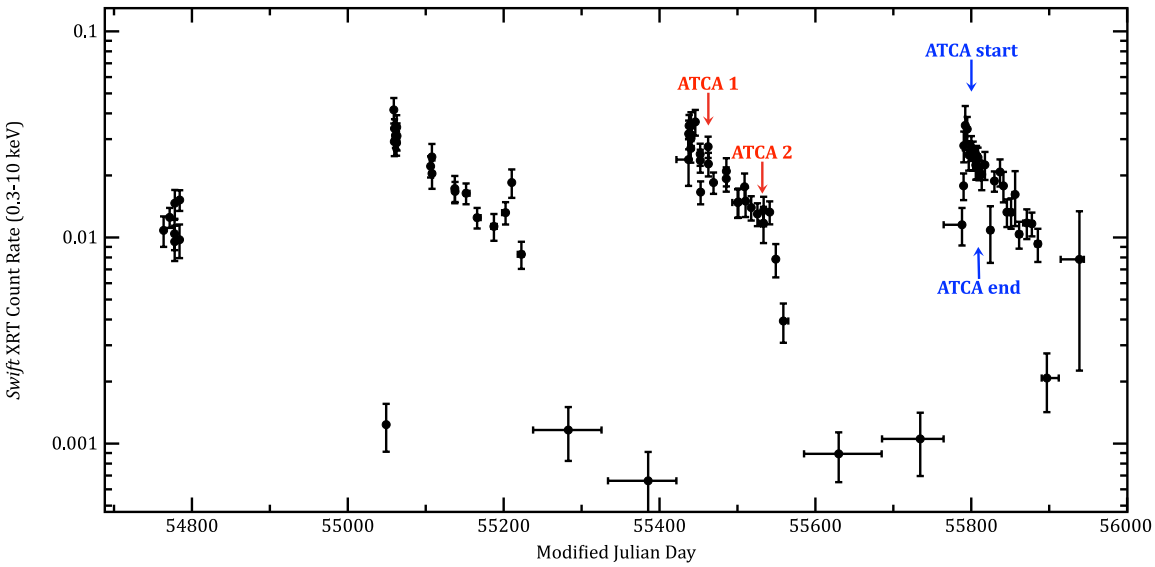

Figure 7.1: Longterm Swift lightcurve showing the dates of the first two ATCA observations and the period during which the subsequent five ATCA observations were taken. Three X-ray state transitions from the low/hard state (count rate $\leq$ 0.002, 0.3-10.0 keV) to the high/soft state (0.01 $\leq$ count rate $\leq$ 0.05, 0.3-10.0 keV) can be seen.

ponential decay, which is reminiscent to Galactic black hole binaries (GBHBs). If HLX-1 harbors an intermediate mass black hole, it accretes at comparable fractions of the Eddington luminosity, as stellar mass black holes in binaries. Hence one expects HLX-1 to display similarities with the latter class of objects (see also later). In that respect spectral state transitions (Fig. 7.2) reminiscent of black hole binaries have already been reported (Godet et al., 2009; Servillat et al., 2011). It is therefore an ideal object in which to search for jet emission, in order to verify the scale-invariance of jets from black holes. Moreover, HLX-1 follows the standard disk law (Fig. 7.3.), which makes the source even more close to GBHBs. Also, this is another strong argument supporting the IMBH nature of HLX-1, ruling out super-Eddington accretion.

7.2 Radio Observations and Analysis

HLX-1 in ESO 243-49 was observed with the Australia Telescope Compact Array (ATCA) seven times as shown in Table 7.1, using the upgraded Compact Array Broadband Backend (CABB) (Wilson et al., 2011). The data were taken using the CFB 1M-0.5k correlator configuration with 2 GHz bandwidth and 2048 channels, each with 1 MHz resolution. Each observation was performed at the central frequencies of 5.5 GHz and 9 GHz simultaneously. During the first observation the array was in the 750 m configuration (giving baselines up to 5 km when all 6 antennas are used). During the second and subsequent observations it was in the 6 km configuration. The total on-source integration time was $\sim$11 h for each observation. The primary calibrator PKS 1934-638 was used for absolute flux and bandpass calibration, while the secondary calibrator 0048-427 was used for the phase and antenna gain calibration. For each observation, we observed 1934-638 for 10 min and the phase calibrator was observed every 15 min.

The data reduction and analysis was performed with the Multichannel Image Re-

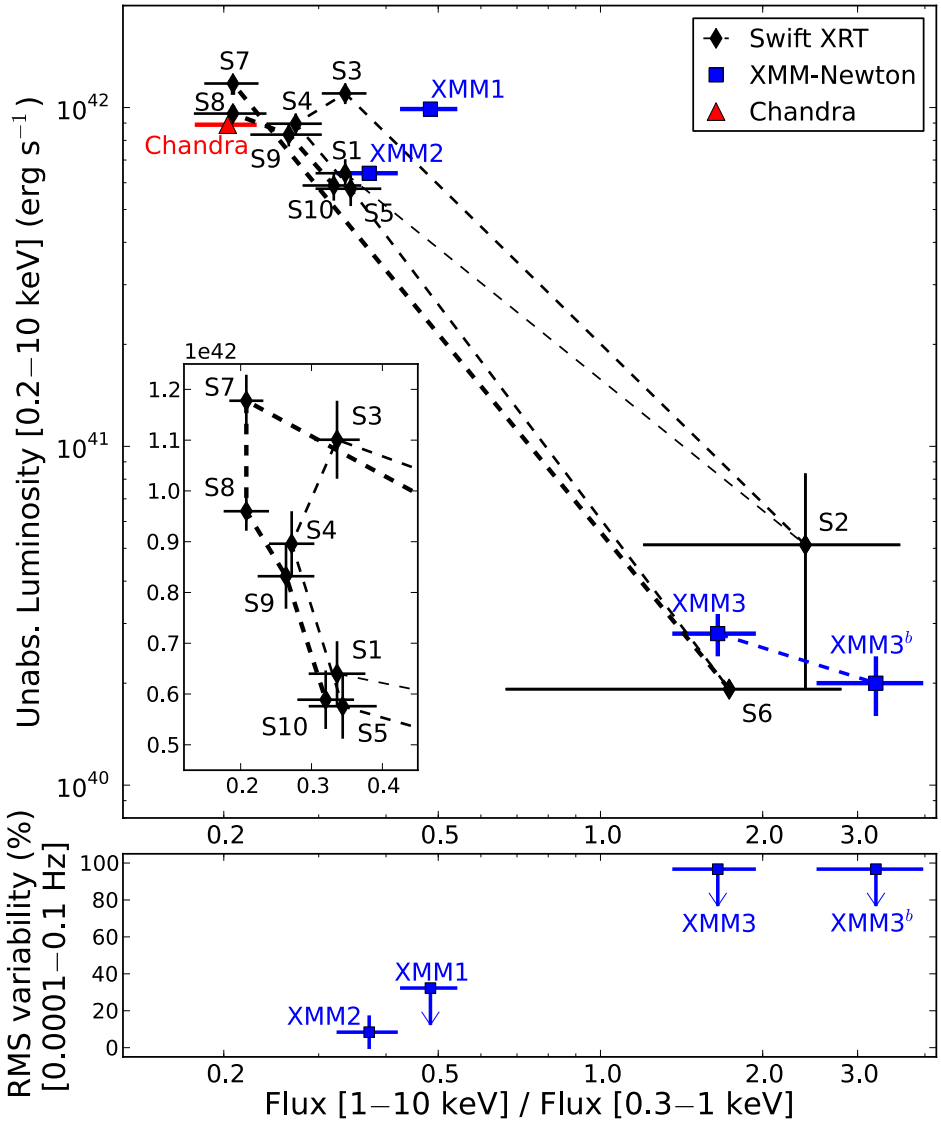

Figure 7.2: Hardness intensity diagram (HID) of HLX-1 showing all the available Chandra and X-ray measurements (Servillat et al., 2011).

construction, Image Analysis and Display (MIRIAD) software (Sault et al., 1995). We loaded the data into MIRIAD using the ATLOD task with options birdie, xycorr, rfiflag, and noauto, which flags out the channels affected by self-interference, correcting the phase difference between the X and Y channels, discarding any autocorrelation data, and automatically flagging out frequency bands that are known to be heavily affected by Radio Frequency Interference (RFI). The standard data reduction steps were flagging, bandpass, phase and amplitude calibration, following the MIRIAD User Guide. We used multi-frequency synthesis (MFS) methods (Wilson et al., 2011) to produce the dirty maps. Imaging was carried out using the multi-frequency (Wilson et al., 2011) clean algorithms. We note that imaging did not involve any self-calibration.

The detections with the associated 1 σ noise level and the 3 σ non-detections for the 5 GHz, 9 GHz and combined observations are given in Table 7.1. All the images were nat-

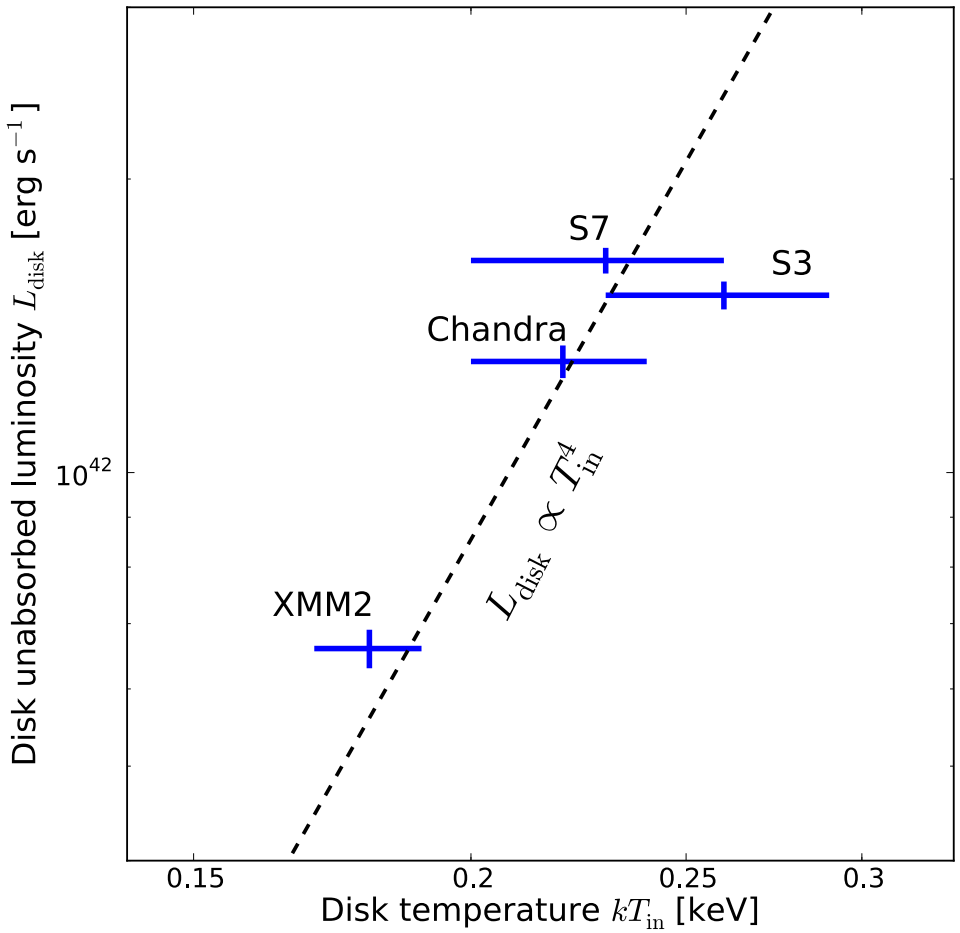

Figure 7.3: Disk luminosity of HLX-1 is plotted against the inner disk temperature (Servillat et al., 2011).

urally weighted in order to reach the best sensitivity, with the exception of the September 2010 5 GHz (and the 5+9 GHz) image which was weighted with robust=0 due to the lower resolution of this data. We also combined the 5-GHz and 9-GHz data sets in order to enhance sensitivity.

We estimated the position errors by adding the errors due to phase calibration, the position of the phase calibrator and the point-source model fit in quadrature. We note that as we have a Very Long Baseline Interferometry measurement for the phase calibrator, its positional error is negligible. The error due to phase calibration depends on the distance between the target and the calibrator of 11.5 degrees which corresponds to a positional uncertainty of $\sim$0.2″. We find the error on the RA is 0.43″ and on the dec. is 0.67″. We verified that the radio source was consistent with a point-like object by comparing the fluxes and the fitted point source model fluxes. For all of our detections, the radio source was consistent with a point source.

Table 7.1: Summary of radio observations

	5 GHz flux (μJy/b.)		9 GHz flux (μJy/b.)		5+9 GHz flux (μJy/b.)	
Observation date	Detection (1 σ rms)	Non-det. (3 σ)	Detection (1 σ rms)	Non-det. (3 σ)	Detection (1 σ rms)	Non-det. (3 σ)
13 Sep. 10	45 (11)			36	50 (11)	
3 Dec. 10		33		63		36
25 Aug. 11		36		45		30
31 Aug. 11	44 (11.5)			51	51 (10)	
1 Sep. 11		36		48		31
3 Sep. 11		36	81(17)		45 (10.5)	
4 Sep. 11		27		39	30 (7.5)	

The 7 radio observations organised by date and showing the radio detection with the associated 1 σ noise level or the 3 σ non-detection for the 5 GHz, 9 GHz and combined observations.

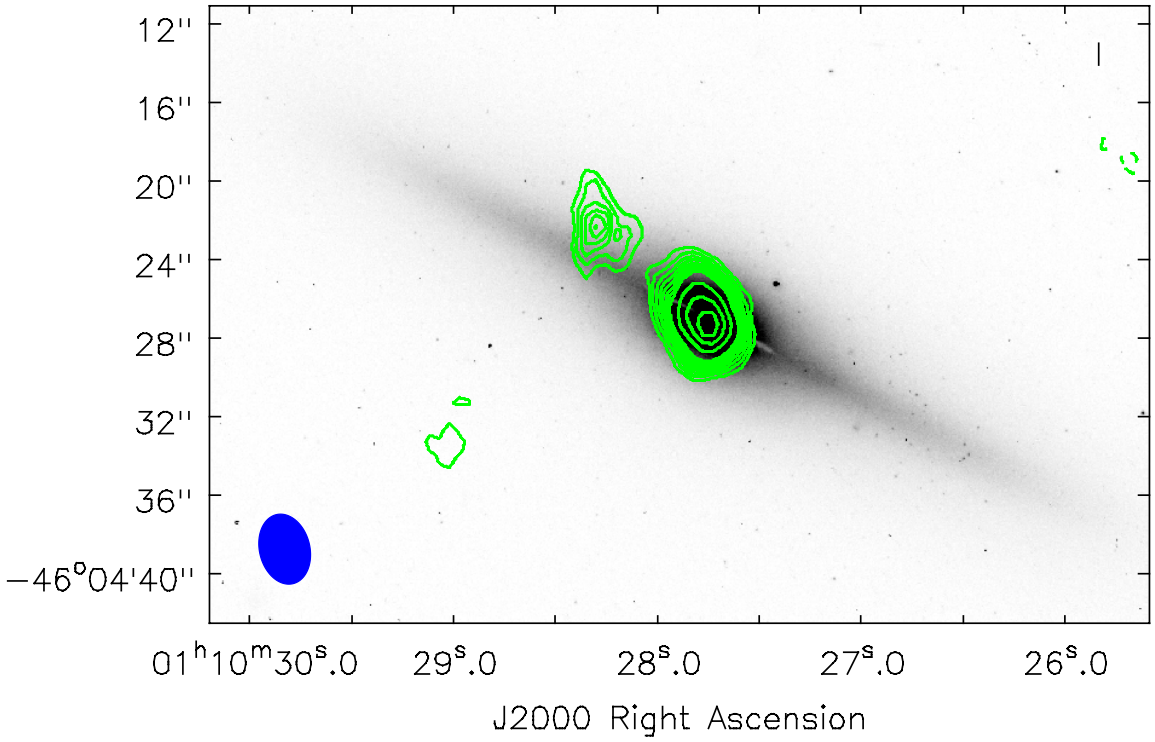

Figure 7.4: 5 and 9 GHz combined radio observations (contours: -3, 3, 4, 5, 6, 7, 8, 9, 10, 15, 20, 25 times the 1 σ rms noise level (5.6 μJy/beam)) using the radio data taken on the 13th September 2010, 31st August 2011, 3rd and 4th September 2011 with the ATCA and superimposed on an I-band Hubble Space telescope image of ESO 243-49 (inverted colour map). The beam size is shown in the bottom left hand corner. The galaxy, ESO 243-49, is clearly detected in radio. An 8-σ point source falls at RA = 01h10m28.28s and declination = -46°04'22.3" (1 σ error on the position of RA=0.43" and dec.=0.67"), well within the 0.3" Chandra error circle of HLX-1.

7.3 Discussion

We observed HLX-1 with the ATCA in the 750 m configuration on the 13th September 2010, when our regular X-ray monitoring of HLX-1 with the Swift satellite (Gehrels et al.,

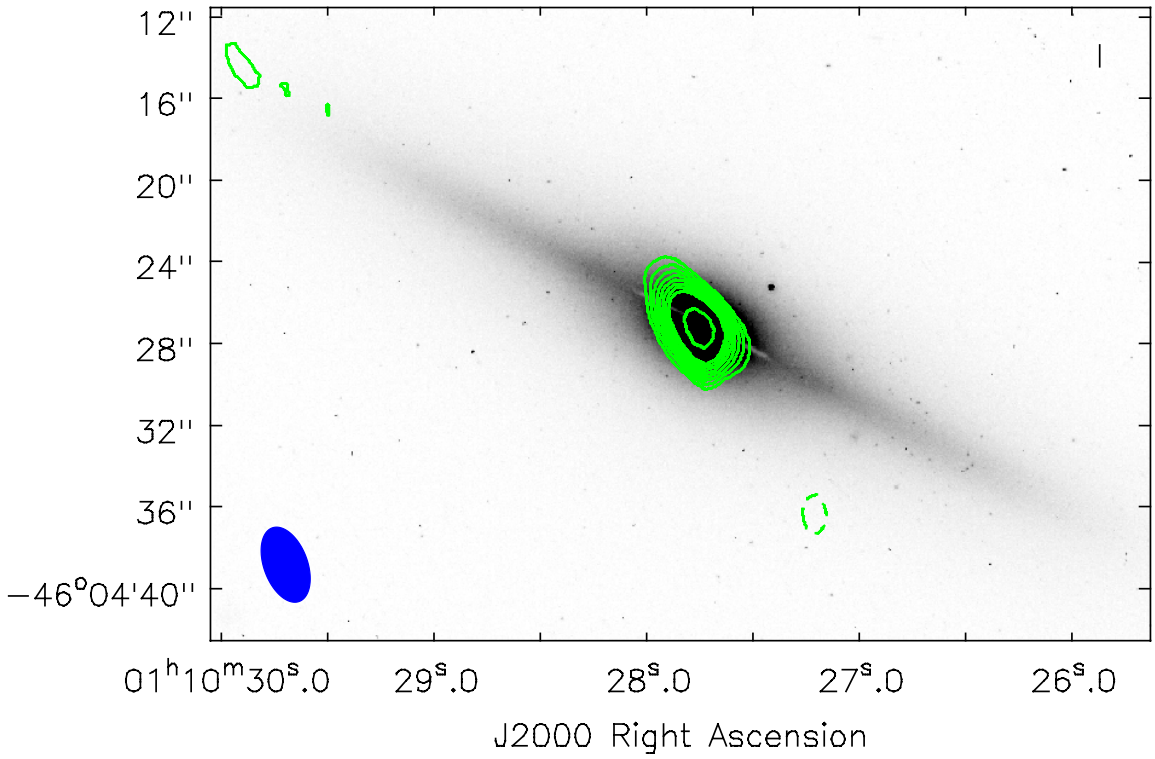

Figure 7.5: 5 and 9 GHz combined radio observations (contours: -3, 3, 4, 5, 6, 7, 8, 9, 10, 15, 20, 25 times the 1 σ rms noise level (7.0 μJy/beam)) made from the 3rd December 2010, 25th August 2011 and 1st September 2011 ATCA observations and superimposed on the same I-band Hubble Space telescope image of ESO 243-49. The galaxy ESO 243-49 is again clearly detected, but no source is found within the Chandra error circle. Again the beam size is shown in the bottom left hand corner.

2004) showed that HLX-1 had just undergone a transition from the low/hard X-ray state to the high/soft X-ray state. The transition occurs for HLX-1 when the count rate increases by more than a factor 10 in just a few days, see Figure 7.1 and (Servillat et al., 2011; Godet et al., 2012). GBHBs are known to regularly emit radio flares around the transition from the low/hard to the high/soft state, e.g. (Corbel et al., 2004; Fender et al., 2009). These are associated with ejection events, where, for example, the jet is expelled which can lead to radio flaring when the higher velocity ejecta may collide with the lower-velocity material produced by the steady jet. As well as detecting radio emission from the nucleus of the galaxy, we detected a radio point source at Right Ascension (RA) = 01h10m28.28s and declination (dec.) = -46°04'22.3", coincident with the Chandra X-ray position of HLX-1 (Webb et al., 2010). Combining the 5 GHz and 9 GHz data gives a detection of 50 μJy/beam, and a 1 σ noise level of 11 μJy, thus a 4.5 σ detection at the position of HLX-1, at a time when such emission can be expected, see Figure 7.4 and Table 7.1.

The radio flares in Galactic black hole binaries are typically a factor 10-100 (and even more) brighter than the non-flaring radio emission (Körding et al., 2005) and generally last one to several days, e.g. XTE J1859+226 (Brocksopp et al., 2002). Once the high/soft state has been reached, emission from the core jet is suppressed, e.g. (Fender et al., 2009). To determine whether the radio emission that we detected was transient and thus associated with a radio flare, we made another observation with the ATCA in the 6 km config-

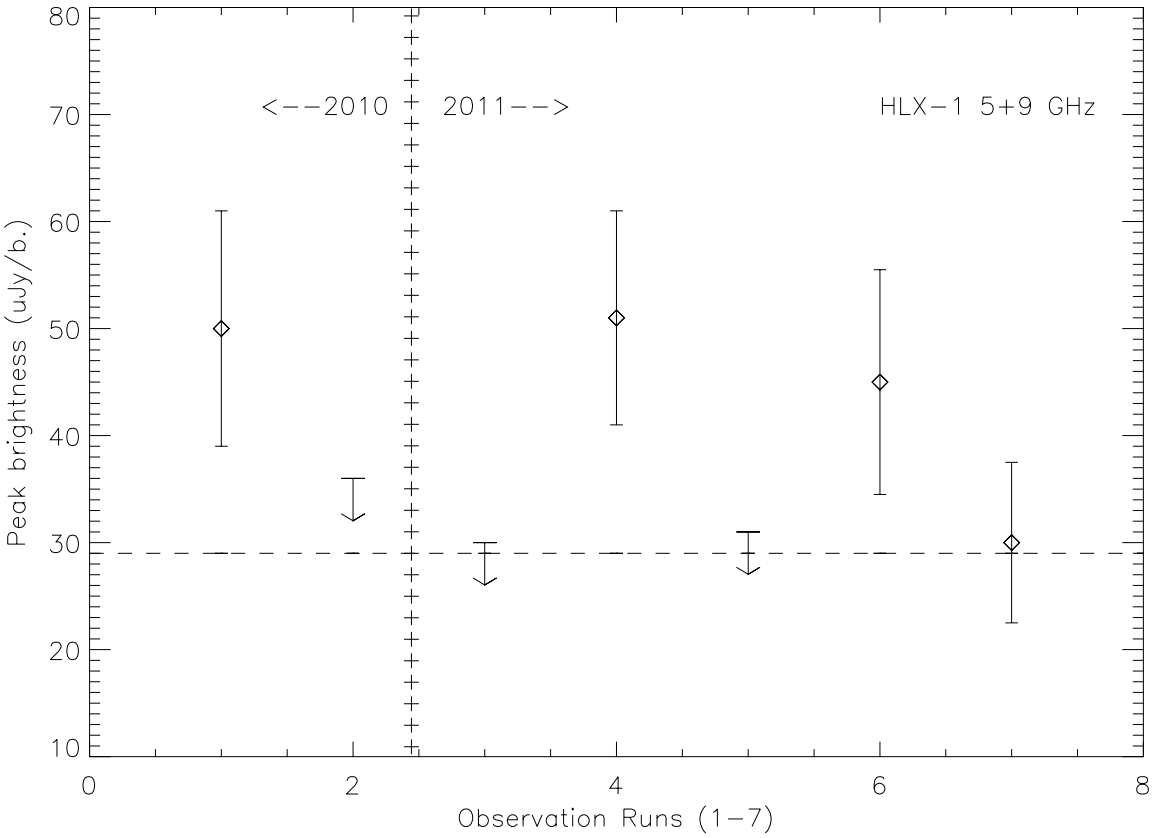

Figure 7.6: ATCA observations to date covering the 2010 and the 2011 outbursts: 13 Sep 2010, 3 Dec 2010, 25 Aug 2011, 31 Aug 2011, 1 Sep 2011, 3 Sep 2011, 4 Sep 2011. The 7-GHz (combined 5 and 9 GHz) peak intensities are plotted with an uncertainty of 1-σ rms noise level, or the 3-σ upper limit in case of non-detections. The dotted line indicates the average flux, the dashed line indicates the 3-σ upper limit of the EVLA.

uration on 3rd December 2010, when HLX-1 was declining from the high/soft state and when no flaring is expected. This observation again showed emission from the nucleus of the galaxy, consistent with that of the previous radio observation, but revealed no source at the position of HLX-1. The 3 σ non-detection for the combined 5 GHz and 9 GHz data is 36 μJy/beam, see Figure 7.5 and Table 7.1. These observations suggest that the radio source at the location of HLX-1 is variable.

To confirm the variability, we reobserved HLX-1 when it had just undergone a new transition from the low/hard X-ray state to the high/soft X-ray state in August 2011, see Figure 7.4. Five observations were made, see Table 7.1. All five of the 2011 observations were made in a similar configuration to the December 2010 observation. The source was again observed to be variable, with three non-contiguous detections (> 4 σ) and two non-contiguous non-detections, see Fig. 7.6 and Table 7.1. This points towards the idea that two flares were detected during this period, and the variability observed rules out emission from a nebula. Combining all of the detections (5 and 9 GHz), the source is observed at 45 μJy/beam, with a 1 σ noise level of 5.5 μJy, which shows a confident detection at the 8 σ level. Combining, in a similar fashion, the data in which no radio emission was detected, we obtained a 3 σ upper limit in the combined 5+9 GHz data of 21 μJy/beam. The observed point-like variable radio emission is then again consistent

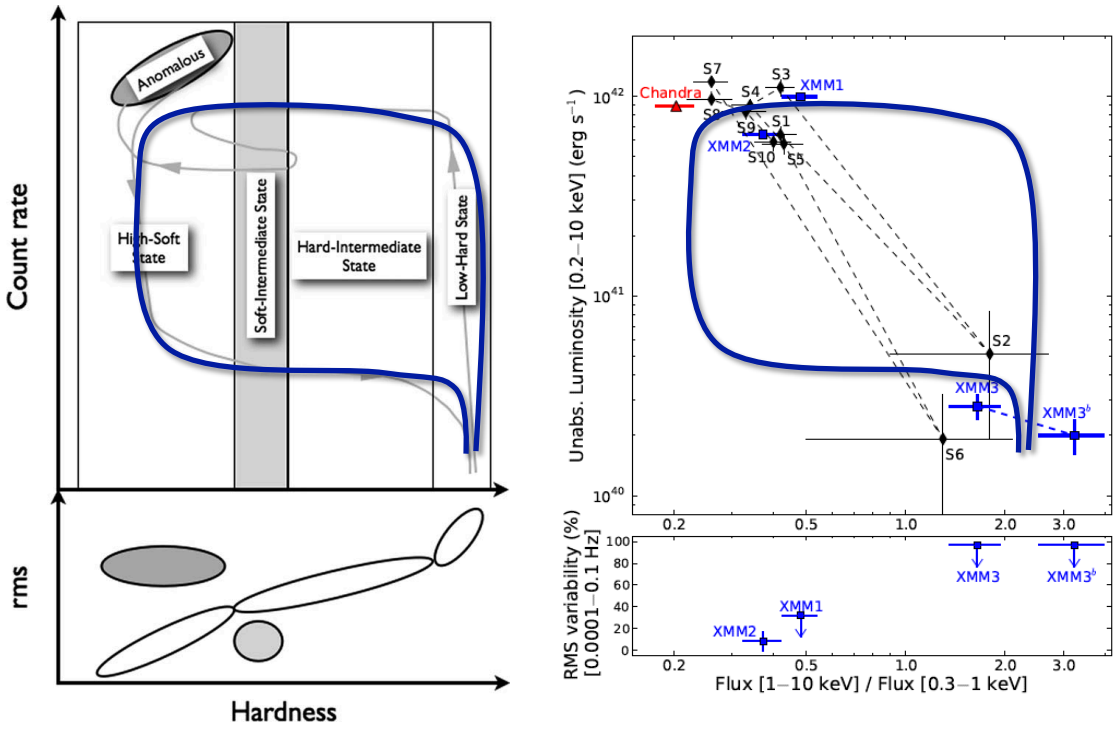

Figure 7.7: Comparison of the hardness-intensity diagram of GBHBs and HLX-1. The overplotted so-called "turtle head" represents the evolutionary track of an outburst. The image on the left is from Belloni (2010) and the on the right is the previously shown HID (Servillat et al., 2011).

with a transient jet ejection event.

However, the more significant way to confirm variability is with a statistical test. To this purpose, I used the actual flux values of HLX-1 in the case of the non-detections, and not the $3-\sigma$ upper limits. I treated the errors as the $1-\sigma$ noise level. I performed a χ^2 test to compare the measured fluxes with constant values. I added the error to the constant test values randomly, using random generators to decide whether to add or subtract the error and what amount of error. I tested this using 10000 trials. Thus, this test is equivalent to Monte Carlo'ing 10000 test measurements to compare with the real data by using a χ^2 test. Then, the result is obtained as the minimum χ^2 statistics among the 10000. The result is a χ^2 statistic of 16.21, with a probability of 0.012 at a significance level of 0.05. In other words, the hypothesis that the measured fluxes are constant has to be rejected, further confirming the variability. Note that, using three times the noise level as error on the measured values would not allow us to rule out constant fluxes using the above statistical method. Similarly, considering only measurements made during an outburst would not allow to prove variability during this period, but our aim is the contrary, to prove variability during a state transition.

It has been shown that observations of supermassive black holes and stellar-mass black holes support the scale invariance of jets (Merloni et al., 2003; Körding et al., 2006a). This was done by comparing X-ray and radio measurements, tracers of mass accretion rate and total jet power respectively, with the black hole mass, to form a "fundamental plane of black hole activity". Under the hypothesis that HLX-1 is indeed an intermediate mass black hole, we can test the proposed relation. We take what is generally considered to be the maximum mass of intermediate mass black holes, $\sim 1 \times 10^5$ $M_\odot$ (Miller & Col-

bert, 2004), and the X-ray luminosity, 5.43×10^{41} erg s^{-1} (0.5-10.0 keV), determined from the Swift X-ray telescope (Burrows et al., 2005) observations made at the same time as our radio detection. Continuum (non flaring) radio emission could then be estimated with the aforementioned relationship (Merloni et al., 2003), which is a sample that includes black holes in all different X-ray states. Using their relation we determine continuum radio emission at the $\sim$20μJy level. This is slightly lower than the 3 σ non-flaring upper limit, suggesting that the mass of the black hole is likely to be less than $\sim 1 \times 10^5$ M$_\odot$.

As another approach, radio flares are seen to occur in GBHBs when the X-ray luminosity is 10-100 per cent of the Eddington luminosity (Fender et al., 2004). HLX-1 has already shown similar behavior to the GBHBs, therefore assuming that the radio flares that we observed also occur when the X-ray luminosity is 10-100 per cent of the Eddington luminosity indicates a black hole mass between $\sim 9.2 \times 10^3$ M$_\odot$ and $\sim 9.2 \times 10^4$ M$_\odot$, commensurate with the mass estimate above and those of Servillat et al. (2011); Godet et al. (2012); Davis et al. (2011).

I note that additionally, one can consider that typical GBHB flares have a radio flux of 1-10 Jy at $\sim$ 5 kpc. Scaling this flux by distance and linear mass, one obtains that the expected mass of HLX-1 is between $\sim 5 \times 10^3$ M$_\odot$ and $\sim 5 \times 10^4$ M$_\odot$ (for a measured flux density of $\sim$45 μJy). This is also in good agreement with the above estimation.

We have thus demonstrated that the ULX HLX-1 shows transient radio emission during a hard to soft state transition that is consistent with a jet ejection event. These observations reinforce the idea that this intermediate mass black hole candidate behaves in a similar way to Galactic black hole binaries and supports the proposed scale invariance of jets, relating the mass accretion to the power output for black holes in all mass ranges. These observations have also allowed us to refine the mass estimate of the intermediate mass black hole to be between $\sim 9 \times 10^3$ M$_\odot$ and $\sim 9 \times 10^4$ M$_\odot$, confirming the intermediate mass black hole status.

7.4 Black Hole Unification

Here I intend to show that HLX-1 is a very promising candidate for black hole unification. HLX-1 is not just exhibiting X-ray state transition, but it likely follows the canonical X-ray states of GBHBs (Fig. 7.7). Although, one can argue that the high/hard and low/soft state is not measured, ie. parts of the "turtle head" pattern are missing. There could be several reasons for this, such as the fast rise of the X-ray flux and sensitivity limits, and/or one would need to define different hardness ratio. Assuming that HLX-1 is an IMBH that follows the standard disk law, then it is expected to have a lower inner disk temperature than a GBHB. As a matter of fact, the inner disk temperature is indeed much lower than 1-2 keV, as shown in Fig. 7.3. Thus, plotting the luminosity versus a hardness ratio that clearly reflects the disk and power-law fraction of the X-ray flux, might help to better "sample" the HID pattern. In any case, there is certainly a good match with the GBHB phenomenology.

It was also shown that the disk-fraction luminosity diagram shows the same pattern (Fig. 7.8), not just for black holes, but also for other accreting objects like neutron stars and cataclysmic variables. Therefore the common link between all accreting objects is the universal disk/jet coupling and/or the same jet launching mechanisms (Körding et al., 2008a).

The idea of the disk/jet coupling was developed even further for accreting black holes. This means, when considering only black holes, a mass scaling of the disk/jet

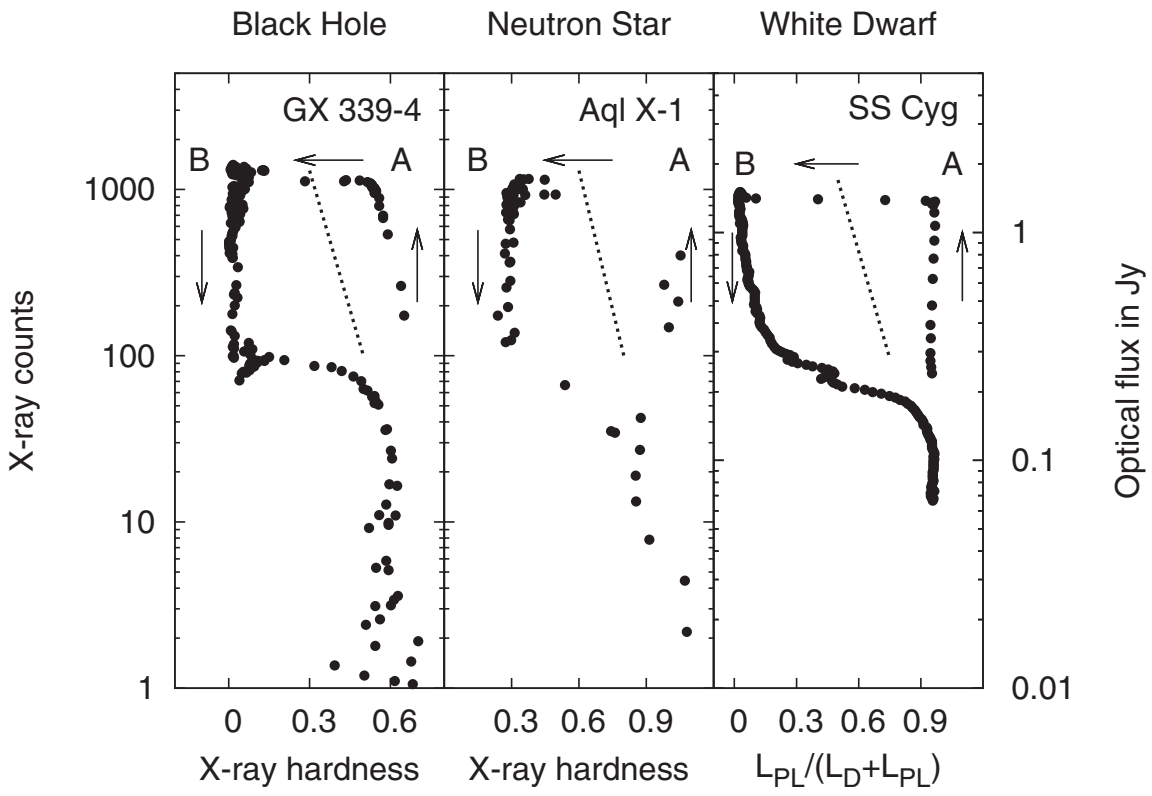

Figure 7.8: Unification of HIDs in different type of compact objects (Körding et al., 2008a). For a black hole (GX 339-4) and for a neutron star (Aql X-1) the HID is shown. For a white dwarf (SS cyg) the disk fraction luminosity diagram is shown as an equivalence to the HID. The jet line is also shown, to the left hand side from the jet line the jet is quenched.

coupling holds. This is manifested in the "fundamental plane" of black holes, which relates the radio core luminosity to the X-ray luminosity and scales by mass. Thus, broadly speaking, it is valid for both SMBHs and StMBHs. However, the ultimate question is whether this empirical relationship holds for IMBHs as well – in other words, whether the fundamental plane is able to describe the entire black hole population. To this purpose I tentatively plot the location of HLX-1 on the fundamental plane, see Fig. 7.9. As the flux of the hard state compact jet is likely below our detection threshold, I assumed a hard state flux of a factor of 10-100 lower than the flux of the flaring emission. Also, the high uncertainty in the mass estimation leads to a "zone" on the fundamental plane, rather than a well-defined point. However, it is clear that if one could detect the flux of the compact jet, then HLX-1 would indeed likely fall between the two well-known population of black holes.

It is interesting to note that even taking a wide range of parameters for HLX-1, its position seems to fall above the position of Sgr A*. This is because the inferred mass of HLX-1 is only a factor of 10-100 below the mass of Sgr A*. Furthermore, Sgr A* is thought to be in quiescence with very little accretion activity. The plotted value of Sgr A* is coming from episodes when the central black hole shows radio flares. Additionally, Sgr A* thought to accrete at or below a level of 10^{-9} Eddington units, while hard state objects typically accrete in the regime of $10^{-1} - 10^{-6}$ Eddington units. On the other hand, there is no discrepancy, because the expected radio and X-ray luminosity scales with the

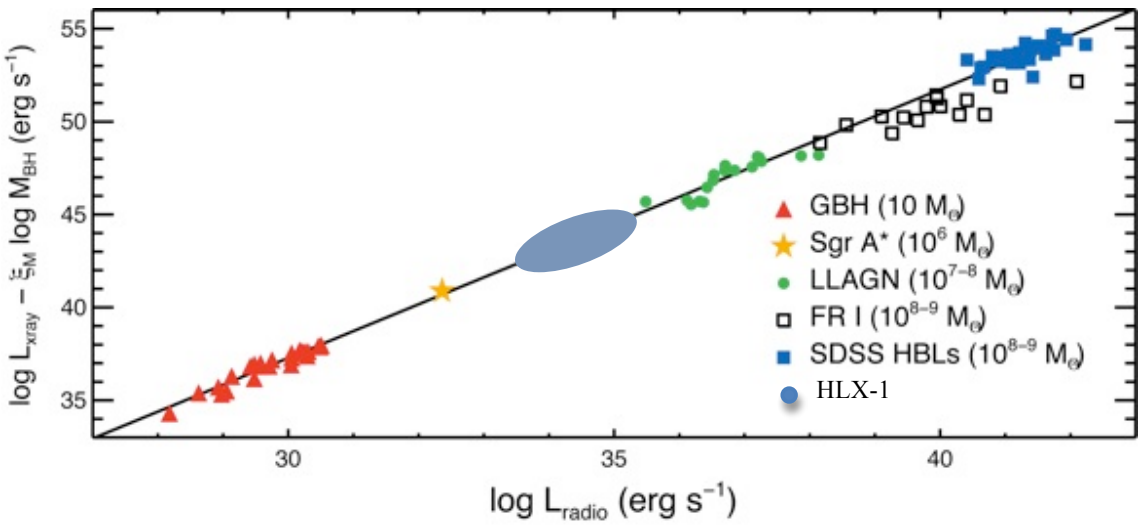

Figure 7.9: The fundamental plane of accreting black holes are shown (Plotkin et al., 2012). The image also shows the overplotted, approximate position of HLX-1.

accretion rate, not just by mass. This is indeed also true for HLX-1, where the assumed flux of the compact jet is a factor of 10-100 below the flaring activity, which is only an approximation as I assumed a hard state accretion rate of $10^{-1} - 10^{-2}$ in Eddington units. It is clear that the accretion rate of Sgr A* is orders of magnitude lower than the accretion rate of any of the objects plotted on Fig. 7.9.

7.5 Conclusion

HLX-1 is the best IMBH candidate to date, and it is showing a periodic outburst that might correlate with the orbital period of the system (Lasota et al., 2011). It is also undergoing X-ray state transitions, and when in a thermal state, it is best described with the standard disk model. Therefore, it likely shows the same phenomenology as GBHBs during an X-ray outburst. Its mass is estimated to be $\sim 10^4$ $M_\odot$ from several multiwavelength observations, however we are lacking a dynamical mass measurement. We detected for the first time radio flares from HLX-1 during its state transition from low/hard to high/soft state. This further confirms that HLX-1 is a good candidate to fill the gap between StMBHs and SMBHs.

In the future, I intend to study the evolution of the flares, i.e. the variability timescale, and also to better confirm the radio spectral index of the flares.

8 Conclusions and Perspectives

Contents

8.1 Conclusions

8.1.1 Dynamical Mass Constraints on NGC 5408 X-1

In this thesis various aspects of ultraluminous X-ray sources and intermediate-mass black holes were investigated. From the optical side, there is crucial need to measure the dynamical mass of ULXs to break down the degeneracies between the numerous theoretical models. To this purpose several attempts have been made, but none resulted in firm mass estimate. This is because the majority of the ULXs are too faint, and in most cases the optical emission is dominated by disk irradiation and not the donor star (see Chapter 4). Furthermore, there are very few examples where the absorption lines from a donor star can be seen (e.g. Motch et al., 2011). This boosted the idea that a dynamical mass might be obtained by using the He II line, because this line traces the orbital motion of the system in certain cases of X-ray binaries. Despite some early measurements demonstrated random variations of this line (e.g. Roberts et al., 2011), in the case of NGC5408 X-1 we

might be able to obtain the orbital periodicity of the system. I discovered that between the observing runs the HeII line is markedly shifted in wavelength. I revealed that the line profile has two components, a broad and a narrow, and showed that the broad component can be consistent with an origin in the accretion disk. This is the main reason why we might be able to trace the orbital motion, because in early measurements the width of the He II line was not consistent with an origin in the accretion disk.

Using the velocity of the broad component, I determined the size of the line-emitting region as a function of the black hole mass. I used the mass function and determined the upper limit on the mass of the black hole as a function of orbital period. Moreover, I determined the possible orbital separation between the donor star and the black hole as a function of the orbital period, from which I also set upper limits on the mass of the black hole. For the previously inferred orbital period, I showed that it is likely not valid if the black hole is Roche-lobe fed and if the line shift truly traces the orbital motion of the system. Assuming a reasonable mass for the donor star and considering some dynamical arguments, I set an upper limit on the mass of the black hole, which is of the order of 100 $M_\odot$ (Cseh et al., 2011).

8.1.2 An Intermediate-mass Black Hole in the Globular Cluster NGC 6388?

Several studies were made on globular clusters, young stellar clusters and dwarf irregulars aiming to detect accretion signatures from predicted IMBHs. These predictions are typically related to the downscaling of the $M - \sigma$ relationship and to other optically determined dynamical constraints on the masses in clusters. For globular clusters, the dynamical mass estimates predict much higher mass for IMBHs than seen from accretion signatures. Also, deep radio observations already start to set strong constraints on the masses (or accretion rates) below these predictions (see Chapter 3). In particular, I placed an upper limit on the mass of the putative central intermediate-mass black hole (IMBH) in the globular cluster NGC 6388. First, I revealed three previously unknown X-ray sources in the center of the cluster and showed that one of these sources can be consistent with a black hole. Then I showed that none of the X-ray sources have radio counterpart at a flux level of 81 μJy. Using the X-ray flux and the radio upper limit on the putative IMBH, I determined an upper limit on its mass by using the fundamental plane of accreting black holes, an empirical correlation between the X-ray, and radio luminosity, and the mass of the black hole. I also showed that the X-ray source can be consistent with spherical accretion from the interstellar medium onto a black hole (Bondi-Hoyle accretion). By calculating the allowed accretion rates and accretion efficiencies I also obtained an upper limit on the mass of the black hole, which is consistent with the one obtained from the fundamental plane of 735 ± 244 $M_\odot$. (Cseh et al., 2010). A more recent, deeper radio observation placed an upper limit of 600 $M_\odot$ (Bozzo et al., 2011). Furthermore, a new optical study estimates the mass of the putative IMBH to be $(17 \pm 9) \times 10^3$ $M_\odot$ (Lützgendorf et al., 2011), which is a factor of 3.5 higher than previous predictions from dynamical arguments. In general, the high difference between the dynamical and radiative method can be made consistent with an accretion rate of 10^{-10} in Eddington units. These accretion rates certainly indicate black holes in quiescence. However, Sgr A, A0620-20 and V404 Cyg show radio emission at accretion rates of 10^{-9}, which could indicate that accretion does not happen via an accretion disk in globular clusters. Therefore, current radio observations cannot exclusively rule out the presence of an IMBH which is accreting at very low Eddington rates, or being in quiescence (if Bondi-accretion is a

valid assumption).

8.1.3 Black Hole Powered Nebulae Around ULXs – Inflation by Jets?

A way to gain more information on whether ULXs are beamed is to study their environment. There are a number of ULXs associated with bubbles. Since the optical luminosity is isotropic, it places a lower limit on the X-ray luminosity illuminating the nebula. Based on models of X-ray reprocessing where the X-ray source is located inside the nebula, early studies concluded that the optical radiation is consistent with an isotropic X-ray source and not with significant beaming (e.g. Pakull & Mirioni, 2002). On the other hand, the precise mechanism for the ionization is not well established. Jet ionization is a possible alternative to supernova shock ionization. I studied both, photo- and shock-ionization in three ULX bubbles. We discovered a radio bubble around IC342 X-1 and I investigated the total energy content of this shock-ionized bubble (see Chapter 5). I compared its energy content of 6×10^{52} erg to a canonical initial energy of a SN of 10^{51} erg, which indicates that there is a substantial need for additional energy supply, possibly in the form of jets. Then I showed that the age of the bubble is much less than the age of the stellar environment, which might indicate that the formation of the nebula is not necessarily related to the formation of the black hole progenitor. I also showed that the energy carried by the relativistic material in IC342 X-1 is even higher than in sources like S26 and a Type Ic supernova remnant. This might also favor jet inflation. Interestingly, I showed that the minimum energy content of IC342 X-1 might not violate the total energy content if relativistic protons are present inside the bubble, (i.e. proton acceleration might be possible) (Cseh et al., 2012).

Using the fundamental plane of accreting black holes, I also set an upper limit on the mass of the black hole of 1000 ± 300 $M_\odot$. I also determined the time-averaged jet accretion rate of IC342 X-1 as well as an upper limit on the mass accretion rate of 8.2×10^{19} g s^{-1}, which might indicate that super-Eddington accretion is not necessary to explain IC342 X-1 if it has a black hole mass at or above 100 $M_\odot$ (Cseh et al., 2012).

8.1.4 Early Results on ULX Radio Surveys

Using archival and new data I set the strongest upper limits on the fluxes of possible radio bubbles associated to existing optical ULX bubbles. I also set upper limits on putative compact jets associated to ULXs and showed that (future) deep radio surveys could rule out black hole masses above $\sim$ 1000 $M_\odot$ for a large number of ULXs (see Chapter 6). Additionally, I found a new radio source in our ULXs survey and argued that it might be consistent with a flaring extragalactic microquasar.

8.1.5 Jet Ejection Events from the Best Candidate IMBH HLX-1

There is an emerging subclass of ULXs, called hyperluminous X-ray sources (HLXs), with their major characteristic: an X-ray luminosity above $L_X > 10^{41}$ erg/s. This extremely large luminosity cannot be explained either with beaming or super-Eddington accretion, or with even the combination of these processes (see Chapter 7). Given that relativistic jets have been observed from stellar mass black holes and supermassive black holes, jets should also be produced by intermediate mass black holes as well, due to the (predicted) scale invariance of jets (e.g. Heinz & Sunyaev, 2003). Although evidence for compact radio emission from either ULXs/HLXs or IMBHs have recently been weak. I observed and

analyzed ATCA data of HLX-1 to detect the source in the radio band. We discovered variable radio emission associated to HLX-1 during X-ray state transitions from low/hard to high/soft state (Webb et al., 2012). I determined the mass of the black hole with the method of scaling the flux of the flares of Galactic sources by distance and linear mass. This estimates the mass to be between 5×10^3 $M_\odot$ and 5×10^4 $M_\odot$, which is consistent with previous estimates from other wavelengths. HLX-1 is showing a periodic outburst, undergoing X-ray state transitions, and when in a thermal state, it is best described with the standard disk model. These properties, in addition to the flaring behavior, are consistent with the same phenomenology as GBHBs during an X-ray outburst. Then, I showed that HLX-1 is probably a very good candidate for black hole unification and it fells between stellar-mass and supermassive black holes on the fundamental plane, if a compact jet flux is assumed to be a factor of 10-100 lower than the flaring flux.

8.2 Perspectives

8.2.1 Visible and NIR Wavelengths

Concerning the future perspectives from the optical side, the European Extremely Large Telescope (EELT) is currently being considered with a primary mirror of a diameter of 39 meters. This telescope will be able to collect 26 times more light than VLT, and probably will reveal emission light from the donor star in a ULX system, thus allowing to measure mass functions and deduce black hole masses. This would immediately solve many theoretical questions (see Chapter 1). Additionally, the James Webb Space Telescope (JWST) is also under construction and it is supposed to be launched in 2018. This NIR telescope will help to study the SED of ULXs and to distinguish between emission from a donor star or disk irradiation. This might allow us to determine whether ULXs are more similar to LMXBs or rather to HMXBs. This is particularly important from the aspect of the age of ULXs, because knowing their age could shed light on their origin and evolution as well as on the importance of their feedback, e.g. on their active lifetime, their contribution at the Epoch of Reionization. Moreover, JWST might be valuable to study jet emission from ULXs, which might dominate the SED in certain cases. This is important because the high-frequency break in the synchrotron spectrum of a jet is predicted to scale with the mass of the black hole and the accretion rate. With this knowledge, distinguishing between the sub- and super-Eddington scenarios would be possible.

8.2.2 The Radio Domain

From the radio side there is plenty of place to improve the science case of ULXs and IMBHs. It is very interesting to see whether future observations could rule out the presence of IMBHs in globular clusters, or will support the idea that, these black holes cannot accrete at a high rate from the ISM due to the low gas content. This would be an important knowledge for related fields, such as galaxy evolution and black hole formation and growth. Moreover, these future observations might be able to disentangle between different type of accretion processes, like Bondi-Hoyle or inefficient accretion from a disk.

It is also important to continue the research on the environment of ULXs and discover more and more optical and radio bubbles. Certainly, in-depth study of the ionization processes and the total energy contents of these bubbles can further constrain the significance of beaming, the jet characteristics over the lifetime of the bubble, the formation of these

bubbles and perhaps the formation of the progenitor black hole as well. These calorimeters are also important because they provide means to constrain the average accretion rate needed to supply or inflate the bubble, which is crucial to discriminate between the various accretion scenarios, e.g. sub- or super-Eddington. Moreover, they might also help to establish a link between the physical parameters of these bubbles and the nature of the central X-ray sources.

To this purpose, systematic optical and radio surveys are planned or already on the way, such as the LeMMINGs key science project with e-MERLIN (Multi-Element Radio Linked Interferometer Network), or the pilot surveys carried out with ATCA and EVLA. Furthermore, the nature of these bubbles are completely unknown in the millimeter, submillimeter domain. The Atacama Large Millimeter/submillimeter Array (ALMA) is currently under construction and will operate in full swing in the next coming years. Thanks to the spatial and energy resolution of ALMA, measuring the ionized emission line widths coming from a small spatial region, one might be able to gain more information on the dynamics or velocity distribution inside the bubbles, which could constrain the properties of the outflows from the central engine. Similarly, by using line diagnostics and PDR/XDR codes like MAPPINGS and CLOUDY, one can learn more about the ionization processes. Additionally, the Low-Frequency Array (LOFAR) could pioneer in the search for ULX radio bubbles, because LOFAR operates at few tens of MHz frequencies, where synchrotron sources dominate the sky. Given that the radio spectrum of ULX bubbles is optically thin, their emission is much stronger at low frequencies.

There have been no compact jets or flares detected from ULXs until now. The detection of compact radio emission from ULXs opens up an entirely new window. This could mean that some of them behaves similarly to GBHBs, and may be used to fill the gap between the two populations of stellar-mass and supermassive black holes. Additionally, deep radio surveys will either detect further jets and/or will rule out masses above 1000 $M_{\odot}$ for ULXs. In the long term, using ULXs on the fundamental plane might help better constrain the predicted scaling laws with accretion rate and mass, so that it will be possible to distinguish between advection and jet dominated accretion flows for hard state objects. As seen from HLX-1, we detected transient radio emission. This opens up the possibility to increase the number of potential transients on the radio sky. One of the main key science projects of LOFAR is to detect radio transients, which is also one of the aims of the planned arrays of MeerKAT and ASKAP, the precursors of the Square Kilometer Array (SKA). These facilities will bring new possibilities to detect transient emission from ULXs, which might constrain their outburst and jet properties. With this knowledge, the physics behind the jet line of the Hardness Intensity Diagram might be revealed as well as the mystery of the jet quenching.

8.2.3 The X-ray Band

On the other hand, further important knowledge can be obtained on the X-ray properties of ULXs. Three missions will start soon, NuSTAR (Nuclear Spectroscopic Telescope Array), eROSITA (extended ROentgen Survey with an Imaging Telescope Array) and ASTRO-H. These telescopes, particularly ASTRO-H, might be sensitive enough in a broader energy band allowing to better constrain models of the X-ray spectra. The broadband X-ray behavior properties of ULXs could also shed light on new features e.g. hard tail which might be indicative of jets as in the case of Cyg X-1. Additionally, a

broadband and sensitive X-ray spectrum could also better constrain the presence of optically thick outflows. One of the best hopes from these instruments is to detect further Hyperluminous X-ray sources out to far distances. A growing number of HLXs would certainly support the idea that there is a significant number of sources in the ULX population which cannot be explained with beaming or hyperaccretion. This population might also represent an entirely new class of black holes, bringing us towards revealing the Unknown.

Bibliography

Abbott, B. P., Abbott, R., Adhikari, R., et al. 2009, Phys. Rev. D, 80, 062001

Abdo, A. A., Ackermann, M., Ajello, M., et al. 2010, ApJ, 710, L92

Abel, T., Anninos, P., Norman, M. L., & Zhang, Y. 1998, ApJ, 508, 518

Abolmasov, P., Fabrika, S., Sholukhova, O., & Afanasiev, V. 2007, Astrophysical Bulletin, 62, 36

Abolmasov, P., Fabrika, S., Sholukhova, O., & Kotani, T. 2008, ArXiv e-prints, 0809.0409A

Abramowicz, M. A., Czerny, B., Lasota, J. P., & Szuszkiewicz, E. 1988, ApJ, 332, 646

Acciari, V. A., Aliu, E., Arlen, T., et al. 2011, ApJ, 730, L20

Allen, M. G., Groves, B. A., Dopita, M. A., Sutherland, R. S., & Kewley, L. J. 2008, ApJS, 178, 20

Armijo, M. M. 2012, astro-ph.CO

Arnaud, K. A. 1996, in Astronomical Society of the Pacific Conference Series, Vol. 101, Astronomical Data Analysis Software and Systems V, ed. G. H. Jacoby & J. Barnes, 17

Bahcall, J. N. & Ostriker, J. P. 1975, Nature, 256, 23

Bash, F. N., Gebhardt, K., Goss, W. M., & Vanden Bout, P. A. 2008, AJ, 135, 182

Bauer, F. E. & Brandt, W. N. 2004, ApJ, 601, L67

Baumgardt, H., Makino, J., & Hut, P. 2005, ApJ, 620, 238

Begelman, M. C. 1979, MNRAS, 187, 237

Begelman, M. C. 2002, ApJ, 568, L97

Begelman, M. C., Hatchett, S. P., McKee, C. F., Sarazin, C. L., & Arons, J. 1980, ApJ, 238, 722

Belloni, T. M. 2010, in Lecture Notes in Physics, Berlin Springer Verlag, Vol. 794, Lecture Notes in Physics, Berlin Springer Verlag, ed. T. Belloni, 53

Benacquista, M. J. & Downing, J. M. B. 2011, ArXiv e-prints, 1110.4423B

Binney, J. Tremaine, S. 1987, Princeton University Press

Blandford, R. D. & Königl, A. 1979, ApJ, 232, 34

Blundell, K. M., Bowler, M. G., & Schmidtobreick, L. 2008, ApJ, 678, L47

Bondi, H. & Hoyle, F. 1944, MNRAS, 104, 273

Bozzo, E., Ferrigno, C., Stevens, J., et al. 2011, A&A, 535, L1

Brocksopp, C., Fender, R. P., McCollough, M., et al. 2002, MNRAS, 331, 765

Burrows, D. N., Hill, J. E., Nousek, J. A., et al. 2005, Space Sci. Rev., 120, 165

Cardelli, J. A., Clayton, G. C., & Mathis, J. S. 1989, ApJ, 345, 245

Chevalier, R. A. 1974, ApJ, 188, 501

Cioffi, D. F., McKee, C. F., & Bertschinger, E. 1988, ApJ, 334, 252

Clark, G. W. 1975, ApJ, 199, L143

Colbert, E. J. M. & Mushotzky, R. F. 1999, ApJ, 519, 89

Colbert, E. J. M. & Ptak, A. F. 2002, ApJS, 143, 25

Corbel, S., Fender, R. P., Tomsick, J. A., Tzioumis, A. K., & Tingay, S. 2004, ApJ, 617, 1272

Corbel, S., Koerding, E., & Kaaret, P. 2008, MNRAS, 389, 1697

Corbel, S., Nowak, M. A., Fender, R. P., Tzioumis, A. K., & Markoff, S. 2003, A&A, 400, 1007

Corbel, S., Tomsick, J. A., & Kaaret, P. 2006, ApJ, 636, 971

Coriat, M., Corbel, S., Prat, L., et al. 2011, MNRAS, 414, 677

Cseh, D., Corbel, S., Kaaret, P., et al. 2012, ApJ, 749, 17

Cseh, D., Grisé, F., Corbel, S., & Kaaret, P. 2011, ApJ, 728, L5

Cseh, D., Kaaret, P., Corbel, S., et al. 2010, MNRAS, 406, 1049

Czerny, B., Goosmann, R., & Janiuk, A. 2008, Chinese Journal of Astronomy and Astrophysics Supplement, 8, 302

Dalessandro, E., Lanzoni, B., Ferraro, F. R., et al. 2008, ApJ, 677, 1069

Davis, S. W., Narayan, R., Zhu, Y., et al. 2011, ApJ, 734, 111

de Gasperin, F., Merloni, A., Sell, P., et al. 2011, MNRAS, 415, 2910

de Rijcke, S., Buyle, P., & Dejonghe, H. 2006, MNRAS, 368, L43

Diamond, P. J. 1995, in Astronomical Society of the Pacific Conference Series, Vol. 82, Very Long Baseline Interferometry and the VLBA, ed. J. A. Zensus, P. J. Diamond, & P. J. Napier, 227

Dopita, M. A. & Sutherland, R. S. 1996, ApJS, 102, 161

Dubner, G. M., Holdaway, M., Goss, W. M., & Mirabel, I. F. 1998, AJ, 116, 1842

Ebisuzaki, T., Makino, J., Tsuru, T. G., et al. 2001, ApJ, 562, L19

Fabbiano, G. & Trinchieri, G. 1987, ApJ, 315, 46

Fabbiano, G., Zezas, A., & Murray, S. S. 2001, ApJ, 554, 1035

Fabrika, S. 2004, Astrophysics and Space Physics Reviews, 12, 1

Falcke, H. & Biermann, P. L. 1995, A&A, 293, 665

Falcke, H. & Biermann, P. L. 1996, A&A, 308, 321

Falcke, H. & Biermann, P. L. 1999, A&A, 342, 49

Falcke, H., Körding, E., & Markoff, S. 2004, A&A, 414, 895

Farrell, S. A., Servillat, M., Pforr, J., et al. 2012, ApJ, 747, L13

Farrell, S. A., Webb, N. A., Barret, D., Godet, O., & Rodrigues, J. M. 2009, Nature, 460, 73

Fender, R. P. 2003, MNRAS, 340, 1353

Fender, R. P., Belloni, T. M., & Gallo, E. 2004, MNRAS, 355, 1105

Fender, R. P., Gallo, E., & Jonker, P. G. 2003, MNRAS, 343, L99

Fender, R. P., Garrington, S. T., McKay, D. J., et al. 1999, MNRAS, 304, 865

Fender, R. P., Homan, J., & Belloni, T. M. 2009, MNRAS, 396, 1370

Feng, H. & Kaaret, P. 2006, ApJ, 650, L75

Feng, H. & Kaaret, P. 2008, ApJ, 675, 1067

Feng, H. & Kaaret, P. 2009, ApJ, 696, 1712

Feng, H. & Soria, R. 2011, NewAR, 55, 166

Fornasa, M. & Bertone, G. 2008, International Journal of Modern Physics D, 17, 1125

Foschini, L., Di Cocco, G., Ho, L. C., et al. 2002, A&A, 392, 817

Foster, D. L., Charles, P. A., & Holley-Bockelmann, K. 2010, ApJ, 725, 2480

Frank, J., King, A., & Raine, D. J. 2002, Accretion Power in Astrophysics, 3rd edn. (Cambridge Univerity Press)

Freeland, M., Kuncic, Z., Soria, R., & Bicknell, G. V. 2006, MNRAS, 372, 630

Freire, P. C., Kramer, M., Lyne, A. G., et al. 2001, ApJ, 557, L105

Fryer, C. L., Woosley, S. E., & Heger, A. 2001, ApJ, 550, 372

Gallo, E., Fender, R., Kaiser, C., et al. 2005, Nature, 436, 819

Gallo, E., Fender, R. P., & Pooley, G. G. 2003, MNRAS, 344, 60

Gao, Y., Wang, Q. D., Appleton, P. N., & Lucas, R. A. 2003, ApJ, 596, L171

Gehrels, N. 1986, ApJ, 303, 336

Gehrels, N., Chincarini, G., Giommi, P., et al. 2004, ApJ, 611, 1005

Gladstone, J. C., Roberts, T. P., & Done, C. 2009, MNRAS, 397, 1836

Godet, O., Barret, D., Webb, N. A., Farrell, S. A., & Gehrels, N. 2009, ApJ, 705, L109

Godet, O., Plazolles, B., Kawaguchi, T., et al. 2012, ApJ, 752, 34

González Delgado, R. M., Pérez, E., Cid Fernandes, R., & Schmitt, H. 2008, AJ, 135, 747

Greisen, E. W. 2003, Information Handling in Astronomy - Historical Vistas, 285, 109

Grindlay, J. E., Heinke, C., Edmonds, P. D., & Murray, S. S. 2001, Science, 292, 2290

Grisé, F., Kaaret, P., Corbel, S., et al. 2012, ApJ, 745, 123

Grisé, F., Kaaret, P., Feng, H., Kajava, J. J. E., & Farrell, S. A. 2010, ApJ, 724, L148

Grisé, F., Kaaret, P., Pakull, M. W., & Motch, C. 2011, ApJ, 734, 23

Grisé, F., Pakull, M., & Motch, C. 2006, in ESA Special Publication, Vol. 604, The X-ray Universe 2005, ed. A. Wilson, 451

Grisé, F., Pakull, M. W., Soria, R., et al. 2008, A&A, 486, 151

Guedes, J., Madau, P., Kuhlen, M., Diemand, J., & Zemp, M. 2009, ApJ, 702, 890

Gültekin, K., Cackett, E. M., Miller, J. M., et al. 2009, ApJ, 706, 404

Gültekin, K., Miller, M. C., & Hamilton, D. P. 2004, ApJ, 616, 221

Gürkan, M. A., Freitag, M., & Rasio, F. A. 2004, ApJ, 604, 632

Hameury, J.-M., Barret, D., Lasota, J.-P., et al. 2003, A&A, 399, 631

Heinz, S. & Sunyaev, R. A. 2003, MNRAS, 343, L59

Hutchings, J. B., Crampton, D., Cowley, A. P., Bianchi, L., & Thompson, I. B. 1987, AJ, 94, 340

Jeltema, T. E., Canizares, C. R., Buote, D. A., & Garmire, G. P. 2003, ApJ, 585, 756

Jenkins, L. P., Roberts, T. P., Warwick, R. S., Kilgard, R. E., & Ward, M. J. 2005, MNRAS, 357, 401

Jin, J., Feng, H., Kaaret, P., & Zhang, S.-N. 2011, ApJ, 737, 87

Kaaret, P. 2002, ApJ, 578, 114

Kaaret, P., Alonso-Herrero, A., Gallagher, J. S., et al. 2004a, MNRAS, 348, L28

Kaaret, P. & Corbel, S. 2009, ApJ, 697, 950

Kaaret, P., Corbel, S., Prestwich, A. H., & Zezas, A. 2003, Science, 299, 365

Kaaret, P., Feng, H., Wong, D. S., & Tao, L. 2010, ApJ, 714, L167

Kaaret, P., Prestwich, A. H., Zezas, A., et al. 2001, MNRAS, 321, L29

Kaaret, P., Simet, M. G., & Lang, C. C. 2006, ApJ, 646, 174

Kaaret, P., Ward, M. J., & Zezas, A. 2004b, MNRAS, 351, L83

Kaiser, C. R. & Alexander, P. 1997, MNRAS, 286, 215

Karachentsev, I. D., Sharina, M. E., Dolphin, A. E., et al. 2002, A&A, 385, 21

King, A. R. 2009, MNRAS, 393, L41

King, I. R. 1966, AJ, 71, 64

Kirshner, R. P. & Chevalier, R. A. 1980, ApJ, 242, L77

Kong, A. K. H. 2007, ApJ, 661, 875

Kong, A. K. H., Heinke, C. O., di Stefano, R., et al. 2010, MNRAS, 407, L84

Körding, E., Colbert, E., & Falcke, H. 2005, A&A, 436, 427

Körding, E., Falcke, H., & Corbel, S. 2006a, A&A, 456, 439

Körding, E., Falcke, H., & Markoff, S. 2002, A&A, 382, L13

Körding, E., Rupen, M., Knigge, C., et al. 2008a, Science, 320, 1318

Körding, E. G., Fender, R. P., & Migliari, S. 2006b, MNRAS, 369, 1451

Körding, E. G., Jester, S., & Fender, R. 2008b, MNRAS, 383, 277

Kubota, A., Done, C., & Makishima, K. 2002, MNRAS, 337, L11

Kubota, A., Mizuno, T., Makishima, K., et al. 2001, ApJ, 547, L119

Lacey, C., Duric, N., & Goss, W. M. 1997, ApJS, 109, 417

Lang, C. C., Kaaret, P., Corbel, S., & Mercer, A. 2007, ApJ, 666, 79

Lang, K. R. 1999, Astrophysical formulae (Springer Verlag Berlin Heidelberg New York)

Lanzoni, B., Dalessandro, E., Ferraro, F. R., et al. 2007, ApJ, 668, L139

Lasota, J.-P., Alexander, T., Dubus, G., et al. 2011, ApJ, 735, 89

Lehmann, I., Becker, T., Fabrika, S., et al. 2005, A&A, 431, 847

Levin, L., Bailes, M., Bates, S., et al. 2010, ApJ, 721, L33

Lira, P., Lawrence, A., & Johnson, R. A. 2000, MNRAS, 319, 17

Longair, M. S. 1994, High energy astrophysics. Vol.2: Stars, the galaxy and the interstellar medium (Cambridge: Cambridge University Press, —c1994, 2nd ed.)

Lozinskaya, T. A. & Moiseev, A. V. 2007, MNRAS, 381, L26

Lu, T.-N. & Kong, A. K. H. 2011, ApJ, 729, L25

Lützgendorf, N., Kissler-Patig, M., Noyola, E., et al. 2011, A&A, 533, A36

Maccarone, T. & Koerding, E. 2006, Astronomy and Geophysics, 47, 060000

Maccarone, T. J. 2004, MNRAS, 351, 1049

Maccarone, T. J., Fender, R. P., & Tzioumis, A. K. 2005, MNRAS, 356, L17

Maccarone, T. J., Kundu, A., Zepf, S. E., & Rhode, K. L. 2011, MNRAS, 410, 1655

Madau, P. & Rees, M. J. 2001, ApJ, 551, L27

Makishima, K., Kubota, A., Mizuno, T., et al. 2000, ApJ, 535, 632

Markoff, S., Falcke, H., & Fender, R. 2001, A&A, 372, L25

Matonick, D. M. & Fesen, R. A. 1997, ApJS, 112, 49

McClintock, J. E. & Remillard, R. A. 2006, Black hole binaries (Cambridge University Press), 157–213

McHardy, I. M., Koerding, E., Knigge, C., Uttley, P., & Fender, R. P. 2006, Nature, 444, 730

Merloni, A., Heinz, S., & di Matteo, T. 2003, MNRAS, 345, 1057

Meylan, G., Sarajedini, A., Jablonka, P., et al. 2001, AJ, 122, 830

Mezcua, M. & Lobanov, A. P. 2011, Astronomische Nachrichten, 332, 379

Miller, J. M., Fabian, A. C., & Miller, M. C. 2004, ApJ, 614, L117

Miller, M. C. & Colbert, E. J. M. 2004, International Journal of Modern Physics D, 13, 1

Miller, M. C. & Hamilton, D. P. 2002, MNRAS, 330, 232

Miller, N. A., Mushotzky, R. F., & Neff, S. G. 2005, ApJ, 623, L109

Miller-Jones, J. C. A., Wrobel, J. M., Sivakoff, G. R., et al. 2012, ApJ, 755, L1

Miocchi, P. 2007, MNRAS, 381, 103

Mirabel, F. 2011, in AGN Physics in the CTA Era (AGN 2011)

Mirabel, I. F. & Rodríguez, L. F. 1999, ARA&A, 37, 409

Moon, D.-S., Harrison, F. A., Cenko, S. B., & Shariff, J. A. 2011, ApJ, 731, L32

Moretti, A., Piotto, G., Arcidiacono, C., et al. 2009, A&A, 493, 539

Motch, C., Pakull, M. W., Grisé, F., & Soria, R. 2011, Astronomische Nachrichten, 332, 367

Narayan, R. & Yi, I. 1994, ApJ, 428, L13

Neilsen, J. & Lee, J. C. 2009, Nature, 458, 481

Nucita, A. A., de Paolis, F., Ingrosso, G., Carpano, S., & Guainazzi, M. 2008, A&A, 478, 763

Osterbrock, D. E. & Ferland, G. J. 2006, Astrophysics of gaseous nebulae and active galactic nuclei, 2nd edn. (CA: University Science Books)

Ostriker, J. P. & McKee, C. F. 1988, Reviews of Modern Physics, 60, 1

Pakull, M. W. & Angebault, L. P. 1986, Nature, 322, 511

Pakull, M. W. & Grisé, F. 2008, in American Institute of Physics Conference Series, Vol. 1010, A Population Explosion: The Nature & Evolution of X-ray Binaries in Diverse Environments, ed. R. M. Bandyopadhyay, S. Wachter, D. Gelino, & C. R. Gelino, 303–307

Pakull, M. W. & Mirioni, L. 2002, ArXiv Astrophysics e-prints, 0202488

Pakull, M. W. & Mirioni, L. 2003, in Revista Mexicana de Astronomia y Astrofisica Conference Series, Vol. 15, Revista Mexicana de Astronomia y Astrofisica Conference Series, ed. J. Arthur & W. J. Henney, 197–199

Pakull, M. W., Soria, R., & Motch, C. 2010, Nature, 466, 209

Paragi, Z., Taylor, G. B., Kouveliotou, C., et al. 2010, Nature, 463, 516

Paragi, Z., Vermeulen, R. C., Fejes, I., et al. 1999, A&A, 348, 910

Pellegrini, S. 2005, ApJ, 624, 155

Perez M., S. & Blundell, K. M. 2009, MNRAS, 397, 849

Pérez-Ramírez, D., Mezcua, M., Leon, S., & Caballero-García, M. D. 2011, Astronomische Nachrichten, 332, 384

Perna, R., Narayan, R., Rybicki, G., Stella, L., & Treves, A. 2003, ApJ, 594, 936

Pizzolato, F., Wolter, A., & Trinchieri, G. 2010, MNRAS, 406, 1116

Plotkin, R. M., Markoff, S., Kelly, B. C., Körding, E., & Anderson, S. F. 2012, MNRAS, 419, 267

Ponti, G., Fender, R. P., Begelman, M. C., et al. 2012, MNRAS, L417

Pooley, D. & Rappaport, S. 2006, ApJ, 644, L45

Portegies Zwart, S. F., Baumgardt, H., Hut, P., Makino, J., & McMillan, S. L. W. 2004, Nature, 428, 724

Portegies Zwart, S. F. & McMillan, S. L. W. 2000, ApJ, 528, L17

Portegies Zwart, S. F. & McMillan, S. L. W. 2002, ApJ, 576, 899

Porter, R. L. 2010, MNRAS, 407, L59

Poutanen, J., Lipunova, G., Fabrika, S., Butkevich, A. G., & Abolmasov, P. 2007, MNRAS, 377, 1187

Press, W. H., Teukolsky, S. A., Vetterling, W. T., & Flannery, B. P. 1992, Numerical recipes in C. The art of scientific computing, 2nd edn. (Cambridge: University Press)

Pretorius, M. L. & Knigge, C. 2012, MNRAS, 419, 1442

Roberts, T. P. & Colbert, E. J. M. 2003, MNRAS, 341, L49

Roberts, T. P., Gladstone, J. C., Goulding, A. D., et al. 2011, Astronomische Nachrichten, 332, 398

Roberts, T. P., Goad, M. R., Ward, M. J., & Warwick, R. S. 2003, MNRAS, 342, 709

Roberts, T. P., Goad, M. R., Ward, M. J., Warwick, R. S., & Lira, P. 2002a, ArXiv Astrophysics e-prints, 0202017

Roberts, T. P., Goad, M. R., Ward, M. J., et al. 2001, MNRAS, 325, L7

Roberts, T. P. & Warwick, R. S. 2000, MNRAS, 315, 98

Roberts, T. P., Warwick, R. S., Ward, M. J., & Murray, S. S. 2002b, MNRAS, 337, 677

Rushton, A., Spencer, R., Fender, R., & Pooley, G. 2010, A&A, 524, A29

Russell, D. M., Fender, R. P., Gallo, E., & Kaiser, C. R. 2007, MNRAS, 376, 1341

Russell, D. M., Maitra, D., Dunn, R. J. H., & Fender, R. P. 2011a, MNRAS, 416, 2311

Russell, D. M., Yang, Y.-J., Gladstone, J. C., Wiersema, K., & Roberts, T. P. 2011b, Astronomische Nachrichten, 332, 371

Sánchez-Sutil, J. R., Muñoz-Arjonilla, A. J., Martí, J., et al. 2006, A&A, 452, 739

Sarazin, C. L., Kundu, A., Irwin, J. A., et al. 2003, ApJ, 595, 743

Sault, R. J., Teuben, P. J., & Wright, M. C. H. 1995, in Astronomical Society of the Pacific Conference Series, Vol. 77, Astronomical Data Analysis Software and Systems IV, ed. R. A. Shaw, H. E. Payne, & J. J. E. Hayes, 433

Sądowski, A. 2009, ApJS, 183, 171

Servillat, M., Farrell, S. A., Lin, D., et al. 2011, ApJ, 743, 6

Shakura, N. I. & Sunyaev, R. A. 1973, A&A, 24, 337

Shepherd, M. C., Pearson, T. J., & Taylor, G. B. 1994, in Bulletin of the American Astronomical Society, Vol. 26, Bulletin of the American Astronomical Society, 987–989

Silk, J. & Arons, J. 1975, ApJ, 200, L131

Sirianni, M., Jee, M. J., Benítez, N., et al. 2005, PASP, 117, 1049

Skrutskie, M. F., Cutri, R. M., Stiening, R., et al. 2006, AJ, 131, 1163

Soria, R., Fender, R. P., Hannikainen, D. C., Read, A. M., & Stevens, I. R. 2006a, MNRAS, 368, 1527

Soria, R., Hau, G. K. T., Graham, A. W., et al. 2010a, MNRAS, 405, 870

Soria, R., Kuncic, Z., Broderick, J. W., & Ryder, S. D. 2006b, MNRAS, 370, 1666

Soria, R., Pakull, M. W., Broderick, J. W., Corbel, S., & Motch, C. 2010b, MNRAS, 409, 541

Soria, R., Wickramasinghe, D. T., Hunstead, R. W., & Wu, K. 1998, ApJ, 495, L95

Strickland, D. K., Colbert, E. J. M., Heckman, T. M., et al. 2001, ApJ, 560, 707

Strohmayer, T. E. 2009, ApJ, 706, L210

Strohmayer, T. E. & Mushotzky, R. F. 2003, ApJ, 586, L61

Strohmayer, T. E., Mushotzky, R. F., Winter, L., et al. 2007, ApJ, 660, 580

Sutton, A. D., Roberts, T. P., Walton, D. J., Gladstone, J. C., & Scott, A. E. 2012, MNRAS, 423, 1154

Swartz, D. A., Soria, R., Tennant, A. F., & Yukita, M. 2011, ApJ, 741, 49

Swartz, D. A., Tennant, A. F., & Soria, R. 2009, ApJ, 703, 159

Tao, L., Feng, H., Grisé, F., & Kaaret, P. 2011, ApJ, 737, 81

Thornton, K., Gaudlitz, M., Janka, H.-T., & Steinmetz, M. 1998, ApJ, 500, 95

Tikhonov, N. A. & Galazutdinova, O. A. 2010, Astronomy Letters, 36, 167

Tody, D. 1993, in Astronomical Society of the Pacific Conference Series, Vol. 52, Astronomical Data Analysis Software and Systems II, ed. R. J. Hanisch, R. J. V. Brissenden, & J. Barnes, 173

Trudolyubov, S. & Priedhorsky, W. 2004, ApJ, 616, 821

Tudose, V., Fender, R. P., Kaiser, C. R., et al. 2006, MNRAS, 372, 417

Ulvestad, J. S., Greene, J. E., & Ho, L. C. 2007, ApJ, 661, L151

van Dyk, S. D., Sramek, R. A., Weiler, K. W., Hyman, S. D., & Virden, R. E. 1994, ApJ, 425, L77

Vesperini, E. & Trenti, M. 2010, ApJ, 720, L179

Volonteri, M. 2012, Science, 337, 544

Walton, D. J., Roberts, T. P., Mateos, S., & Heard, V. 2011, MNRAS, 416, 1844

Wang, Y.-Y., Wang, L., Xiang, S.-P., et al. 2010, Research in Astronomy and Astrophysics, 10, 199

Weaver, R., McCray, R., Castor, J., Shapiro, P., & Moore, R. 1977, ApJ, 218, 377

Webb, N., Cseh, D., Lenc, E., et al. 2012, Science, 337, 554

Webb, N. A., Barret, D., Godet, O., et al. 2010, ApJ, 712, L107

Weisskopf, M. C., Brinkman, B., Canizares, C., et al. 2002, PASP, 114, 1

Wiersema, K., Farrell, S. A., Webb, N. A., et al. 2010, ApJ, 721, L102

Wilms, J., Allen, A., & McCray, R. 2000, ApJ, 542, 914

Wilson, W. E., Ferris, R. H., Axtens, P., et al. 2011, MNRAS, 416, 832

Winter, L. M., Mushotzky, R. F., & Reynolds, C. S. 2006, ApJ, 649, 730

Wrobel, J. M., Greene, J. E., & Ho, L. C. 2011, AJ, 142, 113

Wyithe, S. & Loeb, A. 2011, ArXiv e-prints, 1111.5424W

Yang, H. & Skillman, E. D. 1993, AJ, 106, 1448

Zampieri, L. & Roberts, T. P. 2009, MNRAS, 400, 677

Zezas, A., Ward, M. J., & Murray, S. S. 2003, ApJ, 594, L31

Appendix

A&A 523, A34 (2010)
DOI: 10.1051/0004-6361/201015145

Astronomy & Astrophysics

Radio interferometric observations of two core-dominated triple radio sources at $z > 3$

D. Cseh[1], S. Frey[2,4], Z. Paragi[3,4], L. I. Gurvits[3,5], and K. É. Gabányi[2,4]

[1] Laboratoire Astrophysique des Interactions Multi-echelles (UMR 7158), CEA/DSM-CNRS-Université Paris Diderot, CEA Saclay, 91191 Gif-sur-Yvette, France
e-mail: david.cseh@cea.fr
[2] FÖMI Satellite Geodetic Observatory, PO Box 585, 1592 Budapest, Hungary
e-mail: [frey;gabanyik]@sgo.fomi.hu
[3] Joint Institute for VLBI in Europe, Postbus 2, 7990 AA Dwingeloo, The Netherlands
e-mail: [zparagi;lgurvits]@jive.nl
[4] MTA Research Group for Physical Geodesy and Geodynamics, PO Box 91, 1521 Budapest, Hungary
[5] Institute of Space and Astronautical Science, Japan Aerospace Exploration Agency, 3-1-1 Yoshinodai Chuo-ku, Kanagawa, Sagamihara 252-5210, Japan

Received 3 June 2010 / Accepted 5 August 2010

ABSTRACT

Aims. We selected two radio quasars (J1036+1326 and J1353+5725) based on their 1.4-GHz radio structure, which is dominated by a bright central core and a pair of weaker and nearly symmetric lobes at ∼10″ angular separation. They are optically identified in the Sloan Digital Sky Survey (SDSS) at spectroscopic redshifts $z > 3$. We investigate the possibility that their core-dominated triple morphology can be a sign of restarted radio activity in these quasars, involving a significant repositioning of the radio jet axis.
Methods. We present the results of high-resolution radio imaging observations of J1036+1326 and J1353+5725, performed with the European Very Long Baseline Interferometry (VLBI) Network (EVN) at 1.6 GHz. These data are supplemented by archive observations from the Very Large Array (VLA). We study the large- and small-scale radio structures and the brightness temperatures, then estimate relativistic beaming parameters.
Results. We show that the central emission region of these two high-redshift, core-dominated triple sources is compact but resolved at ∼10 milli-arcsecond resolution. We find that it is not necessary to invoke large misalignment between the VLBI jet and the large-scale radio structure to explain the observed properties of the sources.

Key words. radio continuum: galaxies – galaxies: active – galaxies: jets – quasars: general – quasars: individual: J1036+1326 – quasars: individual: J1353+5725

1. Introduction

Active galactic nuclei (AGNs) are believed to be powered by mass accretion onto supermassive (from $\sim 10^6$ up to $\sim 10^{10}$ $M_\odot$) black holes. However, only a small fraction of them (less than 10%) appear luminous at radio frequencies. A typical lifetime of a radio-loud quasar is $\sim 10^6$ yr, so the radio jet activity can be regarded as intermittent in the whole lifetime of an object.

We use the term "restarted activity" for a re-occurence of *radio* activity over the lifetime of a source. This can involve interruption and re-ignition of the radio activity (Kaiser et al. 2000), which can be episodic or not. This does not necessarily involve a complete cessation of the radio activity (Schoenmakers et al. 2000b).

The most spectacular examples of recurrent activity in radio-loud AGNs demonstrate rare double-double (e.g. Lara et al. 1999; Schoenmakers et al. 2000a,b; Kaiser et al. 2000) or triple-double (Brocksopp et al. 2007) radio galaxies. In these objects, the inner and outer pairs of lobes have a common centre and are generally well aligned (within 8°). The only double-double radio quasar candidate to date, 4C 02.27, has been identified by Jamrozy et al. (2009). A recent review of recurrent activity in AGNs, along with a list of known double-double sources has been published by Saikia & Jamrozy (2009). The two highest redshift objects known with confirmed episodic activity are 3C 294 ($z = 1.877$) and J1835+6204 ($z = 0.51$) (Saikia & Jamrozy 2009).

A modest fraction of AGNs exhibit triple structures at ∼10″ angular separation with fainter, nearly symmetric extended lobes, and relatively bright compact cores. We call these core-dominated triple sources (CDTs, Marecki et al. 2006). The cores of these sources are typically unresolved (<5″) in the NRAO[1] Very Large Array (VLA) Faint Images of the Radio Sky at Twenty-centimeters (FIRST) survey (White et al. 1997) at 1.4 GHz. In a 1.4-GHz VLA imaging survey of a complete flux-density limited sample of powerful core-dominated sources (with core flux density $S_{5\,\mathrm{GHz}} > 1$ Jy), Murphy et al. (1993) found that less than 10% of the sources showed similar triple structures below $z \sim 1.5$. No CDTs were found above this redshift among their 87 sources.

The CDT structure has been interpreted as a possible signature of once ceased and then restarted activity. It could be coupled with the repositioning of the central radio jet axis (Marecki et al. 2006). A plausible explanation is that new infalling

[1] The National Radio Astronomy Observatory (NRAO) is a facility of the National Science Foundation operated under cooperative agreement by Associated Universities, Inc.

material from, e.g., a galaxy merger triggers the re-occurence of accretion. The process could eventually result in the merger of the central supermassive black holes. The coalescence of the black holes might cause a sudden flip in the black hole spin, consequently in the orientation of the jet axis (e.g. Merritt & Ekers 2002; Gergely & Biermann 2009). The jet reorientation could also be caused by the precession of the spin axis. According to the standard unified model of radio-loud AGN (Urry & Padovani 1995), emission from relativistic jets pointing close to our line of sight will be Doppler-boosted. A change in jet orientation thus may lead to an observed increase in core dominance. Very Long Baseline Interferometry (VLBI) can provide information on the milli-arcsecond scale (mas) properties of these compact jets.

When an extended radio source lacks fuelling from the central engine, it may eventually become an ultra-steep-spectrum source (Röttgering et al. 1994; De Breuck et al. 2000). Deep, low-frequency surveys that are sensitive to this diffuse emission have not provided clear signatures of earlier activity cycles (Cohen et al. 2005; Mack et al. 2005; Sirothia et al. 2009). This suggests that restarted activity is a rather rare phenomenon.

Here we report on radio-interferometric observations of two high-redshift quasars, J1036+1326 ($z = 3.10$) and J1353+5725 ($z = 3.46$). We observed these sources with the European VLBI Network (EVN) at 1.6 GHz. We compared their high-resolution radio images with those obtained from archive VLA data on the arcsecond scale. In Sect. 2, we describe the selection of the two target sources. In Sects. 3 and 4, we present our observations and describe the radio properties of the two quasars. Finally, we estimate the viewing angles and analyse the source parameters in the context of possibly restarted activity (Sect. 5). Throughout this paper we assume a cosmological model with $H_0 = 70$ km s^{-1} Mpc^{-1}, $\Omega_m = 0.3$, and $\Omega_\Lambda = 0.7$.

2. Target selection

We searched for those compact, high-redshift ($z > 3$) radio sources that are unresolved (<5″) in the FIRST survey catalogue[2] (White et al. 1997), that have an integral flux density $S_{1.4\,\mathrm{GHz}} > 20$ mJy, and that are optically identified with quasars in the Sloan Digital Sky Survey[3] (SDSS). Their spectroscopic redshifts were taken from the 4th edition of the SDSS Quasar Catalog (Schneider et al. 2007) which consists of objects in the SDSS 5th Data Release (DR5). The ultimate goal was to define a sample of radio-loud, optically identified, high-redshift quasars that are good candidates for VLBI imaging observations. Earlier experience gained from the Deep Extragalactic VLBI-Optical Survey (DEVOS, Mosoni et al. 2006; Frey et al. 2008) suggests that the majority (nearly 90%) of the carefully pre-selected compact FIRST-SDSS objects show compact mas-scale radio emission and thus are suitable targets for VLBI imaging observations at centimetre wavelengths, regardless of spectral index.

We found two peculiar objects (J1036+1326 and J1353+5725) in the sample of ∼100 compact high-redshift radio quasars selected using the method above. Although they are catalogued as close pairs of separate, unresolved sources in FIRST, the analysis of archival 1.4-GHz VLA A-array images clearly revealed extended triple structures (see Sect. 3). Both of the bright quasars are associated with weaker two-sided radio lobes; i.e., they satisfy the criteria for CDT sources. We did not apply any selection based on the radio spectrum.

[2] http://sundog.stsci.edu

[3] http://www.sdss.org

3. Observations and data analysis

3.1. VLA observations

The quasar J1036+1326 was observed with the VLA on 1991 July 8 (project code: AT126). The source J1353+5725 was observed on 1991 June 29 (project code: AR250). For both experiments, the array was in its most extended A configuration, which provided angular resolution of 1″−1.″6. The observing frequency was 1.4 GHz. The total on-source integration times were 16 min and 2.5 min for J1036+1326 and J1353+5725, respectively. The data sets were obtained from the NRAO Data Archive[4]. For spectral information, we also obtained and analysed archive 8-GHz VLA observations of J1036+1326 (project AR415; 1999 August 9) and 5-GHz VLA observations of J1353+5725 (project AW748; 2008 October 15). The on-source integration time in these two last experiments were 1 min and 9.5 min, respectively. The data calibration was performed using the NRAO Astronomical Image Processing System (AIPS, e.g. Greisen 2003) in a standard way. The 1.4-GHz VLA images of the two sources are shown in Figs. 1 and 2.

3.2. EVN observations

To check whether the VLA cores of J1036+1326 and J1353+5725 are resolved (for example, show a small separation double structure, thus indicating a restarting AGN activity) or unresolved (thus showing evidence of a compact jet) on 10 milli-arcsecond scales, we carried out EVN observations at 1.6 GHz. The 6-h observations were accommodated in the 2009 September 10–11 e-VLBI run. The data were transferred from the telescopes in real-time to the EVN Data Processor at the Joint Institute for VLBI in Europe (JIVE) in Dwingeloo, the Netherlands (Szomoru 2008). The participating VLBI stations were Effelsberg (Germany), Jodrell Bank Lovell Telescope, Cambridge (United Kingdom), Medicina (Italy), Toruń (Poland), Onsala (Sweden), Sheshan (PR China), and the phased array of the Westerbork Synthesis Radio Telescope (WSRT; The Netherlands). The total aggregate bitrate per station was 512 Mbps. There were eight 8 MHz intermediate frequency channels (IFs) in both left and right circular polarisations.

The sources were observed in phase-reference mode. This allowed us to increase the coherent integration time spent on the target source and thus to improve the sensitivity of the observations. Phase-referencing involves regularly interleaving observations between the target source and a nearby, bright, and compact reference source (e.g. Beasley & Conway 1995). The delay, delay rate, and phase solutions derived for the phase-reference calibrators (J1025+1253 and J1408+5613 in our experiment) were interpolated and applied to the respective target within the target-reference cycle time of 7 min. The target source was observed for 5-min intervals in each cycle. The total accumulated observing time on each target source was 1.6 h.

The AIPS was used for the VLBI data calibration following standard procedures (e.g. Diamond 1995). The visibility amplitudes were calibrated using system temperatures and antenna gains measured at the antennas. Fringe-fitting was performed for the calibrator sources using 3-min solution intervals. The calibrated visibility data were exported to the Caltech Difmap program (Shepherd et al. 1994) where the VLBI images (Figs. 3, 4) were made after several cycles of CLEAN and phase-only (later amplitude and phase) self-calibration iterations.

[4] http://archive.nrao.edu

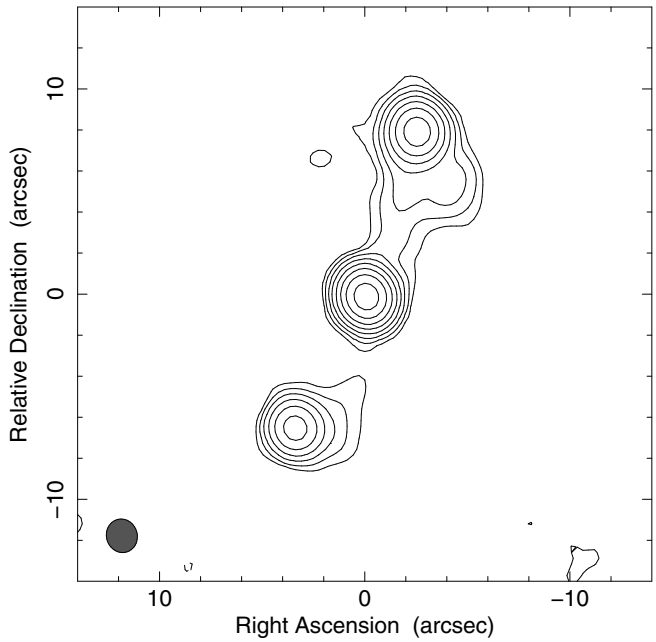

Fig. 1. The naturally-weighted 1.4-GHz VLA A-array image of J1036+1326. The first contours are drawn at ±0.25 mJy/beam. The positive contour levels increase by a factor of 2. The peak brightness is 48 mJy/beam. The Gaussian restoring beam displayed in the lower-left corner is 1.″6 × 1.″5 (full width at half maximum, FWHM) at a major axis position angle PA = 17°.

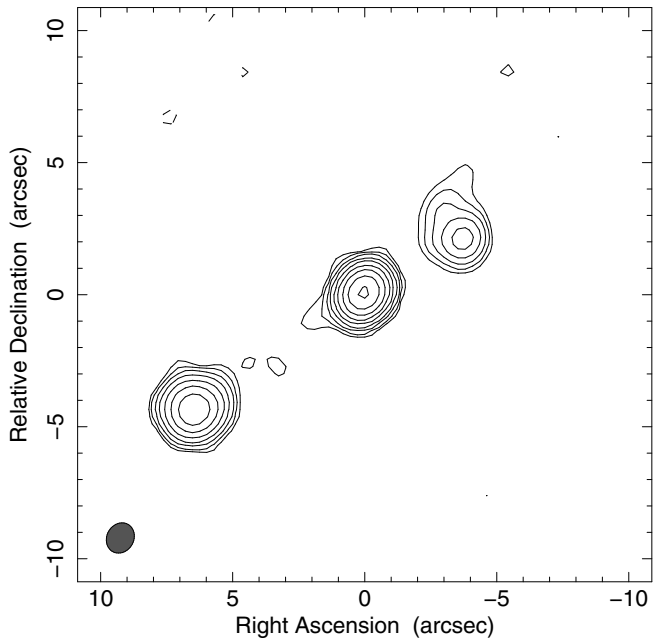

Fig. 2. The naturally-weighted 1.4-GHz VLA A-array image of J1353+5725. The first contours are drawn at ±0.6 mJy/beam. The positive contour levels increase by a factor of 2. The peak brightness is 172 mJy/beam. The Gaussian restoring beam is 1.″2 × 1.″0 at PA = −29°.

4. Results

Observing in phase-reference mode allowed us to determine accurate coordinates of the target sources. For J1036+1326, we obtained right ascension $10^{h}36^{m}26\overset{s}{.}88565$, declination +13°26′51.″7598 with an error of 1 mas. For J1353+5725, we obtained $13^{h}53^{m}26\overset{s}{.}03368$, +57°25′52.″9097 with an error of 2 mas.

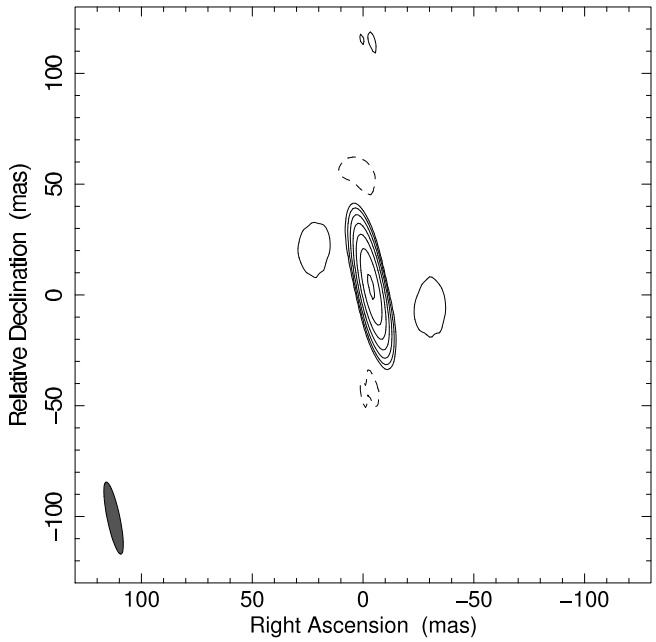

Fig. 3. The 1.6-GHz VLBI image of the core of J1036+1326. The first contours are drawn at ±0.71 mJy/beam. The positive contour levels increase by a factor of 2. The peak brightness is 50 mJy/beam. The Gaussian restoring beam is 33 mas × 6 mas at PA = 12°.

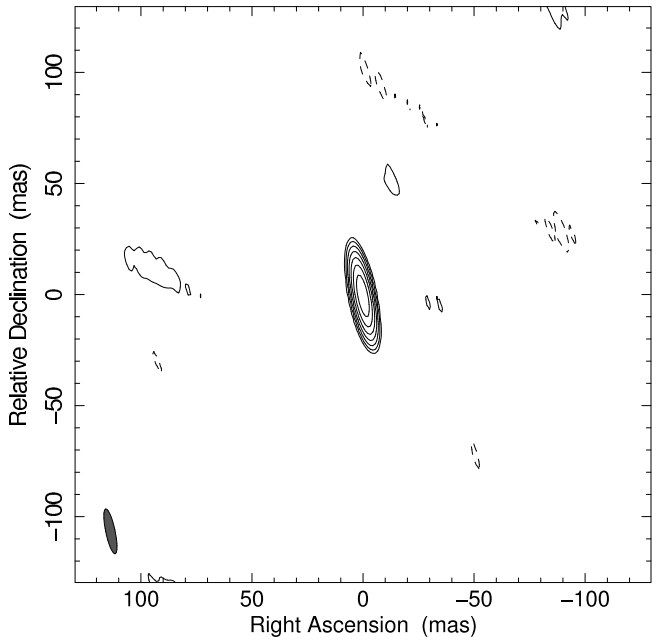

Fig. 4. The 1.6-GHz VLBI image of the core of J1353+5725. The first contours are drawn at ±1.7 mJy/beam. The positive contour levels increase by a factor of 2. The peak brightness is 197 mJy/beam. The Gaussian restoring beam is 21 mas × 4 mas at PA = 12°.

The angular extent of the large-scale 1.4-GHz radio structure of J1036+1326 (Fig. 1) is 15.″8, which corresponds to a projected linear size of ∼120 kpc at $z = 3.10$. For the quasar J1353+5725 (Fig. 2), the angular size is 12.″23, and the linear size is ∼90 kpc at $z = 3.46$.

To characterise the source brightness distributions on the VLA scale with simple models, we used Difmap to fit circular Gaussian model components to the self-calibrated interferometric visibility data. The flux density of the best-fit model

Table 1. Observed and derived parameters of the two quasars from the VLA measurements.

Name	Component	$S_{1.4\,\mathrm{GHz}}$ [mJy]	$S_{5/8\,\mathrm{GHz}}$ [mJy]	α
J1036+1326	Core	50.4 ± 1.1	62.6 ± 1.3	+0.1
	North	27.8 ± 0.6	2.9 ± 0.2	−1.2
	South	13.0 ± 0.4	1.7 ± 0.2	−1.1
J1353+5725	Core	177.9 ± 3.6	144.9 ± 2.9	−0.2
	North	18.6 ± 0.7	3.9 ± 0.5	−1.3
	South	94.0 ± 2.0	20.9 ± 0.7	−1.3

Notes. $S_{1.4\,\mathrm{GHz}}$ is the flux density at 1.4 GHz (in the L band), while $S_{5/8\,\mathrm{GHz}}$ denotes the 8 GHz (X-band) flux density in the case of J1036+1326, and the 5 GHz (C-band) flux density in the case of J1353+5725.

Table 2. Observed and derived parameters of the two quasar cores from the EVN measurements.

Name	Redshift*	$S_{1.6\,\mathrm{GHz}}$ [mJy]**	ϑ [mas]	T_b [K]
J1036+1326	3.10	58.1 ± 2.9	4.7	5×10^9
J1353+5725	3.46	231.1 ± 11.6	2.2	1×10^{11}

Notes. * 4th edition of the SDSS Quasar Catalog (Schneider et al. 2007); ** errors correspond to 1-σ.

components are listed in Table 1, along with two-point spectral indices derived from the flux densities measured at different frequencies. The spectral index (α) was calculated by assuming a power-law dependence of the flux density (S) and the observing frequency (ν): $S \sim \nu^\alpha$. The flux density errors were estimated following the approach by Fomalont (1999) and correspond to 1-σ. The 1-σ error of the spectral indices is less than 0.05.

In Table 2, we list the parameters of the circular Gaussian models (flux density, size) fitted to the 1.6-GHz EVN visibility data in Difmap. We also derived the brightness temperatures according to the following formula (e.g. Condon et al. 1982):

$$T_\mathrm{b} = 1.22 \times 10^{12}(1+z)\frac{S}{\vartheta^2\nu^2}\ \ [\mathrm{K}] \tag{1}$$

where S is the flux density (Jy), ν is the observed frequency (GHz) and ϑ the FWHM size of the Gaussian (mas).

5. Discussion

5.1. Large-scale morphologies and viewing angles

In order to investigate whether the large-scale morphology is dominated by beamed or unbeamed emission, we estimated the arm-length ratio. The latter corresponds to the light travel time for the radio emission morphological components on the approaching and receding sides. We assumed that the observed arm-length ratios are the result of relativistic motions over the lifetime of the sources rather than the difference in the environment on the two sides. The 1.4-GHz VLA images (Figs. 1 and 2) allowed us to determine the arm-length ratios (R) of the north and south components. For the sources J1036+1326 and J1353+5725, we get $R_1 = 1.15$ and $R_2 = 1.84$, respectively.

To place approximate limits on the expansion speed and the viewing angle we used

$$\beta\cos\phi = (R-1)/(R+1), \tag{2}$$

where $\beta = v/c$ is the velocity of the plasma blob (v) expressed in the units of the speed of light (c), and ϕ is the angle between the approaching jet direction and the line of sight (e.g. Taylor & Vermeulen 1997).

We can thus derive a lower limit to β (because $\cos\phi \leq 1$), and an upper limit to ϕ (because $\beta < 1$). For J1036+1326, the constraints ($\phi_1 < 86°$ and $\beta_1 \geq 0.07$) are not very strict, but for J1353+5725 ($\phi_2 < 73°$ $\beta_2 \geq 0.30$) they are more meaningful. In particular, from the arm-length ratio alone, we can infer that there is mildly relativistic motion in the case of J1353+5725. This method is valid regardless of the specifics of the jet model. It remains valid for the spots or discrete blobs in the head of the jet created by shocks (Schoenmakers et al. 2000b) and for pairs of unequally-sized edge-brightened lobes of an FR-II morphology (Fanaroff & Riley 1974).

5.2. Small-scale morphologies and viewing angles

As a starting hypothesis, we assume that the inner radio jets that remain compact with VLBI (Figs. 3 and 4) are well aligned with the ~100-kpc scale radio structure we see in the VLA images (Figs. 1 and 2). Using the range of the allowed viewing angles ($\phi_1 < 86°$ and $\phi_2 < 73°$) estimated above, we can calculate the Doppler boosting factors (δ) and compare the expected brightness temperatures with our measured values (Table 2, Col. 5), in order to determine whether we need to introduce large misalignments to describe the observed morphology.

The observed and intrinsic brightness temperatures are related as

$$\delta = T_\mathrm{b}/T_\mathrm{b,int}, \tag{3}$$

where δ is the Doppler factor. Here we assume a typical intrinsic brightness temperature of $T_\mathrm{b,int} \simeq 5 \times 10^{10}$ K, which is valid if energy equipartition holds between the magnetic field and the particles in the radio source (Readhead 1994). We obtain Doppler factors $\delta_1 = 0.1$ (which in fact means de-amplification) and $\delta_2 = 2$ for J1036+1326 and J1353+5725, respectively.

The Doppler boosting factor can be expressed as

$$\delta = \frac{1}{\Gamma(1-\beta\cos\phi)}, \tag{4}$$

where the Lorentz factor is $\Gamma = (1-\beta^2)^{-1/2}$.

For J1036+1326, $\delta_1 = 0.1$, and even the possible maximum value of $\phi_1 = 86°$ can be made consistent if the bulk speed in the inner jet is $\beta_\mathrm{inn} = 0.9957$. It would correspond to a Lorentz factor $\Gamma \simeq 11$, a value often measured in other radio-loud AGNs (e.g. Lister et al. 2009). However, models of the inner jet with much higher Lorentz factors, hence smaller viewing angles, should be considered because of the quasar identification of the source. If we allow for a very high $\Gamma \simeq 30$, the misalignment would be ~40°. For comparison, the largest measured misalignment between the inner and outer lobes in 3C 293, a double-double radio galaxy, is ~35°, although this is higher than the typical values (Saikia & Jamrozy 2009, and references therein). In our case, the pc-scale structure detected is insufficient for making definitive conclusions about alignment of pc- and kpc-scale structures.

In the case of J1353+5725, the measured Doppler factor ($\delta_2 = 2$) implies a maximum of 30° for the viewing angle because $\sin\phi \leq 1/\delta$ (e.g. Urry & Padovani 1995). Thus we cannot assume $\phi_2 = 72°$ for the inner jet, i.e. we cannot use the same approach as in case of the first source. We can construct a set of reasonable physical and geometric parameters which *does not require jet repositioning* and is fully consistent with our observations. On the other hand, the largest possible misalignment could reach about 70°.

In addition, we can set a boundary for the outer β parameter by considering the outer structure as an FR-II, since the hot spot advance speeds for high-luminosity FR-II radio galaxies is $\beta \lesssim 0.3$ (e.g. Liu et al. 1992; O'Dea et al. 2009). Even if we use this boundary, we can explain the source without any misalignment; e.g., if the approaching inner and outer jets are both inclined by $\phi = 20^\circ$ to the line of sight, then a bulk jet speed $\beta_{\rm inn} = 0.9903$ would be consistent with the measured Doppler factor in the inner region (Eq. (4)). The corresponding Lorentz factor is $\Gamma \simeq 7$. On the other hand, $\beta_{\rm out} = 0.31$ and $\phi = 20^\circ$ would be consistent with the observed arm-length ratio (Eq. (2)) of the outer structures of J1353+5725 where the jet flow most likely becomes mildly relativistic. Therefore, the observed morphologies do not require invoking the concept of jet repositioning, although our data cannot rule out the possibility of misaligned inner and outer structures.

5.3. The radio spectra

We obtained a two-point radio spectral index of each component in our VLA images (Figs. 1 and 2) and listed in Col. 5 of Table 1. In general, the steep spectra of the outer components ($\alpha \simeq -1.2$) may indicate radiative losses. The steep-spectrum sources are good candidates for finding fossils from earlier episodic activity (Sirothia et al. 2009). However, it is not convincing that we see relic lobes in the present case, because, at least for J1036+1326, there is a clear indication of a jet-like feature connecting the core and the northern lobe in the VLA image (Fig. 1). In addition, the core dominance of these sources is somewhat expected at high redshift because the relatively high emitted (rest-frame) frequency is $(1 + z)$ times the observing frequency. Considering the steep spectra of the radio lobes (Table 1), if one places these sources at e.g. $z \simeq 0.5$, then the (observed) 1.4-GHz flux density of the brighter lobes in these objects would far exceed that of the flat-spectrum core.

6. Conclusions

We used radio interferometric imaging observations to study the structure of two high-redshift quasars, J1036+1326 ($z = 3.10$) and J1353+5725 ($z = 3.46$). Archive VLA data show that the sources are extended to ~100 kpc projected linear sizes. They are dominated by a bright central core and a pair of weaker and nearly symmetric lobes. On the other hand, EVN observations at angular resolution that is almost three orders of magnitude higher confirmed that the central jets are compact, at least on ~10 pc linear scales. CDT sources are sometimes interpreted as examples of once ceased and then restarted radio-loud AGNs. It has been claimed that the reignition of their central engine could be coupled with a change in the spin axis of the central accreting, supermassive black hole, hence with the repositioning of the radio jet direction.

We described a general method for testing the misalignments between the small- and large-scale structures of triple radio sources, using VLA and VLBI imaging observations. We applied this method for two CDT quasars at high redshift ($z > 3$), J1036+1326 and J1353+5725. There is no evidence that their morphology would require any misalignment between their characteristic inner and outer radio structures, although misalignments cannot be ruled out by our data.

Considering the radio spectra of the sources we concluded that the core-dominance of these sources can be explained by their high redshift. The relatively high emitted frequency is $(1+z)$ times the observing frequency. Taking the steep spectra of the radio lobes into account, if placed to $z \simeq 0.5$, the 1.4-GHz flux density of the brighter lobes in these objects would far exceed that of the flat-spectrum core.

Acknowledgements. The EVN is a joint facility of European, Chinese, South African, and other radio-astronomy institutes funded by their national research councils. This activity is supported by the European Community Framework Programme 7, Advanced Radio Astronomy in Europe, grant agreement No. 227290. The e-VLBI developments in Europe were supported by the EC DG-INFSO funded Communication Network Developments project "EXPReS", Contract No. 02662. The research leading to these results has received funding from the European Community's Seventh Framework Programme (FP7/2007-2013) under grant agreement number ITN 215212 "Black Hole Universe", and the Hungarian Scientific Research Fund (OTKA, grant No. K72515).

References

Beasley, A. J., & Conway, J. E. 1995, in Very Long Baseline Interferometry and the VLBA, ed. J. A. Zensus, P. J. Diamond, & P. J. Napier, ASP Conf. Ser., 82, 327
Brocksopp, C., Kaiser, C. R., Schoenmakers, A. P., & de Bruyn, A. G. 2007, MNRAS, 382, 1019
Cohen, A. S., Röttgering, H. J. A., Jarvis, M. J., Kassim, N. E., & Lazio, T. J. W. 2004, ApJS, 150, 417
Condon, J. J., Condon, M. A., Gisler, G., & Puschell, J. J. 1982, ApJ, 252, 102
De Breuck, C., van Breugel, W., Röttgering, H. J. A., & Miley, G. 2000, A&AS, 143, 303
Diamond, P. J. 1995, in Very Long Baseline Interferometry and the VLBA, ed. J. A. Zensus, P. J. Diamond, & P. J. Napier, ASP Conf. Ser., 82, 227
Fanaroff, B. L., & Riley, J. M. 1974, MNRAS, 167, 31
Fomalont, E. B. 1999, ASPC 180, 301
Frey, S., Gurvits, L. I., Paragi, Z., et al. 2008, A&A, 477, 781
Gergely, Á. L., & Biermann, P. L. 2009, ApJ, 697, 1621
Greisen, E. W. 2003, in Astrophysics and Space Science Library, ed. A. Heck, 285, 109
Jamrozy, M., Saikia, D. J., & Konar, C. 2009, MNRAS, 399, L141
Lara, L., Marquez, I., Cotton, W. D., et al. 1999, A&A, 348, 699
Kaiser, C. R., Shoenmakers, A. P., & Röttgering, H. J. 2000, MNRAS, 315, 381
Lister, M. L., Cohen, M. H., Homan, D. C., et al. 2009, AJ, 138, 1874
Liu, C., Pooley, G., & Riley, J. M. 1992, MNRAS, 257, 545
Mack, K.-H., Vigotti, M., Gregorini, L., et al. 2005, A&A, 435, 863
Marecki, A., Thomasson, P., Mack, K.-H., & Kunert-Bajraszewska, M. 2006, A&A, 448, 479
Merritt, D., & Ekers, R. D. 2002, Science, 297, 1310
Mosoni, L., Frey, S., Gurvits, L. I., et al. 2006, A&A, 445, 413
Murphy, D. W., Browne, I. W. A., & Perley, R. A. 1993, MNRAS, 264, 298
O'Dea, C. P., Daly, R. A., Kharb, P., Freeman, K. A., & Baum, S. A. 2009, A&A, 494, 471
Readhead, A. C. S. 1994, ApJ, 426, 51
Röttgering, H. J. A., Lacy, M., Miley, G. K., Chambers, K. C., & Saunders, R. 1994, A&AS, 108, 79
Saikia, D. J., & Jamrozy, M. 2009, Bull. Astr. Soc. India, 37, 63
Sirothia, S. K., Saikia, D. J., Ishwara-Chandra, C. H., & Kantharia, N. G. 2009, MNRAS, 392, 1403
Shepherd, M. C., Pearson, T. J., & Taylor, G. B. 1994, BAAS, 26, 987
Schneider D. P., Hall P. B., Richards G. T., et al. 2007, AJ, 134, 102
Schoenmakers, A. P., de Bruyn, A. G., Röttgering, H. J. A., van der Laan, H., & Kaiser, C. R. 2000a, MNRAS, 315, 371
Schoenmakers, A. P., de Bruyn, A. G., Röttgering, H. J. A., van der Laan, H., & Kaiser, C. R. 2000b, MNRAS, 315, 395
Szomoru, A. 2008, Proceedings of Science, PoS(IX EVN Symposium)040
Taylor, G. B., & Vermeulen, R. C. 1997, ApJ, 485, 9
Urry, C. M., & Padovani, P., 1995, PASP, 107, 803
White, R. L., Becker, R. H., Helfand, D. J., & Gregg, M. D. 1997, ApJ, 475, 479

The Astrophysical Journal, 745:123 (12pp), 2012 February 1 doi:10.1088/0004-637X/745/2/123

OPTICAL EMISSION OF THE ULTRALUMINOUS X-RAY SOURCE NGC 5408 X-1: DONOR STAR OR IRRADIATED ACCRETION DISK?

F. Grisé[1], P. Kaaret[1], S. Corbel[2], H. Feng[3], D. Cseh[2], and L. Tao[3]
[1] Department of Physics and Astronomy, University of Iowa, Van Allen Hall, Iowa City, IA 52242, USA; fabien-grise@uiowa.edu
[2] Laboratoire Astrophysique des Interactions Multi-échelles (UMR 7158), CEA/DSM-CNRS-Université Paris Diderot, CEA Saclay, F-91191 Gif sur Yvette, France
[3] Department of Engineering Physics and Center for Astrophysics, Tsinghua University, Beijing 100084, China
Received 2011 May 31; accepted 2011 September 5; published 2012 January 9

ABSTRACT

We obtained three epochs of simultaneous *Hubble Space Telescope* (*HST*)/Wide Field Camera 3 and *Chandra* observations of the ultraluminous X-ray source (ULX) NGC 5408 X-1. The counterpart of the X-ray source is seen in all *HST* filters, from the UV through the near-IR (NIR), and for the first time, we resolve the optical nebula around the ULX. We identified a small OB association near the ULX that may be the birthplace of the system. The stellar association is young, ∼5 Myr, contains massive stars up to 40 $M_{\odot}$, and is thus similar to associations seen near other ULXs, albeit younger. The UV/optical/NIR spectral energy distribution (SED) of the ULX counterpart is consistent with that of a B0I supergiant star. We are also able to fit the whole SED from the X-rays to the NIR with an irradiated disk model. The three epochs of data show only marginal variability and thus, we cannot firmly conclude on the nature of the optical emission.

Key words: accretion, accretion disks – black hole physics – X-rays: binaries – X-rays: individual (NGC 5408 X-1)

Online-only material: color figures

1. INTRODUCTION

Ultraluminous X-ray sources (ULXs) are extragalactic sources that are not at the nucleus of their galaxy and emit well above the Eddington limit of a 20 $M_{\odot}$ black hole ($L_X \sim 3 \times 10^{39}$ erg s^{-1}). The most important, still unresolved question is whether these objects contain intermediate-mass black holes—IMBHs—($M > 100\ M_{\odot}$) or stellar mass black holes with super-Eddington or beamed emission.

A direct answer regarding the mass of compact objects in ULXs would be possible if a radial velocity curve of absorption lines from the companion star, or emission lines coming from the accretion disk, could be obtained. To date, this has proven to be a real challenge due to the lack of absorption lines in ULX optical spectra and what seem to be non-periodic variations of the only traceable emission line, He IIλ4686, in Holmberg IX X-1 and NGC 1313 X-2 (Roberts et al. 2011). The only exception, to date, is the optically very luminous source P13 in NGC 7793 (Motch et al. 2011) where absorption lines from a late B supergiant star (in addition to an He II emission line) have been observed. This is a very promising candidate to constrain the mass function of the system. However, this is the only example out of more than 10 identified optical counterparts.

In all other ULXs, the true nature of the donor star is mostly unknown. The X-ray light curve of M82 X-1 shows a 62 day periodicity consistent with a strictly periodic signal and hence is likely the orbital period of the binary system (Kaaret & Feng 2007). If the companion star fills its Roche lobe, this means that such star has to be of low-density and hence would be a giant or supergiant star (Kaaret et al. 2006). Other constraints on the nature of the donor stars rely on studies of their environment. Indeed, some counterparts belong to or are located nearby small stellar associations (Soria et al. 2005; Grisé et al. 2008, 2011), where it is possible to constrain the association age, and thus the maximum mass for a member star. This has led to maximum mass estimates of 15–20 $M_{\odot}$ that apply as well to the donor star of the ULX systems, if mass transfer did not play an important role. In some other cases (Feng & Kaaret 2008; Yang et al. 2011), the constraints arise from field stars in the absence of such associations. But these estimates are based on indirect evidence and the precise stellar type of those stars remains unknown.

The most obvious problem in identifying the companion star in the optical emission of ULXs is that the flux contribution coming from the accretion disk (direct and irradiated) is not known but is definitely present in some sources. The best hint comes from NGC 1313 X-2, where its optical light curve is contaminated by short-term, stochastic variations that are likely due to X-ray reprocessing in the accretion disk (Grisé et al. 2008; Liu et al. 2009; Impiombato et al. 2011) and also from X-ray heating in the companion star (Zampieri et al. 2012). Broad He II emission lines with equivalent widths up to 10 times higher than in the brightest Galactic high-mass X-ray binaries are present in the optical spectrum of some counterparts (e.g., Pakull et al. 2006; Roberts et al. 2011; Cseh et al. 2011) and are also a direct proof of significant X-ray reprocessing in these systems.

The counterpart optical colors have often been used to place constraints on the companion star. The high optical/UV luminosities and blue colors suggest early-type, OB stars (e.g., Liu et al. 2002; Kaaret et al. 2004; Soria et al. 2005). But, as suggested by Kaaret (2005) and Pakull et al. (2006), the optical light may be contaminated, or even dominated, by the irradiated accretion disk (Kaaret & Corbel 2009; Tao et al. 2011). This is similar to active low-mass X-ray binaries, although ULXs have higher X-ray luminosities and may have more massive donor stars. Unfortunately, the optical spectral energy distributions (SEDs) of hot, irradiated disks look rather like those of OB stars.

Our present work is devoted to a well-studied ULX, NGC 5408 X-1 (hereafter N5408X1), located at 4.8 Mpc (Karachentsev et al. 2002). N5408X1 is a bona fide ULX with an average luminosity (0.3–10 keV) of 1×10^{40} erg s^{-1}

(Strohmayer 2009) that displays clear variability within a factor of ∼2 (Kaaret & Feng 2009; Strohmayer 2009; Kong 2011). Intensive *Swift* monitoring of the source has been used to infer a ∼115 day period that has been interpreted as the orbital period of the ULX system (Strohmayer 2009), although Foster et al. (2010) suggests that this modulation may instead be superorbital. The X-ray spectrum of N5408X1 does not seem to vary much (Kaaret & Feng 2009). All observations performed to date show a soft spectrum $\Gamma \sim 2.5$ and the presence of a soft component. Different interpretations have been put forward: if interpreted in the framework of Galactic black hole binaries (GBHBs), standard models (power law plus disk component) point to the presence of a massive black hole if the temperature of the disk scales as in Galactic counterparts (Kaaret et al. 2003; Soria et al. 2004; Strohmayer et al. 2007). The power law would be in that case the signature of a corona as seen in GBHBs. Instead, the interpretation in the context of super-critical accreting systems would mean that the black hole is much smaller, with the possibility that a strong wind is the origin of the soft component, while the high energy part of the spectrum would be due to disk emission inside the spherization radius (Poutanen et al. 2007). Alternatively, the soft component may represent emission from the outer disk with the hard emission associated with thermal Comptonization (Gladstone et al. 2009; Middleton et al. 2011). Finally, the soft excess may arise from reflection from the disk (Caballero-García & Fabian 2010).

N5408X1 is also one of the few ULXs where quasi-periodic oscillations (QPOs) have been discovered (Strohmayer et al. 2007; Strohmayer 2009). Analogous to GBHBs, Strohmayer (2009) have interpreted this feature as a type C low-frequency QPO (LFQPO), which would indicate that N5408X1 hosts an IMBH. Middleton et al. (2011) have challenged this conclusion and concluded that even the most super-Eddington BHB, GRS 1915+105, is not really a good match to the properties of N5408X1. They hypothesized that the temporal and spectral properties are more consistent with the feature seen in some Narrow Line Seyfert 1 galaxies which are supposed to be even higher super-Eddington sources, which would indicate a black hole with mass $\lesssim 100\ M_{\odot}$. But the large uncertainties associated with the black hole masses in those systems avoids any definitive conclusion.

N5408X-1 is also seen at other wavelengths. This source is one of the few ULXs detected in radio, the emission being consistent with a powerful nebula surrounding the ULX (Kaaret et al. 2003; Soria et al. 2006; Lang et al. 2007; Cseh et al. 2012). This nebula is also detected in optical wavelengths (Pakull & Mirioni 2003; Soria et al. 2006; Kaaret & Corbel 2009) where the optical emission is consistent with X-ray photoionization. The optical counterpart of the ULX, first uniquely identified in a *Hubble Space Telescope* (*HST*)/WFPC2 image by Lang et al. (2007) as a $V_0 = 22.2$ mag object, has been subsequently studied using Very Large Telescope spectroscopy by Kaaret & Corbel (2009) and Cseh et al. (2011). The optical spectrum of N5408X1 is similar to many other ULXs, displaying a blue continuum with superimposed strong and narrow emission lines coming from the nebula. Of prime interest is the presence of broad components with widths of ∼750 km s^{-1} in the He II and H_{β} lines (Cseh et al. 2011) that appear spatially point-like, similar to the optical continuum of the counterpart. The radial velocity of the broad He II line varies, which may represent the motion of the compact object or motions within the accretion disk (see Roberts et al. 2011 for the behavior of this line in other sources).

In this paper, we present new, simultaneous *Chandra* and *HST* observations of N5408X1. *HST* observations that allow us to present for the first time the SED of a ULX from the ultraviolet (UV) to the near-infrared (NIR) wavelengths. Combined with simultaneous X-ray data, we are able to show that an irradiated disk model fits well all the data. We discuss other alternatives and suggest a way to confirm this result with new observations.

2. OBSERVATIONS AND DATA ANALYSIS

We obtained three series of multiwavelength observations using the recently installed Wide Field Camera 3 (WFC3) instrument on board the *HST* (Program ID 12010, PI: P. Kaaret, along with simultaneous *Chandra* X-ray observations (Program ID 11400085, PI: P. Kaaret).

2.1. Optical Observations

Each *HST* visit consisted of observations in UV, optical, and near-infrared filters. UV and optical observations were carried out in the F225W, F336W, F547M, and F845M filters using the WFC3/UVIS camera. We used the WFC3/IR camera for the near-infrared observations, in the F105W and F160W filters. A single observation was done with the WFC3/UVIS using the narrow F502N filter to isolate emission due to the forbidden [O III]λ5007 line. A summary of the observations can be found in Table 1.

We performed aperture and point-spread function (PSF) photometry on the drizzled images. Aperture photometry was done only on the four UVIS images, since the crowding is really severe in the infrared images, preventing any reliable photometry in the region nearby the ULX with this method. We performed the aperture photometry with SExtractor version 2.5.0 (Bertin & Arnouts 1996), using an aperture 2 pixels in radius (i.e., 0.″08). The background was estimated by relying on the global mapping done by SExtractor. Aperture corrections were calculated using relatively bright and isolated stars, performing photometry using a 0.″4 radius (i.e., 10 pixels).

PSF photometry was performed using DAOPHOT II (Stetson 1987) under ESO-MIDAS. For the UVIS images, we used a 2.5 pixel aperture (i.e., 0.″10) which corresponds approximately to 60%–70% of the enclosed energy (Kalirai et al. 2009b) depending on the filter. The background was chosen to be a 10 pixel width annulus located at 15 pixels from the object centroid. Given the use of a subarray for the UVIS observations, we used a constant PSF across the frame. Aperture corrections were calculated using the aperture photometry routine within the DAOPHOT package in the same way as previously described. A similar procedure was applied to the IR images, with a 2.0 pixel aperture (i.e., 0.″26), corresponding to 70%–80% of the enclosed energy (Kalirai et al. 2009a). The IR observations were performed in full frame mode; thus we used a quadratically varying PSF in the field. Aperture corrections were measured as for the UVIS images. Finally, zero points calculated for a 0.″4 radius were taken out of Kalirai et al. (2009a, 2009b) for UVIS and IR observations.

It turns out that the main uncertainty in the photometry is due to the aperture correction. Indeed, the use of a window for the UVIS observations means that the number of bright stars is low, which forces us to rely on fewer stars, or less bright stars, for the correction.

In the rest of this paper, we will use the results coming from the PSF photometry, but the two methods give consistent results for bright or isolated stars, with differences below 0.1 mag.

Table 1
The *HST*/WFC3 Observations for NGC 5408 X-1

	ID	Instrument	Filter	Date	Exposure Time (s)
Epoch 1	ibde01030	UVIS	F225W	2010 May 2	560
	ibde01020	UVIS	F336W	2010 May 2	280
	ibde01010	UVIS	F547M	2010 May 2	200
	ibde01040	UVIS	F845M	2010 May 2	280
	ibde01060	IR	F105W	2010 May 2	298.5
	ibde01050	IR	F160W	2010 May 2	498.5
Epoch 2	ibde02030	UVIS	F225W	2010 May 15	560
	ibde02020	UVIS	F336W	2010 May 15	280
	ibde02010	UVIS	F547M	2010 May 15	200
	ibde02040	UVIS	F845M	2010 May 15	280
	ibde02060	IR	F105W	2010 May 15	298.5
	ibde02050	IR	F160W	2010 May 15	498.5
Epoch 3	ibde53030	UVIS	F225W	2010 Sep 12	560
	ibde53020	UVIS	F336W	2010 Sep 12	280
	ibde53010	UVIS	F547M	2010 Sep 12	200
	ibde53040	UVIS	F845M	2010 Sep 12	280
	ibde53060	IR	F105W	2010 Sep 12	298.5
	ibde53050	IR	F160W	2010 Sep 12	498.5
	ibde04010	UVIS	F502N	2010 Dec 26	2600

2.2. X-Ray Observations

N5408X1 was observed with *Chandra* using the Advanced CCD Imaging Spectrometer (ACIS) instrument. For each series of *HST* observations, we obtained a simultaneous 12 ks *Chandra* exposure. Given the high count rate expected of N5408X1, only one chip (ACIS S3) was used, with a one-eighth subarray mode. This reduces the frame time to 0.441 s which mitigates pile-up in the data. The observed count rate in the three observations varies from ∼0.3 to ∼0.4 counts s^{-1}. Standard extraction of spectra was done using the CIAO 4.3 package (Fruscione et al. 2006) with CALDB 4.4.1. We rebinned the spectra to a minimum of a 5σ significance per bin. All fitting was performed using ISIS version 1.6.1-26 (Houck & Denicola 2000).

3. RESULTS

The optical counterpart of the ULX, as identified by Lang et al. (2007), is visible in all the *HST* filters used in this study. Figure 1 shows a composite image including the F225W, F502N ([O III]) and F845M filters. Magnitudes and corresponding fluxes of the ULX counterpart are presented in Table 2. This image highlights the presence of a small stellar association, close to the ULX at about 4″ (∼93 pc) northeast with ∼20 bright, resolved stars. In the field of view of our WFC3 observations, the other nearest association is at ∼8″ northwest from the ULX, and is likely connected to the super star clusters that are located farther north as seen on previous broadband *HST* and Subaru images (Kaaret et al. 2003; Soria et al. 2006). This image also shows the nebula to be well resolved, with a diameter ∼2.″5 (∼60 pc), consistent with the size of the radio nebula (Lang et al. 2007; Cseh et al. 2012). From optical long-slit spectroscopy, Kaaret & Corbel (2009) derived a size of 30 pc (FWHM) for the He III region along the slit. The size of the nebula in lower ionization emission lines, e.g., [O III], is broader, about 40 pc (FWHM) with broad wings. This is quite consistent with the *HST* imaging.

3.1. Stellar Environment

We used color–magnitude diagrams to investigate the stellar environment of the ULX. Data have been corrected by the reddening derived from the nebula surrounding the ULX, $E(B-V) = 0.08$ (Kaaret & Corbel 2009) using the extinction law of Cardelli et al. (1989) with $R_V = 3.1$. The metallicity of NGC 5408 has been estimated to be about a tenth of the solar metallicity, with $12 + \log(O/H) = 7.99$ (Mendes de Oliveira et al. 2006), which translates into $Z = 0.002$ (based on a standard solar composition, Grevesse & Sauval 1998). We note that the age of the young and blue stars that are most common in the color–magnitude diagrams are not really sensitive to metallicity and therefore our age estimate does not depend on this parameter. However, the stars on the red supergiant branch are more sensitive to this effect; the red supergiants apparent in the (F547M,F845M) diagram indicate a subsolar metallicity, but with a best fit consistent with $Z = 0.008$.

Thus, we overplotted isochrones from the Padova library (Bertelli et al. 1994; Marigo et al. 2008; Girardi et al. 2008, 2010) with a metallicity $Z = 0.008$. We present (Figure 2) three diagrams using the F225W, F336W, F547M, and F845M filters. The diagrams with blue colors (upper panels of Figure 2) show that the stars associated with the relatively dense association nearby the ULX form a young upper main-sequence/supergiant branch that is well fitted by an isochrone of age ∼5 Myr. A young age for the association is supported by the presence of six bright ($M_{F547M} \sim M_V = -6$ to -7) stars with blue colors that are most likely blue supergiants. Again, we emphasize that the age of these young stars does not depend much on the metallicity, using $Z = 0.008$ instead of $Z = 0.002$ introduces at most an uncertainty of 1 Myr, which is smaller than the uncertainties due to photometric errors and isochrones models. We also overplotted Padova evolutionary tracks with various masses on the color–magnitude diagrams (Figure 3). From those, it is apparent that numerous stars from the association (and from the field) are massive objects with masses up to 30–40 $M_\odot$.

3.2. ULX

We present (Figure 4) a detailed SED of this ULX, from 2400 to 15400 Å. The three SEDs taken at different epochs are very consistent with each other. In each case, we fitted the SED by

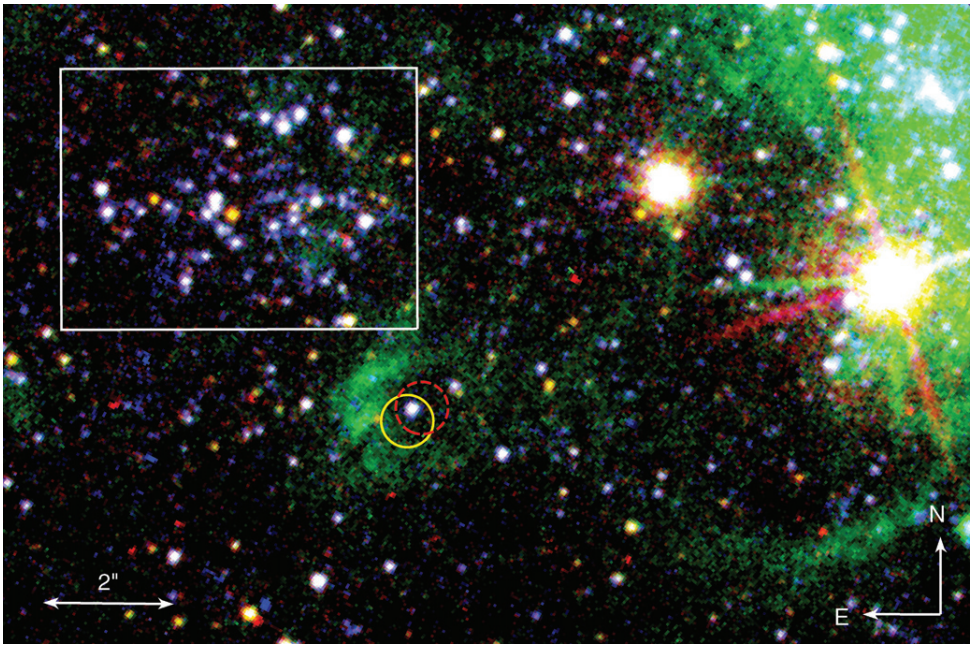

Figure 1. *HST*/WFC3 composite image (blue—F225W, green—F502N, red—F845M) of the field surrounding NGC 5408 X-1. 1″ represents 23.3 pc at the distance of NGC 5408 X-1. Overplotted are the radio positions from Very Large Array (yellow full circle) and ATCA observations (red dashed circle; Lang et al. 2007) with a conservative error circle of 0.″4 in radius. The white box (5.″5 × 4.″0) shows the nearby stellar association. Stars located inside this rectangle were plotted differently in the color–magnitude diagrams (see Figures 2 and 3).

(A color version of this figure is available in the online journal.)

Table 2
Brightness of the ULX Counterpart in Different Filters, from the *HST*/WFC3 Observations

	Filter	Aperture Correction	VEGAmag	Flux (10^{-18} erg s^{-1} cm^{-2} Å^{-1})
Epoch 1	F225W	0.44 ± 0.03	20.09 ± 0.04 (0.024)	38.60 ± 1.42
	F336W	0.42 ± 0.06	20.64 ± 0.07 (0.029)	18.02 ± 1.16
	F547M	0.53 ± 0.06	22.43 ± 0.07 (0.029)	3.91 ± 0.25
	F845M	0.59 ± 0.04	22.42 ± 0.08 (0.067)	1.03 ± 0.08
	F105W	0.06 ± 0.03	22.84 ± 0.09 (0.072)	0.34 ± 0.03
	F160W	0.20 ± 0.05	22.48 ± 0.10 (0.091)	0.12 ± 0.01
Epoch 2	F225W	0.42 ± 0.04	20.04 ± 0.05 (0.034)	40.42 ± 1.86
	F336W	0.45 ± 0.05	20.55 ± 0.05 (0.022)	19.58 ± 0.90
	F547M	0.50 ± 0.06	22.30 ± 0.07 (0.026)	4.41 ± 0.28
	F845M	0.54 ± 0.04	22.37 ± 0.07 (0.052)	1.08 ± 0.07
	F105W	0.22 ± 0.07	22.63 ± 0.10 (0.090)	0.41 ± 0.04
	F160W	0.22 ± 0.05	22.37 ± 0.10 (0.073)	0.14 ± 0.01
Epoch 3	F225W	0.49 ± 0.04	19.97 ± 0.04 (0.028)	43.11 ± 1.59
	F336W	0.53 ± 0.08	20.56 ± 0.08 (0.021)	19.40 ± 1.43
	F547M	0.51 ± 0.08	22.26 ± 0.08 (0.014)	4.58 ± 0.34
	F845M	0.61 ± 0.04	22.26 ± 0.06 (0.038)	1.20 ± 0.07
	F105W	0.16 ± 0.07	22.55 ± 0.12 (0.076)	0.44 ± 0.05
	F160W	0.14 ± 0.06	22.44 ± 0.10 (0.100)	0.13 ± 0.01

Notes. Magnitudes are expressed in the *HST*/WFC3 Vegamag system. The errors on the magnitude include the aperture correction uncertainty. The value between brackets is the photometric error, as derived by DAOPHOT.

using a simple power law with $F_\nu \propto \nu^\alpha$, F_ν being the flux in units of erg s^{-1} cm^{-2} Hz^{-1}. The indices of the power-law fits are, respectively, 1.37 ± 0.03, 1.33 ± 0.03, and 1.31 ± 0.03 for SEDs 1, 2, and 3. However, these fits are unacceptable with χ^2_ν of 7.7, 7.7, and 5.0 for 4 degrees of freedom. Using only the F336W, F547M and F845M values to constrain the fit, we obtain a good fit with $\chi^2_\nu < 1$. The indices are not too different, with 1.38 ± 0.08, 1.40 ± 0.07, and 1.28 ± 0.08 for SEDs 1, 2, and 3 and the normalizations at $\lambda = 5500$Å are, respectively, 4.87 ± 0.16, 5.30±0.15, and 5.54±0.17 in units of 10^{-18} erg s^{-1} cm^{-2}. This result is consistent with the index value found by Tao et al. (2011; 1.41 ± 0.14) from four simultaneous observations obtained by *HST*/WFPC2 in 2009 April and covering the same wavelength range (3300-8000 Å). As can be seen on Figure 4, those fits show a clear deviation from a straight power law in the NIR wavelengths, and also show marginal evidence for a

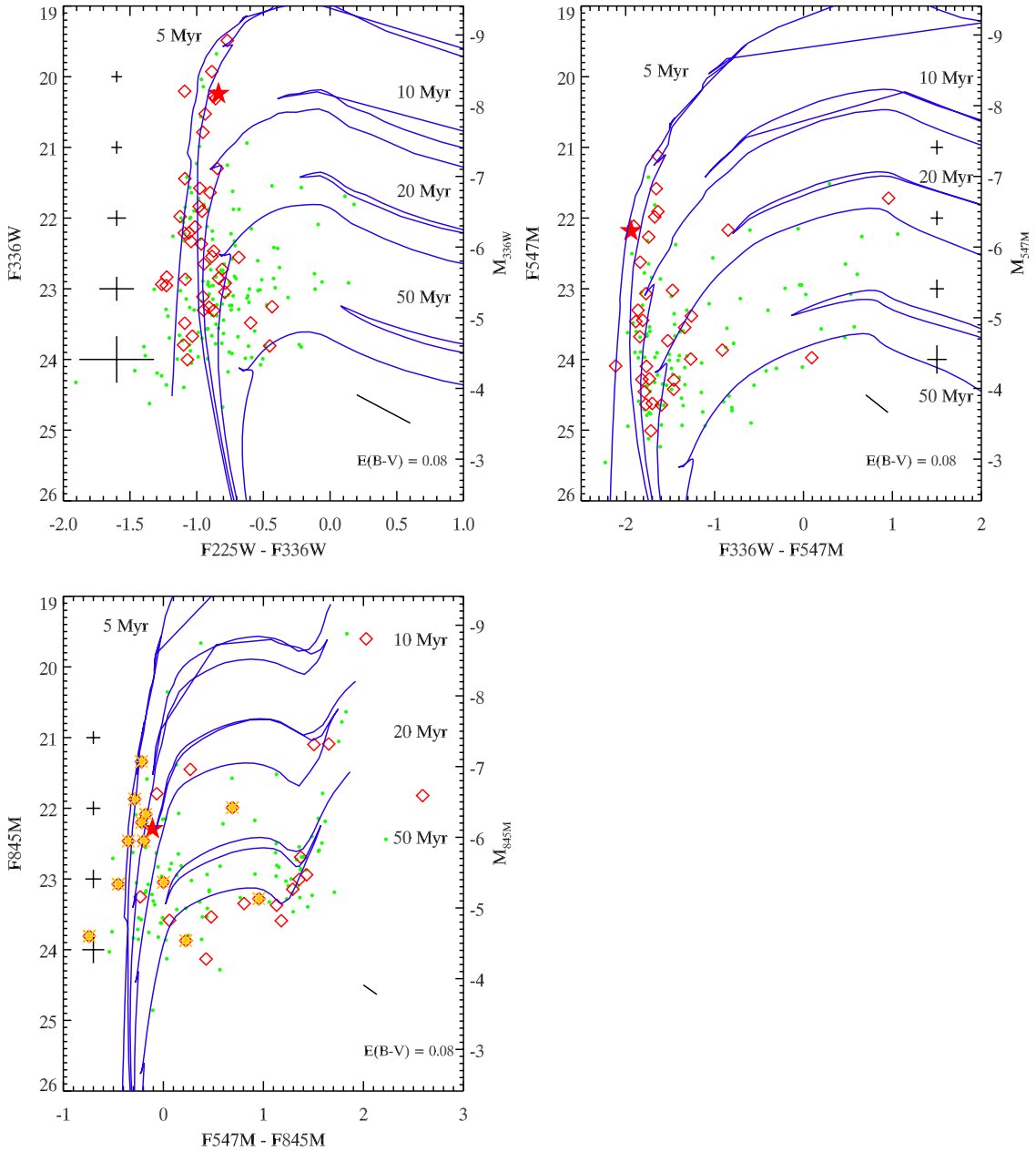

Figure 2. *HST*/WFC3 color–magnitude diagrams for the stellar field (512 × 512 pixels, i.e., 20″ × 20″) around the ULX. Padova isochrones for stars of different ages are overplotted. Typical photometric errors are also plotted. Data have been corrected for an extinction of E($B-V$) = 0.08 mag, the bar at the bottom right corner illustrating this effect. Upper left panel: Color–magnitude diagram in the (F225W, F336W) system. Upper right panel: Color–magnitude diagram in the (F336W, F547M) system. Lower left panel: Color–magnitude diagram in the (F547M, F845M) system. The same isochrones are plotted in the three panels, i.e. for 5, 10, 20, and 50 Myr at Z = 0.008. Filled green circles are stars in the field, red diamonds are stars located in a rectangle of 5.″5 × 4.″0 coincident with a nearby OB association. The red star is the position of the ULX counterpart. In the bottom panel, we show as orange X's stars from the OB association that are in common with the upper panels. The smaller number of stars in common with the upper panels is simply due to the fact that we mainly see redder stars in the F845M filter that are not strong UV emitters (and vice versa in the top panels where the strong UV emitters are not seen in the redder filters).

(A color version of this figure is available in the online journal.)

turn-off at the shortest wavelengths. Interestingly, the deviations at these wavelengths seem to correspond to what is expected from a B0I star (Figure 4, right panel). Only the flux at 15400 Å does not follow the decreasing trend that should continue in the infrared. We note that the power-law index of the continuum in the 4000–6000 Å interval found by Kaaret & Corbel (2009) ($2.0^{+0.1}_{-0.2}$), is likely contaminated by the nebular emission. The spatial resolution of *HST*/WFC3 allows us to measure the flux of the continuum of the counterpart, with a very low contamination of the nebula as can be seen in the composite image (Figure 1) that contains the nebular [O III] emission.

The three X-ray spectra observed simultaneously with the *HST* data have count rates of 0.30, 0.32, and 0.42 counts s^{-1}. Their moderate exposure times imply that the number of counts is limited (∼4000) and thus complex models such as used recently in the literature (Gladstone et al. 2009; Caballero-García & Fabian 2010; Walton et al. 2011) cannot be constrained accurately. Specifically, the lack of counts at high energy does

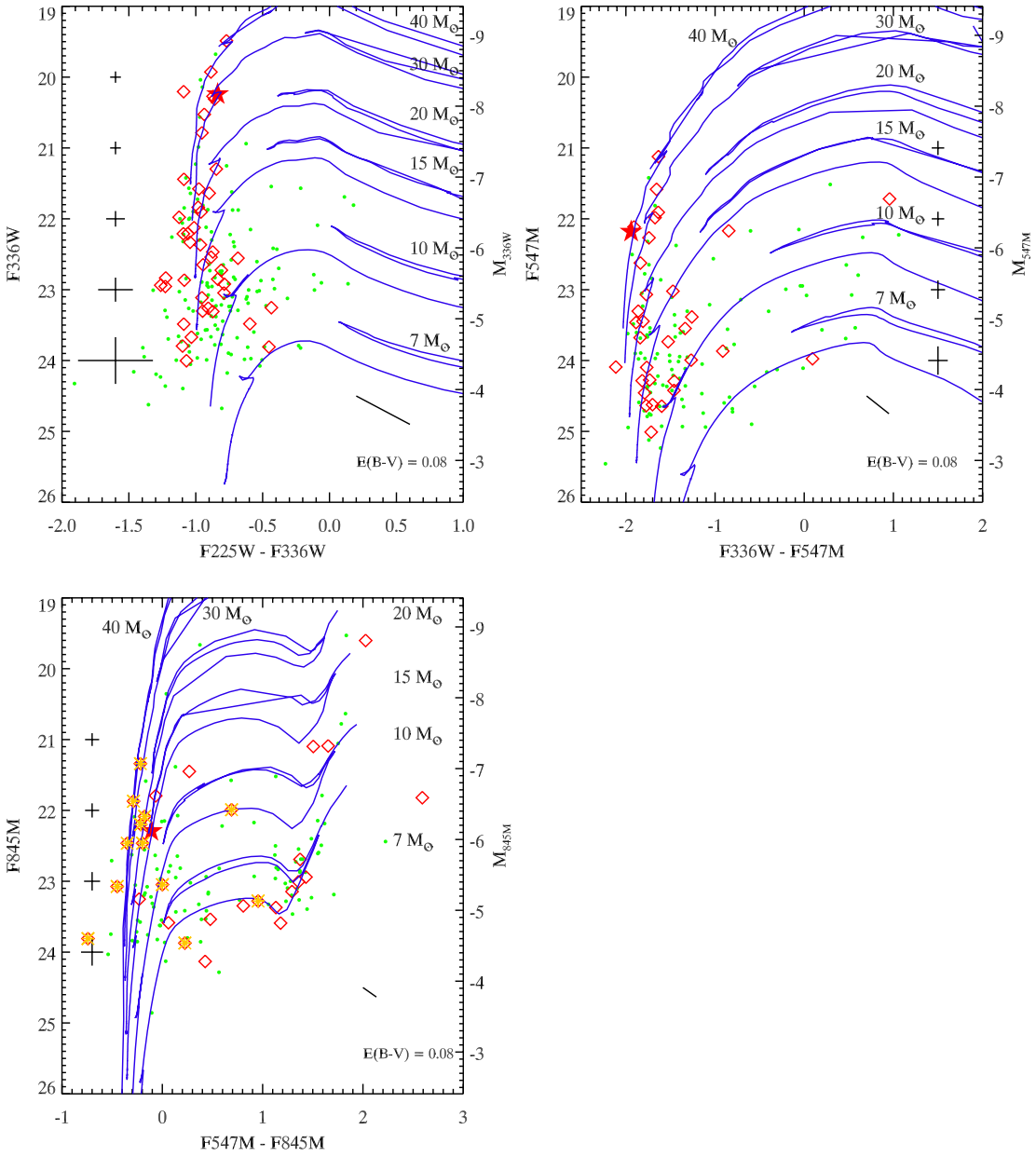

Figure 3. *HST*/WFC3 color–magnitude diagrams with Padova evolutionary tracks for stars of different initial masses (7, 10, 15, 20, 30, and 40 $M_{\odot}$) with $Z = 0.008$. The legend is the same as Figure 2. Upper left panel: color–magnitude diagram in the (F225W, F336W) system. Upper right panel: color–magnitude diagram in the (F336W, F547M) system. Lower right panel: color–magnitude diagram in the (F547M, F845M) system.

(A color version of this figure is available in the online journal.)

not allow one to see the high-energy curvature as shown by Stobbart et al. (2006). We modeled the X-ray spectra using basic models such as an absorbed power law and a power law plus disk blackbody (DISKBB; Mitsuda et al. 1984) combination to compare with previous results in the literature. Extinction was modeled using the Tuebingen-Boulder ISM absorption model (TBABS; Wilms et al. 2000). We used a fixed component related to the Galactic extinction with $n_{\rm H} = 0.057 \times 10^{22}$ cm^{-2} (Dickey & Lockman 1990), and let a second extinction component vary freely. N5408X1 does not appear to show any strange behavior. The fits parameters for these simple models (Table 4) are in agreement with previous observations (Kajava & Poutanen 2009) where the authors argue that N5408X1 displays an L_X–Γ correlation, which holds here.

To further understand the whole SED and the effect of X-ray emission at lower energies, we extrapolated the emission of the disk component. As shown by Kaaret et al. (2004) in the case of Holmberg II X-1, some precautions need to be taken since the X-ray emission of most ULXs is largely dominated by the power-law component and not the accretion disk, and extrapolating the power law to lower energies would be non-physical. In the case of N5408X1, the ratio between the two components is about 50% (Table 3), requiring care. Following Berghea et al. (2010), we modeled separately the power law and the accretion disk component (Table 3). We fitted a power-law model to the spectra between 1 and 7 keV, and a disk blackbody model between 0.3 and 1 keV. As can be seen in Figure 5, the extrapolated disk model underestimates the *HST* fluxes by about

Table 3
Spectral Fit Parameters

No.[a]	$n_{\rm H}$[b] (10^{22} cm^{-2})	Γ[c] (kT_e)[d] (/keV)	$\Gamma_{\rm norm}$[e] (Compt. Norm)[f] 10^{-4}	$kT_{\rm in}$[g]	Disk$_{\rm norm}$[h]	τ[i]	Flux[j] ($\times10^{-12}$ erg s^{-1} cm^{-2})	L_X[k] ($\times10^{40}$ erg s^{-1})	$f_{X_{\rm MCD}}$[l]	χ^2/DoF[m]
				POWERLAW						
1	$0.044^{+0.014}_{-0.014}$	$2.66^{+0.08}_{-0.08}$	$5.8^{+0.3}_{-0.3}$	...	...	...	$1.76^{+0.11}_{-0.14}$	$0.63^{+0.04}_{-0.04}$	...	154.36 (91)
2	$0.03^{+0.02}_{-0.02}$	$2.67^{+0.13}_{-0.12}$	$5.9^{+0.5}_{-0.4}$	...	...	...	$1.83^{+0.10}_{-0.14}$	$0.79^{+0.08}_{-0.05}$	...	121.0 (94)
3	$0.10^{+0.02}_{-0.02}$	$3.17^{+0.13}_{-0.12}$	$9.9^{+0.2}_{-0.7}$	...	...	...	$2.10^{+0.11}_{-0.12}$	$1.54^{+0.23}_{-0.17}$	...	136.5 (101)
				POWERLAW + DISKBB						
1	$0.10^{+0.05}_{-0.04}$	$2.43^{+0.12}_{-0.12}$	$4.9^{+0.6}_{-0.6}$	$0.15^{+0.02}_{-0.02}$	284^{+577}_{-187}	...	$1.76^{+0.15}_{-0.76}$	$0.85^{+0.44}_{-0.19}$	$0.28^{+0.44}_{-0.18}$	132.03 (89)
2	$0.07^{+0.07}_{-0.05}$	$2.40^{+0.18}_{-0.19}$	$4.7^{+0.9}_{-0.9}$	$0.16^{+0.04}_{-0.03}$	162^{+809}_{-129}	...	$1.86^{+0.1}_{-0.76}$	$1.02^{+0.56}_{-0.25}$	$0.36^{+0.51}_{-0.20}$	100.6 (92)
3	$0.13^{+0.05}_{-0.05}$	$2.85^{+0.18}_{-0.20}$	$1.6^{+1.5}_{-1.5}$	$0.15^{+0.04}_{-0.02}$	427^{+1614}_{-327}	...	$2.15^{+0.31}_{-0.72}$	$2.13^{+1.25}_{-0.62}$	$0.48^{+0.52}_{-0.26}$	110.7 (99)
				Modified POWERLAW + DISKBB						
1	$0.01^{+0.04}_{-0.01}$	$2.51^{+0.11}_{-0.10}$	$5.0^{+0.3}_{-0.3}$	$0.27^{+0.04}_{-0.05}$	18^{+48}_{-9}	...	...	...	...	85.7 (54) / 59.8 (38)
2	$0.0^{+0.06}_{-0.0}$	$2.51^{+0.11}_{-0.10}$	$5.2^{+0.6}_{-0.3}$	$0.26^{+0.02}_{-0.02}$	23^{+34}_{-7}	...	...	...	...	61.7 (55) / 37.3 (39)
3	$0.02^{+0.05}_{-0.02}$	$2.92^{+0.10}_{-0.10}$	$7.9^{+0.4}_{-0.4}$	$0.26^{+0.04}_{-0.04}$	39^{+80}_{-23}	...	...	...	...	69.9 (62) / 44.6 (40)
				DISKPN + COMPTT						
1	$0.06^{+0.06}_{-0.05}$	$1.1^{+37.2}_{-0.3}$	$9.1^{+3.8}_{-9.1}$	$0.15^{+0.04}_{-0.03}$	$3.5^{+12.2}_{-2.5}$	$9.2^{+2.8}_{-9.2}$	$1.69^{+0.11}_{-0.05}$	$0.60^{+0.33}_{-0.03}$	$0.42^{+0.37}_{-0.15}$	128.5 (88)
2	$0.03^{+0.06}_{-0.03}$	$1.0^{+3.5}_{-0.3}$	$8.3^{+3.7}_{-2.8}$	$0.17^{+0.04}_{-0.03}$	$2.0^{+6.9}_{-1.2}$	$10.2^{+2.2}_{-7.3}$	$1.80^{+0.1}_{-1.4}$	$0.59^{+0.28}_{-0.03}$	$0.43^{+0.57}_{-0.15}$	94.8 (91)
3	$0.09^{+0.07}_{-0.06}$	$9.8^{+17.2}_{-8.6}$	$2.4^{+0.3}_{-2.4}$	$0.14^{+0.03}_{-0.02}$	$10.1^{+18.0}_{-7.0}$	$1.4^{+5.8}_{-1.4}$	$2.14^{+0.35}_{-0.71}$	$1.73^{+1.08}_{-0.56}$	$0.56^{+0.44}_{-0.32}$	109.2 (98)

Notes. All errors are at the 90% confidence level.
[a] Spectrum index used in the text.
[b] External absorption column (in addition of the galactic extinction towards the source, $n_{\rm H} = 0.057 \times 10^{22}$ cm^{-2}).
[c] Power-law photon index.
[d] Electron temperature in keV, for the Comptonization model.
[e] Power-law normalization.
[f] Comptonization normalization.
[g] Inner-disk temperature.
[h] Disk normalization (for the diskpn model, units are in terms of 10^{-3}).
[i] Plasma optical depth.
[j] Absorbed flux (0.3–10 keV).
[k] Unabsorbed luminosity (0.3–10 keV) for $D = 4.8$ Mpc.
[l] Fraction of the total unabsorbed flux (0.3–10 keV) in the disk component.
[m] χ^2 and degrees of freedom.

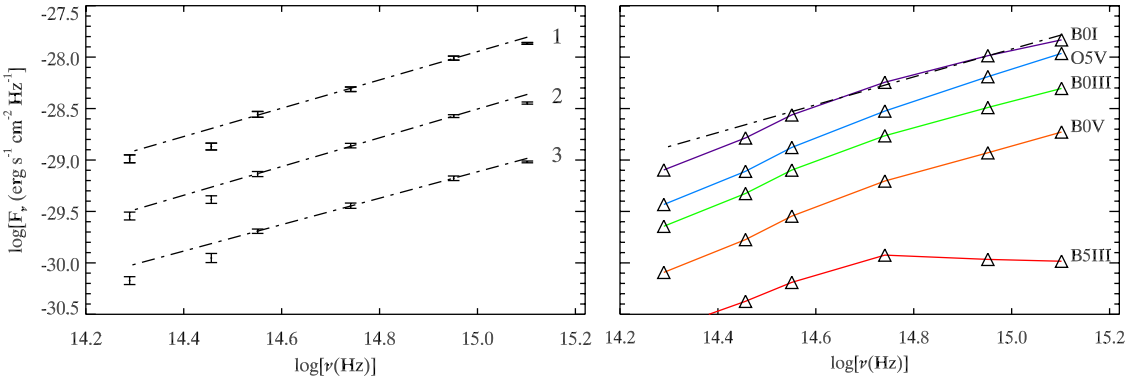

Figure 4. Spectral energy distribution of NGC 5408 X-1 (corrected for extinction) for each observation (left), compared to stellar templates (right). SEDs 2 and 3 of NGC 5408 X-1 have been shifted down by 0.6 in log(F_ν) for clarity purposes. Fluxes of stellar templates in the *HST*/WFC3 filters have been calculated using SYNPHOT and the Castelli and Kurucz stellar atmosphere models (Castelli & Kurucz 2004). In the right panel is overplotted (black dot dashed line) an average power-law fit from the three *HST* observations.

(A color version of this figure is available in the online journal.)

Table 4
Spectral Fit Parameters of the Irradiated Disk Model

No.[a]	n_H[b] (10^{22} cm^{-2})	diskir$_{norm}$[c]	Γ[d]	kT_{in}[e] (keV)	kT_e[f] (keV)	L_C/L_D[g]	r_{irr}[h]	f_{out}[i]	log(r_{out})[j]	χ^2/DoF[k]
				DISKIR						
1	$0.16^{+0.06}_{-0.05}$	666^{+21}_{-470}	$2.42^{+0.16}_{-0.17}$	$0.13^{+0.02}_{-0.02}$	50	$0.57^{+0.56}_{-0.28}$	1.1	$0.043^{+0.030}_{-0.022}$	$3.04^{+0.27}_{-0.25}$	144.6 (93)
2	$0.12^{+0.08}_{-0.05}$	401^{+1}_{-285}	$2.40^{+0.17}_{-0.19}$	$0.14^{+0.02}_{-0.02}$	50	$0.71^{+0.66}_{-0.37}$	1.1	$0.046^{+0.027}_{-0.024}$	$3.21^{+0.28}_{-0.28}$	101.7 (96)
3	$0.16^{+0.07}_{-0.05}$	794^{+34}_{-557}	$2.82^{+0.18}_{-0.19}$	$0.14^{+0.02}_{-0.02}$	50	$0.43^{+0.25}_{-0.20}$	1.1	$0.030^{+0.019}_{-0.018}$	$3.07^{+0.27}_{-0.29}$	114.0 (103)

Notes. All errors are at the 90% confidence level.
[a] Spectrum index used in the text.
[b] Total absorption column, including the Galactic extinction toward the source ($n_H = 0.057 \times 10^{22}$ cm^{-2}).
[c] Model normalization.
[d] Power-law photon index.
[e] Innermost temperature of the unilluminated disk.
[f] Electron temperature.
[g] Ratio of luminosity in the Compton tail to that of the unilluminated disk.
[h] Radius of the Compton illuminated disk in terms of the inner disk radius.
[i] Fraction of bolometric flux which is thermalized in the outer disk.
[j] log10 of the outer disk radius in terms of the inner disk radius.
[k] χ^2 and degrees of freedom.

an order of magnitude, by a factor ∼38/36/24 at 2400 Å and by a factor ∼5/5/3 at 15400 Å. We also used a model that consists of a disk plus a thermal Comptonization component (DISKPN + COMPTT, Table 3), as used in a recent study of N5408X1 (Middleton et al. 2011). The Comptonization component is a better choice since it is negligible in the optical wavelengths, so that there is no flux contamination in the disk component, as is the case for the model based on a power law. Using that model, we found that the extrapolated disk spectrum is 11/16/6 times lower at 2400 Å and 5/8/3 times lower at 5400 Å compared to *HST* fluxes. At 15400 Å the extrapolated disk is 1.5/2.3 lower in the two first observations and slightly above for the third observation compared to *HST* fluxes (Figure 5). We note that these extrapolations assume a very large outer disk radius ($\gtrsim 1 \times 10^{13}$ cm). Assuming narrower disks (or truncated disks) would reduce their flux in the IR, optical, and UV.

Reprocessed X-ray irradiation is likely to be significant in ULXs, the optical light curves of, e.g., NGC 1313 X-2 (Grisé et al. 2008; Impiombato et al. 2011) show short-term, stochastic variability that does not seem compatible with solely the ellipsoidal variations due to a companion star. Thus, following Kaaret & Corbel (2009), we fitted the X-ray and the *HST* data with the irradiated disk model of Gierliński et al. (2009), DISKIR. It is based on the standard DISKBB model but includes effects due to disk irradiation and Comptonization. The irradiated inner disk and the Comptonized tail illuminate the outer disk, which implies a higher luminosity for this part of the disk. This model has been applied successfully on a Galactic black hole binary (Gierliński et al. 2009) where the authors conclude that the optical/UV emission in the soft state is consistent with reprocessing of a constant fraction of the bolometric X-ray luminosity. It has also been applied to the microquasar GRS 1915+105 where the Rahoui et al. 2010 show that an excess of mid-IR emission (∼4–8 μm) is probably related to some reprocessed soft X-ray emission in the outer part of the disk.

The DISKIR model contains nine parameters with two of them being constrained by the UV/optical/NIR measurements. Three parameters were frozen: f_{in}, the fraction of luminosity in the Compton tail, which is thermalized in the inner disk, was set to 0.1. The electron temperature and the irradiated radius were found to be poorly constrained so we fixed them, respectively, to 50 keV and 1.1 × R_{in}. The electron temperature does not seem to have a strong impact on the other parameters. We tested

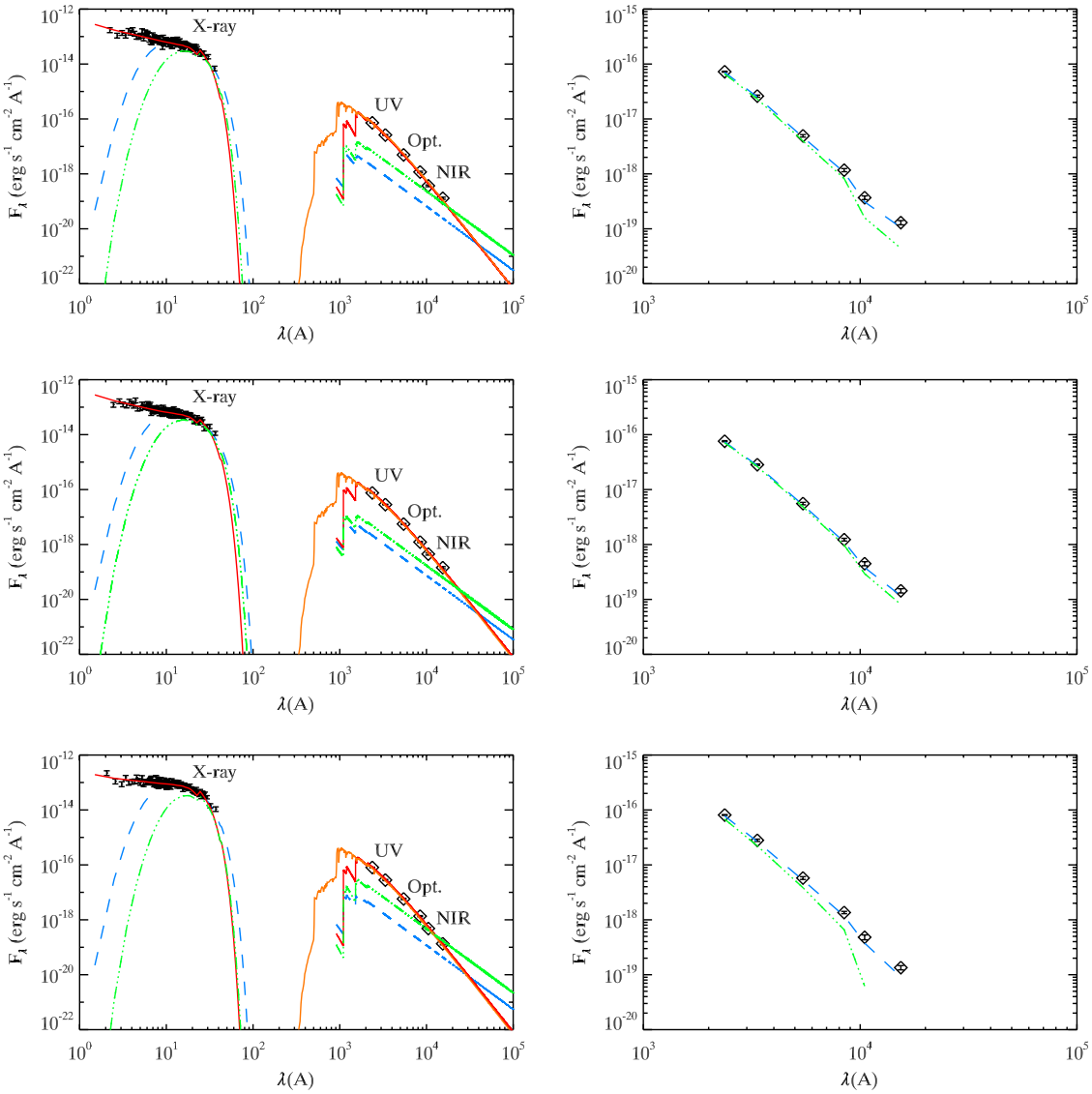

Figure 5. Left: best fits for the simultaneous X-ray–UV/optical/NIR data of NGC 5408 X-1. The three plots correspond to the three independent observations. In each plot, the two accretion disk models (see the text) extrapolated from the X-ray data fit to lower energies are shown in green (dot-dashed line) and in blue (dashed line), respectively, corresponding to the disk model associated with a Comptonized component and the disk model associated with a power-law component. They underestimate the UV/optical/NIR fluxes. The best fitting model is an irradiated disk (red line) that explains both the high energy and low energy data. This supports the interpretation that a standard, thin disk is present in NGC 5408 X-1. The spectrum of a B0I supergiant star (from the Castelli and Kurucz stellar atmosphere models, Castelli & Kurucz 2004) is overplotted in orange. It fits the *HST* data as well as the irradiated disk model. Note that the apparent gap between ∼100 and ∼1000 Å is due to the extinction. Right: required flux needed to explain the *HST* measurements, after subtraction of the two extrapolated disk components seen in the left panels (the same color/linestyle is used to differentiate the two disk models).

(A color version of this figure is available in the online journal.)

with two other values (1.5 and 500 keV), but the effect on all parameters is within 20%. Changing the irradiated radius from 1.1 to 2.0 × $R_{\rm in}$ increases the inner temperature of the disk by 10%, the ratio $L_{\rm C}/L_{\rm D}$ by 80% and $f_{\rm out}$ by 20%, but this does not affect our conclusions. The results of the fits are shown in Table 4 and Figure 5 and are consistent for the three spectra. We note that spectrum 1 has a worse χ^2 than the other spectra. The residuals have positive peaks between 0.5 and 1 keV and could be due to low energy emission lines. Caballero-García & Fabian (2010) has suggested that ULXs may produce highly ionized oxygen and iron emission lines via reflection off the disk. However, it is not clear why such lines would be present in the first spectrum only (which has the lowest number of counts). This interesting issue should be looked into with deeper spectra. In this paper we limit ourselves to the continuum modeling.

4. DISCUSSION

4.1. Environment of the ULX

ULXs are usually located inside or near stellar-forming regions that look like OB associations (Soria et al. 2005; Grisé et al. 2008; Swartz et al. 2009). This has strengthened their identification with X-ray binaries containing a massive companion star that is needed to explain their high, persistent X-ray luminosity. The fact that N5408X1 is located nearby (but not inside) to what appears to be an OB association (Figure 1) is thus not unusual. For example, NGC 1313 X-2 (Grisé et al.

2008) is displaced from its apparent parent cluster by ∼100 pc. This is a good argument that such X-ray binaries may have been ejected from their host cluster (Kaaret et al. 2004).

Kaaret et al. (2003) has shown that the ULX is located at about 12″ from the star formation regions of NGC 5408 that contain super star clusters. The runaway-coalescence scenario studied by Vanbeveren et al. (2009 and references therein) is able to explain the formation of massive black holes up to several 100 $M_\odot$ in subsolar metallicity environments. It is not clear whether IMBHs could be produced by this way, but in any case the formation of such massive remnants would need massive and dense clusters. As noted by Kaaret et al. (2003), the projected displacement of ∼280 pc from the super star clusters could be consistent with an ejected X-ray binary. Using reasonable ejection speed (10 km s^{-1}), Kaaret et al. (2003) concluded that the binary could traverse this distance in 30 million years and thus have moved to the present location within the lifetime of a massive companion star. We remark here that 30 Myr would in fact exclude most early types of stars, since 30 Myr is the lifetime of a ∼10 $M_\odot$ star.

Another possibility, as noted above, is that the binary comes from the closer OB association located 100 pc from its position. In that case, it is very unlikely that an IMBH has been formed in such a stellar environment. We also note that the age of the association, ∼5 Myr, would imply an escape velocity of ∼25–50 km s^{-1} with the assumption that the binary was ejected between 1 and 3 Myr after the stellar association was formed. These velocities, albeit large, cannot be ruled out since some OB-supergiant binaries have been seen with runaway velocities of that order (e.g., van den Heuvel et al. 2000). In that case, a more massive donor star would be allowed in the system, in comparison with the super star cluster hypothesis.

4.2. UV/Optical/NIR SED

The fact that the SED of N5408 X-1 may be described approximately by a power law, and does not show any clear clue of a peak of a blackbody leads to several conclusions. As can be seen in Figure 4, only early type stars display a power law extending far in the UV because the peak of their spectrum is located at shorter wavelengths than our observing limit (∼2250 Å equivalent to a peak temperature of ∼13000 K). Basically, this means that if the light of N5408 X-1 was dominated by a star, we could rule out any star of spectral type later than B5 (this is quite independent of the luminosity class). But, the fact that the counterpart is intrinsically bright, $M_V \sim -6.2$ would exclude the smallest stars. Looking again at Figure 4 (right panel) we see that the SED of N5408 X-1 is very consistent with that of a B0I supergiant star (scaled at the magnitude of an Iab class) and rules out all main-sequence stars. The turnoff in the F225W filter seems to match the spectral template of the B0I star. Also, a drop compared to a power law is expected in the NIR (Figure 4, right panel) and is clearly observed at 1 μm (Filter F105W). However, this drop should be even more prominent at longer wavelengths but is not really seen at 1.5 μm (Filter F160W). Proving that the companion star dominates the optical emission would be possible if optical spectroscopy of the optical counterpart would reveal absorption lines, such as in the ULX P13 (Motch et al. 2011). But the signal to noise of the optical spectra studied by Kaaret & Corbel (2009) and Cseh et al. (2011) are not high enough to rule out the presence of an early B supergiant star because absorption lines in the wavelength range observed are not very deep.

4.3. X-Ray to NIR SED

The disk emission, extrapolated from two different models that we used to fit the X-ray data (a disk blackbody with the addition of either a power law or a thermal Comptonization model) does not fit the UV/optical/IR at all (Figure 5). For the power law plus disk blackbody model, the extrapolated disk model underestimates the *HST* fluxes by about an order of magnitude (Figure 5), which basically means that the accretion disk emission would be negligible at optical wavelengths and the companion star would dominate.

For the disk plus Comptonization model, the extrapolated disk spectrum has a higher flux at lower energies but is still unable to explain the UV/optical/IR measurements (Figure 5). The excess emission could come from the donor star. However, the shape of the excess emission drops at the longest wavelengths, especially in the third observation where the NIR flux predicted by the accretion disk model is above the flux measured with *HST* (Figure 5). This is not consistent with the spectrum of any known star.

Another possibility is that the emission in excess from the extrapolation of the disk may not come primarily from a stellar component. The irradiated disk model that we used is able to fit all the data quite well (see Table 4). All three data sets give similar results within the errors, which is expected given the lack of significant variability both at X-rays and at lower energies. In this model, the UV/optical/IR emission is from the irradiated outer disk that thermalizes a fraction of the bolometric luminosity $f_{\rm out} \sim 0.03$. This fraction is higher than seen from Galactic X-ray binaries in the thermal dominant state (Gierliński et al. 2009; Zurita Heras et al. 2011) but similar fractions have been obtained from observations of the microquasar GRS1915+105 in its most X-ray active phase (Rahoui et al. 2010).

Cseh et al. (2011) have discussed the size of the accretion disk in N5408X1, based on the broad emission lines seen in the optical spectrum of the counterpart. They concluded that the disk has a radius lower than $2.35 \times M_{\rm BH}/1500\,M_\odot$ AU which translates to 2.4×10^{11}–10^{13} cm for a 10–1000 $M_\odot$ black hole. According to the results from the irradiated disk model, we found that the disk would have a size ∼1–5 × 10^{12} cm depending on the inclination of the disk. This is comparable to the size of the disk inferred in GRS1915+105 with $\sim 3 \times 10^{12}$ cm, where an irradiated accretion disk may also be present (Rahoui et al. 2010). In N5408X1, the irradiated disk model gives $R_{\rm out}/R_{\rm in} \sim$ 1100–1600 which is in the upper range of other ULXs, like in NGC 1313 X-1 (Yang et al. 2011) with $R_{\rm out}/R_{\rm in} \sim$ 100–2000 and in NGC 6946 X-1 (Kaaret et al. 2010) with $R_{\rm out}/R_{\rm in} \sim$ 40–6000.

While disk irradiation is able to explain the observational properties of N5408X1, we cannot make a definitive statement that irradiation is occurring in this system. First, no detection of significant, associated variability between the UV/optical/NIR and X-ray has been made (see below). Second, it is possible that the X-ray soft component is not emitted by an accretion disk, but by the photosphere of an outflow/wind (e.g., Poutanen et al. 2007; Middleton et al. 2011) that would be due to supercritical accretion onto the accretion disk.

In that context, it may be interesting to draw a comparison with the X-ray transient V4641 Sgr. This is an interesting source because it may be a closer example to ULXs than low-mass X-ray binaries (LMXBs) thanks to its companion that is a quite massive star ($M \sim 6.5\ M_\odot$). V4641 Sgr went into outburst in 1999 reaching an X-ray luminosity near or above the Eddington

limit of its ∼10 $M_{\odot}$ black hole (Revnivtsev et al. 2002b). Along with the X-ray outburst, the optical emission increased by at least 4.7 mag. It has been shown that irradiation in the accretion disk cannot be reconciliated with the observed parameters. Instead, Revnivtsev et al. (2002a, 2002b) argue that an extended envelope surrounding the source absorbs the X-ray flux and re-emits it in the optical and UV. This would be the signature of a massive outflow driven by the supercritical accretion. The optical nebulae present around some ULXs and around N5408X1 (Figure 1) argue for the presence of such outflows. As noted in Kaaret & Corbel (2009) the difficulty with the supercritical model is that the soft X-rays expected from the photosphere of the wind would not thermalize in the disk and thus would not contribute to the reprocessed emission in the optical bands. This is a natural consequence of the supercritical accretion models because they predict geometric beaming (Poutanen et al. 2007; Ohsuga & Mineshige 2011). If the irradiated disk model is valid, it means that such beaming can be ruled out in N5408X1, because of the high fraction of thermalized bolometric luminosity in the disk. This would challenge the supercritical model. On the contrary, if the optical spectrum is dominated by the donor emission, then mild geometric beaming consistent with the constraints from the surrounding He II 4686 nebula would be allowed. Thus confirming or not that the optical emission comes mainly from the donor star is important.

We finally note that the reflection-based model used to model the X-ray spectrum of N5408X1 (Caballero-García & Fabian 2010) would probably imply a negligible contribution of the accretion disk in the optical wavelengths. This is because there is apparently no need for thermal emission from the disk in that model. This may be explained by magnetic extraction of energy from the disk, that would suggest that the energy is extracted before it is able to thermalize in the disk (Caballero-García & Fabian 2010). In that context, irradiation in the outer parts of the disk would be at best limited, and the observed optical emission would be mainly due to the donor star.

4.4. Variability

Observing X-ray/optical correlated variability would be a direct test of the irradiated disk model. A lack of significant optical variability in response to a significant X-ray variation would rule out the model, and would probably argue for the dominance of the companion star at non-X-ray wavelengths. The X-ray variability we measure is limited, with a 40% change in the count rate between the first and last observation, and with the second observation displaying a flux consistent with that of the first one. At longer wavelengths, there is no clear, statistically significant variability in the *HST* filters. In practically all filters, the magnitudes in all three epochs are consistent within the errors, with only marginal evidence of variability between the first and third epoch, at a level $\lesssim 2\sigma$. Thus, we can only provide an upper limit on the variability in the *HST* filters, consistent with $\lesssim$0.1 mag in most filters. If the situation is comparable to that of LMXBs, we would expect the amplitude of optical variability to be roughly the square root of the amplitude of the X-ray variability (van Paradijs & McClintock 1994). Our results are not inconsistent with this because the X-ray variability would imply a change of the optical flux of only ∼18%, which is close enough to 10% and also because other processes can affect the optical luminosity of the system with approximately the same amplitude (i.e., ellipsoidal variations).

Perhaps the best evidence of variability may be seen in the normalization of the power-law fits. At 5500 Å the difference in the normalization factors between the first and last observation is $0.67 \pm 0.23 \times 10^{-18}$ erg s^{-1} cm^{-2}, which is almost significant at a 3σ level. We tried to look for a correlation between the X-ray flux and the magnitude/normalization in all filters but the errors on both parameters are too large (see Figure 6).

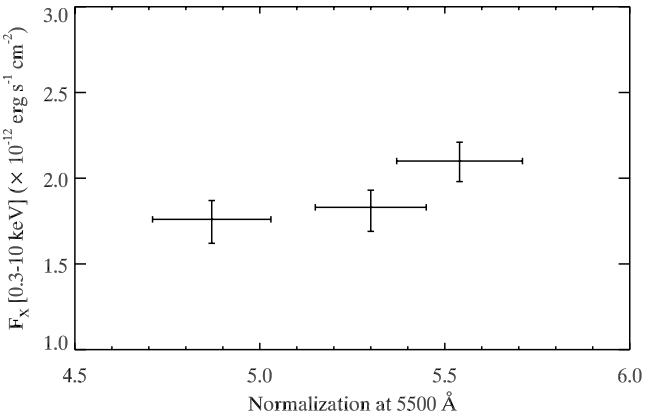

Figure 6. Absorbed X-ray flux (0.3–10 keV) vs. normalization at 5500 Å. X-ray fluxes are taken from the power-law fits and normalizations come from the F336W/F547M/F845M fits.

The long-term X-ray light curve of N5408 X-1 measured with *Swift* shows dips quite regularly (Kong 2011), with the X-ray luminosity decreasing by nearly an order of magnitude compared to the long-term average. In the context of an irradiated disk, this would imply a drop in the optical flux by a factor of ∼3, i.e., ∼1 mag and thus would be easily measurable. Gierliński et al. (2009) noted that this "reprocessing signature" is approximate, depending on parameters such as the size of the disk, but given the order of magnitude of the variability that we expect, it should still be detectable, even if reduced, in the UV/optical/NIR SED of the source. Finally, another additional signature would be an associated decrease in the flux of the He II emission line visible in the optical spectrum of the source (Cseh et al. 2011), if the emission of He II is really associated with reprocessing in the accretion disk. Thus, it would be of interest to perform optical observations during an X-ray dip.

5. CONCLUSION

We have studied NGC 5408 X-1 using three epochs of simultaneous *Chandra*/*HST* observations. The optical counterpart of the ULX is visible from the UV to the NIR. The *HST*/WFC3 observations reveal that the source is located near a young, ∼5 Myr old, OB association containing massive stars up to 40 $M_{\odot}$, with a few blue supergiants. This could be the birthplace of the ULX system, but it cannot be ruled out that it was formed instead in a superstar cluster in NGC 5408.

The UV to NIR SED is compatible with that of a B0I supergiant star. Using the simultaneous X-ray data, we show that the intrinsic emission of a standard accretion disk cannot explain the UV/optical/NIR fluxes. Instead, a model that takes into account irradiation in the disk fits all the data well. Further testing of this model requires observing the source with a lower or higher X-ray flux and studying the correlation with the optical flux. This would be a good discriminant toward determining the physical origin of the optical emission.

We thank Leo Girardi for making available the Padova evolutionary tracks in the *HST*/WFC3 medium filters. F.G.

and P.K. acknowledge support from Chandra grant GO0-11050 and STScI grant HST-12021. S.C. and D.C. are grateful for support from the European Community's Seventh Framework Program (FP7/2007-2013) under grant agreement number ITN 215212 "Black Hole Universe." We thank the anonymous referee for comments which improved this paper.

REFERENCES

Berghea, C. T., Dudik, R. P., Weaver, K. A., & Kallman, T. R. 2010, ApJ, 708, 354
Bertelli, G., Bressan, A., Chiosi, C., Fagotto, F., & Nasi, E. 1994, A&AS, 106, 275
Bertin, E., & Arnouts, S. 1996, A&AS, 117, 393
Caballero-García, M. D., & Fabian, A. C. 2010, MNRAS, 402, 2559
Cardelli, J. A., Clayton, G. C., & Mathis, J. S. 1989, ApJ, 345, 245
Castelli, F., & Kurucz, R. L. 2004, arXiv:astro-ph/0405087
Cseh, D., Corbel, S., Kaaret, P., et al. 2012, ApJ, submitted
Cseh, D., Grisé, F., Corbel, S., & Kaaret, P. 2011, ApJ, 728, L5
Dickey, J. M., & Lockman, F. J. 1990, ARA&A, 28, 215
Feng, H., & Kaaret, P. 2008, ApJ, 675, 1067
Foster, D. L., Charles, P. A., & Holley-Bockelmann, K. 2010, ApJ, 725, 2480
Fruscione, A., McDowell, J. C., Allen, G. E., et al. 2006, Proc. SPIE, 6270, 62701V
Gierliński, M., Done, C., & Page, K. 2009, MNRAS, 392, 1106
Girardi, L., Dalcanton, J., Williams, B., et al. 2008, PASP, 120, 583
Girardi, L., Williams, B. F., Gilbert, K. M., et al. 2010, ApJ, 724, 1030
Gladstone, J. C., Roberts, T. P., & Done, C. 2009, MNRAS, 397, 1836
Grevesse, N., & Sauval, A. J. 1998, Space Sci. Rev., 85, 161
Grisé, F., Kaaret, P., Pakull, M. W., & Motch, C. 2011, ApJ, 734, 23
Grisé, F., Pakull, M. W., Soria, R., et al. 2008, A&A, 486, 151
Houck, J. C., & Denicola, L. A. 2000, in ASP Conf. Ser. 216, Astronomical Data Analysis Software and Systems IX, ed. N. Manset, C. Veillet, & D. Crabtree (San Francisco, CA: ASP), 591
Impiombato, D., Zampieri, L., Falomo, R., Grisé, F., & Soria, R. 2011, Astron. Nachr., 332, 375
Kaaret, P. 2005, ApJ, 629, 233
Kaaret, P., Alonso-Herrero, A., Gallagher, J. S., et al. 2004, MNRAS, 348, L28
Kaaret, P., & Corbel, S. 2009, ApJ, 697, 950
Kaaret, P., Corbel, S., Prestwich, A. H., & Zezas, A. 2003, Science, 299, 365
Kaaret, P., & Feng, H. 2007, ApJ, 669, 106
Kaaret, P., & Feng, H. 2009, ApJ, 702, 1679
Kaaret, P., Feng, H., Wong, D. S., & Tao, L. 2010, ApJ, 714, L167
Kaaret, P., Simet, M. G., & Lang, C. C. 2006, ApJ, 646, 174
Kaaret, P., Ward, M. J., & Zezas, A. 2004, MNRAS, 351, L83
Kajava, J. J. E., & Poutanen, J. 2009, MNRAS, 398, 1450
Kalirai, J. S., MacKenty, J., Bohlin, R., et al. 2009a, Instrument Science Report WFC3 2009-30, 30
Kalirai, J. S., MacKenty, J., Rajan, A., et al. 2009b, Instrument Science Report WFC3 2009-31, 21
Karachentsev, I. D., Sharina, M. E., Dolphin, A. E., et al. 2002, A&A, 385, 21
Kong, A. K. H. 2011, arXiv:1102.3212
Lang, C. C., Kaaret, P., Corbel, S., & Mercer, A. 2007, ApJ, 666, 79
Liu, J., Bregman, J. N., & McClintock, J. E. 2009, ApJ, 690, L39
Liu, J.-F., Bregman, J. N., & Seitzer, P. 2002, ApJ, 580, L31
Marigo, P., Girardi, L., Bressan, A., et al. 2008, A&A, 482, 883
Mendes de Oliveira, C. L., Temporin, S., Cypriano, E. S., et al. 2006, AJ, 132, 570
Middleton, M. J., Roberts, T. P., Done, C., & Jackson, F. E. 2011, MNRAS, 411, 644
Mitsuda, K., Inoue, H., Koyama, K., et al. 1984, PASJ, 36, 741
Motch, C., Pakull, M. W., Grisé, F., & Soria, R. 2011, Astron. Nachr., 332, 367
Ohsuga, K., & Mineshige, S. 2011, ApJ, 736, 2
Pakull, M. W., Grisé, F., & Motch, C. 2006, in IAU Symp. 230, Populations of High Energy Sources in Galaxies, ed. E. J. A. Meurs & G. Fabbiano (Cambridge: Cambridge Univ. Press), 293
Pakull, M. W., & Mirioni, L. 2003, Rev. Mex. Astron. Astrofis. Ser. Conf., 15, 197
Poutanen, J., Lipunova, G., Fabrika, S., Butkevich, A. G., & Abolmasov, P. 2007, MNRAS, 377, 1187
Rahoui, F., Chaty, S., Rodriguez, J., et al. 2010, ApJ, 715, 1191
Revnivtsev, M., Gilfanov, M., Churazov, E., & Sunyaev, R. 2002a, A&A, 391, 1013
Revnivtsev, M., Sunyaev, R., Gilfanov, M., & Churazov, E. 2002b, A&A, 385, 904
Roberts, T. P., Gladstone, J. C., Goulding, A. D., et al. 2011, Astron. Nachr., 332, 398
Soria, R., Cropper, M., Pakull, M., Mushotzky, R., & Wu, K. 2005, MNRAS, 356, 12
Soria, R., Fender, R. P., Hannikainen, D. C., Read, A. M., & Stevens, I. R. 2006, MNRAS, 368, 1527
Soria, R., Motch, C., Read, A. M., & Stevens, I. R. 2004, A&A, 423, 955
Stetson, P. B. 1987, PASP, 99, 191
Stobbart, A.-M., Roberts, T. P., & Wilms, J. 2006, MNRAS, 368, 397
Strohmayer, T. E. 2009, ApJ, 706, L210
Strohmayer, T. E., Mushotzky, R. F., Winter, L., et al. 2007, ApJ, 660, 580
Swartz, D. A., Tennant, A. F., & Soria, R. 2009, ApJ, 703, 159
Tao, L., Feng, H., Grise, F., & Kaaret, P. 2011, ApJ, 737, 81
van den Heuvel, E. P. J., Portegies Zwart, S. F., Bhattacharya, D., & Kaper, L. 2000, A&A, 364, 563
van Paradijs, J., & McClintock, J. E. 1994, A&A, 290, 133
Vanbeveren, D., Belkus, H., van Bever, J., & Mennekens, N. 2009, Ap&SS, 324, 271
Walton, D. J., Gladstone, J. C., Roberts, T. P., et al. 2011, MNRAS, 414, 1011
Wilms, J., Allen, A., & McCray, R. 2000, ApJ, 542, 914
Yang, L., Feng, H., & Kaaret, P. 2011, ApJ, 733, 118
Zampieri, L., Impiombato, D., Falomo, R., Grisé, F., & Soria, R. 2012, MNRAS, 419, 1331
Zurita Heras, J. A., Chaty, S., Cadolle Bel, M., & Prat, L. 2011, MNRAS, 413, 235

Monthly Notices
of the
ROYAL ASTRONOMICAL SOCIETY

Mon. Not. R. Astron. Soc. **414,** 677–690 (2011) doi:10.1111/j.1365-2966.2011.18433.x

Radiatively efficient accreting black holes in the hard state: the case study of H1743−322

M. Coriat,[1⋆†] S. Corbel,[1,2] L. Prat,[1] J. C. A. Miller-Jones,[3,4] D. Cseh,[1]
A. K. Tzioumis,[5] C. Brocksopp,[6] J. Rodriguez,[1] R. P. Fender[7] and G. R. Sivakoff[8]

[1]*Laboratoire AIM, CEA-IRFU/CNRS/Université Paris Diderot, CEA Saclay, F-91191 Gif-sur-Yvette, France*
[2]*Institut Universitaire de France, 75005 Paris, France*
[3]*NRAO Headquarters, 520 Edgemont Road, Charlottesville, VA 22903, USA*
[4]*International Centre for Radio Astronomy Research – Curtin University, GPO Box U1987, Perth, WA 6845, Australia*
[5]*Australia Telescope National Facility, CSIRO, PO Box 76, Epping, NSW 1710, Australia*
[6]*Mullard Space Science Laboratory, University College London, Holmbury St. Mary, Dorking, Surrey RH5 6NT*
[7]*School of Physics and Astronomy, University of Southampton, Highfield, Southampton SO17 1BJ*
[8]*Department of Astronomy, University of Virgina, PO Box 400325, Charlottesville, VA 22904-4325, USA*

Accepted 2011 January 26. Received 2011 January 26; in original form 2010 June 9

ABSTRACT

In recent years, much effort has been devoted to unravelling the connection between the accretion flow and the jets in accreting compact objects. In the present work, we report new constraints on these issues, through the long-term study of the radio and X-ray behaviour of the black hole candidate H1743−322. This source is known to be one of the 'outliers' of the universal radio/X-ray correlation, i.e. a group of accreting stellar-mass black holes displaying fainter radio emission for a given X-ray luminosity than expected from the correlation. Our study shows that the radio and X-ray emission of H1743−322 are strongly correlated at high luminosity in the hard spectral state. However, this correlation is unusually steep for a black hole X-ray binary: $b \sim 1.4$ (with $L_{\rm radio} \propto L_{\rm X}^{b}$). Below a critical luminosity, the correlation becomes shallower until it rejoins the standard correlation with $b \sim 0.6$. Based on these results, we first show that the steep correlation can be explained if the inner accretion flow is radiatively efficient during the hard state, in contrast to what is usually assumed for black hole X-ray binaries in this spectral state. The transition between the steep and the standard correlation would therefore reflect a change from a radiatively efficient to a radiatively inefficient accretion flow. Finally, we investigate the possibility that the discrepancy between 'outliers' and 'standard' black holes arises from the outflow properties rather than from the accretion flow.

Key words: accretion, accretion discs – ISM: jets and outflows – radio continuum: stars – X-rays: binaries – X-rays: individual: H1743−322.

1 INTRODUCTION

Black hole X-ray binaries (BHXBs) are binary systems consisting of a black hole primary in orbit with a less evolved companion star. These systems spend most of their time in a faint quiescent state, being barely detectable at almost all wavelengths. They may undergo sudden and bright few-month-long X-ray outbursts with typical recurrence periods of many years (Tanaka & Shibazaki 1996). The picture commonly accepted to explain the emission of such objects involves an optically thick and geometrically thin accretion disc, mostly emitting at typical energies of ∼1 keV. This region is probably surrounded by a corona of hot plasma, where ultraviolet (UV) and soft X-ray photons originating from the disc undergo inverse Compton scattering, producing a power-law spectrum in the hard X-ray band. In addition to this 'X-ray picture', BHXBs are also characterized by the intermittent presence of relativistic outflows. This ejected material is mainly detected at radio wavelengths (see e.g. Hjellming & Johnston 1981; Mirabel & Rodriguez 1994; Fender 2006) though it can sometimes dominate the low-frequency emission up to the near-infrared (Corbel et al. 2001; Jain et al. 2001; Corbel & Fender 2002; Homan et al. 2005b; Russell et al. 2006; Coriat et al. 2009). These jets are undoubtedly coupled to the accretion flow, although the nature of this connection is still unclear.

⋆E-mail: m.coriat@soton.ac.uk
†Present address: School of Physics and Astronomy, University of Southampton, Southampton SO17 1BJ.

Several spectral states have been identified based on the relative strengths and properties of the different X-ray emitting components (see e.g. Homan & Belloni 2005; McClintock & Remillard 2006). The two main spectral states are the soft state, dominated by thermal emission from the accretion disc, and the hard state, dominated by emission from the corona. Various instances (hard or soft) of the intermediate state have also been defined to describe the transition phases between the two main states. During these phases the X-ray spectra usually display hardnesses in between those of the hard and the soft state as a result of comparable contributions to the emission from the disc and the corona. These spectral characteristics are also coupled to different levels of X-ray variability (see e.g. van der Klis 2006; Belloni 2010, for a review).

The radio emission in the hard state is usually characterized by a flat or slightly inverted spectrum ($S_\nu \propto \nu^\alpha$ with $\alpha \sim 0$). This is interpreted as self-absorbed synchrotron emission from steady, collimated, compact jets, in analogy with those observed in active galactic nuclei (Blandford & Königl 1979; Hjellming & Johnston 1988). During the soft state these compact jets are thought to be quenched (Fender et al. 1999; Corbel et al. 2000) and any radio emission, if present, is attributed to residual optically thin synchrotron emission from transient ejecta (Corbel et al. 2004; Fender, Belloni & Gallo 2004).

Observations of several sources have provided evidence that a strong connection exists between radio and X-ray emission during the hard state (Hannikainen et al. 1998; Corbel et al. 2000, 2003; Gallo, Fender & Pooley 2003). This connection takes the form of a non-linear flux correlation, $F_{\rm Rad} \propto F_{\rm X}^b$, where $F_{\rm Rad}$ is the radio flux density, $F_{\rm X}$ is the X-ray flux and $b \sim 0.5$–0.7. It was subsequently shown that this same correlation also holds between optical–infrared (OIR) and X-ray fluxes (Homan et al. 2005b; Russell et al. 2006, 2007; Coriat et al. 2009). These correlations indicate that the compact jets are strongly connected with the accretion flow (disc and/or corona), and possibly that their emission (synchrotron and/or inverse Compton) can comprise a significant contribution to the observed high-energy flux (see e.g. Markoff, Falcke & Fender 2001; Markoff et al. 2003; Markoff, Nowak & Wilms 2005; Rodriguez et al. 2008a; Russell et al. 2010). This radio/X-ray correlation, initially established for the source GX 339-4, has been extended to other Galactic black holes (mainly V404 Cyg; Gallo et al. 2003; Corbel, Körding & Kaaret 2008b) and even active galactic nuclei (Merloni, Heinz & di Matteo 2003; Falcke, Körding & Markoff 2004; Körding, Falcke & Corbel 2006a). Migliari & Fender (2006) also showed that a similar correlation exists for neutron star X-ray binaries (NSXBs), but with a steeper correlation coefficient ($b \sim 1.4$) and fainter radio emission for a given X-ray luminosity than seen in black holes (Fender & Hendry 2000; Fender & Kuulkers 2001; Muno et al. 2005).

However, in the following years, a few Galactic black hole candidates (BHCs) were found to lie well outside the scatter of the original radio/X-ray correlation (e.g. XTE J1720−318, Brocksopp et al. 2005; XTE J1650−500, Corbel et al. 2004; IGR J17497−2821, Rodriguez et al. 2007; Swift J1753.5−0127, Cadolle Bel et al. 2007; Soleri et al. 2010), thus either increasing its scatter or challenging the universality of the correlation itself. Some of them could also be false identifications of black holes. For a given X-ray luminosity, these outliers show a radio luminosity fainter than expected from the correlation (thus are sometimes dubbed 'radio-quiet' BHCs). However, for most of these outliers, there are no radio measurements available at low X-ray luminosities. Therefore we do not know whether they remain underluminous in the radio band at low accretion rates. The current lack of data also precludes a precise measurement of the slope of the correlation (if any) for the outliers. It is therefore unclear whether they follow a correlation similar to the 'standard' BHXBs but with a lower normalization or whether their inflow/outflow connection is intrinsically different. Moreover, we do not know if their behaviour is recurrent over several outbursts. These are some of issues that we address in this work.

Note that in the following, we will use the term 'outliers' rather than 'radio-quiet BHCs' to describe these sources. As we will show, they could be considered 'X-ray loud' as well. However, it should be borne in mind that the term 'outliers' might not be appropriate either. Indeed, given the increasing number of these sources, the 'outliers' could in fact turn out to be the norm.

1.1 H1743−322

The X-ray transient H1743−322 was discovered with the *Ariel V* and *HEAO-1* satellites by Kaluzienski & Holt (1977) during a bright outburst in 1977. In 2003, another bright outburst was first detected with the *International Gamma-ray Astrophysics Laboratory* (*INTEGRAL*). The source was initially dubbed IGR J17464−3213, before it was identified as H1743−322 (Markwardt & Swank 2003). This outburst was extensively studied at all wavelengths (see e.g. Parmar et al. 2003; Capitanio et al. 2005; Homan et al. 2005a; Joinet et al. 2005; Lutovinov et al. 2005; Kalemci et al. 2006; Miller et al. 2006; McClintock et al. 2009). It was shown in particular that the spectral and timing features of H1743−322 were similar to those of other, dynamically confirmed, black hole X-ray transients (McClintock et al. 2009). It was thus classified as a BHC.

During the return to quiescence following this outburst, Corbel et al. (2005) reported the detection of large-scale, synchrotron-emitting jets moving away from the central source. These jets were detected at both radio and X-ray wavelengths as a consequence of the interaction between the ejected plasma and the interstellar medium (ISM). Using the observed proper motions of the X-ray jets, these authors also derived an upper limit to the source distance of 10.4 ± 2.9 kpc. Given its location ($l = 357.255$ and $b = -1.83$) in the direction of the Galactic bulge, and a rather high column density, this upper limit is consistent with a Galactic Centre distance for H1743−322. In the following, we will therefore assume a distance of 8 kpc.

The 2003 outburst was followed by weaker outbursts (see Fig. 1) in 2004 (Swank 2004) and 2005 (Rupen, Mioduszewski & Dhawan 2005) which were poorly sampled at both X-ray and radio wavelengths. Therefore, no detailed studies of these two phases have been carried out to date. Further outbursts were observed in the first months of 2008 (2008a in the following; Kalemci et al. 2008; Jonker et al. 2010) and in 2008 September–November (2008b in the following; Corbel et al. 2008a). During the outburst decay of the 2008a outburst, Jonker et al. (2010) reported a radio/X-ray correlation slope of $b = 0.18 \pm 0.01$. The authors also found that H1743−322 lies well below the 'universal' radio/X-ray correlation making of H1743−322 another outlier. The weak 2008b outburst was classified as 'failed'. The source made a short cycle between the hard and the hard intermediate state but never reached the soft state (Capitanio et al. 2009; Prat et al. 2009). The source entered another outburst phase in 2009 (Krimm et al. 2009; Chen et al. 2010) and also in early 2010 (Yamaoka et al. 2009). In 2009, the system followed the canonical evolution through all the characteristic states (Motta, Muñoz-Darias & Belloni 2010). The variation of the flux associated with the two main spectral components (i.e. disc and power law) allowed Motta et al. (2010) to set a lower limit to the orbital inclination of the system of $\geq 43^\circ$.

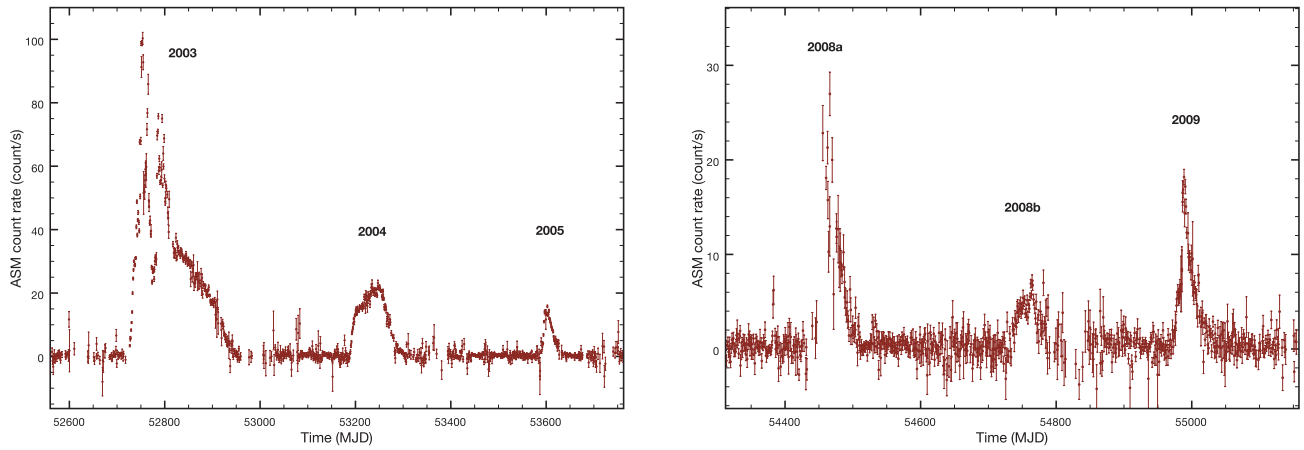

Figure 1. *RXTE*/ASM light curve of H1743−322 between 2003 and 2009. We note a major outburst in 2003 followed by five minor activity periods between 2004 and 2009. Note the different scaling between the two plots. The 2010 light curve is not presented due to the very low number of counts detected by the ASM during this short outburst.

In this work, we focus on the long-term study of the radio/X-ray correlation over the six outbursts mentioned above. We aim to investigate in detail the accretion–ejection coupling in this system in the global context of the 'outliers' of the radio/X-ray correlation. The sequence of observations and data reduction processes is described in Section 2. In Section 3, we present the analysis of the radio/X-ray correlation, the selection process that we applied to isolate and study the connection between the compact jets and the inner accretion flow and finally a comparison with other black hole and neutron star X-ray binaries. These results are then discussed in Section 4, in which we investigate several possible interpretations. Our conclusions are summarized in Section 5.

2 OBSERVATIONS

2.1 X-ray

2.1.1 RXTE: data reduction and spectral analysis

We analysed all publicly available observations of H1743−322 in the *RXTE* archive taken between 2003 January 1 and 2010 February 13. The data were reduced using the HEASOFT software package v6.8, following the standard steps described in the *RXTE* cookbook.[1] Spectra were extracted from the Proportional Counter Array (PCA; Jahoda et al. 2006) in the 3–25 keV range. We only used the top layer of the Proportional Counter Unit (PCU) 2 as it is the only operational unit across all observations and is the best-calibrated detector out of the five PCUs. Systematic errors of 0.5 per cent were added to all channels. In the 20–150 keV range, we used data from the High Energy X-ray Timing Experiment (HEXTE), which we reduced following standard steps. From 2005 December, due to problems in the rocking motion of Cluster A, we extracted spectra from Cluster B only. Because of the low count rate in the HEXTE data in most of the observations, all channels were rebinned by a factor of 4.

In addition, we constructed hardness–intensity diagrams (HIDs) from PCA data. These data were extracted from PCU2 (all layers) and corrected for background. Averaged count rates were extracted in two bands: (standard 2) channels 2–10 and 19–40, corresponding to 2.5–6.1 and 9.4–18.5 keV, respectively. The hardness ratio was defined as the ratio of the flux in the second band to that in the first band, and the intensity was calculated as the sum of the fluxes in both bands. The HIDs are presented in Fig. 2.

We performed a simultaneous fit to the PCA and HEXTE spectra in XSPEC V12.5.1n, using a floating normalization constant to allow for cross-calibration uncertainties. The main objective of the X-ray spectral analysis was to obtain a correct estimation of the unabsorbed flux in the 3–9 keV band. Consequently, we used simple models to reproduce the spectra and achieve statistically acceptable fits (i.e. a reduced $\chi^2 < 2$). We used a power law (*powerlaw*) and an absorption component (*phabs*) as a starting model. When required by an *F* test, we added a multitemperature disc blackbody (*diskbb*) and/or a high-energy cut-off (*highecut*). Eventually, when the residuals indicated the presence of reflection features, we used a Gaussian emission line (*Gaussian*, constrained in energy between 6 and 7 keV) and smeared absorption edge (*smedge*, constrained in energy between 7 and 9 keV). The hydrogen column density was fixed at the value obtained by Prat et al. (2009)[2] using *Swift* and *XMM–Newton* observations, i.e. $N_{\rm H} = 1.8 \pm 0.2 \times 10^{22}\,{\rm cm}^{-2}$. At low count rates, when H1743−322 was not significantly detected by HEXTE, fits were made to the PCA spectrum only. We finally obtained an average reduced χ^2 of 1.04 with a minimum of 0.64 and a maximum of 1.35. Unabsorbed fluxes were then estimated in the 3–9 keV energy ranges, according to the PCA normalization.

Because of the location of the source close to the Galactic plane, the Galactic ridge emission starts to significantly contaminate the estimated 3–9 keV PCA flux below $\sim 10^{-10}\,{\rm erg\,s^{-1}\,cm^{-2}}$. Kalemci et al. (2006) determined a 3–25 keV unabsorbed flux from the ridge emission of $1.08 \times 10^{-10}\,{\rm erg\,s^{-1}\,cm^{-2}}$, based on the analysis of nine observations in 2004 (MJD 53021–53055). We analysed the same data set to estimate the ridge emission in the 3–9 keV band and found an unabsorbed flux of $(6.0 \pm 0.6) \times 10^{-11}\,{\rm erg\,s^{-1}\,cm^{-2}}$. Consequently, we subtracted this value from all 3–9 keV PCA fluxes. To

[1] http://heasarc.gsfc.nasa.gov/docs/xte/data_analysis.html

[2] Note that several estimates of the hydrogen column density are found in the literature. The values range from 1.6×10^{22} (e.g. Capitanio et al. 2009) to $2.3 \times 10^{22}\,{\rm cm}^{-2}$ (e.g. Miller et al. 2006). However, within this range, the precise value of the $N_{\rm H}$ and its possible variation during the outburst has little influence on the unabsorbed flux above 3 keV. We thus used the intermediate value found by Prat et al. (2009).

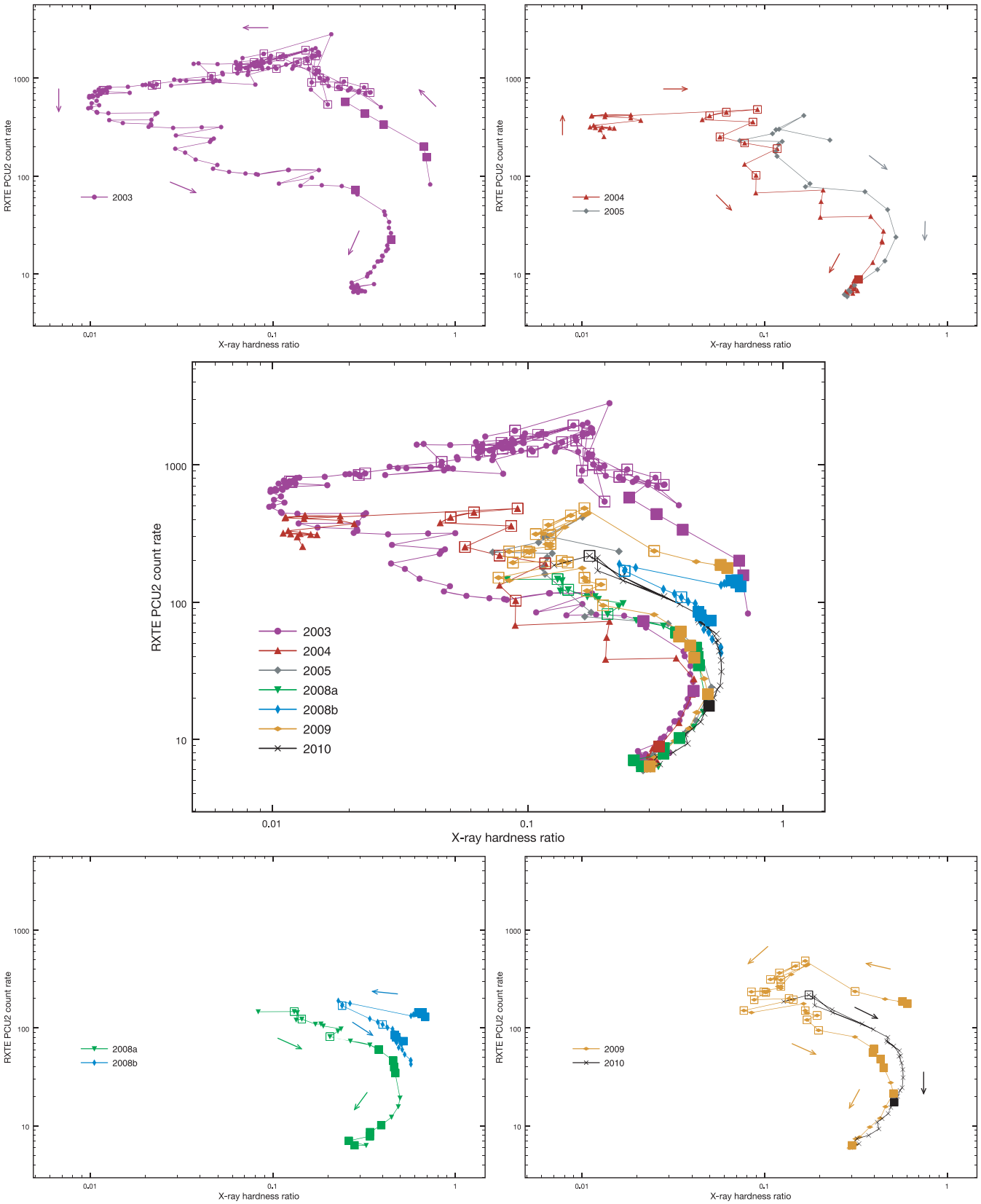

Figure 2. HIDs of H1743−322 from 2003 to 2010. Squares (open and filled) indicate the radio detections, plotted on top of the HIDs at the location of the nearest *RXTE* observation. Filled squares indicate the data selected for the radio/X-ray diagram in Fig. 4. The radio and X-ray fluxes corresponding to this selection are detailed in Table 1. Arrows indicate the temporal evolution during the outbursts. X-ray observations are indicated by purple circles for the outburst in 2003, red triangles for 2004, grey diamonds for 2005, inverted green triangles for 2008a, blue diamonds for 2008b, orange lozenges for 2009 and black crosses for 2010.

check whether a simple subtraction was appropriate to correct the measured source flux for the contamination from the ridge emission, we combined the spectra of the nine observations mentioned above to obtain a typical ridge spectrum. We then used this as an additional background spectrum for several on-source observations, where the ridge emission made a significant contribution. Finally, we compared the 3–9 keV fluxes obtained using this method with those obtained via simple flux subtraction. There was no significant difference within the error bars.

2.1.2 Other X-ray satellites

Jonker et al. (2010) studied the decay of the 2008a outburst using *Chandra* and *Swift* X-ray data simultaneous with radio observations from the Very Large Array (VLA). Since they provide important constraints on the correlation at low luminosity, we included in our study the X-ray fluxes published in their paper. We converted the unabsorbed 0.5–10 keV fluxes into absorbed 3–9 keV fluxes with the WEBPIMMS tool[3] using the $N_{\rm H}$ and photon index provided by the authors. For consistency with the *RXTE* data, we then calculated the unabsorbed 3–9 keV fluxes using $N_{\rm H} = 1.8 \times 10^{22}\,{\rm cm}^{-2}$.

2.1.3 X-ray state classification

Since the definition and nature of the X-ray states is still debated, in the following, we will adopt a simplified classification adapted to the purpose of this work. Our aim is to understand the nature of the connection between the corona and the compact jets for the outliers of the radio/X-ray correlation. Therefore, we will be mainly interested in phases where the compact jets are present and where the X-ray emission in the 3–9 keV band is dominated by the power-law emitting component. Consequently, we will define only three states: hard, soft and intermediate. To be classified as hard state, we require that the power-law component dominates the X-ray spectrum in the sense that an accretion disc component was not required (by an F test) to correctly fit the data above 3 keV. We also require a power-law photon index $\Gamma < 2$. We define the soft state by a power-law photon index $\Gamma > 2$ and a disc flux comprising >75 per cent of the 3–9 keV flux. All observations that do not correspond to either of these criteria are classified as intermediate states.

2.2 Radio

2.2.1 ATCA

Between 2003 April 24 (MJD 52753) and 2010 February 13 (MJD 55240), we performed a total of 38 observations of H1743−322 with the Australia Telescope Compact Array (ATCA). From 2009 April, the observations were carried out using the Compact Array Broadband Backend (CABB). This upgrade has provided a new broad-band backend system for the ATCA, increasing the maximum bandwidth from 128 MHz to 2 GHz. Each observation was conducted simultaneously in two different frequency bands, with central frequencies of 4.8 and 8.64 GHz (5.5 and 9 GHz, respectively, following the CABB upgrade). Various array configurations were used during these observations.

The ATCA has orthogonal linearly polarized feeds and full Stokes parameters (I, Q, U, V) are recorded at each frequency. We used PKS 1934−638 for absolute flux and bandpass calibration, and PMN 1729−37 to calibrate the antenna gains and phases as a function of time. We determined the polarization leakages using either the primary or the secondary calibrator, depending on the parallactic angle coverage of the secondary. Imaging was carried out using a combination of multifrequency (Sault & Wieringa 1994) clean and standard clean algorithms. The editing, calibration, Fourier transformation, deconvolution and image analysis were carried out with the Multichannel Image Reconstruction, Image Analysis and Display (MIRIAD) software (Sault, Teuben & Wright 1995).

2.2.2 VLA

H1743−322 has also been regularly observed between 2003 and 2010 with the VLA. To extend our data set, we made use of the radio flux densities at 4.86 and 8.46 GHz published in McClintock et al. (2009) for the 2003 outburst, in Rupen, Mioduszewski & Dhawan (2004) and Rupen et al. (2005) for the 2004 and 2005 outbursts and in Rupen, Dhawan & Mioduszewski (2008a,b) and Jonker et al. (2010) for the 2008a outbursts. We collected a total of 68 VLA pointings. All VLA data are summarized in the aforementioned references in which data reduction and analysis are detailed. In addition, we retrieved unpublished archival data of the 2004 outburst (PI: Rupen) from the National Radio Astronomy Observatory (NRAO) data base. All data were reduced using standard procedures within the NRAO AIPS software package, using 3C 286 as our primary calibrator, and J1744−3116 as the secondary calibrator.

For the 2009 outburst, we triggered VLA observations of H1743−322 after detection of an X-ray flare by *Swift*/Burst Alert Telescope (BAT) on 2009 May 26 (Krimm et al. 2009). On 2009 May 27, we detected unresolved radio emission at 8.4 GHz and triggered a monitoring campaign to cover the outburst of the source from the rising hard state through the decay back to quiescence. Our final observation was taken on 2009 August 6. Observations were made in dual circular polarization in each of two contiguous intermediate frequency pairs, giving a total bandwidth of 100 MHz per polarization. We observed primarily at 8.4 and 4.8 GHz, but also at 1.4 GHz when the source flux density was predicted to be above 0.3 mJy, and at 22.4 GHz for two epochs at the peak of the flare, although the source was not detected in either observation at this frequency. The array was in its intermediate CnB and C configurations throughout the duration of our observing campaign.

2.3 Simultaneity

For the vast majority of the radio data, we found quasi-simultaneous ($\Delta t \leq 1$ d) *RXTE* observations. Otherwise, we interpolated the X-ray flux from a polynomial fit to the PCA light curve. We estimated that the uncertainty introduced by this method should be less than 15 per cent as the flux evolution was found to be smooth in all cases. When the missing flux was not framed by at least two X-ray pointings, we converted the *RXTE*/All Sky Monitor (ASM) count rate into 3–9 keV unabsorbed flux with WEBPIMMS, using the spectral parameters of the nearest X-ray observation.

3 RADIO/X-RAY CORRELATION

3.1 Overview

In a first approach to characterize the global radio-X-ray behaviour of H1743−322, we use the complete data set without restricting

[3] http://heasarc.gsfc.nasa.gov/Tools/w3pimms.html

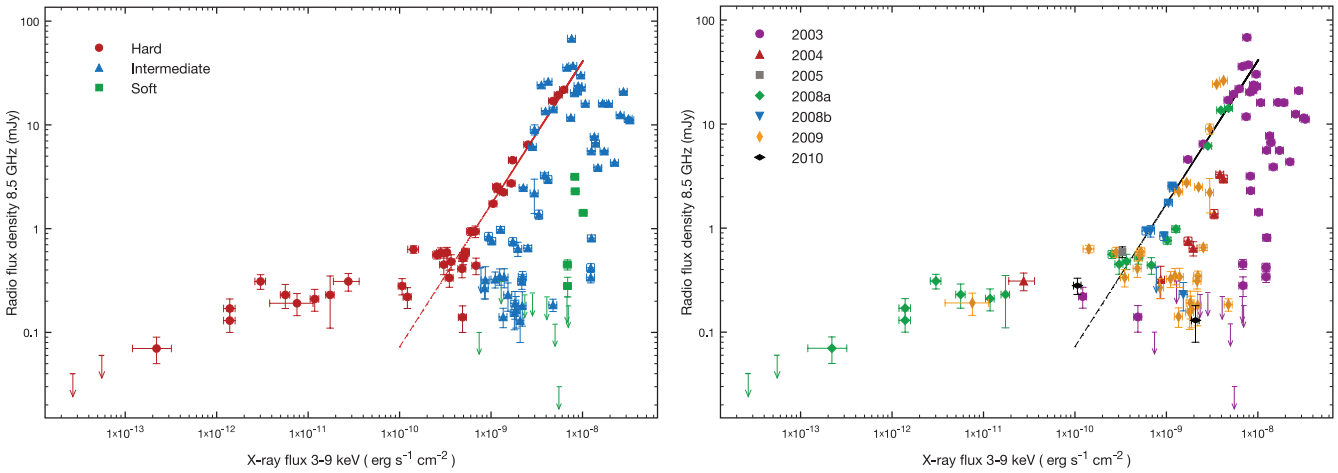

Figure 3. Quasi-simultaneous 8.5 GHz radio flux density versus 3–9 keV X-ray flux during the seven outbursts. (a) Left-hand panel: data are colour coded according to X-ray state. Red circles, green squares and blue triangles indicate the hard, soft and intermediate state, respectively. Dashed line indicates the power-law fit to the selected hard state data (see Section 3.2). (b) Right-hand panel: same as left-hand panel but with the colour code indicating the outburst, as labelled in the figure legend.

either the X-ray state or the origin of the radio emission (e.g. compact jet, discrete ejecta, interaction with the ISM). Fig. 3 shows the 8.5 GHz radio flux density[4] versus the 3–9 keV unabsorbed flux over the 2003, 2004, 2005, 2008a, 2008b, 2009 and 2010 outbursts. The left-hand panel of Fig. 3 shows the data grouped according to the X-ray state. The right-hand panel shows the data grouped by outburst.

3.1.1 Behaviour at high flux

Above a 3–9 keV X-ray flux $\sim 2 \times 10^{-10}$ erg s^{-1} cm^{-2}, the behaviour of H1743−322 seems compatible, on first inspection, with the radio/X-ray behaviour typically observed during an outburst of a BHXB (for a detailed discussion on this unified picture see e.g. Fender, Homan & Belloni 2009 and references therein). The hard state shows correlated radio and X-ray emissions over two orders of magnitude in radio flux density. On average, it is the most radio loud state for a given X-ray luminosity. During the intermediate state, the X-ray emission increases but is not correlated with the radio emission. For most of the radio observations during the intermediate state, the spectral index is indicative of optically thin synchrotron emission from transient ejecta ($\alpha \lesssim -0.5$, where radio flux density S_ν scales with frequency ν as $S_\nu \propto \nu^\alpha$). During the soft state, the radio emission is usually not detected as illustrated by the upper limits, however, we note several radio detections during the soft state of the 2003 outburst. This residual emission shows optically thin spectra and could originate from the interaction of the ejected matter with the environment, as was later observed on larger scales (Corbel et al. 2005).

3.1.2 Behaviour at low flux

If we consider now the entire plot including the low flux data, we note several data points that clearly depart from the main hard state correlation below $\sim 2 \times 10^{-10}$ erg s^{-1} cm^{-2} in the 3–9 keV X-ray band. Most of these points (green diamonds in Fig. 3b) belong to the decay phase of the 2008a outburst and were obtained using the *Chandra* and *Swift* satellites along with the VLA (Jonker et al. 2010). The origin of the radio emission is unclear since most of the VLA observations were conducted at only one frequency. For three of them, however, upper limits at 1.4 GHz are available. The corresponding lower limits on the radio spectral indices ($\alpha \geq -0.58$, -0.53 and -0.60) encompass both possibilities of optically thick and thin spectra. On the other hand, we note that the data from the declining hard state of the 2004 and 2009 outbursts (and possibly also 2003 and 2010) also deviate from the main correlation and seem to follow the same trend as the 2008a data. Moreover, their nearly flat radio spectra are consistent with a compact jet origin. This would suggest that this deviation is a significant evolution of the inflow–outflow connection when the source reaches low luminosities.

3.1.3 Jet quenching factor

The drop in radio flux density during the hard to soft state transition is usually attributed to the quenching of the compact (core) jets. To estimate the level of this suppression, we can use the ratio between the highest radio flux attributed to compact jet emission from the initial hard state of an outburst, and the lowest radio upper limit obtained during the soft state of the same outburst. The 3σ upper limit of 0.03 mJy obtained on MJD 52863 during the soft state of the 2003 outburst, provides a quenching factor of $\sim$700, which is, as far as we know, the strongest constraint to date (Fender et al. 1999; Corbel et al. 2001, 2004) supporting the idea of jet suppression during the soft state.

3.2 Isolating the compact jet–corona connection

The radio/X-ray correlation in BHXBs is usually observed during the canonical hard state where the radio and X-ray emission are assumed to originate from the compact jets and the corona, respectively. To study this connection in detail, we restricted our data set to observations in the hard state for which the radio spectrum was indicative of optically thick synchrotron emission from compact jets, i.e. a radio spectral index whose lower limit is ≥ -0.3. We also

[4] We use an average frequency of 8.5 GHz for simplicity since the radio data come from the VLA (8.46 GHz) and the ATCA (8.64 GHz). Even for an optically thin spectrum with spectral index $\alpha = -0.6$, the effect of this simplification would be <1.5 per cent.

discarded observations that took place following the first radio flare of an outburst, since the compact jets might be disrupted when discrete ejection events take place (see e.g. Corbel et al. 2004; Fender et al. 2004, 2009).

The selected radio and X-ray fluxes are summarized in Table 1 and the radio/X-ray plot obtained using these filtered data is shown in Fig. 4. Above $\sim 2 \times 10^{-10}$ erg s^{-1} cm^{-2} in the 3–9 keV X-ray band, we note a clear correlation over almost two orders of magnitude in radio flux density. We fit the data with a power-law function of the form $F_{\rm Rad} = k F_{\rm X}^{b}$, where $F_{\rm Rad}$ is the radio flux density at 8.5 GHz (in mJy) and $F_{\rm X}$ is the unabsorbed 3–9 keV X-ray flux (in erg s^{-1} cm^{-2}). We obtain a correlation index $b = 1.38 \pm 0.03$ and a normalization constant $k = 4.43 \times 10^{12}$ mJy erg^{-1} s cm^{2}. The correlation index $b \sim 1.4$ clearly differs from the range of values ($b \sim 0.5$–0.7) observed for other BHXBs (e.g. GX 339-4, V404 Cyg, XTE J1118+480; see Corbel et al. 2003, 2008b; Gallo et al. 2003; Xue & Cui 2007). Interestingly, it corresponds to the correlation index found for atoll source neutron stars in the island state (Migliari & Fender 2006), a state that shares similar properties with the hard state of BHXBs. We also note that our derived correlation index is not consistent with the one found by Jonker et al. (2010), i.e. $b = 0.18 \pm 0.01$. However, this index is obtained by fitting the low-luminosity data of the 2008a outburst. Our work suggests that this low value likely reflects a transition phase (see Section 3.3).

We note however that it is the high-flux data from 2003 that mostly constrain the correlation index since it is the brightest outburst observed to date from H1743−322. None the less, if we exclude the 2003 data from the fitting process, we obtain the following

Table 1. X-ray fluxes and radio flux densities selected for the correlation presented in Fig. 4. Unless otherwise stated, the X-ray data are from the *RXTE*-PCA instrument. All *RXTE* fluxes are corrected for the Galactic ridge emission. We also indicate the interferometer used for the radio observations.

Calendar date	MJD	X-ray 3–9 keV unabs. flux (10^{-11} erg s^{-1} cm^{-2})	Radio 8.5 GHz flux density (mJy)	Notes
2003 March 30	52728.59	172 ± 20	4.57 ± 0.12	VLA (1,A)
2003 April 01	52730.55	253 ± 1	6.45 ± 0.12	VLA (1)
2003 April 03	52732.55	474 ± 50	16.99 ± 0.12	VLA (1,B)
2003 April 04	52733.55	626 ± 2	21.81 ± 0.13	VLA (1)
2003 April 06	52735.47	545 ± 7	19.43 ± 0.16	VLA (1)
2003 November 05	52948.00	12.16 ± 0.91	0.22 ± 0.05	VLA (1)
2004 November 01	53310.87	2.75 ± 0.86	0.31 ± 0.06	ATCA
2005 August 07	53589.25	33.0 ± 1.5	0.59 ± 0.07	VLA (2,A)
2008 January 28	54493.32	68.5 ± 5.3	0.44 ± 0.09	ATCA
2008 February 03	54499.74	49.5 ± 3.6	0.52 ± 0.07	VLA (3)
2008 February 05	54501.64	36.5 ± 4	0.48 ± 0.08	VLA (3)
2008 February 06	54502.56	30.424 ± 3	0.45 ± 0.09	VLA (3)
2008 February 09	54505.67	25.60 ± 3	0.56 ± 0.05	VLA (3)
2008 February 19	54515.63	1.74 ± 0.25	0.23 ± 0.12	*Swift* – VLA (3,4)
2008 February 20	54516.55	1.18 ± 0.3	0.21 ± 0.05	*Chandra* – VLA (3,4)
2008 February 23	54519.69	0.56 ± 0.06	0.23 ± 0.06	*Chandra* – VLA (3,4)
2008 February 24	54520.69	0.30 ± 0.04	0.31 ± 0.05	*Swift* – VLA (3,4)
2008 March 01	54526.59	0.14 ± 0.02	0.17 ± 0.04	*Chandra* – VLA (3,4)
2008 March 02	54527.53	0.14 ± 0.02	0.13 ± 0.03	*Chandra* – VLA (3,4)
2008 March 08	54533.56	0.022 ± 0.01	0.07 ± 0.02	*Chandra* – VLA (3,4)
2008 October 05	54744.21	105 ± 14	1.74 ± 0.07	ATCA
2008 October 08	54747.44	115 ± 2	2.54 ± 0.08	ATCA
2008 October 09	54748.44	119 ± 2	2.43 ± 0.09	ATCA
2008 October 10	54749.36	121 ± 3	2.38 ± 0.11	ATCA
2008 November 04	54774.43	67.3 ± 2.5	0.94 ± 0.12	ATCA
2008 November 09	54779.35	60.1 ± 1.9	0.94 ± 0.08	ATCA
2009 May 27	54978.38	137 ± 14	2.24 ± 0.03	VLA (A)
2009 May 30	54981.95	166 ± 7	2.73 ± 0.10	VLA
2009 July 07	55019.46	52.8 ± 5.8	0.592 ± 0.055	VLA
2009 July 08	55020.30	50.7 ± 5	0.546 ± 0.06	VLA (B)
2009 July 09	55021.42	48.1 ± 5.3	0.41 ± 0.074	VLA
2009 July 12	55024.28	35.0 ± 3	0.335 ± 0.063	VLA (B)
2009 July 13	55025.28	28.2 ± 1.9	0.587 ± 0.066	VLA
2009 July 19	55031.29	14.2 ± 1.9	0.631 ± 0.052	VLA
2009 August 06	55049.60	0.76 ± 0.38	0.191 ± 0.046	VLA
2010 February 13	55240.01	10.6 ± 0.9	0.28 ± 0.05	ATCA

Note. (1) VLA flux density from McClintock et al. (2009); (2) VLA flux density from Rupen et al. (2005); (3) VLA flux density from Jonker et al. (2010); (4) *Swift* and *Chandra* fluxes from Jonker et al. (2010) (see Section 2.1.2);
(A) ASM count rate converted into 3–9 keV unabsorbed flux using WEBPIMMS (see Section 2.3); (B) X-ray flux obtained by interpolation of the PCA light curve (see Section 2.3).

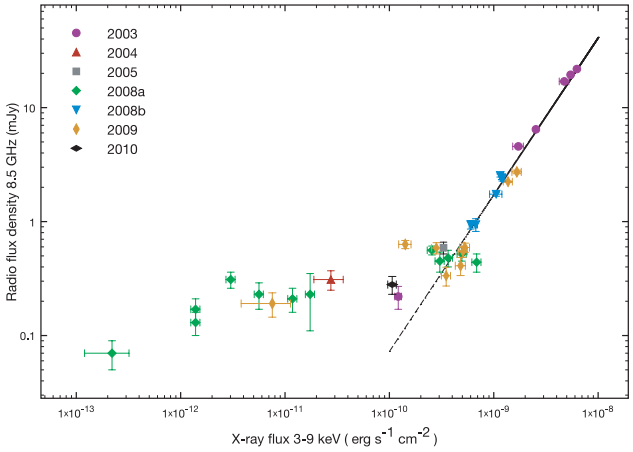

Figure 4. Radio flux density at 8.5 GHz versus the unabsorbed 3–9 keV X-ray flux. This plot shows the data set restrained to the 'canonical' hard state where the radio emission can be attributed to partially self-absorbed synchrotron emission from the compact jets and where the X-ray spectra are dominated by the power-law component. Dashed line indicates the fit to the data above 2×10^{-10} erg s^{-1} cm^{-2} with a function of the form $F_{\rm Rad} = k\, F_{\rm X}^{b}$, with $b = 1.38 \pm 0.03$ and $k = 4.43 \times 10^{12}$ mJy erg^{-1} s cm^{2}.

99.99 per cent confidence interval for the correlation index: [1.19, 1.65]. This remains in good agreement with the previous results and seems to favour a constant slope for all outbursts.

3.3 Comparison with the 'standard' radio/X-ray correlation

To compare the relationship between radio and X-ray fluxes in H1743−322 with the standard radio/X-ray correlation of black hole and neutron star X-ray binaries, we plot in Fig. 5 the hard state data from H1743−322, GX 339-4 (the data cover seven outbursts over the period 1997–2010 and will be detailed in Corbel et al., in preparation), V404 Cyg (Gallo et al. 2003; Corbel et al. 2008b) and the atoll neutron stars Aql X-1 (Tudose et al. 2009; Miller-Jones et al. 2010) and 4U 1728−34 (Migliari & Fender 2006) in the island state. To convert fluxes into luminosity, we used a distance of 8 kpc for GX 339-4 (Zdziarski et al. 2004) and the new distance of 2.39 kpc for V404 Cyg, that was derived using accurate astrometric very long baseline interferometry (VLBI) observations (Miller-Jones et al. 2009). For the neutron stars, we used 5.2 kpc for Aql X-1 (Jonker & Nelemans 2004) and 4.6 kpc for 4U 1728−34 (Galloway et al. 2003).

Fig. 5 shows that for intermediate luminosities ($\sim 10^{36-37}$ erg s^{-1}), H1743−322 lies significantly below the 'standard' correlation for BHXBs but is not compatible either with the neutron star relation. In addition, the figure shows that the deviant points at low luminosity seem to rejoin the standard correlation and then follow it below 2×10^{34} erg s^{-1}. The data points between 2×10^{34} and 2×10^{36} erg s^{-1} seem thus to reflect a transition between the correlation of slope $b = 1.4$ and the standard correlation of slope $b = 0.6$. This supports the idea of a significant change in the coupling between the jets and the corona in H1743−322 when the source reaches low accretion rates.

This transition can be crudely fit with a power-law function with index $b = 0.23 \pm 0.07$ between the 3–9 keV luminosities 2×10^{34} and 2×10^{36} erg s^{-1}. The corresponding bolometric (3–100 keV) luminosities in Eddington units are $L_{\rm stand} \sim 5 \times 10^{-5} L_{\rm Edd}$ and $L_{\rm trans} \sim 5 \times 10^{-3} L_{\rm Edd}$ for a 10 $M_{\odot}$ black hole.

As mentioned in the Introduction, H1743−322 is identified as an outlier of the standard radio/X-ray correlation, as confirmed by

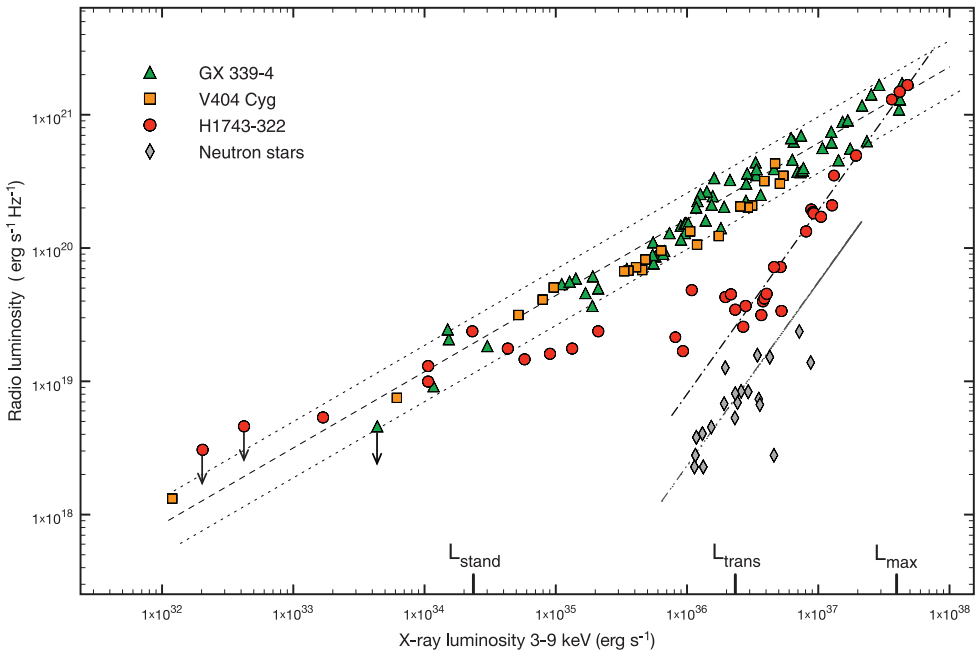

Figure 5. 8.5 GHz radio luminosity against 3–9 keV X-ray luminosity for the BHCs H1743−322, GX 339−4 and V404 Cyg in the hard state. For comparison, we also plot the data from the atoll neutron stars Aql X-1 and 4U 1728−34 in the island state. The dashed line indicates the fit to the GX 339-4 and V404 Cyg data with a relation of the form $L_{\rm radio} \propto L_{\rm X}^{b}$ with a correlation index $b \sim 0.6$. The two dotted lines demarcate the dispersion around the correlation. The dashed–dotted and dashed–dotted–dotted lines indicate the fit to the high-luminosity data of H1743−322 and the neutron star data, respectively, with a correlation index $b \sim 1.4$. On the x-axis, we also indicate three characteristic X-ray luminosities that will ease the discussion. $L_{\rm stand}$ and $L_{\rm trans}$ are, respectively, the lower and the upper bound of the transition between the two correlations. $L_{\rm max}$ indicates the point where the steep correlation of H1743−322 connects to the 'standard' correlation at high luminosity. Note that these three luminosities are defined in the 3–100 keV band in the text.

our results. Some of the numerous questions associated with this outlier population of sources are whether they follow the same correlation slope as the other BHXBs but with a lower normalization, and whether they remain below the standard correlation at low and high luminosity. In the case of H1743−322, we obtain a correlation index of $b = 1.38 \pm 0.03$. This is the first precise measurement of the radio/X-ray correlation of an outlier. If H1743−322 is representative of these 'radio-quiet' Galactic black holes, our results suggest that their location below the 'standard' correlation is a consequence of an intrinsically different coupling between the jets and the corona rather than just a variation of normalization. In this respect, we point out the recent work by Soleri et al. (2010) on the outlier Swift J1753.5−0127. These authors report a slope of the radio/X-ray correlation of the source lying between 1.0 and 1.4, in good agreement with our results on H1743−322. Finally, our results suggest that at high ($\sim L_{\rm max}$) and low luminosity ($\leq L_{\rm stand}$), the outliers might not remain below the standard correlation if they follow the same behaviour as H1743−322 (see Fig. 5).

4 DISCUSSION

4.1 Nature of the compact object

As mentioned above, the mass of the compact object is not yet constrained, so its nature is still uncertain. Based on the radio/X-ray correlation alone and considering the results of Migliari & Fender (2006), the 1.4 power-law index could suggest that the accreting compact object is a neutron star. However and more tellingly, the overall behaviour of the source during an outburst, and its X-ray spectral and timing features are very similar to other, dynamically confirmed, black hole binaries (e.g. XTE J1550−564; McClintock et al. 2009). The source is thus more likely to be a black hole than a neutron star. In the following discussion, we will therefore consider it as such, but note the caveat that a neutron star primary cannot be entirely ruled out.

4.2 Radio-quiet or X-ray-loud microquasar?

As shown in Fig. 5, H1743−322 spans the same range of X-ray and radio luminosity in the hard state as 'standard' microquasars. Consequently, should we consider that it displays dimmer radio emission for a given X-ray luminosity or the contrary? In other words, are we facing a radio-quiet or an X-ray-loud microquasar? In the following, we investigate both hypotheses. First (Section 4.3), we consider that the outliers have a more radiatively efficient X-ray emitting component than the 'standard' microquasars (X-ray loud hypothesis). Then (Section 4.4), we consider that the discrepancy between the two populations of sources arise from different jet properties (radiative efficiency, injected power etc.) leading the outliers to produce fainter radio emission.

4.3 Radiatively efficient accretion flow in the hard state: the X-ray loud hypothesis

We usually define two general classes of accretion flow, depending on whether the gravitational energy of the accreted matter is preferentially released through radiation (radiatively efficient) or carried away with the flow (radiatively inefficient).

Radiatively efficient flows include, for instance, the standard optically thick and geometrically thin accretion disc model (Shakura & Sunyaev 1973), some models of accretion disc coronae (ADC; see e.g. Galeev, Rosner & Vaiana 1979; Haardt & Maraschi 1991; Di Matteo, Celotti & Fabian 1999; Merloni & Fabian 2002) or the luminous hot accretion flow (LHAF) model (Yuan 2001). From simple physical assumptions, the scaling of the X-ray luminosity with accretion rate, in most radiatively efficient flows, is expected to be linear, $L_{\rm X} \propto \dot{M}$.

Radiatively inefficient flows are expected to produce X-ray emission with $L_{\rm X} \propto \dot{M}^{2-3}$. This is the case of accretion flows dominated by advection in which a significant fraction of the energy is advected instead of radiated away. This advected energy can either cross the event horizon [advection-dominated accretion flow (ADAF); Ichimaru 1977; Narayan & Yi 1994; Abramowicz et al. 1996] and/or be expelled in outflows [advection-dominated inflow–outflow solution (ADIOS); Blandford & Begelman 1999]. In such models, the X-ray emission arises mainly from Compton up-scattering of internal (synchrotron, bremsstrahlung) or external (blackbody emission from outer thin disc) photon fields. A similar relation ($L_{\rm X} \propto \dot{M}^{2-3}$) is also obtained in systems dominated by jet emission, where most of the energy is channelled into the jets (Markoff et al. 2003, 2005). The X-rays, in that case, can originate at the base of the jets as optically thin synchrotron emission and/or inverse Compton scattering by the outflowing particles of the jet synchrotron photons [synchrotron self-Compton (SSC)] and disc photons (external Compton).

We will now show that if we assume the standard emission model of compact jets is valid for the outliers, the steep radio/X-ray correlation we have found implies that the accretion flow is radiatively efficient in the hard state, in contrast to what is usually assumed for BHXBs in this X-ray state.

Let us thus consider the classical assumption stating that the total jet power $Q_{\rm jet}$ is a fraction $f_{\rm j} < 1$ of the (maximal) accretion power $Q_{\rm accr}$:

$$Q_{\rm accr} = \dot{M}c^2 \qquad \text{and} \qquad Q_{\rm jet} = f_{\rm j}\, Q_{\rm accr}. \tag{1}$$

The fraction $f_{\rm j}$ is usually considered as constant or at least independent of the accretion rate (see e.g. Blandford & Königl 1979; Falcke & Biermann 1995; Heinz & Sunyaev 2003). $Q_{\rm jet}$ should therefore scale linearly with $\dot{M}$. Since we restrict ourselves to the standard jet emission model, we will adopt this assumption. However, there is no strong physical argument justifying that $f_{\rm j}$ is independent of $\dot{M}$, so we shall discuss it in the next section about the radio-quiet hypothesis.

From the standard equations for synchrotron emission (e.g. Rybicki & Lightman 1979), one can obtain the following scaling between the jet luminosity L_ν at a given frequency and the jet power (see e.g. Heinz & Sunyaev 2003):

$$L_\nu \propto Q_{\rm jet}^{\xi} \qquad \text{with} \qquad \xi = \frac{2p - (p+6)\alpha + 13}{2(p+4)}, \tag{2}$$

and where α is the spectral index of the jet spectrum (with the convention $L_\nu \propto \nu^\alpha$). This relation is valid under the assumptions of the standard model, i.e. a conical jet with an initial energy distribution of relativistic electrons in the form of a power law with index p (for the impact of different assumptions see e.g. Pe'er & Casella 2009). The classical values assumed for p are in the range 2–3 (see e.g. Bell 1978; Blandford & Ostriker 1978; Drury, Axford & Summers 1982; Gallant, Achterberg & Kirk 1999; Achterberg et al. 2001), while the spectral index α of the compact jets in the radio range is usually observed between −0.2 and 0.2. Fig. 6 shows the variation of the exponent ξ as a function of p for different values of α. We note that for the fiducial values of p and α, ξ varies between 1.22 and 1.58 with an average value of $\sim$1.4.

If the observing frequency is located in the radio range, equations (1) and (2) give $L_{\rm radio} \propto \dot{M}^{\xi}$. If we assume that the X-ray luminosity

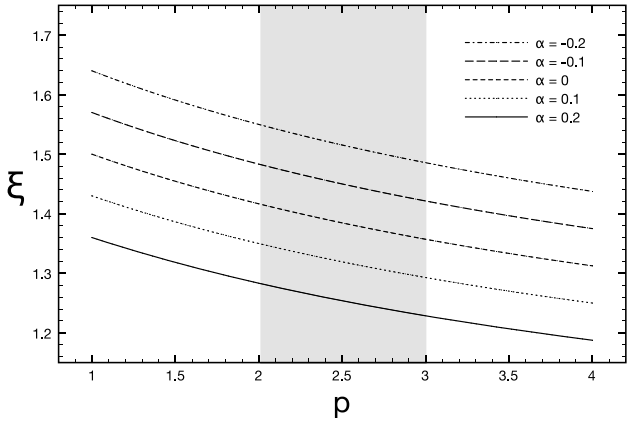

Figure 6. Variation of the exponent ξ in the relation $L_\nu \propto Q_{\rm jet}^{\xi}$, as a function of the power-law index p of the electron distribution, for several values of the spectral index α of the compact jets. Grey zone delimits the range of values usually assumed for the power-law index p.

in the hard state can be written in a general way as $L_{\rm X} \propto \dot{M}^q$, we expect the following relation between radio and X-ray luminosities:

$$L_{\rm radio} \propto L_{\rm X}^{\xi/q}. \quad (3)$$

Consequently, for ξ between 1.22 and 1.58, the radio/X-ray correlation usually found for microquasars ($L_{\rm radio} \propto L_{\rm X}^{0.5-0.7}$), requires $q \sim 2$–3 and thus a radiatively inefficient accretion flow. On the other hand, the $L_{\rm radio} \propto L_{\rm X}^{1.4}$ relation of H1743−322 implies $q \sim 1$, which suggests the X-ray emission in the hard state is produced by a radiatively efficient flow. In this respect, we note that a radiatively efficient flow during the hard state of Cyg X-1 has been found by Malzac, Belmont & Fabian (2009). Moreover, Rushton et al. (2010) have shown that GRS 1915+105 could be radiatively efficient during its plateau state. This in turn would be consistent with the fact that it lies on the extension, at high luminosity, of the correlation of H1743−322 (Coriat et al. 2011).

As mentioned previously, to obtain the radio/X-ray plot in Fig. 4, we filtered the X-ray data to minimize the thermal contribution of the thin disc. We can thus exclude the possibility that the disc contaminates the 3–9 keV emission enough to produce the observed correlation.

As far as we know, besides the standard accretion disc solution, the other models of radiatively efficient accretion flows can be divided in two categories according to their geometry.

(i) Hot accretion flow: the standard accretion disc extends to a truncation radius, where it is replaced by a hot and geometrically thick flow in the inner parts.

(ii) ADC: the standard accretion disc extends close to the black hole and is 'sandwiched' by a corona of hot plasma.

In both categories, several models have been developed to explain the properties of BHXBs in the hard state by coupling the accretion flow with steady jets. While the aim of this work is not to review all these models, we briefly examine some examples below.

4.3.1 Hot accretion flows

Most hot accretion flow models are found to be radiatively inefficient, at least at low accretion rates (e.g. ADAF, ADIOS, CDAF), and can only exist below a critical accretion rate ($\sim 10^{-1}$–$10^{-2}(L_{\rm Edd}/c^2)$). However, Yuan (2001) has shown that a hot flow may be maintained above the critical accretion rate when Coulomb coupling between electrons and ions becomes more effective due to increasing density. The obtained accretion flow solution named the LHAF is described as an extension of the ADAF regime to high accretion rates and is found to be radiatively efficient (see also Yuan & Zdziarski 2004; Yuan et al. 2006). We can thus check if the luminosity range where we observe the steep correlation is compatible with the LHAF regime. We can write the X-ray luminosity of the accretion flow as $L_{\rm X} = \eta \dot{M} c^2$ with η the efficiency coefficient. η should be constant to get $L_{\rm X} \propto \dot{M}$, which is roughly the case for the LHAF (Yuan, private communication). Let us thus assume that H1743−322 is in the LHAF regime in the luminosity range where we observe the correlation of slope 1.4. According to Yuan (2001), an ADAF should become a LHAF when $\dot{M}$ exceeds the critical accretion rate $\dot{M}_{\rm crit} \sim 10\alpha_v^2 \dot{M}_{\rm Edd}$, where α_v is the viscosity coefficient and where we have defined the Eddington accretion rate as $\dot{M}_{\rm Edd} = L_{\rm Edd}/c^2$. For the standard value $\alpha_v = 0.1$, we thus have $\dot{M}_{\rm crit} \sim 0.1\dot{M}_{\rm Edd}$. Our results show that the steep correlation starts from a 3–100 keV luminosity $L_{\rm trans} \sim 5 \times 10^{-3} L_{\rm Edd}$. Then, for $L_{\rm X} = L_{\rm trans} = \eta \dot{M}_{\rm trans} c^2$, we have

$$\eta \dot{M}_{\rm trans} = 5 \times 10^{-3} \dot{M}_{\rm Edd}. \quad (4)$$

If $\dot{M}_{\rm trans}$ corresponds to the critical accretion rate $\dot{M}_{\rm crit}$ where the LHAF regime starts, then $\eta = 0.05$. The steep correlation is maintained up to the 3–100 keV luminosity $L_{\rm max} \sim 6 \times 10^{-2} L_{\rm Edd}$ where the intersection with the standard correlation occurs (see Fig. 5). If η is indeed constant in the LHAF regime, then for $L_{\rm X} = L_{\rm max}$, the corresponding accretion rate $\dot{M}_{\rm max}$ should be of the order of the Eddington accretion rate. The LHAF hypothesis thus leads to a high but not implausible value of the maximal accretion rate reached in the hard state.

Alternatively, we can estimate $\dot{M}_{\rm trans}$ from the radio luminosity and compare it to the critical accretion rate $\dot{M}_{\rm crit} \sim 0.1\dot{M}_{\rm Edd}$. Assuming $L_{\rm radio} \propto \dot{M}^{17/12}$ (equivalent to equation 2 in the case $\alpha = 0$ and $p = 2$), Körding, Fender & Migliari (2006b) found an estimate of the normalization constant between the radio luminosity of the compact jets and the accretion rate:

$$\dot{M} = \dot{M}_0 \left(\frac{L_{\rm radio}}{10^{30}\,{\rm erg\,s^{-1}}} \right)^{12/17} \text{with} \;\; \dot{M}_0 = 4.0 \times 10^{17}\,{\rm g\,s^{-1}}. \quad (5)$$

From Fig. 5, the radio luminosity corresponding to $L_{\rm trans}$ is $\sim 2.5 \times 10^{19}$ erg s^{-1} Hz^{-1}. Using equation (5) we thus derive $\dot{M}_{\rm trans} \sim 1.5 \times 10^{17}$ g s^{-1}. For a 10 $M_\odot$ black hole, this corresponds to $0.1\dot{M}_{\rm Edd}$, in agreement with the expected accretion rate at the transition to the LHAF regime. The LHAF model is thus a possible explanation for the behaviour of H1743−322 at high luminosity.

In a similar fashion, hot flow solutions have recently been found (Petrucci, private communication) for the jet emitting disc (JED) model (see e.g. Ferreira 2002, 2008; Ferreira et al. 2006; Combet & Ferreira 2008, and references therein), in which the flow goes from radiatively inefficient to radiatively efficient as the accretion rate increases. These JED hot solutions have properties very similar to those of one-temperature accretion flow studied by Esin et al. (1996) in the ADAF regime and revisited for higher accretion rates by Yuan et al. (2006) in the LHAF regime. The originality of the JED solutions resides in the fact that, by construction, they integrate self-consistently stationary and powerful self-collimated jets.

4.3.2 Accretion disc corona

Some ADC models could be also radiatively efficient in the hard state (see e.g. Galeev et al. 1979; Haardt & Maraschi 1991; Di Matteo et al. 1999; Malzac, Beloborodov & Poutanen 2001; Merloni

& Fabian 2002; Merloni 2003). In these models, a fraction f_c of the accretion power is dissipated in the corona, likely due to magnetic reconnection, and eventually emerges as X-ray radiation. The X-ray luminosity can be written as $L_X \sim f_c \dot{M} c^2$. In the case where the coronal plasma is heated by magnetic dissipation, Merloni & Fabian (2002) and Merloni (2003) have shown that f_c is constant when gas pressure dominates in the disc and therefore $L_X \propto \dot{M}$ which would explain the steep radio/X-ray correlation. When the radiation pressure dominates in the disc, Merloni et al. (2003) have shown that we should also expect a radio/X-ray correlation of the form $L_{radio} \propto L_X^{1.4}$. From the estimates of Merloni (2003), f_c should be of the order of 0.02 to 0.07 (for sub-Eddington systems) and would therefore be consistent with the X-ray luminosity range in which we observe the steep correlation.

From the radio/X-ray correlation point of view, ADC models could be therefore responsible for the X-ray emission in the high-luminosity hard state of H1743−322. However, the geometry assumed in these models leads naturally to the debate (beyond the scope of this paper) of whether or not the accretion disc extends close to the black hole.

4.3.3 Efficient to inefficient transition

When $L_X < L_{trans}$, our results suggest that H1743−322 undergoes a transition from the steep to the standard correlation. Under the assumptions on jet emission considered in this section, this transition to a relation $L_{radio} \propto L_X^{0.6}$ indicates that the accretion flow becomes radiatively inefficient, with $L_X \propto \dot{M}^{2-3}$ below L_{stand}. If we assume that equation (2) is valid during this transition (i.e. the radio luminosity is a good tracer of the accretion rate), the variation of radio luminosity between L_{trans} and L_{stand} should correspond to a variation of the accretion rate by a factor of ∼2. The corresponding variation of the X-ray luminosity is $L_{trans}/L_{stand} \sim 100$ and this transition occurs on a time-scale of 15 d. If the accretion rates varies little, as suggested by the almost constant level of radio emission during this transition, the radiative efficiency coefficient η of the accretion flow should vary significantly (by a factor of ∼50).

A transition from an efficient to an inefficient regime could be interpreted as a transition from an LHAF to an ADAF. In the framework of the ADC models, this could arise from changes in the properties of the corona heating mechanism. These details should be investigated on theoretical grounds.

Rather than being due to changes in the intrinsic properties of the accretion flow (as in the LHAF–ADAF case), the transition could results from the contribution of two emitting components, one inefficient with $L_X \propto \dot{M}^{2-3}$ and the other radiatively efficient with $L_X \propto \dot{M}$. When both components are present, the efficient component dominates the X-ray flux. Below a given $\dot{M}$ it disappears, leaving only the inefficient component. As an illustration, we can point to the work on XTE J1550−564 by Russell et al. (2010). The authors demonstrate the possibility that the origin of the X-ray emission evolves throughout the hard state, being alternatively dominated by thermal Comptonization or direct synchrotron emission from the compact jets. We also point out the work by Rodriguez et al. (2008a,b) on GRS 1915+105, where it is reported that two components are present in the hard X-ray spectrum during the plateau state. One of these components appears to be linked to the radio emission while the other is not. This supports the idea that several components co-exist and can dominate alternatively the X-ray band during the hard state. In our case, we could consider that above L_{trans} the X-ray emission is dominated by the contribution of an efficient accretion flow (as e.g. those mentioned previously). Below L_{stand}, the X-rays become dominated, for instance, by the synchrotron or SSC emission from the base of the jets.

4.3.4 The radio/X-ray diagram of BHXBs under the X-ray loud hypothesis

Regardless of the specific models that could explain our results, we can conclude that, as long as the assumptions about the jet physics stated in equations (2) and (3) are correct, the accretion flow has to be radiatively efficient (with $L_X \propto \dot{M}$) above $\sim 5 \times 10^{-3} L_{Edd}$. At lower X-ray luminosities, the radiative efficiency of the accretion flow should decrease significantly to reproduce the transition between the two correlations. Our results suggest that the X-ray luminosity scales as $\dot{M}^{2-3}$. If H1743−322 is indeed representative of the behaviour of the other outliers, we can thus represent the universal radio/X-ray diagram of BHXBs by the sketch shown in Fig. 7. This figure summarizes the X-ray loud interpretation. We can then distinguish two branches in the radio/X-ray diagram of BHXBs, according to the efficiency of the accretion flow and the consequent scaling of the X-ray luminosity with the mass accretion rate. For a still unknown reason, some BHXBs would remain radiatively inefficient in the hard state up to the transition to the soft state while others (the outliers) would develop a more radiatively efficient accretion flow leading them to follow the efficient branch. We also illustrate the possibility of the transition between branches below the critical accretion rate $\dot{M}_{trans}$.

If this sketch correctly describes the situation, the major issue to address now is to determine which fundamental parameter influences the global evolution of the accretion flow with mass accretion rate and will lead some black hole systems to follow the 'efficient' branch and others the 'inefficient' branch. In future works we thus need to investigate the influence of parameters such as the orbital period, the environment (e.g. magnetic) of the binary or perhaps the nature or evolutionary stage of the companion star. The physical conditions at outer boundary of the accretion disc could also have an influence on the dynamical and radiative structure of the flow (Yuan et al. 2000).

4.4 Beyond the standard assumptions on compact jet emission: the radio-quiet hypothesis

Another way to assess the problem would be to consider that the difference between the standard microquasars and the outliers arises from different jet properties rather than from different accretion flows. In this case we can relax the assumptions leading to equations (2) and (3).

We can first consider that the fraction f_j (in $Q_{jet} = f_j Q_{accr}$) of accretion energy injected into the jets is in fact dependent on the accretion rate. For simplicity, we will consider a linear dependence, $f_j \propto \dot{M}$. In that case, equation (3) becomes $L_{radio} \propto L_X^{2\xi/q}$. For a radiatively inefficient accretion flow ($q \sim 2$), this gives the correlation we observe for H1743−322.

Whether or not f_j is dependent on the accretion rate depends on the details of the jet launching mechanism e.g. mass loading into the jet, the specific acceleration mechanism or the origin of the magnetic field. A detailed theoretical study is therefore required to address this issue. However, as an example, if we consider the standard theories of magnetically driven jets, we note that the material is accelerated from a given region of the disc. The size of this region is usually

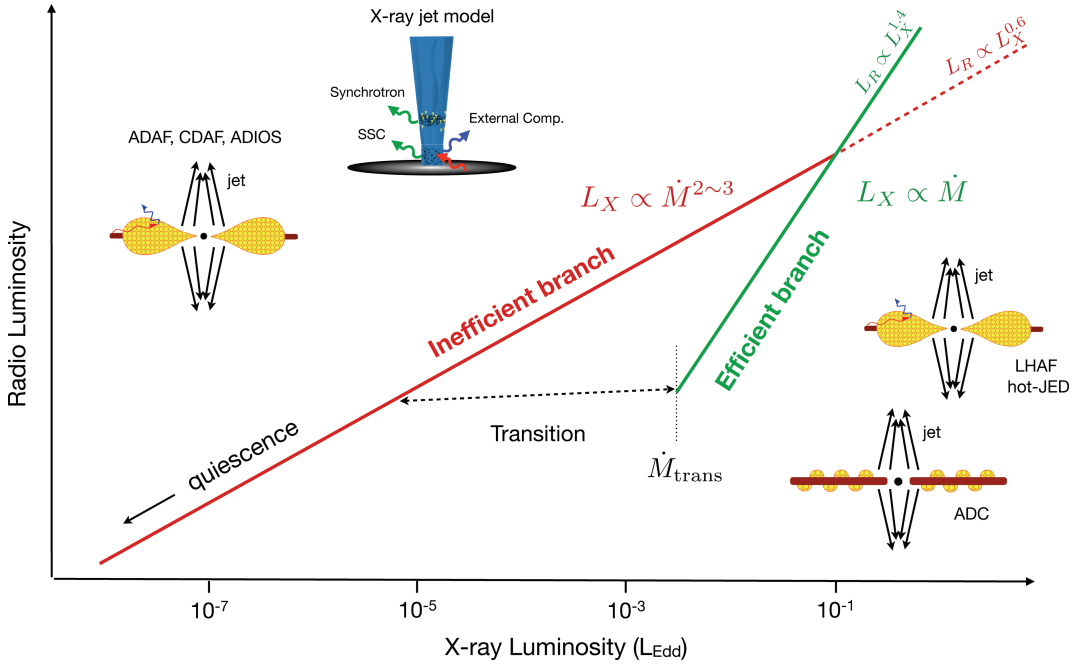

Figure 7. A schematic drawing of the global radio/X-ray correlation for Galactic black holes. The X-ray luminosity is expressed in terms of the Eddington luminosity for a 10 $M_\odot$ black hole. This figure illustrates the case where the correlation $L_{\rm radio} \propto L_{\rm X}^{1.4}$ of the outliers is a consequence of the coupling between a radiatively efficient accretion flow and a steady compact jet whose radio emission can be described by the relation $L_{\rm radio} \propto \dot{M}^{1.4}$. We distinguish two branches in this diagram according to the efficiency of the accretion flow and the consequent scaling of the X-ray luminosity with the mass accretion rate. The inefficient branch corresponds to the 'standard' radio/X-ray correlation observed for black holes systems like GX 339-4 or V404 Cyg. The inner flow in these systems can be described by e.g. a hot and inefficient accretion flow such as an ADAF, or by X-ray jet models as proposed by Markoff and collaborators. The efficient branch corresponds the radio/X-ray correlation of the outliers for which the X-ray luminosity in the hard state varies linearly with mass accretion rate. The X-ray emitting component in these systems could be described by e.g. a hot and efficient accretion flow such as the LHAF or hot-JED solutions or by some magnetic corona models. We also illustrate in this figure the possibility of a transition between the two branches as suggested by the behaviour of H1743−322. The pictures representing the different models are adapted from Markoff & Nowak (2004) and Nowak et al. (2004).

considered as constant in the models (and is often the entire disc). However, if we assume that, for any reason, this size evolves with accretion rate, it would therefore introduce a dependency of $f_{\rm j}$ on $\dot{M}$. This is however very speculative and we would have to explain why the size of this region changes in some systems and not in others.

Another parameter that could strongly influence the jet emission is of course the strength of the magnetic field embedded in the jet plasma. This will modify the synchrotron emission as a function of the jet power (equation 2). Pe'er & Casella (2009) presented a new model for jet emission in XRBs, in which they showed that the flux at radio wavelengths depends on the value of the magnetic field in a non-trivial way. Above a critical magnetic field strength, the outflowing electrons cool rapidly close to the jet base, leading to a strong suppression of the radio emission. Based on these results, Casella & Pe'er (2009) proposed that the outliers are sources with magnetic fields above the critical value. With respect to our results, it could also explain the transition phase between the two correlations. If we consider that the magnetic field strength evolves throughout the outburst (e.g. with the accretion rate), the transition could be due to the magnetic field decreasing below the critical value, leading H1743−322 to the same level of radio emission as GX 339-4 and V404 Cyg. However, the model does not explain precisely how the radio luminosity evolves with the injected power and thus with the accretion rate. Therefore, we cannot judge whether or not it is able to reproduce the correlation index of 1.4 we found. We thus encourage further developments of this model.

5 CONCLUSIONS

In this work we have studied the long-term radio/X-ray correlation of the BHC H1743−322. This source belongs to a group of Galactic black hole X-ray binaries dubbed as outliers of the 'universal' radio/X-ray correlation, for being located below the main $L_{\rm radio} \propto L_{\rm X}^{\sim0.5-0.7}$ relation. We therefore concentrated our efforts on providing new constraints and improving our understanding of these sources. Our main conclusions can be summarized as follows:

(i) In the brightest phase of the hard state, we find a tight power-law correlation with a slope $b = 1.38 \pm 0.03$, between the radio flux from the compact jets and the X-ray emission from the inner flow. This correlation is much steeper than usually found for black hole X-ray binaries and is the first precise measurement for an outlier.

(ii) When the source reaches a luminosity below $\sim 5 \times 10^{-3} L_{\rm Edd}\,(M/10\,{\rm M}_\odot)^{-1}$, we found evidence of a transition from the steep $b \sim 1.4$ relation to the standard $b \sim 0.6$ correlation seen in e.g. V404 Cyg and GX 339−4.

(iii) Additionally, we find that H1743−322 provides the best constraint to date (with a jet quenching factor of ∼700) supporting the idea of jet suppression during the soft state.

From these results, we discuss several hypotheses that could explain the correlation index along with the transition toward the standard correlation.

(i) We first show that if the standard scaling, $L_{\rm radio} \propto \dot{M}^{1.4}$, between the jet radio emission and the accretion rate is valid, then

our results require a radiatively efficient accretion flow that produces the X-ray emission in the hard state at high accretion rate. Ultimately, the flow has to become radiatively inefficient below a critical accretion rate, to account for the transition.

(ii) We also investigate the possibility that our results arise from the outflow properties of the source rather than from the accretion flow. We show in particular that if we relax the assumption that the jet power is a fixed fraction of the accretion power and we consider this fraction linearly dependent on the accretion rate, we can obtain the required correlation with an inefficient accretion flow.

Further investigations are now needed to determine which fundamental parameter of the binary systems or their environments can lead BHXBs of similar appearance to develop different accretion or ejection flows.

ACKNOWLEDGMENTS

MC and SC would like to thank Julien Malzac, Pierre-Olivier Petrucci, Elmar Körding, Sera Markoff, Feng Yuan and Michiel van der Klis for useful comments and discussions and Philip Edwards for prompt scheduling of the ATCA observations. The data on the 2009 outburst were collected by the JACPOT XRB collaboration (Miller-Jones et al. 2011), as part of an ongoing VLBA large project. In particular, the authors would like to acknowledge the roles played by Ron Remillard, Michael Rupen and Vivek Dhawan in this effort. The authors would also like to thank the anonymous referee for his critical reading that helped to improve the style and content of this paper.

The research leading to these results has received partial funding from the European Communitys Seventh Framework Programme (FP7/2007-2013) under grant agreement number ITN 215212 Black Hole Universe. This research has made use of data obtained from the High Energy Astrophysics Science Archive Research Center (HEASARC), provided by NASA's Goddard Space Flight Center. The ATCA is part of the Australia Telescope funded by the Commonwealth of Australia for operation as a National Facility managed by CSIRO. The National Radio Astronomy Observatory is a facility of the National Science Foundation operated under cooperative agreement by Associated Universities, Inc.

REFERENCES

Abramowicz M. A., Chen X., Granath M., Lasota J., 1996, ApJ, 471, 762
Achterberg A., Gallant Y. A., Kirk J. G., Guthmann A. W., 2001, MNRAS, 328, 393
Bell A. R., 1978, MNRAS, 182, 147
Belloni T. M., 2010, in Belloni T., ed., Lecture Notes in Physics, Vol. 794, States and Transitions in Black Hole Binaries. Springer-Verlag, Berlin, p. 53
Blandford R. D., Begelman M. C., 1999, MNRAS, 303, L1
Blandford R. D., Königl A., 1979, ApJ, 232, 34
Blandford R. D., Ostriker J. P., 1978, ApJ, 221, L29
Brocksopp C., Corbel S., Fender R. P., Rupen M., Sault R., Tingay S. J., Hannikainen D., O'Brien K., 2005, MNRAS, 356, 125
Cadolle Bel M. et al., 2007, ApJ, 659, 549
Capitanio F. et al., 2005, ApJ, 622, 503
Capitanio F., Belloni T., Del Santo M., Ubertini P., 2009, MNRAS, 398, 1194
Casella P., Pe'er A., 2009, ApJ, 703, L63
Chen Y. P., Zhang S., Torres D. F., Wang J. M., Li J., Li T. P., Qu J. L., 2010, A&A, 522, A99
Combet C., Ferreira J., 2008, A&A, 479, 481
Corbel S., Fender R. P., 2002, ApJ, 573, L35
Corbel S., Fender R. P., Tzioumis A. K., Nowak M., McIntyre V., Durouchoux P., Sood R., 2000, A&A, 359, 251
Corbel S. et al., 2001, ApJ, 554, 43
Corbel S., Nowak M. A., Fender R. P., Tzioumis A. K., Markoff S., 2003, A&A, 400, 1007
Corbel S., Fender R. P., Tomsick J. A., Tzioumis A. K., Tingay S., 2004, ApJ, 617, 1272
Corbel S., Kaaret P., Fender R. P., Tzioumis A. K., Tomsick J. A., Orosz J. A., 2005, ApJ, 632, 504
Corbel S., Tzioumis T., Coriat M., Brocksopp C., Fender R., 2008a, Astron. Telegram, 1766, 1
Corbel S., Körding E., Kaaret P., 2008b, MNRAS, 389, 1697
Coriat M., Corbel S., Buxton M. M., Bailyn C. D., Tomsick J. A., Körding E., Kalemci E., 2009, MNRAS, 400, 123
Coriat M. et al., 2011, in Romero G. E., Sunyaev R. A., Belloni T., eds, Proc. IAU Symp. 275, Jets at All Scales. Cambridge Univ. Press, Cambridge, p, 255
Di Matteo T., Celotti A., Fabian A. C., 1999, MNRAS, 304, 809
Drury L. O., Axford W. I., Summers D., 1982, MNRAS, 198, 833
Esin A. A., Narayan R., Ostriker E., Yi I., 1996, ApJ, 465, 312
Falcke H., Biermann P. L., 1995, A&A, 293, 665
Falcke H., Körding E., Markoff S., 2004, A&A, 414, 895
Fender R., 2006, Jets from X-Ray Binaries. Cambridge Univ. Press, Cambridge, p. 381
Fender R. P., Hendry M. A., 2000, MNRAS, 317, 1
Fender R. P., Kuulkers E., 2001, MNRAS, 324, 923
Fender R. et al., 1999, ApJ, 519, L165
Fender R. P., Belloni T. M., Gallo E., 2004, MNRAS, 355, 1105
Fender R. P., Homan J., Belloni T. M., 2009, MNRAS, 396, 1370
Ferreira J., 2002, in Bouvier J., Zahn J.-P., eds, EAS Publ. Ser. Vol. 3, Theory of Magnetized Accretion Discs Driving Jets. EDP Sciences, Les Ulis, p. 229
Ferreira J., 2008, New Astron. Rev., 52, 42
Ferreira J., Petrucci P., Henri G., Saugé L., Pelletier G., 2006, A&A, 447, 813
Galeev A. A., Rosner R., Vaiana G. S., 1979, ApJ, 229, 318
Gallant Y. A., Achterberg A., Kirk J. G., 1999, A&AS, 138, 549
Gallo E., Fender R. P., Pooley G. G., 2003, MNRAS, 344, 60
Galloway D. K., Psaltis D., Chakrabarty D., Muno M. P., 2003, ApJ, 590, 999
Haardt F., Maraschi L., 1991, ApJ, 380, L51
Hannikainen D. C., Hunstead R. W., Campbell-Wilson D., Sood R. K., 1998, A&A, 337, 460
Heinz S., Sunyaev R. A., 2003, MNRAS, 343, L59
Hjellming R. M., Johnston K. J., 1981, Nat, 290, 100
Hjellming R. M., Johnston K. J., 1988, ApJ, 328, 600
Homan J., Belloni T., 2005, Ap&SS, 300, 107
Homan J., Miller J. M., Wijnands R., van der Klis M., Belloni T., Steeghs D., Lewin W. H. G., 2005a, ApJ, 623, 383
Homan J., Buxton M., Markoff S., Bailyn C. D., Nespoli E., Belloni T., 2005b, ApJ, 624, 295
Ichimaru S., 1977, ApJ, 214, 840
Jahoda K., Markwardt C. B., Radeva Y., Rots A. H., Stark M. J., Swank J. H., Strohmayer T. E., Zhang W., 2006, ApJS, 163, 401
Jain R. K., Bailyn C. D., Orosz J. A., McClintock J. E., Remillard R. A., 2001, ApJ, 554, L181
Joinet A., Jourdain E., Malzac J., Roques J. P., Schönfelder V., Ubertini P., Capitanio F., 2005, ApJ, 629, 1008
Jonker P. G., Nelemans G., 2004, MNRAS, 354, 355
Jonker P. G. et al., 2010, MNRAS, 401, 1255
Kalemci E., Tomsick J. A., Rothschild R. E., Pottschmidt K., Corbel S., Kaaret P., 2006, ApJ, 639, 340
Kalemci E., Tomsick J. A., Yamaoka K., Ueda Y., 2008, Astron. Telegram, 1348
Kaluzienski L. J., Holt S. S., 1977, IAU Circular, 3099, 3
Körding E., Falcke H., Corbel S., 2006a, A&A, 456, 439
Körding E. G., Fender R. P., Migliari S., 2006b, MNRAS, 369, 1451
Krimm H. A. et al., 2009, Astron. Telegram, 2058, 1

Lutovinov A., Revnivtsev M., Molkov S., Sunyaev R., 2005, A&A, 430, 997
McClintock J. E., Remillard R. A., 2006, Black Hole Binaries. Cambridge Univ. Press, Cambridge, p. 157
McClintock J. E., Remillard R. A., Rupen M. P., Torres M. A. P., Steeghs D., Levine A. M., Orosz J. A., 2009, ApJ, 698, 1398
Malzac J., Beloborodov A. M., Poutanen J., 2001, MNRAS, 326, 417
Malzac J., Belmont R., Fabian A. C., 2009, MNRAS, 400, 1512
Markoff S., Nowak M. A., 2004, ApJ, 609, 972
Markoff S., Falcke H., Fender R., 2001, A&A, 372, L25
Markoff S., Nowak M., Corbel S., Fender R., Falcke H., 2003, A&A, 397, 645
Markoff S., Nowak M. A., Wilms J., 2005, ApJ, 635, 1203
Markwardt C. B., Swank J. H., 2003, Astron. Telegram, 133
Merloni A., 2003, MNRAS, 341, 1051
Merloni A., Fabian A. C., 2002, MNRAS, 332, 165
Merloni A., Heinz S., di Matteo T., 2003, MNRAS, 345, 1057
Migliari S., Fender R. P., 2006, MNRAS, 366, 79
Miller J. M. et al., 2006, ApJ, 646, 394
Miller-Jones J. C. A., Jonker P. G., Dhawan V., Brisken W., Rupen M. P., Nelemans G., Gallo E., 2009, ApJ, 706, L230
Miller-Jones J. C. A. et al., 2010, ApJ, 716, L109
Miller-Jones J. C. A. et al., 2011, in Romero G. E., Sunyaev R. A., Belloni T., eds, Proc. IAU Symp. 275, Jets at All Scales. Cambridge Univ. Press, Cambridge, p. 224
Mirabel I. F., Rodriguez L. F., 1994, Nat, 371, 46
Motta S., Muñoz-Darias T., Belloni T., 2011, MNRAS, doi:10.1111/j.1365-2966.2011.18483.x
Muno M. P., Belloni T., Dhawan V., Morgan E. H., Remillard R. A., Rupen M. P., 2005, ApJ, 626, 1020
Narayan R., Yi I., 1994, ApJ, 428, L13
Nowak M. A., Wilms J., Pottschmidt K., Pooley G. G., 2004, BAAS, 36, 946
Parmar A. N., Kuulkers E., Oosterbroek T., Barr P., Much R., Orr A., Williams O. R., Winkler C., 2003, A&A, 411, L421
Pe'er A., Casella P., 2009, ApJ, 699, 1919
Prat L. et al., 2009, A&A, 494, L21
Rodriguez J., Cadolle Bel M., Tomsick J. A., Corbel S., Brocksopp C., Paizis A., Shaw S. E., Bodaghee A., 2007, ApJ, 655, L97
Rodriguez J. et al., 2008a, ApJ, 675, 1436
Rodriguez J. et al., 2008b, ApJ, 675, 1449
Rupen M. P., Mioduszewski A. J., Dhawan V., 2004, Astron. Telegram, 314, 1
Rupen M. P., Mioduszewski A. J., Dhawan V., 2005, Astron. Telegram, 575, 1
Rupen M. P., Dhawan V., Mioduszewski A. J., 2008a, Astron. Telegram, 1352, 1
Rupen M. P., Dhawan V., Mioduszewski A. J., 2008b, Astron. Telegram, 1384, 1
Rushton A., Spencer R., Fender R., Pooley G., 2010, A&A, 524, A29
Russell D. M., Fender R. P., Hynes R. I., Brocksopp C., Homan J., Jonker P. G., Buxton M. M., 2006, MNRAS, 371, 1334
Russell D. M., Maccarone T. J., Körding E. G., Homan J., 2007, MNRAS, 379, 1401
Russell D. M., Maitra D., Dunn R. J. H., Markoff S., 2010, MNRAS, 405, 1759
Rybicki G. B., Lightman A. P., 1979, Radiative Processes in Astrophysics. Wiley Interscience, New York, p. 395
Sault R. J., Wieringa M. H., 1994, A&AS, 108, 585
Sault R. J., Teuben P. J., Wright M. C. H., 1995, in Shaw R. A., Payne H. E., Hayes J. J. E., eds, ASP Conf. Ser. Vol. 77, Astronomical Data Analysis Software and Systems IV. Astron. Soc. Pac., San Francisco, p. 433
Shakura N. I., Sunyaev R. A., 1973, A&A, 24, 337
Soleri P. et al., 2010, MNRAS, 406, 1471
Swank J., 2004, Astron. Telegram, 301, 1
Tanaka Y., Shibazaki N., 1996, ARA&A, 34, 607
Tudose V., Fender R. P., Linares M., Maitra D., van der Klis M., 2009, MNRAS, 400, 2111
van der Klis M., 2006, Rapid X-Ray Variability. Cambridge Univ. Press, Cambridge, p. 39
Xue Y. Q., Cui W., 2007, A&A, 466, 1053
Yamaoka K. et al., 2009, Astron. Telegram, 2364, 1
Yuan F., 2001, MNRAS, 324, 119
Yuan F., Zdziarski A. A., 2004, MNRAS, 354, 953
Yuan F., Peng Q., Lu J., Wang J., 2000, ApJ, 537, 236
Yuan F., Taam R. E., Xue Y., Cui W., 2006, ApJ, 636, 46
Zdziarski A. A., Gierliński M., Mikołajewska J., Wardziński G., Smith D. M., Harmon B. A., Kitamoto S., 2004, MNRAS, 351, 791

This paper has been typeset from a TEX/LATEX file prepared by the author.

A&A 531, L5 (2011)
DOI: 10.1051/0004-6361/201117341

Astronomy & Astrophysics

L E

Into the central 10 pc of the most distant known radio quasar

VLBI imaging observations of J1429+5447 at $z = 6.21$

S. Frey[1,5], Z. Paragi[2,5], L. I. Gurvits[2,3], K. É. Gabányi[1,5], and D. Cseh[4]

[1] FÖMI Satellite Geodetic Observatory, PO Box 585, 1592 Budapest, Hungary
e-mail: [frey;gabanyik]@sgo.fomi.hu
[2] Joint Institute for VLBI in Europe, Postbus 2, 7990 AA Dwingeloo, The Netherlands
e-mail: [zparagi;lgurvits]@jive.nl
[3] Department of Astrodynamics and Space Missions, Delft University of Technology, Kluyverweg 1, 2629 HS Delft, The Netherlands
[4] Laboratoire Astrophysique des Interactions Multi-echelles (UMR 7158), CEA/DSM-CNRS-Université Paris Diderot, CEA Saclay, 91191 Gif-sur-Yvette, France
e-mail: david.cseh@cea.fr
[5] MTA Research Group for Physical Geodesy and Geodynamics, PO Box 91, 1521 Budapest, Hungary

Received 25 May 2011 / Accepted 3 June 2011

ABSTRACT

Context. There are about 60 quasars known at redshifts $z > 5.7$ to date. Only three of them are detected in the radio above 1 mJy flux density at 1.4 GHz frequency. Among them, J1429+5447 ($z = 6.21$) is the highest-redshift radio quasar known at present. These rare, distant, and powerful objects provide important insight into the activity of the supermassive black holes in the Universe at early cosmological epochs and into the physical conditions of their environment.
Aims. We studied the compact radio structure of J1429+5447 on the milli-arcsecond (mas) angular scale to compare the structural and spectral properties with those of another two $z \sim 6$ radio-loud quasars, J0836+0054 ($z = 5.77$) and J1427+3312 ($z = 6.12$).
Methods. We performed Very Long Baseline Interferometry (VLBI) imaging observations of J1429+5447 with the European VLBI Network (EVN) at 1.6 GHz on 2010 June 8, and at 5 GHz on 2010 May 27.
Results. Based on its observed radio properties, the compact but somewhat resolved structure on linear scales of <100 pc, and the steep spectrum, the quasar J1429+5447 is remarkably similar to J0836+0054 and J1427+3312. To answer the question whether the compact steep-spectrum radio emission is a "universal" feature of the most distant radio quasars, it is essential to study more yet to be discovered radio-loud active galactic nuclei at $z > 6$.

Key words. techniques: interferometric – radio continuum: galaxies – galaxies: active – quasars: individual: J1429+5447

1. Introduction

Observations of quasars at the highest redshifts can constrain models of the birth and early cosmological evolution of active galactic nuclei (AGNs) and the growth of their central supermassive (up to $\sim 10^9$ $M_\odot$) black holes. Currently, the object CFHQS J021013−045620 holds the redshift record among quasars with $z = 6.44$ (Willott et al. 2010a). There are about 60 quasars known at redshifts $z > 5.7$ to date. Despite the steadily growing number of known $z \sim 6$ quasars (e.g. Fan et al. 2001, 2003, 2004, 2006; Jiang et al. 2009; Willott et al. 2007, 2009, 2010b), the measured maximum redshift practically did not increase over the last decade (e.g. SDSS J1148+5251, $z = 6.43$; Fan et al. 2003). It remains to be seen whether this is a selection effect owing to current limitations of the high-redshift identification techniques, or if the first quasars in the Universe indeed started to "turn on" at around this cosmological epoch. Intriguingly, many of the intrinsic properties observed in the infrared, optical, and X-ray wavebands make the highest-redshift quasars hardly distinguishable from the lower-redshift ones. However, Jiang et al. (2010) found two out of twenty-one $z \sim 6$ quasars that do not show infrared emission originating from hot dust. According to these authors, the amount of hot dust may increase in parallel with the growth of the central black hole. Therefore, at least some of the most distant quasars known are less evolved than their low-redshift counterparts. Near-infrared spectroscopy of a sample of Canada-France High-z Quasar Survey (CFHQS) objects indicates that these AGNs are accreting close to the Eddington limit and are in the early stage of their evolutionary cycle, building up the mass of the central black hole exponentially from the material of their young host galaxies (Willott et al. 2010a).

Only three of the $z > 5.7$ quasars (J0836+0054, $z = 5.77$, Fan et al. 2001; J1427+3312, $z = 6.12$, McGreer et al. 2006; J1429+5447, $z = 6.21$, Willott et al. 2010b) are found in the radio with 1.4-GHz flux density $S_{1.4} > 1$ mJy. Most recently, Zeimann et al. (2011) detected radio emission ($S_{1.4} = 0.31$ mJy) from another distant quasar, J2228+0110 ($z = 5.95$). These radio-emitting high-redshift objects are particularly valuable, because the ultimate evidence for AGN jets can be found in the radio by high-resolution Very Long Baseline Interferometry (VLBI) observations. Synchrotron radio emission of the jets originates from the close vicinity of the spinning supermassive black hole. The radio-emitting plasma is fueled from an accretion disk and is accelerated and collimated by the magnetic field. Two of the $z \sim 6$ radio sources (J0836+0054, J1427+3312)

have already been investigated with VLBI. The radio structure of J0836+0054 on ∼10 milli-arcsec (mas) angular scale (Frey et al. 2003, 2005) is characterised by a single compact but somewhat resolved component, with steep radio spectrum ($\alpha = -0.8$) between the observed frequencies of 1.6 and 5 GHz. (The power-law spectral index α is defined as $S \propto \nu^{\alpha}$, where S is the flux density and ν the frequency.) The 1.4-GHz and 1.6-GHz VLBI images of the first $z > 6$ radio quasar, J1427+3312 (Momjian et al. 2008; Frey et al. 2008, respectively) revealed a prominent double structure. The two resolved components are separated by ∼28 mas (∼160 pc); to calculate linear sizes and luminosities, we assume a flat cosmological model with $H_0 = 70$ km s^{-1} Mpc^{-1}, $\Omega_{\rm m} = 0.3$, and $\Omega_{\Lambda} = 0.7$. This structure is similar to that of the compact symmetric objects (CSOs). It is one of the indications of the youth of J1427+3312. The brighter component also detected with VLBI at 5 GHz (Frey et al. 2008) has a steep radio spectrum ($\alpha = -0.6$).

A census of VLBI-imaged radio quasars at $z > 4.5$ and the European VLBI Network (EVN) imaging of five new sources at $4.5 < z < 5$ was made recently by Frey et al. (2010). The slightly resolved mas- and 10-mas-scale radio structures, the measured moderate brightness temperatures (∼10^8–10^9 K), and the steep spectra in the majority of the cases suggest that the sample of compact radio sources at $z > 4.5$ is dominated by objects that do not resemble blazars, that are characterised by highly Doppler-boosted, compact, flat-spectrum radio emission. At frequencies lower than the turnover value that corresponds to the peak flux density, the rising radio spectrum is determined by synchrotron self-absorption (Slysh 1963). Above the turnover frequency, the emitting plasma becomes optically thin and the spectrum is steep. According to the model of Falcke et al. (2004), the high-redshift steep-spectrum objects may represent gigahertz-peaked-spectrum (GPS) sources at early cosmological epochs. The first generation of supermassive black holes could have had powerful jets that developed hot spots well inside their forming host galaxy, on linear scales of 0.1−10 kpc. Taking the relation between the source size and the turnover frequency observed for GPS sources into account, and for hypothetical sources matching the luminosity and spectral index of "typical" quasars in the VLBI sample with $z \sim 5$ or higher, the angular size of the smallest (∼100 pc) of these early radio-jet objects would be of the order of 10 mas, and the observed turnover frequency in their radio spectra would be around 500 MHz in the observer's frame (Falcke et al. 2004).

We report on dual-frequency VLBI observations of the currently most distant known radio quasar, one of the only two at $z > 6$. The object CFHQS J142952+544717 (J1429+5447 in short) was discovered by Willott et al. (2010b). Its spectroscopic redshift is $z = 6.21$ measured from the Lyα emission line. The quasar appears in the Very Large Array (VLA) Faint Images of the Radio Sky at Twenty-centimeters (FIRST) survey (White et al. 1997) list as an unresolved (<5″) radio source with an integral flux density of $S_{1.4} = 2.95$ mJy. Strong molecular CO (2–1) emission was detected in the host galaxy of J1429+5447 by Wang et al. (2011), who resolved the source into two components separated by 1.″2. It indicates a gas-rich major merger system. The rapid galaxy formation and starburst activity apparently goes in parallel with the radio-active phase of the accreting supermassive black hole in the western component. The redshift of the source is $z = 6.18$ based on the CO (2–1) line.

Our aim was to reveal its high-resolution radio structure and spectral properties, and then compare them with those of the two other $z \sim 6$ quasars already known, on linear scales of ∼10–100 pc. In the adopted cosmological model, the redshift $z = 6.21$ corresponds to 0.875 Gyr after the Big Bang (6.5% of the present age of the Universe), and 1 mas angular separation is equivalent to a projected linear distance of 5.6 pc.

2. EVN observations and data reduction

The EVN observations of J1429+5447 took place on 2010 May 27 (5 GHz frequency) and on 2010 June 8 (1.6 GHz). At a recording rate of 1024 Mbit s^{-1}, eleven antennas of the inter-continental radio telescope network participated in the experiment at 5 GHz: effelsberg (Germany), Jodrell Bank Lovell and Mk2 telescopes (UK), Medicina (Italy), Toruń (Poland), Onsala (Sweden), Sheshan, Nanshan (PR China), Badary, Zelenchukskaya (Russia), and the phased array of the Westerbork Synthesis Radio Telescope (WSRT, The Netherlands). All but the Jodrell Bank Mk2 telescope participated in the 1.6-GHz experiment as well. Both experiments lasted for 6 h. Eight intermediate frequency channels (IFs) were used in both left and right circular polarisations. The total bandwidth was 128 MHz per polarisation. The correlation of the recorded VLBI data took place at the EVN data processor at the Joint Institute for VLBI in Europe (JIVE), Dwingeloo, The Netherlands.

The weak target source, J1429+5447 was observed in phase-reference mode to increase the coherent integration time spent on the source and thus to improve the sensitivity of the observations. We refer to Frey et al. (2008) for the details of the observing and data reduction in a much similar dual-frequency EVN experiment on J1427+3312. The phase-reference calibrator source we used in the present case, J1429+5406, is separated from the target by 0.°69 in the sky. The target–reference cycles of ∼5.5 min allowed us to spend ∼3.5 min on the target source in each cycle, providing almost 3 h total integration time on J1429+5447. Phase-referencing also allows us to determine the accurate relative position of the target source with respect to the well-known absolute position of the reference source.

The US National Radio Astronomy Observatory (NRAO) Astronomical Image Processing System (AIPS) was used for the data calibration in a standard way. The calibrated data were then exported to the Caltech Difmap package for imaging (see, e.g. Frey et al. 2008, for the details and references). The naturally-weighted images at 1.6 GHz (Fig. 1) and 5 GHz (Fig. 2) were made after several cycles of CLEANing in Difmap. No self-calibration was applied. The lowest contours indicate ∼3σ image noise levels. The theoretical thermal noise values were ∼10 μJy/beam (1σ) at both frequencies.

3. Results and discussion

There is a single dominant radio feature detected in the quasar J1429+5447 at both 1.6 and 5 GHz. The images in Figs. 1, 2 are centred on the 5-GHz brightness peak, whose phase-referenced absolute equatorial coordinates are right ascension $14^{\rm h}29^{\rm m}52.^{\rm s}17629$ and declination 54°47′17.″6309 (J2000), each with the accuracy of 0.4 mas, determined by the phase-reference calibrator source position accuracy, the target-calibrator separation, the angular resolution of the interferometer array, and the signal-to-noise ratio. The images show a slightly resolved mas-scale structure. Difmap was used to fit circular Gaussian brightness distribution model components to the interferometric visibility data at both frequencies. The 5-GHz data are well described by a component with 0.99 mJy flux density and 0.67 mas diameter (Table 1). These imply the rest-frame brightness temperature $T_{\rm B} = (7.7 \pm 0.7) \times 10^8$ K. It confirms the

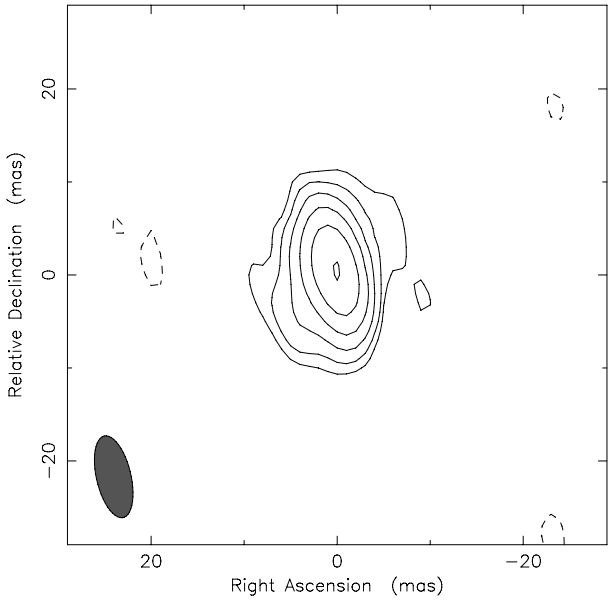

Fig. 1. Naturally weighted 1.6-GHz EVN image of the quasar J1429+5447. The lowest contours are drawn at ±70 μJy/beam. The positive contour levels increase by a factor of 2. The peak brightness is 2.32 mJy/beam. The Gaussian restoring beam is 9.0 mas × 3.7 mas with major axis position angle 13°. The restoring beam (full width at half maximum, FWHM) is indicated with an ellipse in the lower-left corner. The image is centred on the 5-GHz brightness peak.

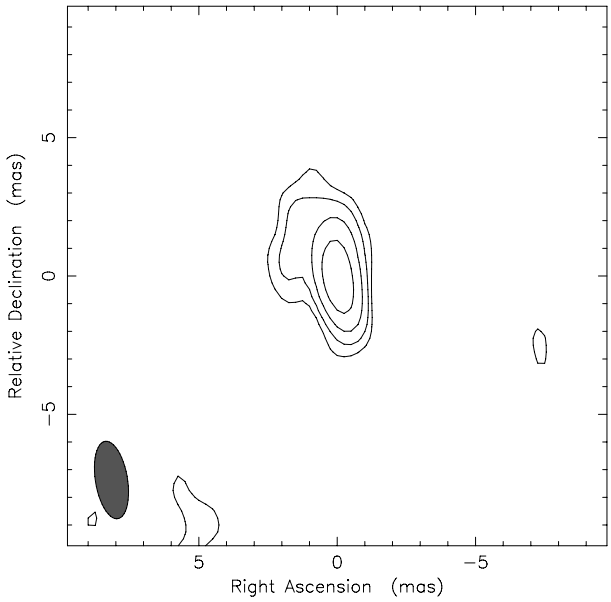

Fig. 2. Naturally weighted 5-GHz EVN image of the quasar J1429+5447. The lowest contours are drawn at ±50 μJy/beam. The positive contour levels increase by a factor of 2. The peak brightness is 0.67 mJy/beam. The Gaussian restoring beam is 2.8 mas × 1.2 mas with major axis position angle 9°. The restoring beam (FWHM) is indicated with an ellipse in the lower-left corner. The image is centred on the brightness peak, whose coordinates are given in the text.

AGN origin of the quasar's radio emission because the brightness temperatures for normal galaxies do not exceed $\sim 10^5$ K (Condon 1992). At 1.6 GHz, the best-fit model is composed of two circular Gaussians (Table 1). A hint on a corresponding weak extension to the south-east can also be found in the image (Fig. 1), where, however, the shape of the lowest (3σ) contour

Table 1. The fitted VLBI model parameters for J1429+5447.

Flux density (mJy)	Relative position north (mas)	east (mas)	Size (mas)	T_B (10^8 K)
3.03 ± 0.05	...	...	2.63 ± 0.03	14.0 ± 0.6
0.27 ± 0.04	−4.74 ± 0.06	4.26 ± 0.06	1.29 ± 0.12	5.2 ± 1.7
0.99 ± 0.06	...	...	0.67 ± 0.01	7.7 ± 0.7

Notes. The parameters are derived from circular Gaussian model-fitting to VLBI visibility data in Difmap, at 1.6 GHz (top) and 5 GHz (bottom). The statistical errors are estimated according to Fomalont (1999). Additional flux density calibration uncertainties are assumed as 5%. Column 1 – model component flux density (mJy); Cols. 2, 3 – separation from the main component to north and east (mas); Col. 4 – diameter (mas, FWHM); Col. 5 – brightness temperature (10^8 K).

line should not be over-interpreted. Considering the calibration uncertainties, the sum of the flux densities in the VLBI components (3.30 mJy) is consistent with or somewhat higher than the FIRST value (2.95 ± 0.15 mJy). We effectively detect the entire radio emission in the 1.4–1.6 GHz band from a ∼10-mas region of J1429+5447, corresponding to the linear size less than 60 pc. At 5 GHz, the comparison between the VLBI component flux density (0.99 mJy) and the result from our analysis of the WSRT array data taken during our EVN experiment (1.2 mJy) allow us to draw a similar conclusion: the entire radio emission originates from a ∼10-pc region in the quasar's centre. In the case of J1429+5447, any other possible secondary component is excluded within an angular radius of ∼2″, at the brightness level of ∼90 μJy/beam or higher (assuming at least 5σ detection and 10% coherence loss) in the 1.6-GHz VLBI image. In particular, we did not detect compact radio emission at the location of the eastern CO (2–1) line-emitting component (Wang et al. 2011). On the other hand, the brightness peaks in our VLBI images coincide with their western component, and also with the 32-GHz continuum emission peak. Wang et al. (2011) measured 257 ± 15 μJy for the flux density at 32 GHz in the continuum source, which is unresolved with the Expanded VLA (C configuration, 0.″71 × 0.″67 synthesized beam).

Based on our VLBI measurements, the two-point spectral index for the dominant component of the source is $\alpha = -1.0$. The 32-GHz continuum flux density (Wang et al. 2011) is consistent with the steep synchrotron radio spectrum. The total rest-frame 5-GHz monochromatic luminosity of J1429+5447 is 4.5×10^{26} W Hz^{-1}, comparable to other high-redshift sources (e.g. Frey et al. 2010).

The inferred $T_B \simeq 10^9$ K brightness temperature is substantially lower than the equipartition value estimated for relativistic compact jets ($T_{B,eq} \simeq 5 \times 10^{10}$ K; Readhead 1994). This suggests that relativistic beaming does not play a major role in the appearance of the source. According to the orientation-based unified picture of radio-load AGNs (Urry & Padovani 1995), the radiation from the jets that are inclined with a sufficiently large angle (θ) to the line of sight is deamplified with a Doppler factor $\delta < 1$. The viewing angle and the Doppler factor are related to the bulk Lorentz factor (Γ) of the plasma as

$$\delta = \frac{1}{\Gamma(1 - \beta \cos\theta)}, \quad (1)$$

where $\beta < 1$ is the bulk speed of the material in the jet, expressed in units of the speed of light c. For J1429+5447, assuming energy equipartition between the particles and the magnetic field in the radio-emitting region, our VLBI measurements imply

$\delta = T_{\rm B}/T_{\rm B,eq} \simeq 0.02$. This, in the extreme case of the jets in the plane of the sky ($\theta = 90°$), would require a minimum Lorentz factor $\Gamma \gtrsim 50$. Values up to $\Gamma = 50$ are indeed inferred from jet kinematics in a sample of powerful lower-redshift radio AGNs (Lister et al. 2009), but such an extreme Lorentz factor and the special geometry with $\theta = 90°$ make this scenario very unlikely for J1429+5447. Because the other two $z \sim 6$ radio quasars have similar or even lower brightness temperatures with respect to the equipartition value (Frey et al. 2005, 2008), the above reasoning is valid for them as well. This is also the case for a significant portion of other radio AGNs at $z > 4.5$ studied with VLBI so far (Frey et al. 2010). This, and the steep spectrum are arguments against the possibility that we see intrinsically powerful but Doppler-deboosted (highly inclined) relativistic radio jets in these sources. Although currently there are about 60 quasars known at $z \gtrsim 6$, we do not know of any with Doppler-boosted radio emission. The steep spectrum between the observed 1.6 and 5 GHz frequencies (12 and 36 GHz in the rest frame of the quasar J1429+5447) is consistent with the assumption that we see the compact "hot spots" confined within a region of <100 pc in a young GPS source at an early cosmological epoch. The spectral peak frequency is possibly redshifted to the ~100 MHz range in the observer's frame (Falcke et al. 2004). This could be verified with low-frequency radio interferometric measurements.

4. Conclusions

Based on our EVN observations at 1.6 and 5 GHz, the mas-scale radio structure of the highest-redshift radio quasar known to date, J1429+5447 ($z = 6.21$), is quite similar to what we have seen in the other two $z \sim 6$ quasars, J0836+0054 and J1427+3312. The source is somewhat resolved on linear scales of <100 pc, although the total radio emission is confined to this central region. The two-point spectral index $\alpha = -1.0$ indicates a steep radio spectrum. The measured brightness temperature shows that relativistic beaming does not influence the appearance of this quasar. Interestingly, the compact steep-spectrum radio emission is common in all three $z \sim 6$ quasars studied with VLBI to date. The puzzle whether this is a rule or an exception could be solved using a prospective larger sample of extremely distant radio-loud AGNs in the future.

Acknowledgements. The EVN is a joint facility of European, Chinese, South African, and other radio astronomy institutes funded by their national research councils. This work was supported by the European Community's Seventh Framework Programme, Advanced Radio Astronomy in Europe, grant agreement No. 227290, the European Community's Seventh Framework Programme (FP7/2007-2013) under grant agreement No. ITN 215212 "Black Hole Universe", and the Hungarian Scientific Research Fund (OTKA, grant no. K72515).

References

Condon, J. J. 1992, ARA&A, 30, 573
Falcke, H., Körding, E., & Nagar, N. M. 2004, NewAR, 48, 1157
Fan, X., Narayanan, V. K., Lupton, R. H., et al. 2001, AJ, 122, 2833
Fan, X., Strauss, M. A., Schneider, D. P., et al. 2003, AJ, 125, 1649
Fan, X., Hennawi, J. F., Richards, G. T., et al. 2004, AJ, 128, 515
Fan, X., Strauss, M. A., Richards, G. T., et al. 2006, AJ, 131, 1203
Fomalont, E. B. 1999, in Synthesis Imaging in Radio Astronomy II, ed. G. B. Taylor, C. L. Carilli, & R. A. Perley, ASP Conf. Ser. 180, 301
Frey, S., Mosoni, L., Paragi, Z., & Gurvits, L. I. 2003, MNRAS, 343, L20
Frey, S., Paragi, Z., Mosoni, L., & Gurvits, L. I. 2005, A&A, 436, L13
Frey, S., Gurvits, L. I., Paragi, Z., & Gabányi, K. É. 2008, A&A, 848, L39
Frey, S., Paragi, Z., Gurvits, L. I., Cseh, D., & Gabányi, K. É. 2010, A&A, 524, A83
Jiang, L., Fan, X., Bian, F., et al. 2009, AJ, 138, 305
Jiang, L., Fan, X., Brandt, W. N., et al. 2010, Nature, 464, 380
Lister, M. L., Cohen, M. H., Homan, D. C., et al. 2009, AJ, 138, 1874
McGreer, I. D., Becker, R. H., Helfand, D. J., & White, R. L. 2006, ApJ, 652, 157
Momjian, E., Carilli, C. L., & McGreer, I. D. 2008, AJ, 136, 344
Readhead, A. C. S. 1994, ApJ, 426, 51
Slysh, V. I. 1963, Nature, 199, 682
Urry, C. M., & Padovani, P. 1995, PASP, 107, 803
Wang, R., Wagg, J., Carilli, C. L., et al. 2011, ApJ, in press [arXiv:1105.4199]
White, R. L., Becker, R. H., Helfand, D. J., & Gregg, M. D. 1997, ApJ, 475, 479
Willott, C. J., Delorme, P., Omont, A., et al. 2007, AJ, 134, 2435
Willott, C. J., Delorme, P., Reylé, C., et al. 2009, AJ, 137, 3541
Willott, C. J., Albert, L., Arzoumanian, D., et al. 2010a, AJ, 140, 546
Willott, C. J., Delorme, P., Reylé, C., et al. 2010b, AJ, 139, 906
Zeimann, G. R., White, R. L., Becker, R. H., et al. 2011, ApJ, in press [arXiv:1105.2047]

A&A 524, A83 (2010)
DOI: 10.1051/0004-6361/201015554

Astronomy & Astrophysics

High-resolution images of five radio quasars at early cosmological epochs

S. Frey[1,4], Z. Paragi[2,4], L. I. Gurvits[2,5], D. Cseh[3], and K. É. Gabányi[1,4]

[1] FÖMI Satellite Geodetic Observatory, PO Box 585, 1592 Budapest, Hungary
e-mail: [frey;gabanyik]@sgo.fomi.hu
[2] Joint Institute for VLBI in Europe, Postbus 2, 7990 AA Dwingeloo, The Netherlands
e-mail: [zparagi;lgurvits]@jive.nl
[3] Laboratoire Astrophysique des Interactions Multi-echelles (UMR 7158), CEA/DSM-CNRS-Université Paris Diderot, CEA Saclay, 91191 Gif sur Yvette, France
e-mail: david.cseh@cea.fr
[4] MTA Research Group for Physical Geodesy and Geodynamics, PO Box 91, 1521 Budapest, Hungary
[5] Institute of Space and Astronautical Science, Japan Aerospace Exploration Agency, 3-1-1 Yoshinodai Chuo-ku, Sagamihara, Kanagawa 252-5210, Japan

Received 9 August 2010 / Accepted 8 September 2010

ABSTRACT

Context. Until now, there have only been seven quasars at $z > 4.5$ whose the high-resolution radio structure had been studied in detail with Very Long Baseline Interferometry (VLBI) imaging.
Aims. We almost double the number of VLBI-imaged quasars at these high redshifts with the aim of studying their redshift-dependent structural and physical properties in a larger sample.
Methods. We observed five radio quasars (J0813+3508, J1146+4037, J1242+5422, J1611+0844, and J1659+2101) at $4.5 < z < 5$ with the European VLBI Network (EVN) at 1.6 GHz on 29 October 2008 and at 5 GHz on 22 October 2008. The angular resolution achieved ranges from 1.5 to 25 milli-arcsec (mas), depending on the observing frequency, the position angle in the sky, and the source's celestial position.
Results. The sources are all somewhat extended on mas scales, but compact enough to be detected at both frequencies. With one exception of a flat-spectrum source (J1611+0844), their compact emission is characterised by a steep radio spectrum. We found no evidence of Doppler-boosted radio emission in the quasars in our sample. The radio structure of one of them (J0813+3508) is extended to ~7″, which corresponds to 43 kpc projected linear size. Many of the highest redshift compact radio sources are likely to be young, evolving objects, far-away cousins of the powerful gigahertz peaked-spectrum (GPS) and compact steep-spectrum (CSS) sources that populate the Universe at lower redshifts.

Key words. radio continuum: galaxies – galaxies: active – quasars: general – techniques: interferometric

1. Introduction

Quasars at the highest redshifts place strong constraints on the early cosmological evolution of active galactic nuclei (AGNs) and the growth of their central supermassive ($\sim 10^9\ M_\odot$) black holes. The AGN activity observed at high z indicates that feedback processes (e.g. Best et al. 2005) may have played an important role in the early galaxy and cluster evolution. The ultimate evidence for AGN jets is provided by Very Long Baseline Interferometry (VLBI) observations in the radio domain.

Compact radio sources have flat spectra (with power-law spectral index $\alpha > -0.5$; $S \propto \nu^\alpha$, where S is the flux density and ν the frequency) from the synchrotron self-absorption (Kellermann & Pauliny-Toth 1969). In the past, VLBI targets were traditionally selected by their flat overall radio spectrum to ensure detectability. Recent surveys that did not apply spectral selection criteria (e.g. Mosoni et al. 2006; Frey et al. 2008a), and VLBI observations of individual $z \sim 6$ quasars (J0836+0054, Frey et al. 2003, 2005; J1427+3312, Frey et al. 2008b; Momjian et al. 2008) indicate that there is a less-known steep-spectrum population of compact radio AGNs at high redshifts. These sources have so far been able to escape discovery for a variety of reasons: (i) their radio flux density is relatively low for VLBI, requiring high data rate phase-referenced observations; (ii) due to their steep spectra, they are generally not considered useful for VLBI experiments; (iii) for most of them, spectroscopic redshifts are simply not yet available. Indeed, the fine-scale radio structure of J0836+0054 ($z = 5.77$) and J1427+3312 ($z = 6.12$) could fortunately be revealed because their record-breaking redshifts made these sources attractive for high-resolution VLBI imaging.

The VLBI images of the highest-redshift, known radio-loud quasar J1427+3312 at 1.4 GHz (Momjian et al. 2008) and 1.6 GHz (Frey et al. 2008b) reveal a prominent double structure. The two resolved components separated by ~28 mas (~160 pc) resemble a compact symmetric object (CSO, Wilkinson et al. 1994). (To calculate linear sizes and luminosities, we assume a flat cosmological model with $H_0 = 70$ km s^{-1} Mpc^{-1}, $\Omega_\mathrm{m} = 0.3$, and $\Omega_\Lambda = 0.7$ throughout this paper.) CSOs are a class of very young ($<10^4$ yr) sources typically found in radio galaxies at much lower redshifts ($z < 1$). Apart from the structural similarity to CSOs, there are several indications of the youthfulness of

Table 1. Quasars at $z > 4.5$ imaged earlier with VLBI by increasing redshift.

Source name	z	ν GHz	Network	Peak mJy/beam	Ref.
J1235−0003	4.69	1.4	VLBA	17	1
J1205−0742N	4.70	1.4	VLBA	0.2	2
J1205−0742S	4.70	1.4	VLBA	0.2	2
J1430+4204	4.72	5	EVN	161	3
		15	VLBA	159 & 200	4
J1451−1512	4.76	5	EVN	50	5
J0913+5919	5.11	1.4	VLBA	19	1
J0906+6930	5.47	15	VLBA	115	6
		43	VLBA	42	6
J0836+0054	5.77	1.6	EVN	0.8	7
		5	EVN	0.3	8
J1427+3312	6.12	1.4	VLBA	1.0	9
		1.6	EVN	0.5	10
		5	EVN	0.2	10

Notes. Column 1 – source name (J2000); Col. 2 – spectroscopic redshift; Col. 3 – observing frequency (GHz); Col. 4 – interferometer array (EVN: European VLBI Network, VLBA: Very Long Baseline Array); Col. 5 – peak brightness (mJy/beam); Col. 6.

References. 1: Momjian et al. (2004); 2: Momjian et al. (2005); 3: Paragi et al. (1999); 4: Veres et al. (2010); 5: L.I. Gurvits et al. (in preparation); 6: Romani et al. (2004); 7: Frey et al. (2003); 8: Frey et al. (2005); 9: Momjian et al. (2008); 10: Frey et al. (2008b).

this quasar: the steep radio spectrum coupled with the compact structure, the broad absorption lines, and the possible intrinsic X-ray absorption.

To our knowledge, there are only seven radio-loud AGNs at $z > 4.5$ that have been imaged with VLBI prior to our experiment reported here (Table 1). Four of them (J0906+6930, J1235−0003, J1430+4204, and J1451−1512) are compact, practically unresolved flat-spectrum radio sources, while others (J0836+0054, J0913+5919, and J1427+3312 with a double structure) have a compact or somewhat resolved appearance and a steep radio spectrum in the GHz frequency range (in the observer's frame). The double quasar J1205−0742 also listed in the table is a special case from our point of view, with measured brightness temperatures indicating extreme nuclear starbursts rather than radio-loud AGNs (Momjian et al. 2005).

Our goal was to substantially increase the number of radio-loud AGNs at $z > 4.5$ imaged with VLBI. One could expect to find either more "classical" core-jet sources or other steep-spectrum quasars, possibly with CSO-like double structures. If the latter are found, in a decade-long term, VLBI monitoring would eventually allow measurements of the component expansions and thus facilitate direct estimations of the kinematic age of the sources. Otherwise, the compact core-jet sources are potentially valuable additions for comparing of the mas-scale structures of quasars at low and high redshift. Efforts to use classical cosmological tests – the angular size-redshift relation (e.g. Gurvits et al. 1999) and the apparent proper motion-redshift relation (e.g. Kellermann et al. 1999) – would also benefit from data on an increased sample of extremely distant quasars, since the predictions of the various cosmological world models are markedly different at the highest redshifts. Despite the practical difficulties, there is continuous interest in these tests in the community (e.g. Sahni & Starobinsky 2000; Vishwakarma 2000, 2001; Lima & Alcaniz 2002; Chen & Ratra 2003; Jackson 2004, 2008).

Table 2. Our VLBI targets, five SDSS/FIRST radio quasars at $z > 4.5$, and a close radio companion of one of them.

Source coordinates	z	r	FIRST peak mJy/beam	$S_{1.4}$ mJy
08 13 33.32 +35 08 10.8	4.92	20.8	23.2	25.2
08 13 32.89 +35 08 14.9*	–	–	11.8	11.8
11 46 57.79 +40 37 08.6	5.01	21.0	12.5	12.5
12 42 30.58 +54 22 57.3	4.73	20.9	19.7	20.2
16 11 05.64 +08 44 35.4	4.54	19.7	8.8	8.8
16 59 13.23 +21 01 15.8	4.78	21.5	28.7	28.8

Notes. Column 1 – a priori source J2000 right ascension ($^{h\,m\,s}$) and declination ($^{\circ}\,'\,''$) from SDSS; Col. 2 – spectroscopic redshift; Col. 3 – SDSS r magnitude (Schneider et al. 2007); Col. 4 – FIRST peak brightness (mJy/beam); Col. 5 – FIRST integral 1.4-GHz flux density (mJy). (*) Optically unidentified radio companion of the previous source; coordinates from FIRST.

In this paper, we report on our dual-frequency VLBI imaging observations of five previously unexplored radio-loud quasars at $4.5 < z < 5$. Our sample selection method is described in Sect. 2. The experiments and the data reduction are explained in Sect. 3. The observed radio properties of the sources are given in Sect. 4. Our results are discussed in Sect. 5. Conclusions are drawn in Sect. 6.

2. Target selection

For the high-resolution VLBI observations, we choose five quasars from the Sloan Digital Sky Survey (SDSS) Data Release 5 (DR5) quasar catalogue (Schneider et al. 2007). All of them are identified with an unresolved (<5″) radio source in the Very Large Array (VLA) Faint Images of the Radio Sky at Twenty-centimeter (FIRST) survey[1] (White et al. 1997), with 1.4-GHz total flux densities 8.8 mJy $\leq S_{1.4} \leq$ 28.8 mJy. These five quasars, together with J0913+5919 (already studied with VLBI by Momjian et al. 2004; see Table 1), are the only such radio quasars in the northern hemisphere in the Schneider et al. (2007) catalogue with $z > 4.5$ and $S_{1.4} > 5$ mJy. Important is that the (otherwise unknown) radio spectral index of the sources was not used as a selection criterion.

One of the sources (J0813+3508, $z = 4.92$) has a close (<7″), optically unidentified radio companion in the FIRST catalogue, which appears compact on an arcsecond scale in the 1.4-GHz VLA FIRST image (Fig. 1). We also included this object as the sixth target in our VLBI experiment, in the hope that any possible relation between the two apparently nearby sources could be studied. The basic parameters of our target sources are listed in Table 2.

Our recent experience with a larger sample of SDSS/FIRST quasars (Mosoni et al. 2006; Frey et al. 2008a) indicates that the sources identified as optical quasars *and* unresolved FIRST objects with $S_{1.4} > 20$ mJy have a nearly 90% chance to be successfully detected with the European VLBI Network (EVN) at 5 GHz, using the SDSS coordinates as a priori values. Although most of the sources are weaker in the present sample, we used longer integration times in the VLBI experiment to ensure safe detections.

[1] http://sundog.stsci.edu

3. VLBI observations and data reduction

We observed our targets with the EVN at 1.6 GHz on 29 October 2008 and at 5 GHz on 22 October 2008. Due to the high redshifts, the observed frequencies correspond to ∼9−10 GHz and ∼28−30 GHz in the rest frame of the quasars. At a recording rate of 1024 Mbit s^{-1}, ten antennas of the EVN participated in the experiment at 1.6 GHz: Effelsberg (Germany), Jodrell Bank Mk2 (UK), Medicina, Noto (Italy), Toruń (Poland), Onsala (Sweden), Sheshan, Nanshan (PR China), Robledo (Spain), and the phased array of the 14-element Westerbork Synthesis Radio Telescope (WSRT, The Netherlands). The eight participating antennas in the 5-GHz experiment were Effelsberg, Jodrell Bank Mk2, Medicina, Noto, Toruń, Sheshan, Nanshan, and the WSRT. On both days, the observations lasted for a total of 11 h. Eight intermediate frequency channels (IFs) were used in both left and right circular polarisations. The total bandwidth was 128 MHz per polarisation. The correlation of the recorded VLBI data took place at the EVN Data Processor at the Joint Institute for VLBI in Europe (JIVE), Dwingeloo, The Netherlands.

All the target sources were observed in phase-reference mode. This allows us to increase the coherent integration time spent on the source and thus to improve the sensitivity of the observations. Phase-referencing involves regularly interleaving observations between the target source and a nearby bright and compact reference source (e.g. Beasley & Conway 1995). The delay, delay rate, and phase solutions derived for the phase-reference calibrator were interpolated and applied for the respective target within the cycle time of ∼7 min. The target sources were observed for ∼4.5-min intervals in each cycle. The exception was the pair of sources, J0813+3508 and its optically unidentified apparent companion (Table 2; Fig. 1). They were observed using the same phase-reference source, for ∼2.5 min subsequently in each cycle. To achieve nearly the same total on-source integration time as for the other targets (∼60 min), more cycles were scheduled for this pair.

The suitable phase-reference calibrator sources (J0815+3635, J1146+3958, J1253+5301, J1608+1029, and J1656+1826) were selected from the Very Long Baseline Array (VLBA) Calibrator Survey[2]. The angular separations between the calibrators and the corresponding targets range from 0.°64 to 2.°65 (Table 3). The positional uncertainties of the calibrators in the International Celestial Reference Frame (ICRF) are 0.4−4.3 mas.

The US National Radio Astronomy Observatory (NRAO) Astronomical Image Processing System (AIPS; Diamond 1995) was used for the data calibration. The visibility amplitudes were calibrated using the antenna gains, and the system temperatures regularly measured at the antennas during the experiments. Fringe-fitting was performed for the five calibrators mentioned above, and the fringe-finder sources (J0555+3948, J0927+3902, J1159+2914, and J1331+3030) using 3-min solution intervals. The data were exported to the Caltech Difmap package (Shepherd et al. 1994) for imaging. The conventional mapping procedure involving several iterations of CLEANing and phase (then amplitude) self-calibration resulted in the images and brightness distribution models for the calibrators. Overall antenna gain correction factors (∼10% or less) were determined and applied to the visibility amplitudes in AIPS. Then fringe-fitting was repeated in AIPS, now taking the clean component models of the phase-reference calibrator sources into account. The residual phase corrections resulted from their non-pointlike structure were considered this way. The solutions obtained were interpolated and applied to the target source data. The visibility data of the target sources, unaveraged in time and frequency, were also exported to Difmap for imaging. The naturally weighted images at 1.6 GHz and 5 GHz (Fig. 2) were made after several cycles of CLEANing in Difmap. Phase-only self-calibration was applied for the brighter sources (i.e. when the sum of the CLEAN component flux densities exceeded ∼10 mJy) over time intervals not shorter than the length of scans spent on the sources (see Table 3). In the cases where phase self-calibration was not attempted at all, we expect a loss of coherence of about 5% (cf. Martí-Vidal et al. 2010) in the phase-referencing process, which may lead to an underestimate of the flux density values by this factor. In the images, the lowest contours are drawn at ∼3σ image noise levels. The expected theoretical thermal noise values were 15−22 μJy/beam (1σ), assuming no data loss during the experiment. The image parameters are summarised in Table 3.

[2] http://www.vlba.nrao.edu/astro/calib/index.shtml

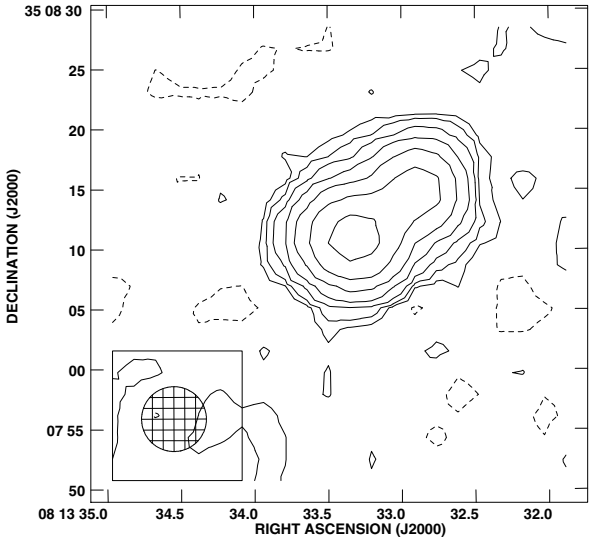

Fig. 1. The 1.4-GHz image of J0813+3508 from the VLA FIRST survey (White et al. 1997). The peak brightness is 22.5 mJy/beam, the lowest contour levels are drawn at ±0.25 mJy/beam, the positive contour levels increase by a factor of 2. The circular Gaussian restoring beam size is 5.″4 (*FWHM*), as indicated in the lower-left corner. The northwestern radio companion (top right) is catalogued as another source in FIRST, 6.″8 away from the quasar (in the centre).

4. Results

The five targeted high-redshift quasars were clearly detected and imaged with the EVN at both 1.6 GHz and 5 GHz (Fig. 2). However, we could not detect any mas-scale compact radio source at the position of the nearby (6.″8) FIRST radio companion (Fig. 1) to J0813+3508, at a brightness level of 0.3 mJy/beam (3σ). This indicates that the secondary source is extended and thus completely resolved in our VLBI experiments; notably, the position angle of the jet-like structure in our VLBI images of J0813+3508, especially at 1.6 GHz (Fig. 2, top left) practically coincides with that of the FIRST companion. Based on this directional coincidence, we believe that there is a physical association between the two radio sources. This is further supported by the fact that the visibility amplitudes on the shortest and most sensitive baseline from Effelsberg to Westerbork were somewhat higher than could be fully accounted for with the CLEAN

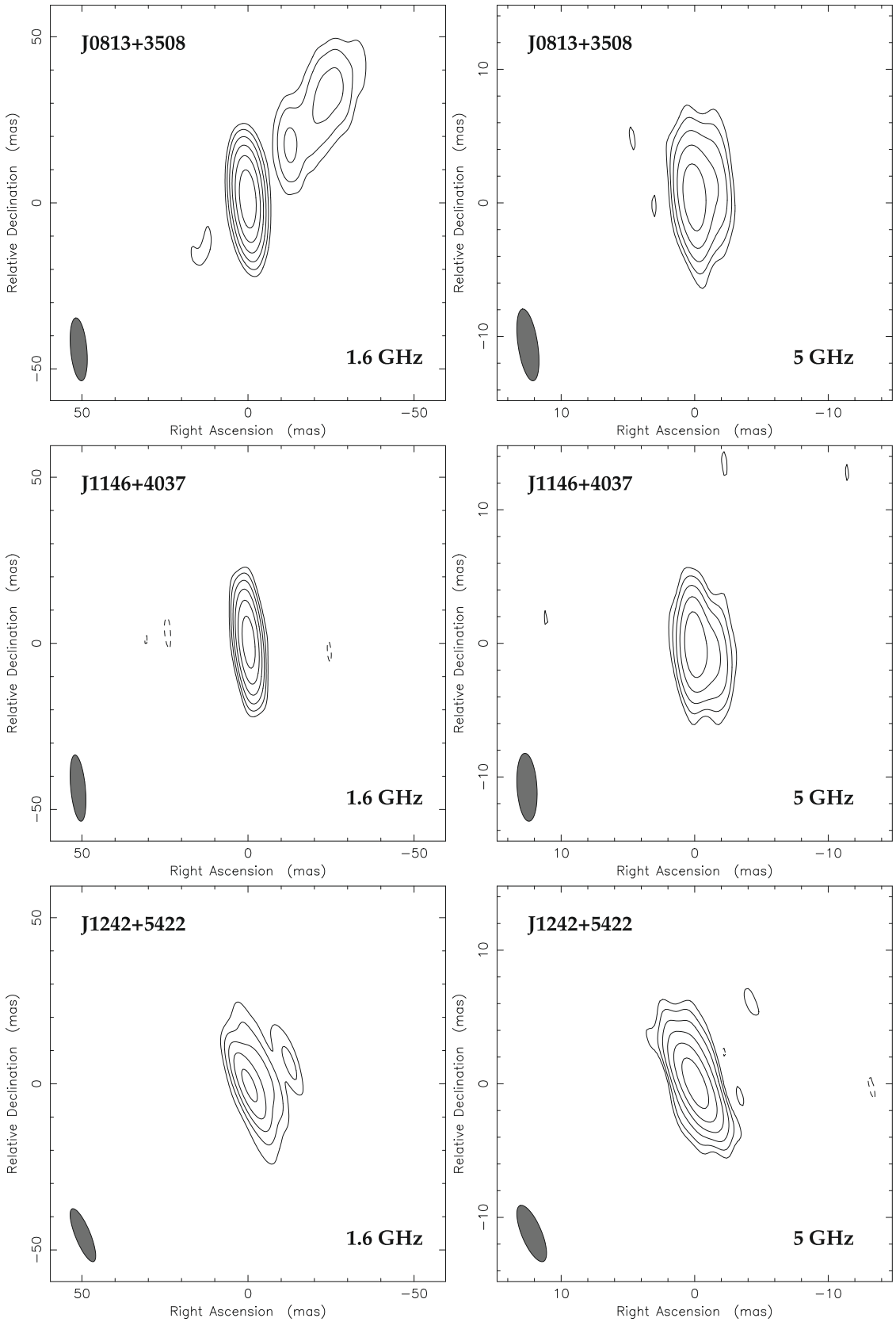

Fig. 2. The naturally weighted 1.6-GHz *(left column)* and 5-GHz *(right column)* VLBI images of the quasars. The image parameters (peak brightness, lowest contour level corresponding to ∼3σ image noise, restoring beam size, and orientation) are listed in Table 3. The full width at half maximum (*FWHM*) of the Gaussian restoring beam is indicated with an ellipse in the lower-left corners. The positive contour levels increase by a factor of 2. The coordinates are related to the brightness peak of which the absolute position is given in Table 4.

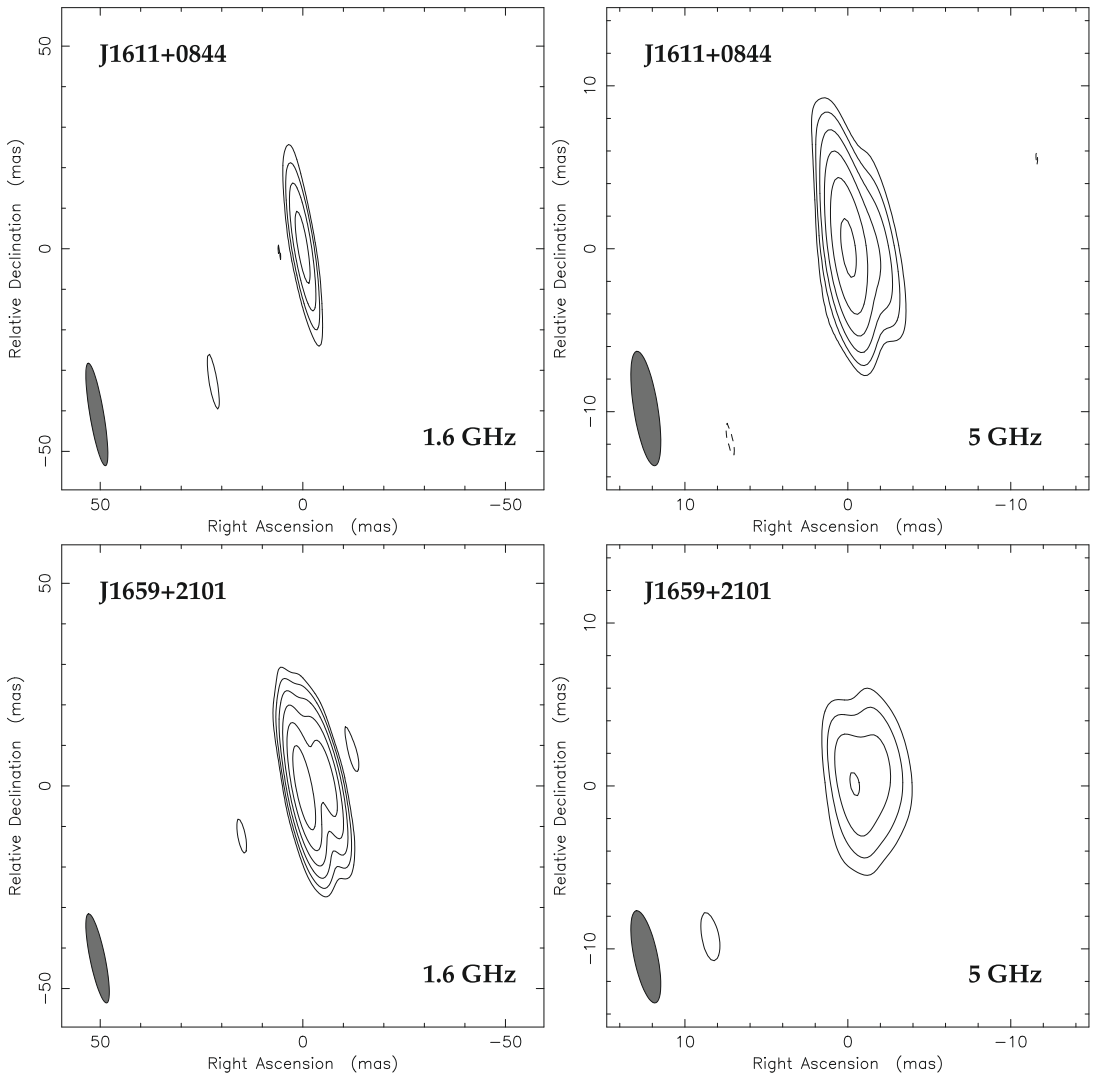

Fig. 2. continued.

Table 3. VLBI image parameters for Fig. 2.

Source name	ϕ	ν	Peak	Contour	Restoring beam	
	°	GHz	mJy/beam		mas×mas	PA (°)
J0813+3508	1.50	1.6	11.4	0.20	19.0 × 4.9	5.3
		5	4.0*	0.15	5.4 × 1.5	8.6
J1146+4037	0.64	1.6	14.7	0.30	20.1 × 4.4	5.4
		5	6.0*	0.20	5.1 × 1.5	3.6
J1242+5422	2.09	1.6	12.1	0.60	17.1 × 4.5	22.2
		5	7.9	0.15	4.5 × 1.5	22.7
J1611+0844	1.83	1.6	11.1	1.00	25.7 × 3.4	9.6
		5	9.4	0.25	7.1 × 1.5	9.1
J1659+2101	2.65	1.6	16.6	0.30	22.4 × 3.7	11.6
		5	4.2	0.50	5.8 × 1.4	11.7

Notes. Column 1 – source name (J2000); Col. 2. – angular separation from the phase-reference calibrator source (°); Col. 3 – observing frequency (GHz); Col. 4 – peak brightness (mJy/beam); cases where phase self-calibration was not applied are marked with asterisks; Col. 5 – lowest contour level (mJy/beam) corresponding to ∼3σ image noise; Col. 6 – Gaussian restoring beam size (mas × mas); Col. 7 – restoring beam major axis position angle (°) measured from north through east.

model components derived from the full VLBI array data. From poorly constrained Gaussian model fitting, there was a hint on an extended component about 0.″6 away from the compact "core" to the northwest in the continuation of the ∼10-mas scale jet and in the direction of the FIRST radio companion.

Table 4. Measured coordinates of the five radio quasars at $z > 4.5$ imaged with VLBI.

Source name	Right ascension	Declination	Uncertainties	
	h m s	° ′ ″	mas	mas
J0813+3508	08 13 33.32789	35 08 10.7698	0.4	0.5
J1146+4037	11 46 57.79043	40 37 08.6256	0.3	0.4
J1242+5422	12 42 30.58994	54 22 57.4524	3.9	1.9
J1611+0844	16 11 05.65000	08 44 35.4776	0.5	0.4
J1659+2101	16 59 13.22857	21 01 15.8087	1.0	1.1

Notes. Column 1 – source name; Col. 2 – J2000 right ascension ($^{h\,m\,s}$); Col. 3 – J2000 declination (° ′ ″); Col. 4 and 5 – estimated positional uncertainties in right ascension and declination (mas).

The coordinates of the brightness peaks are estimated from the 5-GHz images using the AIPS task and listed in Table 4. The uncertainties are determined by the phase-reference calibrator source position accuracy, the target-calibrator angular separation, the angular resolution of the interferometer array, and the signal-to-noise ratio.

Table 5. The parameters derived for the quasars from VLBI imaging.

Source name	Complete VLBI flux density (mJy)		Main component flux density (mJy)		α	Size	T_B	L
	at 1.6 GHz	at 5 GHz	at 1.6 GHz	at 5 GHz		mas	10^9 K	10^{26} W Hz^{-1}
J0813+3508	17.1 ± 0.9	7.3 ± 0.4*	12.8 ± 0.6	6.8 ± 0.3*	−0.6	1.18 ± 0.02	1.5 ± 0.1	8.4 ± 0.4
J1146+4037	15.5 ± 0.8	8.6 ± 0.4*	15.5 ± 0.8	8.4 ± 0.4*	−0.5	0.74 ± 0.01	4.5 ± 0.3	10.7 ± 0.5
J1242+5422	17.7 ± 0.9	9.7 ± 0.5	17.1 ± 0.9	9.4 ± 0.5	−0.5	0.67 ± 0.01	5.9 ± 0.5	9.0 ± 0.5
J1611+0844	13.0 ± 0.8	12.9 ± 0.6	13.0 ± 0.8	12.4 ± 0.6	−0.0	0.85 ± 0.01	4.7 ± 0.3	4.6 ± 0.2
J1659+2101	29.3 ± 1.5	10.6 ± 0.7	19.7 ± 1.0	10.6 ± 0.7	−0.6	3.07 ± 0.12	0.3 ± 0.04	12.3 ± 0.8

Notes. Column 1 – source name; Col. 2-3 – complete VLBI flux density at 1.6 GHz and 5 GHz (mJy); Col. 4–5 – main component VLBI flux density at 1.6 GHz and 5 GHz (mJy); Col. 6 – two-point spectral index of the main component; Col. 7 – fitted circular Gaussian diameter (*FWHM*) for the main component at 5 GHz (mas); Col. 8 – rest-frame brightness temperature at 5 GHz (10^9 K); Col. 9 – rest-frame monochromatic 5-GHz luminosity (10^{26} W Hz^{-1}). The VLBI flux density calibration uncertainties are assumed as 5%. The statistical errors of the fitted model parameters are estimated according to Fomalont (1999).
(*) Flux density value corrected for an estimated coherence loss of 5%.

Difmap was used to fit circular Gaussian brightness distribution model components to the interferometric visibility data of the five quasars detected. We calculated the two-point spectral indices for the bright central components from the model flux densities. From the 5-GHz data, we also derived the brightness temperatures of these dominant components as

$$T_B = 1.22 \times 10^{12}(1+z)\frac{S}{\vartheta^2 \nu^2} \ \text{[K]}, \quad (1)$$

where z is the redshift, S the flux density (Jy), ν the observing frequency (GHz), and ϑ the full width at half maximum (*FWHM*) size of the Gaussian measured in mas (e.g. Condon et al. 1982). The model parameters, and the values derived from them are given in Table 5.

5. Discussion

All of the $z > 4.5$ quasars we imaged are somewhat resolved, often with structures extending up to several 10 mas (Fig. 2). For comparison, a 1 mas angular size corresponds to 6.3–6.6 pc projected linear size, depending on the actual redshift of the object. The measured brightness temperatures ($T_B \sim 10^8$–10^9 K; Table 5) clearly indicate AGN activity, but are at least an order of magnitude lower than the equipartition value estimated for relativistic compact jets ($T_{B,eq} \simeq 5 \times 10^{10}$ K; Readhead 1994). It may suggest that (i) in the radio spectrum of the sources we probe regions far away from the peak frequency caused by synchrotron self-absorption; (ii) the jet viewing angles are at least moderate, and in fact we experience Doppler-deboosting of the emission; or (iii) the intrinsic brightness temperatures of compact jets at very high redshift are significantly lower than the equipartition value. Except for one flat-spectrum source (J1611+0844), the spectra of the quasar "cores" (i.e. the main components) in our sample are steep ($\alpha \leq -0.5$; Table 5). The intrinsic brightness temperature was determined for the blazar J1430+4204 ($z = 4.72$) by comparing the variability brightness temperature and the one measured with VLBI. It was found that $T_{B,int} \simeq T_{B,eq}$ (Veres et al. 2010), so there is no reason to assume that the intrinsic brightness temperatures are generally lower at $z > 4.5$.

A possible signature of the blazar nature of a source is its strong variability. We can look for an indication of long-term variability, if we compare the 1.4-GHz flux densities taken from the VLA FIRST catalogue (Table 2, last column) with our 1.6-GHz flux densities measured in our EVN run (Table 5). Since our angular resolution is much higher, if a source is stationary, then one would expect the VLBI flux densities to be lower than or at best equal to the VLA values within the uncertainties. This is the case for all our sources but J1611+0844. That J1611+0844 – the only flat-spectrum source in our sample – has nearly 50% higher flux density measured at a later epoch at much higher resolution proves its non-stationarity. Both the variability and the flat spectrum argue for Doppler boosting, but the measured brightness temperature of this source does not support it. In the case of J1611+0844, the observed one-sided compact core-jet structure at 5 GHz and the quasar classification can just be made consistent with the simple orientation-dependent unified picture of radio-loud AGNs (e.g. Urry & Padovani 1995). The apparent deboosting (Doppler factor $\delta = T_B/T_{B,eq} \simeq 0.1$) can be explained if, e.g., we assume a $\theta = 45°$ jet angle to the line of sight and an extremely (but not impossibly) large bulk Lorentz factor ($\gamma \simeq 35$).

The case of J0813+3508 is similarly puzzling. If, as our data suggest, its FIRST companion (Fig. 1) is associated with the quasar at $z = 4.92$, the projected linear size of the source is 43 kpc. This means that J0813+3508 could be the quasar with the most extended radio jet known at an extremely high redshift (cf. Cheung et al. 2005, 2008). The markedly one-sided arcsecond-scale radio structure suggests Doppler boosting and a small jet angle to the line of sight. However, the measured $\sim 10^9$ K brightness temperature and the steep spectrum of the compact VLBI component do not support this view. It is possible that there is a significant misalignment between the mas-scale and arcsecond-scale jet, or – less probably – the jet in this quasar is intrinsically one-sided. An alternative scenario is that we see an expanding and extended radio source with double hot spots, of which the nearest and approaching one is detected with VLBI. Future sensitive radio interferometric observations at intermediate angular resolutions could help reveal the true nature of this object (or these objects).

The remaining three sources (J1146+4037, J1242+5422 and J1659+2101) are quite alike in their compact structure (Fig. 2), steep spectra, and luminosity (Table 5). The quasar J1659+2101 is somewhat more resolved than the others. Notably, the two most distant ($z \sim 6$) quasars (J0836+0054, Frey et al. 2003, 2005; J1427+3312, Frey et al. 2008b; Momjian et al. 2008) observed with VLBI to date share much similar properties.

The rest-frame 5-GHz luminosities of the main components of our sources ($L \sim 10^{26}$–10^{27} W Hz^{-1}; Table 5) are comparable to the values of a large sample of gigahertz peaked-spectrum (GPS) and compact steep-spectrum (CSS) sources compiled by O'Dea (1998). Our values refer to the VLBI components and can therefore be regarded as lower limits to the radio luminosities of the whole sources. We found no evidence of any significantly

Doppler-boosted radio emission in our cases, so that the measured luminosities indicate intrinsically powerful sources.

GPS and CSS sources are thought to be young, evolving objects, and/or perhaps "frustrated" ones that are confined by the dense ambient gas (see O'Dea 1998 for a review). A subclass of these sources are the CSOs, which show nearly symmetric double or triple morphology when imaged at VLBI resoulution. According to the model of Falcke et al. (2004), our high-redshift steep-spectrum objects may represent GPS sources at early cosmological epochs. The first generation of supermassive black holes could have powerful jets that developed hot spots well inside their forming host galaxy, on linear scales of 0.1−10 kpc. Taking the relation between the source size and the turnover frequency observed for GPS sources into account, and for hypothetical sources matching the luminosity and spectral index of ours, Falcke et al. (2004) predict that the angular size of the smallest (∼100 pc) of these early radio-jet objects would be in the order of 10 mas at $z \sim 5$, and the observed turnover frequency in their radio spectra would be around 500 MHz. These angular sizes are indeed seen in our VLBI images (Fig. 2). To confirm the low-frequency turnover, high-resolution interferometric flux density measurements would be needed at multiple frequencies down to the 100-MHz range – a task well-suited to the Square Kilometre Array (SKA) now under development, in its high-resolution configuration. In a sense, the observed spectral properties of high-redshift sources are a resurrection of the indication on "humped" spectra of high-redshift quasars found more than 20 years ago when the highest known redshift was below 4 (Peterson et al. 1982; O'Dea 1990).

Currently we do not see many blazars at $z \sim 5$ or higher. According to Table 1, the most distant blazar imaged with VLBI to date (J0906+6930; Romani et al. 2004) has a redshift of 5.47. On the other hand, one would naively expect highly relativistically beamed, flat-spectrum radio sources to dominate the high-redshift VLBI samples. Whether the apparent absence of very high-redshift blazars is a result of some selection effect (i.e. the lack of redshift measurements), the poor statistics due to the small sample, or has a real physical cause, is to be addressed with further observations. Indeed, there are indications that blazars are not very common at the highest redshifts. Based on the evolving gamma-ray luminosity function, Inoue et al. (2010) expect that the Fermi Gamma-ray Space Telescope will find a few (i.e. the order of unity) blazars at $z \sim 6$ over a period of 5 years. For the strong sources, there is a positive correlation between the gamma-ray and the parsec-scale synchrotron radio emission, with the gamma-detected sources having on average higher brightness tempeartures in the radio (e.g. Kovalev et al. 2009). Thus the Fermi Large Area Telescope (LAT) potentially selects the brightest radio sources that would be natural targets for follow-up with VLBI.

6. Conclusions

We imaged five distant radio quasars at $4.5 < z < 5$ with the EVN at two frequencies (1.6 and 5 GHz), almost doubling the currently known sample of quasars imaged with VLBI at $z > 4.5$. The phase-referenced observations allowed us to derive accurate astrometric positions for our targets. The slightly resolved mas- and 10-mas-scale radio structures, the measured moderate brightness temperatures ($\sim 10^8$–10^9 K), and the steep spectra in all but one case suggest that our sample of compact radio sources at $z > 4.5$ is dominated by objects that do not resemble blazars. One of the quasars (J0813+3508) is likely to be extended to ∼7″ which corresponds to a 43 kpc projected linear size. It is possible that we see young, evolving, and compact GPS-like objects that are signatures of early galaxy formation where the expanding powerful synchrotron radio sources are confined by the dense interstellar medium.

Acknowledgements. The EVN is a joint facility of European, Chinese, South African, and other radio astronomy institutes funded by their national research councils. This work has benefitted from research funding from the European Community's Sixth Framework Programme under RadioNet R113CT 2003 5058187, the Hungarian Scientific Research Fund (OTKA, grant No. K72515), and the European Community's Seventh Framework Programme under grant agreement No. ITN 215212 "Black Hole Universe".

References

Beasley, A. J., & Conway, J. E. 1995, in Very Long Baseline Interferometry and the VLBA, ed. J. A. Zensus, P. J. Diamond, & P. J. Napier, ASP Conf. Ser., 82, 327
Best, P. N., Kauffmann, G., Heckman, T. M., et al. 2005, MNRAS, 362, 25
Chen, G., & Ratra, R. 2003, ApJ, 582, 586
Cheung, C. C., Wardle, J. F. C., & Lee, N. P. 2005, in Proc. 22nd Texas Symposium on Relativistic Astrophysics, ed. P. Chen, E. Bloom, G. Madejski, & V. Patrosian (Palo Alto: SLAC), paper 1613
Cheung, C. C., Stawarz, Ł., Siemiginowska, A., et al. 2008, in Extragalactic Jets: Theory and Observation from Radio to Gamma Ray, ed. T. A. Rector, & D. S. De Young, ASP Conf. Ser., 386, 462
Condon, J. J., Condon, M. A., Gisler, G., & Puschell, J. J. 1982, ApJ, 252, 102
Diamond, P. J. 1995, in Very Long Baseline Interferometry and the VLBA, ed. J. A. Zensus, P. J. Diamond, & P. J. Napier, ASP Conf. Ser., 82, 227
Falcke, H., Körding, E., & Nagar, N. M. 2004, NewAR, 48, 1157
Fomalont, E. B. 1999, in Synthesis Imaging in Radio Astronomy II, ed. G. B. Taylor, C. L. Carilli, & R. A. Perley, ASP Conf. Ser., 180, 301
Frey, S., Mosoni, L., Paragi, Z., & Gurvits, L. I. 2003, MNRAS, 343, L20
Frey, S., Paragi, Z., Mosoni, L., & Gurvits, L. I. 2005, A&A, 436, L13
Frey, S., Gurvits, L. I., Paragi, Z., et al. 2008a, A&A, 477, 781
Frey, S., Gurvits, L. I., Paragi, Z., & Gabányi K. É. 2008b, A&A, 484, L39
Gurvits, L. I., Kellermann, K. I., & Frey, S. 1999, A&A, 342, 378
Inoue, Y., Inoue, S., Kobayashi, M. A. R., et al. 2010, MNRAS, in press [arXiv:1007.4379]
Jackson, J. C. 2004, J. Cosmol. Astropart. Phys., 11, 007
Jackson, J. C. 2008, MNRAS, 390, L1
Kellermann, K. I., & Pauliny-Toth, I. I. K. 1969, ApJ, 155, L71
Kellermann, K. I., Vermeulen, R. C., Zensus, J. A., Cohen, M. H., & West, A. 1999, NewAR, 43, 757
Kovalev, Y. Y., Aller, H. D., Aller, M. F., et al. 2009, ApJ, 696, L17
Lima, J. A. S., & Alcaniz, J. S. 2002, ApJ, 566, 15
Martí-Vidal, I., Ros, E., Pérez-Torres, M. A., et al. 2010, A&A, 515, A53
Momjian, E., Petric, A. O., & Carilli, C. L. 2004, AJ, 127, 587
Momjian, E., Carilli, C. L., & Petric, A. O. 2005, AJ, 129, 1809
Momjian, E., Carilli, C. L., & McGreer, I. D. 2008, AJ, 136, 344
Mosoni, L., Frey, S., Gurvits, L. I., et al. 2006, A&A, 445, 413
O'Dea, C. P. 1990, MNRAS, 245, 20
O'Dea, C. P. 1998, PASP, 110, 493
Paragi, Z., Frey, S., Gurvits, L. I., et al. 1999, A&A, 344, 51
Peterson, B. A., Savage, A., Jauncey, D. L., & Wright, A. E. 1982, ApJ, 260, L27
Readhead, A. C. S. 1994, ApJ, 426, 51
Romani, R. W., Sowards-Emmerd, D., Greenhill, L., & Michelson, P. 2004, ApJ, 610, L9
Sahni, V., & Starobinsky, A. 2000, Int. J. Mod. Phys. D, 9, 373
Schneider, D. P., Hall, P. B., Richards, G. T., et al. 2007, AJ, 134, 102
Shepherd, M. C., Pearson, T. J., & Taylor, G. B. 1994, BAAS, 26, 987
Urry, C. M., & Padovani, P. 1995, PASP, 107, 803
Veres, P., Frey, S., Paragi, Z., & Gurvits, L. I. 2010, A&A, 521, A6
Vishwakarma, R. G. 2000, Class. Quantum Grav., 17, 3833
Vishwakarma, R. G. 2001, Class. Quantum Grav., 18, 1159
White, R. L., Becker, R. H., Helfand, D. J., & Gregg, M. D. 1997, ApJ, 475, 479
Wilkinson, P. N., Polatidis, A. G., Readhead, A. C. S., Xu, W., & Pearson, T. J. 1994, ApJ, 432, L87